

# PLASMONIC NANOSTRUCTURES AND METAMATERIALS FOR NANOSCALE LIGHT-MATTER INTERACTION

A Dissertation Proposal  
Presented to  
The Academic Faculty

by

Seyed Hamed Shams Mousavi

In Partial Fulfillment  
of the Requirements for the Degree  
Doctor of Philosophy in the  
School of Electrical and Computer Engineering

Georgia Institute of Technology  
December, 2018

**COPYRIGHT © 2018 BY S. H. SHAMS MOUSAVI**



# PLASMONIC NANOSTRUCTURES FOR NANOSCALE LIGHT-MATTER INTERACTION

Approved by:

Dr. Ali Adibi, Advisor  
School of Electrical and Computer  
Engineering  
*Georgia Institute of Technology*

Dr. Hayk Harutyunyan  
Department of Physics  
*Emory University*

Dr. Wenshan Cai  
School of Electrical and Computer  
Engineering  
*Georgia Institute of Technology*

Dr. Benjamin D.B. Klein  
School of Electrical and Computer  
Engineering  
*Georgia Institute of Technology*

Dr. Mostafa A. El-Sayed  
School of School of Chemistry and  
Biochemistry  
*Georgia Institute of Technology*

Dr. Zhigang Zhiang  
School of Physics  
*Georgia Institute of Technology*

Date Approved: 07 / 11 / 2018

## ACKNOWLEDGMENT

First and foremost, I would like to thank my advisor, Professor Ali Adibi, for his continuous support throughout my time at Georgia Tech. I could not appreciate more the confidence he had in me choosing my own research topic. This work wouldn't have come to fruition without Prof. Adibi's extensive experience in the field, his high standard for academic achievement, and his acumen in guiding the direction of my research.

I would also like to thank Prof. Mostafa El-Sayed for his guidance and support throughout my research, even though he was not officially my advisor. He always dedicated some of his time to discuss my research despite his very busy schedule. It was one of the greatest opportunities of my life to work with him and to learn a great deal from his extensive experience and vision in the field of nanotechnology.

The friendly and scientific nature of Photonic Research Group made it a truly ideal working place for me. I had the privilege of working with outstanding and at the same time humble experts in photonics in this group. In particular, I would like to thank Dr. Reza Eftekhar for dedicating a great amount of time mentoring me throughout my research. Without his help, I would not have been able to overcome the many obstacles that I faced in various research projects. Also special thanks to Dr. Amir Atabaki and Dr. Maysam Chamanzar, from whom I learned a lot about photonics and microfabrication.

I would also like to thank Dr. Farshid Ghasemi, Dr. Nasrin Hooshmand, Dr. Amirhossein Hosseinnia, Dr. Zhixuan Xia, Dr. Hesam Morardinejad and Tianren Fan for all their help and great discussions. I had the privilege to work with them in different projects, resulting in many research achievements.. Also, special thank to Dr. Razi Dehghannasiri, Dr.

Ahmad Usman, Yashar Kiarashi and Mohammad Reza Zand for proofreading this manuscript.

I would like to acknowledge the staff of Institute for Electronics and Nanotechnology (IEN) for their dedication in keeping this place to run smoothly. In particular, I want to acknowledge Gary Spinner, Devin Brown and Eric Woods. Without their help in dire situations, I would have missed some of the very important conference and report deadlines.

Last but not least, I am grateful to my family for their love and support from the very moment I entered their lives. I could not be enjoying my life as much as I do today, if it was not for their support and sacrifices.

# TABLE OF CONTENTS

<b>LIST OF TABLES</b>	<b>v</b>
<b>LIST OF FIGURES</b>	<b>vi</b>
<b>SUMMARY</b>	<b>ix</b>
<b>CHAPTER 1. Introduction</b>	<b>1</b>
1.1 Plasmonics and Light-Matter Interaction	1
1.2 Organization of the Thesis	5
<b>CHAPTER 2. FUNDAMENTAL CONCEPTS AND THEORETICAL BACKGROUND</b>	<b>8</b>
2.1 Fundamental Concepts of Plasmonics	8
2.1.1 What are Surface Plasmons?	8
2.1.2 Surface Plasmon Dispersion Relation	11
2.1.3 Surface Plasmon Propagation Length and Skin Depth	14
2.1.4 Surface plasmons Group Velocity and Density of States	15
2.1.5 Plasmonic Waveguides and Cavities	19
2.2 Plasmonic Material Platforms	22
2.3 Basics of Plasmonic Metamaterials	26
2.4 Light-Matter Interaction in Two-Dimensional Materials	32
2.4.1 Graphene, Hexagonal Boron Nitride and Black Phosphorous	32
2.4.2 Two-Dimensional Transition-Metal Dichalcogenides	35
2.4.3 Polaritons in Two-Dimensional Materials	38
<b>CHAPTER 3. Molecular Sensing Using Plasmonic Nanocubes</b>	<b>40</b>
3.1 Label-Free Biosensing Using Plasmonic Nanocavities	42
3.1.1 Sensitivity Factor of a Nanocavity	42
3.2 Ultrasensitive Molecular Sensing Using Plasmonic Nanocube Chains	45
3.2.1 Classical Electromagnetic Coupling	46
3.2.2 Plasmon Tunnelling Effect in Nanocube Chains	49
<b>CHAPTER 4. Application of Lattice Plasmons in Surface Enhanced Raman Spectroscopy</b>	<b>54</b>
4.1 Collective Resonance of Nanoantennas and Lattice Plasmons	55
4.2 Emission Enhancement by Purcell Effect	57
4.3 Surface-Enhanced Raman Spectroscopy Using Lattice Plasmons	58
<b>CHAPTER 5.</b>	<b>67</b>
5.1 Chirality in Materials and Metamaterials	68
5.1.1 What is chirality?	68
5.1.2 Circular Dichroism, Ellipticity and Optical Rotary Dispersion	69

5.1.3	Chiral Light-Matter Interaction	71
5.1.4	Planar Chirality	72
<b>5.2</b>	<b>Chiroptical Sensing Using an On-Resonance Chiral Metamaterial</b>	<b>73</b>
<b>CHAPTER 6.</b>		<b>88</b>
<b>6.1</b>	<b>Classical Description of Nonlinear Light-Matter Interaction</b>	<b>89</b>
<b>6.2</b>	<b>Nonlinear Plasmonics</b>	<b>91</b>
6.2.1	Second-order Nonlinearity in Plasmonic Nanostructures	91
6.2.2	Other Nonlinear Effects in Plasmonic Nanostructures	92
6.2.3	Phase-Matching and Quasi-Phase-Matching	94
<b>6.3</b>	<b>Phase-Matched Nonlinear Plasmonic Nanostructure</b>	<b>95</b>
<b>6.4</b>	<b>Preliminary Experimental Results</b>	<b>98</b>
6.4.1	Effect of Stationary Band-Edge LPs at the Fundamental Mode	98
6.4.2	Effect of Phase-Matching between Fundamental and Second-Harmonic LPs	100
<b>CHAPTER 7.</b>		<b>103</b>
<b>7.1</b>	<b>Population Inversion, Stimulated Emission and Lasing Action</b>	<b>104</b>
<b>7.2</b>	<b>Temperature-Dependent Photoluminescence of 2D TMDCs</b>	<b>107</b>
<b>7.3</b>	<b>Plasmon-Exciton Coupling and Plasmonic Nanolasers</b>	<b>108</b>
<b>7.4</b>	<b>Monolayer TMDC Plasmonic Nanolaser</b>	<b>110</b>
7.4.1	Design and fabrication of the Plasmonic Nanocavity	111
<b>7.5</b>	<b>Electrification of Monolayer TMDC Plasmonic Nanolaser</b>	<b>119</b>
7.5.1	Two-dimensional TMDC light-emitting diodes	119
7.5.2	Design and fabrication of <i>MoSe2</i> plasmonic diode laser	121
<b>7.6</b>	<b>Lasing Action in monolayer TMDC-Loaded Plasmonic Nanocavities</b>	<b>126</b>
<b>CHAPTER 8.</b>		<b>130</b>
<b>8.1</b>	<b>Brief Summary of Contributions</b>	<b>130</b>
<b>8.2</b>	<b>Future Directions</b>	<b>133</b>
<b>APPENDIX A.</b>		<b>136</b>
<b>A.1.</b>	<b>Theory of Resonant Metamaterial Enhanced Chiral Light-Matter Interaction</b>	<b>136</b>
<b>REFERENCES</b>		<b>139</b>

## LIST OF TABLES

Table 1	Generalized Drude parameters for the four most common plasmonic material platforms.	24
Table 2	Material classification, energy bandgap, main polariton type and field-effect mobility, $\mu_{FE}$ (at room temperature), exciton binding energy, $\mathcal{E}_b$ , radiative lifetime, $\tau_r$ , and workfunction $ e\phi $ for a few 2D materials of interest: $MoS_2$ , $MoSe_2$ , $WS_2$ , $WSe_2$ , Graphene, hexagonal Boron Nitride (h-BN) and Black Phosphorus (Black P).	39
Table 3	Optical properties of the three LSPR modes of the structure shown in Fig. 13 from FDTD simulations.	61

## LIST OF FIGURES

Figure 1	Confinement and light-matter interaction.	3
Figure 2	Excitation of surface plasmons on a thin metallic film.	11
Figure 3	Qualitative representation of dispersion relation and LDOS of an infinite metal slab and a metallic nanosphere.	19
Figure 4	Distribution of electric-field enhancement factor in a few plasmonic and photonic waveguides and resonators of interest.	21
Figure 5	Electronic bandstructure of potential plasmonic material with no interband and intraband transition losses.	25
Figure 6	Two examples of metamaterials designed for sensing applications.	30
Figure 7	New developments in metamaterials research.	31
Figure 8	Atomic structure of graphene, <i>hBN</i> and Black P.	34
Figure 9	Qualitative electronic bandstructure of graphene and TMDCs.	35
Figure 10	Properties of valley excitons in 2D TMDCs.	37
Figure 11	Tuning surface plasmon resonance in plasmonic nanoantennas.	41
Figure 12	Extinction spectra of plasmonic NC chains of different lengths in F-F and E-E configurations.	46
Figure 13	Sensitivity factor $m_b$ of plasmonic NC chains of different lengths in F-F and E-E configurations.	47
Figure 14	Evolution of the sensitivity factor $m_b$ vs. the length of NC chains.	48
Figure 15	Normalized electric-field distribution of AgNC chains in E-E configuration.	49
Figure 16	Naturally dispersed AuNCs on a surface tend to create face-to-face sub-nanometer gaps.	50
Figure 17	Permittivity of the Au Jellium used to estimate the effect of plasmon tunneling in QCM simulation.	51
Figure 18	Effect of plasmon tunneling on the optical response of NC chains.	52
Figure 19	Electromagnetic field distribution calculated for the E-E oriented AuNC trimer at 0.2 nm separation distance from the QCM model.	53

Figure 20	Optical processes used in vibration spectroscopy.	55
Figure 21	Fano resonance in optics.	57
Figure 22	Scanning electron microscope image of the bilayer nanoantenna array with 45 degree tilt, the inset shows a close-up view of one unit-cell.	60
Figure 23	Distribution of the enhancement factor at different wavelengths.	61
Figure 24	Tuning of the LP band-edge by change the periodicity.	62
Figure 25	Excitation and emission enhancement factor spectra.	63
Figure 26	SERS spectra acquired from nanostructure with the overall design of Fig. 12. <i>a</i> and varying periodicity and pillar radius.	65
Figure 27	Two examples of chiral metamaterials.	69
Figure 28	Two enantiomers of a chiral metasurface designed for valley current generation	73
Figure 29	Design and fabrication of the bilayer chiral metamaterial.	77
Figure 30	Distribution of the chirality enhancement $\Upsilon$ and field enhancement $\Gamma$ factors.	79
Figure 31	Schematic diagram of the polarization-resolved reflection setup.	80
Figure 32	Differential reflectance $\Delta r$ of <i>Enant D</i> and <i>Enant L</i> prior to coating with the chiral biomolecules.	82
Figure 33	Metamaterial-Enhanced chiroptical sensing results.	86
Figure 34	Bulk second-order nonlinearity vs. surface second-order nonlinearity.	93
Figure 35	Typical acquired spectrum in SHG measurements from plasmonic nanostructures.	94
Figure 36	Band-diagram of the bilayer nanostructure at the sweeping range of the excitation pump and the SHG signal.	96
Figure 37	Schematic view of bilayer nanostructure used to study the effect of phase-matching	97
Figure 38	Quasi-phase-matching between FM and SH LP modes for $p = 580 \text{ nm}$ .	98
Figure 39	Linear and nonlinear response of the bilayer array at normal incidence.	99

Figure 40	Schematic view of angle-resolved SHG measurement setup.	101
Figure 41	Evolution of SESHG signal vs. excitation angle and pump wavelength	102
Figure 42	Four-level quantum model of the lasing action.	105
Figure 43	Temperature-dependant gain profile of 2D $MoS_2$ and $MoSe_2$ .	108
Figure 44	Lasing action in low-dimensional materials.	109
Figure 45	Schematic view of NS-NG plasmonic nanocavity	112
Figure 46	Optimization of NS-NG nanolaser with monolayer $MoS_2$ gain.	114
Figure 47	Spectral response and $\Gamma_x$ distribution of the $MoS_2$ -loaded nanocavity.	115
Figure 48	Fabrication of the NS-NG plasmonic nanocavity using FIB milling.	116
Figure 49	SEM image of $MoS_2$ plasmonic nanolaser after material transfer	118
Figure 50	Reflection spectra of the designed $MoS_2$ -based plasmonic nanolasers.	118
Figure 51	Two different type of LED designs using 2D TMDCs.	120
Figure 52	Metal-semiconductor Schottkey-Barrier diode in $Au$ and 2D TMDC ( $MX_2$ ) junction.	121
Figure 53	Optimization of NS-NG nanolaser with monolayer $MoSe_2$ as the gain medium.	122
Figure 54	Spectral response and $\Gamma_x$ distribution of the $MoSe_2$ -loaded nanocavity.	123
Figure 55	Fabrication of the 2D TMDC plasmonic diode laser.	124
Figure 56	Optical micrograph of the $MoSe_2$ nanolaser after dry transfer of the single-layer material.	125
Figure 57	Reflection spectra of the desinged $MoSe_2$ -based plasmonic nanolasers	126
Figure 58	Population levels of the $MoS_2$ plasmonic nanolaser at levels $ 0\rangle$ to $ 3\rangle$ for $p_{exc} = 0.99 mW$ .	127
Figure 59	Active numerical simulation of the monolayer $MoS_2$ plasmonic nanolaser with optical pumping using a CW laser polarized in x-direction with $\lambda_{exc} = 500 nm$ .	128
Figure 60	Active numerical modeling of the monolayer $MoSe_2$ plasmonic nanolaser with optical pumping using a CW laser polarized in x-direction with $\lambda_{exc} = 650nm$ .	129

## SUMMARY

The objective of this dissertation is to study the light-matter interaction phenomena at nanoscale in the presence of plasmonic nanostructures and metamaterials. Using the principles of nano-optics, a range of plasmonic nanodevices are developed for molecular sensing, nonlinear optics and surface plasmon lasing. This theoretical and experimental investigation is further extended by studying the effect of plasmon tunneling in sub-nanometer distances and light-matter interaction in atomically thin semiconductors adjacent to plasmonic nanostructures.

More specifically, chemically synthesized plasmonic nanocube dimers and chains are studied for ultrasensitive molecular sensing using the wavelength shift of their localized surface plasmon resonance. The effect of interparticle spacing and relative orientation of the nanocubes in the nanocube chains has also been analyzed. The band-edge lattice plasmon waves in plasmonic nanoantenna arrays have been studied and utilized for surface-enhanced Raman spectroscopy. Superchiral spectroscopy at the molecular level is demonstrated using a novel three-dimensional chiral metamaterial. Furthermore, surface-enhanced second harmonic generation in coupled plasmonic nanostructures that support sharp Fano-type resonance features, is studied theoretically and experimentally. Finally, a plasmonic nanolaser incorporating a plasmonic nanocavity and a monolayer of transition metal dichalcogenide is developed.

# CHAPTER 1.

## INTRODUCTION

### 1.1 Plasmonics and Light-Matter Interaction

Nearly all optical phenomena can be described as some form of interaction between matter and photons with energies in the range of 0.1 to 10 eV. In bulk materials, these interactions can result in many different near-field and far-field effects depending on material properties and the frequency of the incoming light. With optical nanostructures, whether photonic or plasmonic, the electromagnetic waves can be manipulated in a more sophisticated manner to implement functionalities that cannot be achieved in homogenous media. For instance, the law of *diffraction limit*, first formulated by Abbe [1], states that an optical beam with the wavelength  $\lambda$  propagating in a homogenous medium with the refractive index  $n$  and converging with an angle  $\theta$ , cannot be confined in a spot with a radius smaller than  $\lambda/2n \sin(\theta)$  (see Fig. 1. a). This law defines the resolution limit of the far-field optical microscopes, but in *near-field scanning optical microscopy* (NSOM) [2], this resolution limit is lifted using a nanoscale tip that excites and collects the light via evenancemt coupling. The evanescent fields that exist in the near-field of the NSOM tip are not limited by the diffraction limit of the propagative waves in far-field microscopy.

In the realm of integrated photonics, the cut-off frequency, which is directly related to the diffraction limit, determines the minimum feature size of photonic devices, perpendicular to the direction of propagation ( $\sim\lambda/2n$ ), including waveguides and resonators (see Fig. 1. b). This is the first advantage of plasmonic nanostructures. Since the surface plasmons are quasi-two-dimesnional (at the interface between metal and dielectric), it is possible to obtain a confined resonant or guided optical mode with much smaller dimensions in plasmonics,

enabling the design subwavelength optical devices such as waveguides, cavities, couplers, modulators, etc. As an example, Fig. 1.c shows four silver *nanoantenna* arrays, each containing a large array of plasmonic resonators with dimensions below 150 nm. The visible colors in this figure are the direct result of resonant optical modes of the nanoantennas that are tuned at different wavelengths in the visible range of spectrum.

Aside from the overall compactness of the plasmonics devices, the sub-wavelength dimension of plasmonic elements allows the design of a new class of photonic nano-devices, known as plasmonic *metamaterials* and *metasurfaces*<sup>1</sup>. At the core of each plasmonic metamaterial or metasurface is a plasmonic subunit known *meta-atom*, with an optical functionality that either not does not exist or is not pronounced in natural materials. Since the overall dimensions of the plasmonic meta-atoms are smaller than the operating wavelength, the incident light perceives a sufficiently dense 2D or 3D array of these meta-atoms as a uniform layer with designer optical properties, such as chirality, negative refraction, focalization with ultrathin layer, etc, which cannot be achieved with homogenous media.

The second advantage of the plasmonic nanostructures is their superior electromagnetic field *confinement* or *localization* compared to dielectric nanostructures. Higher field confinement results in higher *energy density* or *field enhancement* in the vicinity of plasmonic nanostructures, which is critical in enhancing a host of different optical effects arising from light-matter interaction. As an example, plasmonic nanostructures tend to be much more responsive to any perturbation in their surrounding environment, which can be used in high-sensitivity molecular sensing. In molecular sensing based on the measurement

---

<sup>1</sup> There is no universally accepted definition for the term metamaterial. In literature, other types of photonic structures composed of dielectrics sub-units or multiple layers of thin films are also categorized as optical metamaterials. Here, we are focusing on plasmonic metamaterials.

of resonance wavelength ( $\lambda_{res}$ ) in an optical cavity, which is a perturbation-based sensing method, the magnitude of perturbation, i.e.  $\lambda_{res}$ - shift induced by a molecule is directly proportional to the energy density at the point in space where the molecule is located. On the other hand, the minimum amount of perturbation that can be resolved by a noise-limited measurement system is proportional to its *Q-factor*<sup>1</sup>. Even though, the plasmonic nanocavities typically have lower Q-factors compared to their photonic counterparts (due to the high absorption of the available plasmonic materials), the much higher enhancement in energy density more than compensates for the lower Q-factors. As a result, perturbation-based plasmonic sensors tend to have higher *sensitivities* and *detection limits* compared to their photonic counterparts.

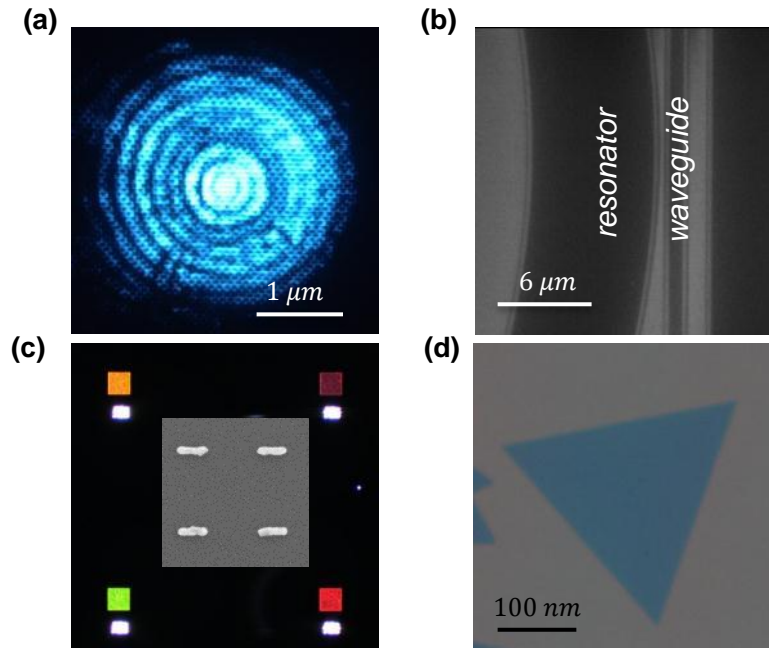


**Figure 1 - Confinement and light-matter interaction. (a) Airy disk [3] generated by focusing a laser beam on a flat surface. The diameter of the smallest disk is  $\lambda/(2 NA)$ ;  $NA = n \cdot \sin(\theta)$  being the numerical aperture of objective lens used to focus the light. (b) Scanning electron microscope (SEM) image of the coupling region between a silicon nitride ( $Si_3N_4$ ) micro-resonator and a  $Si_3N_4$  waveguide designed to operate at  $1550 \text{ nm}$ . This SEM image shows the typical dimensions of dielectric photonic components. (c) Dark-field optical micrograph of nanoantenna arrays with**

<sup>1</sup> The Q-factor of a resonance is defined as  $Q = \omega_0/\Delta\omega$ , where  $\omega_0$  is the center frequency and  $\Delta\omega$  is the full-width at half-maximum (FWHM) or the bandwidth of the resonance.

varying lengths, showing different scattering colors which are due to the difference in  $\lambda_{res}$  of the nanoantennas (d) A single atomic layer of  $MoSe_2$ , a two-dimensional material that we study in this dissertation

Energy localization is also critical in another class of light-matter interaction effects involving generation of light through different optical processes, including *spontaneous emission*, *stimulated emission* and *nonlinear generation of light*. For instance, spontaneous emission processes, including *fluorescence*, *Raman* and *photoluminescence*, occur at two-steps: a) the molecule (or atom) absorbs a photon from the incident light and transitions to an excited state; b) the excited molecule relaxes to the ground state, and radiates a photon with slightly lower energy. Since, both of these two steps scale quadratically with the field enhancement, optical resonators can be used to enhance spontaneous emission. The overall emission enhancement is relatively modest in the case of dielectric resonators, but significant in the case of plasmonic nanocavities (in excess of  $10^8$ ), giving rise to new emission-based sensing techniques, such as *surface-enhanced Raman spectroscopy*, which can be performed at the molecular level.

In the case of stimulated emission, the high localization of the energy density not only increases the efficiency of the emission process, but can induce an optical effect known as *population inversion*, with much lower excitation power threshold. This is the main premise of surface plasmon lasers, also known as *spasers* [4-6] and is particularly important when the *gain material*<sup>1</sup> is geometrically confined in a very small area, e.g. 2D materials with only a single (or few layers) of atoms. In general, given the quasi-2D nature of surface plasmons, plasmonic nanostructures are a great fit to enhance any type of light-matter interaction in all low-dimension materials, including the 2D materials.

---

<sup>1</sup> The gain material is the medium that undergoes the emission process.

A nonlinear optical processes is another example of light-matter interaction processes that strongly depend local energy density. Typically, high intensity excitation (or pump) lasers are needed to observe most nonlinear phenomena, given small *nonlinear susceptibility* of common materials. In general, there are two routes to reduce the intensity levels needed in nonlinear optics: a) utilization of high-Q free-space or intergrated photonic cavities which provide many more passes of the pump through the nonlinear medium, b) high localization of energy density, which can be achieved in plasmonic nanostructures, for instance. In the case of nonlinear optical effects that are bound to the surface, such as *surface second harmonic generation*, the quasi-2D nature of surface plasmons provides an additional advantage similar to the case of light-matter interaction in low-dimensional materials.

## 1.2 Organization of the Thesis

This thesis is organized in eight chapters. This brief introduction is continued with the theoretical background pertinent to plasmonics and light-matter interaction that are used throughout the thesis in Ch. 2. In particular, some relevant terminology such as *plasmon*, *polariton* and *exciton* are defined in this chapter. The conditions for having surface plasmons are derived and some of the basic plasmonic elements and their optical properties are introduced. Additionally, fundamental optical properties of two-dimensional materials are reviewed with a special focus on 2D transition metal dichalocegnides, which we shall see again in Ch. 7.

Chapters 3 – 5 are dedicated to the molecular sensing as an important application of nanoscale light-matter interaction. In Ch. 3, a linear perturbative molecular sensing method is discussed based on monitoring the localized surface plasmon resonance wavelength of

plasmonic nanocavities, with a particular focus on plasmonic nanocube chains, as an example of highly sensitive plasmonic sensors. The optical properties, performance characteristics, and sensitivity of this coupled nanocavity system are studied, first in the purely classical case. The effect of *plasmon tunneling* at sub-nanometer gaps is also discussed at the end this chapter. In Ch. 4, surface-enhanced-Raman spectroscopy is discussed as another sensing method based on detecting the Raman fingerprint of the molecules. A novel bilayer plasmonic nanostructure is introduced in this chapter, and I explain how lattice plasmons and Fano resonance in this system can be utilized for SERS-based sensing. In Ch. 5, I focus on superchirality and chiroptical spectroscopy, as a linear sensing method extended in the two spaces of polarization and wavelength to harvest more data. A new chiral metamaterial specifically designed for sensing is introduced in this chapter, and I explain how the on-resonance chiral interaction between a chiral biomolecule and chiral metamaterial can be utilized for sensing.

Chapters 6,7 are dedicated to the application of nano-optics to the light-matter interactions involving the generation of light by several different optical and electro-optical processes. In Ch. 6, I focus on nonlinear plasmonics and discuss plasmonic nanostructures that can be used to enhance a host of nonlinear optical processes including high harmonic generation and four-wave mixing. The special case of quasi-phase-matching of lattice plasmons is discussed in more detail as a means to increase the conversion efficiency in *surface-second-harmonic generation*. In Ch. 7, I focus on surface plasmon lasing in two-dimensional materials. A plasmonic nano-laser is presented that can achieve stimulated emission of plasmon-polaritons in a monolayer transition-metal dichalcogenides; a very promising class of 2D semiconductors.

Finally, in Ch. 8, we present a summary of our main contributions and discuss potential next steps and new directions that can be undertaken to expand our findings on each topic discussed in this dissertation.

## CHAPTER 2.

# FUNDEMENTAL CONCEPTS AND THEORETICAL BACKGROUND

This chapter is dedicated to the review of the theoretical background and fundamental concepts of plasmonics and nano-optics, as well as the light-matter interaction in 2D materials. In section 2.1, we start by defining plasmon as an important quasiparticle that has given its name to field of plasmonics. We continue by deriving the condition for the existence of surface plasmons, and their key optical properties and introduce plasmonic waveguides and nanocavities as the fundamental building blocks of plasmonic nanostructures. Plasmonic material platforms and their most common applications are reviewed in section 2.2 . In section 2.3, some basics of plasmonic metamaterials are reviewed with a special focus on the most recent developments in the field. Finally, the basic properties of a few 2D materials of interest in nano-optics and their potential applications are reviewed in section 2.4.

### 2.1 Fundamental Concepts of Plasmonics

#### 2.1.1 *What are Surface Plasmons?*

The first observation of plasmons is believed to be done in early twentieth century by *Robert Wood*, when he saw unusual patterns, when shining a metallic grating with polarized light, which is now known as *Wood's anomaly* [7]. However, the proper explanation of this phenomon took effect decades later, when *Pines* and *Bohn* showed that the free electrons in a metal can undergo collective oscillations due to Coulomb interaction and this collective

oscillation can interact strongly with light [8]. They introduced the concept of *plasmon* as the quanta of electron oscillation in a free electron gas, such as the one in metals. The name of this quasiparticle was chosen due to the resemblance of the electron oscillation in an electron gas to the movement of charged particles in a plasma. Later, Ritchie also predicted the formation of plasmons at the boundary of metals and dielectrics with much lower energy compared to the bulk plasmons [9]. In the field of plasmonics, we usually deal with this type of plasmons called *surface plasmons*, which are confined to the boundary of conductive media. Most properties of plasmons and surface plasmons can be described using classical electrodynamics. One notable exception is the *plasmon tunneling* effect, discussed in the next chapter.

Beyond a certain frequency, the electron gas in a conductive medium, can sustain charge density oscillations, meaning that the electric charge density  $\rho(t)$  has oscillatory time dependence [10]. From the Maxwell's equations, the wave equation inside a medium can be written as:

$$\nabla^2 E(\omega) + \left(\frac{\omega}{c}\right)^2 \varepsilon(\omega) E(\omega) = 0 \quad (2.1)$$

where,  $\omega$  is the angular frequency,  $E(\omega)$  is the electric field,  $c$  is the speed of light and  $\varepsilon(\omega)$  is the *complex dielectric constant* or *relative permittivity*<sup>1</sup>. The permittivity itself can be written in terms of the frequency-dependent conductivity of the medium,  $\sigma(\omega)$ .

$$\varepsilon_r(\omega) = 1 + \frac{4\pi i \sigma(\omega)}{\omega} \quad (2.2)$$

$$\sigma(\omega) = \frac{\sigma_0}{1 - i\omega\tau} \quad (2.3)$$

---

<sup>1</sup> Relative permittivity or dielectric constant is the permittivity of the material divided by the permittivity of the vacuum; i.e.  $\varepsilon_r(\omega) = \varepsilon(\omega)/\varepsilon_0$ .

where  $\sigma_0 = \frac{ne^2\tau}{m}$  is the zero-frequency conductivity from the Drude model, with  $n$ ,  $m$  and  $e$  being the electron density per unit volume, electron charge and electron mass, and  $\tau$  being the electron relaxation time. At high frequencies (optical frequencies for most materials), we have  $\omega\tau \gg 1$ , and thus the Eq. 2.2 can be rewritten as:

$$\varepsilon_r(\omega) = 1 - \frac{\omega_p^2}{\omega^2} \quad (2.4)$$

where  $\omega_p = \sqrt{4\pi ne^2/m}$  is the the plasma frequency. From the Eq. 2.1, when  $\varepsilon(\omega)$  is positive ( $\omega \gg \omega_p$ ), the electric field insides the medium becomes oscillatory, and the material becomes transparent. Plasma frequency for most metals is in the ultraviolet range. Below  $\omega_p$ ,  $\varepsilon(\omega)$  is negative and the electric field inside the medium decays exponentially. At this range, coherent oscillation of the electron gas can occur at the boundary of the conductive medium, known as surface plasma oscillation, and the *surface plasmon* is the quanta of this oscillation. This is the range that is commonly used in plasmonics, where we have surface plasmons propagating across the interface with quasi-2D confinement perpendicular to the surface [11]. Plasmons (and surface plasmons) can interact with photons and form a new half-light half-matter quasi-particle known as *plasmon polariton*. *Surface Plasmon Polaritons* (SPPs) in particular can be excited very efficiently using optical beams<sup>1</sup>. Figure 2. *a* shows a common method for the optical excitation of SPPs using the *attenuated total reflection* of an optical beam and the evanescent fields at the reflection region in a dielectric prism, known as Kretschmann-Raether configuration. The dispersion relation for the SPPs excited using this method is shown in Fig. 2. *b*.

---

<sup>1</sup> Surface-plasmons can also be also excited by electron beams. In fact, electron energy-loss spectroscopy has very ofthen used to to study the properties of surface plasmon. In this thesis, however, we focus on the optical excitation of surface plasmons.

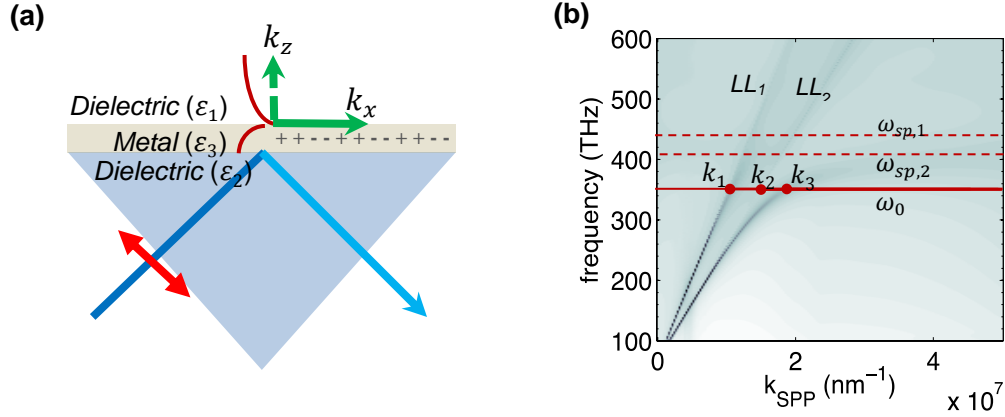


**Figure 2 - Excitation of surface plasmons on a thin metallic film. (a) attenuated total reflection in Kretschmann-Raether configuration for the excitation of SPPs on a thin metallic film. (b) dispersion of SPPs propagating at the interfaces of a thin Au film (30 nm thickness) with air cladding layer and  $SiO_2$  substrate calculated numerically using Finite-Difference Time-Domain (FDTD) method.  $k_{SPP}$  in this figure is the real part of transverse wave-vector,  $k_{SPP} = k_x'$ .**

### 2.1.2 Surface Plasmon Dispersion Relation

The thin metal film shown in Fig. 2. a supports two SPP waves; one at the interface of the metal and cladding (dielectric medium on top with the permittivity of  $\epsilon_1$ ) another at the interface of metal and substrate (bottom dielectric with permittivity of  $\epsilon_3$ ). The transversal and longitudinal electric field of a surface plasmon can be written as:

$$\vec{E}(x, z, t) = \vec{E}_0^+ e^{i(k_x x + k_z z - \omega t)} u(z) + \vec{E}_0^- e^{i(k_x x - k_z z - \omega t)} u(-z) \quad (2.5)$$

where  $\vec{E}_0^\pm$  is the electric field vector at  $z = 0^\pm$  ( $E_z$  has discontinuity at  $z = 0$ ),  $k_x$  and  $k_z$  being the k-vector in transverse and longitudinal direction and  $u(\cdot)$  is the step function. As mentioned earlier, the electric field in the longitudinal direction,  $E_z$ , is evanescent (decays exponentially in  $z$ -direction), which means that  $k_z$  needs to be imaginary. From the conservation of energy, we have:

$$\epsilon_i \left( \frac{\omega}{c} \right)^2 = k_x^2 + k_{z,i}^2 \quad i = 1, 3 \quad (2.6)$$

Additionally, from the Maxwell's equations, the dispersion relation for the plane surface of a semi-infinite metal, can be found as:

$$\frac{k_{z,1}}{\varepsilon_1} + \frac{k_{z,2}}{\varepsilon_3} = 0 \quad (2.7)$$

By substituting  $k_{z,1}$  and  $k_{z,3}$  from Eq. 2.6 into Eq. 2.7, we can find the parallel  $k$ -vector:

$$k_x = \left(\frac{\omega}{c}\right) \sqrt{\frac{\varepsilon_1 \varepsilon_3}{\varepsilon_1 + \varepsilon_3}} \quad (2.8)$$

Now, assuming real  $\varepsilon_1$  and complex  $\varepsilon_3$  ( $\varepsilon_3 = \varepsilon_3' + \varepsilon_3''$ ), the real and imaginary parts of  $k$ -vector can be written as:

$$k_x' = \left(\frac{\omega}{c}\right) \sqrt{\frac{\varepsilon_3' \varepsilon_1}{\varepsilon_3' + \varepsilon_1}} \quad (2.9)$$

$$k_x'' = \left(\frac{\omega}{c}\right) \sqrt{\left(\frac{\varepsilon_3' \varepsilon_1}{\varepsilon_3' + \varepsilon_1}\right)^3 \frac{\varepsilon_3''}{2(\varepsilon_3')^2}} \quad (2.10)$$

In order for  $k_x'$  to be real, as it was previously assumed, we must have:

$$\varepsilon_3' < 0 \quad (2.11)$$

$$|\varepsilon_3'| > \varepsilon_1 \quad (2.12)$$

Equations 2.11,12 are the necessary condition for the existence a SPP at the interface of two media. Finally, by substituting Eq. 2.4, into Eq. 2.9, we can obtain the closed-form dispersion relation of  $SPP_1$ . The most important feature is the overall trend of dispersion curve. At small  $k_x'$ , the dispersion approaches the light-line for the dielectric medium 1,

$\omega \rightarrow c k'_x / \sqrt{\varepsilon_1}$ , but it remains on the left side of the light-line, meaning that the SPP is *non-radiative*. For large  $k'_x$ , the dispersion relation approaches the *surface plasma frequency*,  $\omega_{sp}$ , for the interface between the media 1 and 3, defined as:

$$\omega_{sp,1} = \frac{\omega_p}{\sqrt{1 + \varepsilon_1}} \quad (2.13)$$

At this limit, we have  $\varepsilon'_3(\omega) \cong -\varepsilon_1$ . As, we approach  $\omega_{sp,1}$ , the group velocity<sup>1</sup>  $v_g$  of the  $SPP_1$  decreases and beyond  $\omega_{sp,1}$ , the interface does not support a confined surface-plasmon. Similarly, we have  $\omega_{sp,2} = \omega_p / \sqrt{1 + \varepsilon_3}$  for the  $SPP_2$  wave propagating at the bottom interface.

The excitation of SPP waves using Kretschmann-Raether configuration, as shown in Fig. 2. a, can be explained using the dispersion relation. Let's assume an excitation beam with frequency  $\omega_0$  enters the prism and undergoes attenuated total internal reflection. The two straight lines shown in Fig. 2. b,  $LL_1$  and  $LL_2$ , are the light-lines for the two dielectrics with the permittivities  $\varepsilon_1$  and  $\varepsilon_3$ . Two SPP modes can also be seen tangent to the  $LL_1$  and  $LL_2$  at low values of  $k'_x$  and approaching  $\omega_{sp,1}$  and  $\omega_{sp,2}$  at high  $k'_x$ . These are the numerically calculated dispersion relations for the two SPPs propagating at the top and bottom interface of the metal,  $SPP_1$  and  $SPP_2$ . For an infinitely thick metal, these dispersion relations can be found from Eqs. 2.4 and 2.9, whereas in a thin film, the coupling between the two SPP waves alters the dispersion relations. The impinging light cannot directly excite  $SPP_1$  at the top surface, since there is a momentum mismatch between the momentum of  $P_1 k_3$ , at  $\omega_0$  and the momentum of the excitation beam propagating inside bottom dielectric,  $k_2$  ( $k_3 > k_2$ ).

---

<sup>1</sup> Group velocity for a propagative wave with the k-vector  $k_x$  is defined as the slope of the dispersion curve; i.e.  $v_g = \partial\omega / \partial k'_x$ .

However, this excitation beam can excite  $SPP_2$ , as  $SPP_2$  and  $LL_2$  have an intersection at  $(\omega_0, k_2)$  meaning that they are momentum and frequency matched.  $SPP_1$  is excited indirectly using the evanescent coupling between  $SPP_1$  and  $SPP_2$ , which does not require momentum match, and in fact,  $SPP_2$  is the dominant mode of the thin film.

### 2.1.3 Surface Plasmon Propagation Length and Skin Depth

As we saw in the derivation of the dispersion relation, the parallel  $k$ -vector, for SPP is a complex number, and the real part of  $k$ -vector,  $k'_x$ , determines the dispersion relation of the SPP. The effect of the imaginary part,  $k''_x$ , is the attenuation<sup>1</sup> of the SPP wave, as it propagates along the interface of the conductive medium. In order to quantify this attenuation, we define the *propagation length*,  $L_i$ , as:

$$L_i = \frac{1}{2k''_x} \quad (2.14)$$

$L_i$  can be used as a figure-of-merit to quantify the absorption and radiation loss in any plasmonic or photonic waveguide. For the *Ag*-air interface,  $L_i \simeq 22 \mu m$  in visible range ( $\lambda = 514 nm$ ) and  $L_i \simeq 500 \mu m$  at NIR ( $\lambda = 1060 nm$ ). The value of  $L_i$  can be increased several folds with better waveguide designs, but the numbers are much smaller than what can be achieved with dielectric waveguides. Nonetheless, plasmonic waveguides and nanostructures are still appealing, as SPPs allow many optical processes to occur within a fraction of their  $L_i$ , due to their high *energy-confinement* and *field-enhancement*. Confinement or localization of electromagnetic fields in plasmonic structures stems from the extremely small *skin* or *penetration depth* of the SPPs. Using Eqs. 2.6 and 2.8, we can find the longitudinal wave vectors, at either side of the top interface:

---

<sup>1</sup> The origin of this attenuation is ohmic loss or absorption of the conductive medium.

$$k_{z,i} = \sqrt{\varepsilon_i \left(\frac{\omega}{c}\right)^2 - k_x^2}, \quad i = 1,3 \quad (2.15)$$

Since, the SPP dispersion is on the left side of the light-line; i.e.  $|k_x| > \sqrt{\varepsilon_1} \omega/c$ , and  $\varepsilon_1' < 0$ , both  $k_{z,1}$  and  $k_{z,3}$  are imaginary, leading to evanescent waves in the longitudinal direction. Three characteristic wavelengths can be defined for SPPs: two *longitudinal wavelengths*,  $\lambda_{\perp,i}$  and one *transverse wavelength*,  $\lambda_{\parallel}$ :

$$\lambda_{\parallel} = \frac{2\pi}{|k_x|} \quad (2.16)$$

$$\lambda_{\perp,i} = \frac{2\pi}{|k_{z,i}|} \quad i = 1,3 \quad (2.17)$$

At very large  $|k_x|$  (dispersion approaching  $\omega_{sp}$ ),  $\lambda_{\parallel}$  and  $\lambda_{\perp,i}$  are very small. Small  $\lambda_{\parallel}$  means that the group velocity  $v_g$  is very small and the SPP wave is quasi-stationary. Small  $\lambda_{\perp,i}$  means small skin depth and high electromagnetic field confinement.

#### 2.1.4 Surface plasmons Group Velocity and Density of States

Group velocity  $v_g$  and density of states (DOS) are two other useful quantities that help us estimate the impact of photonic and plasmonic nanostructure in nanoscale light-matter interaction processes. Group velocity is defined as the velocity of a wave packet propagating across a medium or nanostructure. Mathematically,  $v_g$  for a wave-packet with wave-vector  $k = k_x'$  is defined as the slope of the dispersion curve:

$$v_g(k) = \partial\omega/\partial k \quad (2.18)$$

This is different from the *phase velocity*, which is only defined for one frequency component; i.e.  $v_p = \omega/k$ , but on a homogenous and non-dispersive medium  $v_g$  and  $v_p$  are

equal. A smaller  $v_g$  means that the optical wave propagates with a lower speed across the nanostructure, and hence has more time to interact with the material, which often leads to a more pronounced light-matter interaction effect.

Despite all its merits, group velocity has the limitation of only being defined for propagative waves. DOS is a more generalized definition that can be used for both propagative and resonant modes. DOS at the frequency of  $\omega_0$ ,  $g(\omega_0)$ , is defined as the number of channels<sup>1</sup> (or states) per unit volume per energy interval (or frequency interval) available to be occupied by external fields [12,13]:

$$g(\omega_0) = \sum_{n,k} \delta(\omega(k) - \omega_0) \quad (2.19)$$

where  $\omega(k)$  is the dispersion relation,  $n$  is the band number, and  $k$  is the wavevector. Both DOS and group velocity are global quantities defined for the photonic bands<sup>2</sup> of a medium or nanostructure as a whole. *Local density of states* (LDOS),  $\rho(\omega, \vec{r})$ , on the other hand is a local version of DOS defined for every point  $\vec{r}$  in space, using the following equation:

$$\rho(\omega_0, \vec{r}) = \sum_{n,k} |e_n(\vec{r})|^2 \delta(\omega(k) - \omega_0) g(\omega_0) = \sum_{n,k} \delta(\omega(k) - \omega_0) \quad (2.20)$$

where  $|e_n(\vec{r})|$  is the amplitude of the eignemode<sup>3</sup> at point  $\vec{r}$ . In simple terms, LDOS is a measure of spectral density for specific frequencies and specific locations in space. In a uniform homogenous medium with the refractive index  $n$ , it can be shown that:  $\rho(\omega_0, \vec{r}) =$

---

<sup>1</sup> The total number of states occupied by SPPs (or photons) is DOS times the Bose-Einstein distribution since SPPs (and photons) are bosons; i.e.  $N(\omega) = g(\omega)f(\omega)$  with  $f(\omega) = [\exp(\hbar\omega/k_B T) + 1]^{-1}$ , where  $k_B$  is the Boltzmann constant and  $T$  is the temperature .

<sup>2</sup> DOS can also be defined for a single photonic band, i.e.  $g_n(\omega_0) = \sum_k \delta(\omega(k) - \omega_0)$ . Hence the total DOS is the sum of DOS over all supporting bands of the structure,  $g(\omega_0) = \sum_n g_n(\omega_0)$ .

<sup>3</sup> Eigenmodes or simply modes of a medium or structure defined by  $\mathcal{E}(\vec{r})$  are the eigenfunctions of the wave equation (Eq. 2.1) , i.e.  $\nabla^2 e_n(\vec{r}) + (\omega^2/c) \mathcal{E}(\vec{r}) e_n(\vec{r}) = 0$  and  $\int e_m(\vec{r}) \cdot e_n(\vec{r}) d^3r = \delta_{m,n}$ .

$\rho(\omega_0) = \omega_0^2 n^3 / \pi^2 c^3$ . It can also be shown that the LDOS of one propagative mode (one band),  $\rho_n(\mathcal{E}_0, \vec{r})$  is inversely proportional to its group velocity<sup>1</sup>:

$$\rho_n(\mathcal{E}_0, \vec{r}) = \int_{S_n(\mathcal{E}_0)} \frac{dS}{4\pi^3} |e_n(\vec{r})|^2 \frac{1}{|\nabla \mathcal{E}_n(\vec{k})|} \quad (2.21)$$

where  $\mathcal{E}_0 = \hbar\omega_0$  is the energy,  $\vec{k}$  is the 3D  $k$ -vector,  $S_n(\mathcal{E}_0)$  is the constant-energy (or constant frequency) surface of band  $n$  in 3D  $k$ -space and  $v_g^{(n)}(\vec{k}) = \nabla \mathcal{E}_n(\vec{k}) / \hbar$  is the group velocity of the band  $n$  at the wavevector  $\vec{k}$ . Total LDOS is the sum of  $\rho_n$  over all supported bands, i.e.  $\rho(\omega_0, \vec{r}) = \sum_n \rho_n(\omega_0, \vec{r})$ . Derivation of the LDOS for most nanostructures of interest is rather involved, even for most basic geometries. Figures 3. *a – d* illustrate the qualitative curves for the dispersion relation and LDOS for the two simple plasmonic waveguide and nanocavities, namely metal-dielectric interface [14,15] and a metallic nanosphere [15,16]. For most practical nanostructure, the LDOS needs to be calculated numerically.

In the case of a metallic slab of *Au*, similar to a metallic film shown in Fig. 2. *b*, the dispersion curve of the main SPP band (solid red and dashed blue curves), shown in Fig. 3. *a* starts tangent to the light-line for small  $k_{\parallel}$  and reaches a high-energy limit of  $\mathcal{E}_{sp} = \hbar\omega_{sp}$  for high values of  $k_{\parallel}$ . The optical loss inside the metal results in the appearance of the band above  $\omega_{sp}$ , which is highly radiative (specially the part that is on the left side of light-line) and does not have many practical applications. The part of this band that is on the right side of the light-line is sometimes called *quasi-bound SPP band* [17]. As we approach  $\mathcal{E}_{sp}$ ,  $v_g$ , which is the slope of the dispersion curve, decreases monotonically. In a metal slab, due to the geometrical symmetry, LDOS only changes by changing the height  $z$ , from the surface of

---

<sup>1</sup> In 3D  $k$ -space, the definition of  $v_g$  in Eq. 2.18 should be replaced by  $v_g(\vec{k}) = \Delta_{\vec{k}} \omega(\vec{k})$ .

the metal. As we see in Fig. 3. *c*, by increasing the height, LDOS decreases, as we expect. Also, since LDOS is inversely proportional to  $v_g$ , its maximum occurs at  $\mathcal{E}_{sp}$ .

Now, let's consider a simple plasmonic nanocavity: a metallic nanosphere. In a confined geometry such as nanosphere, the plasmon oscillates locally around the surface with a frequency known as *localized surface plasmon resonance* (LSPR) frequency. This oscillation frequency can be tuned by modifying the size and shape of the nanoparticle. Mathematically, the solution of the wave equation for a metallic nanosphere results in the quantization of dispersion relation with discrete LSPR modes shown in Fig. 3. *b*. The condition for the existence of SPPs on a spherical surface are given by  $\varepsilon_3(\omega) = -\varepsilon_1 (\ell + 1)/\ell$ , where  $\varepsilon_3$  and  $\varepsilon_1$  are the permittivity of the plasmonic material and dielectric environment [11]. Hence, this condition will only be satisfied for discrete values of  $\ell = 1, 2, 3 \dots$  and their corresponding  $\omega_\ell$  (or  $\mathcal{E}_\ell$ ), e.g. dipole resonance with  $\ell = 1$ , quadruple resonance for  $\ell = 2$ , etc. Moreover, for each quantum number  $\ell$ , there are  $2\ell + 1$  degenerate LSPR modes with eigen-frequency  $\omega_\ell$ . Each group of these degenerate LSPR modes results in a peak in LDOS curve, as it can be seen in Fig. 3. *d*. In more complex nanoparticle geometries, this degeneracy can be lifted or decreased.

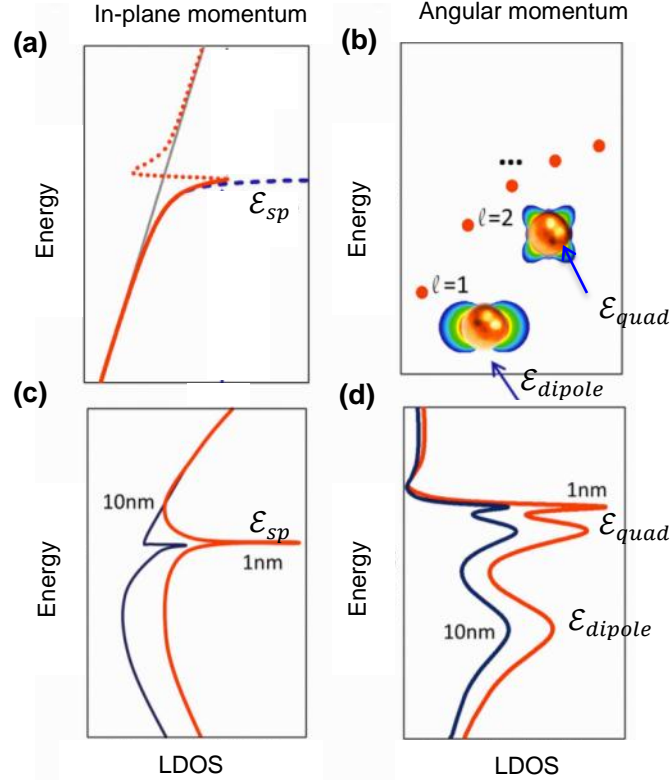


**Figure 3 - Qualitative representation of dispersion relation and LDOS of an infinite metal slab and a metallic nanosphere (image reproduced with permission from Ref. [15]). (a) Energy  $\mathcal{E}$  vs. in-plane  $k_{\parallel}$  dispersion relation for an infinite metal slab in case of lossless metal (blue curves) and lossy metal (red curves). (b) Energy  $\mathcal{E}$  vs. angular momentum  $\ell$  for lossy metallic nanosphere (c) Energy  $\mathcal{E}$  vs. LDOS for the same metallic slab at two different height in air: 1 nm (red curve) and 10 nm away from the metal surface (blue curve). (d) Energy  $\mathcal{E}$ , vs. LDOS for a metallic nanosphere at two different radial distances from the surface in air: 1 nm (red curve) and 10 nm (blue curve) away from the surface.**

### 2.1.5 Plasmonic Waveguides and Cavities

Almost all plasmonic and photonic nanostructures are composed of two fundamental building blocks: waveguides and cavities (or resonators). Among the quantities introduced so far, the propagation length  $L_i$ , and group velocity  $v_g$ , are the two useful figure-of-merits for the propagative modes in waveguides. The quality factor  $Q$  and resonance lifetime  $\tau$  can be used for the resonant modes in optical cavities. LDOS is the only quantity that we have seen so far, which can be used for either type of structures. However, as we saw in the previous section, calculation of LDOS can be quite cumbersome for complex nanostructures. For

most applications, the electric field enhancement factor, defined as  $\Gamma(\vec{r}) = |\vec{E}(\vec{r})|/|\vec{E}_0|$ , where  $\vec{E}(\vec{r})$  is the electric field vector at location  $\vec{r}$ , and  $\vec{E}_0$  is the electric field of the excitation plane wave, can be used as a more intuitive and simple to calculate alternative.

In general, the values of  $\Gamma$  and LDOS, in the vicinity of plasmonic nanostructures, are much higher than their photonic counterparts. On the other hand, photonic structures have higher  $L_i$  and  $Q$ . For instance, Figs. 4. *a, b* shows the distribution of  $\Gamma$  at the cross-section of an *Au* slit, as an example of a plasmonic waveguide with large  $L_i$ , and a  $Si_3N_4$  slot waveguide, which is very often used in sensing applications due to its large field enhancement. The maximum value of  $\Gamma$  is several times larger in *Au* slit, as it can be seen from these figures. Figure 4. *c* shows the distribution of  $\Gamma$  at a horizontal cross-section of a nanocube dimer, as an example of plasmonic nanocavity with large field enhancement. As we can see from this figure, the maximum value of  $\Gamma$  in high electric-field regions, called *hotspots*, can reach a remarkable value of  $8 \times 10^4$ , which is orders of magnitude higher than the  $\Gamma_{max}$  in the vicinity of a photonic resonator, such as the *SiN* microdisk shown in Fig. 4. *d*. On the other hand, the practically achieved values of  $Q$ -factor is between 20 to 100 in plasmonic nanocavities, but it can be in excess of  $10^6$  in photonic cavities.

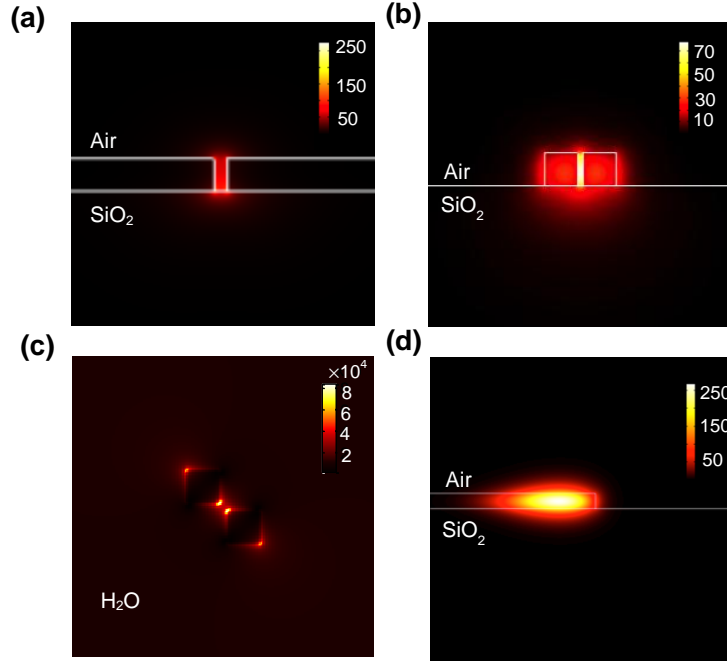


**Figure 4 - Distribution of electric field enhancement factor in a few plasmonic and photonic waveguides and resonators of interest. (a) Au slit of 40 nm width and 100 nm height,  $n_{eff} = 2.223 + 0.036i$  (b) SiN slot waveguide, gap size: 40 nm, SiN width (one side): 250 nm, SiN height: 250 nm,  $n_{eff} = 1.49$ . (c) (d) SiN microdisk of 40  $\mu m$  radius and 250 nm height, first transverse-electric mode ( $TE_{10}$ ), m-number: 510,  $\lambda_{res} = 853.3$  nm**

Energy confinement in photonic and plasmonic structures can be quantified using the optical mode volume  $V_m$ , defined as:

$$V_m = \frac{1}{u_e^{max}} \int u_e(\vec{r}) d^3\vec{r} \quad (2.22)$$

For waveguides, the integration in Eq. 2.22 should be performed over the cross-section perpendicular to the direction of propagation, and for the resonators, over the entire space.  $u_e$  is the generalized energy density defined as  $u_e = \frac{1}{2} \epsilon_0 \left( \epsilon_r + \frac{2\omega}{\gamma} \epsilon_i \right) |\vec{E}|^2$  for a lossy media [18], where  $\epsilon_{r,i}$  are the real and imaginary part of dielectric constant and  $\gamma$  is the damping constant from the Drude model and  $u_e^{max}$  is the maximum of  $u_e$  over the integration space. The mode volume in photonic nanostructures is limited by the diffraction limit; i.e.  $(\lambda_0/2n)^2$

in waveguides and  $(\lambda_0/2n)^3$  in resonant cavities, where  $n$  is the largest dielectric constant. Photonic crystal waveguides and resonators can get very close to this diffraction limit [19]. The SPP modes in plasmonic nanostructures can however confine light much below this diffraction limit [20].

## 2.2 Plasmonic Material Platforms

As we saw in the previous section, the generation of SPP requires at least one material with negative real permittivity,  $\varepsilon'(\omega)$ , which we here call a plasmonic material. A material is desirable for plasmonic applications, if it can provide a large propagation length,  $L_i$  and small skin depth  $\lambda_{\perp,1}$ . Considering the simple case of the SPP at the interface of thin film with two dielectrics considered in previous section, this requires small  $k_x''$  and large  $k_{z,1}$ , according to Eqs. 2.14, 2.17. Large  $k_{z,1}$  infers small  $|k_x|$  according to Eq. 2.15, and hence small  $k_x'$ , for a fixed frequency  $\omega$ . So overall, we need small  $k_x'$  and small  $k_x''$ , which would be possible if,  $|\varepsilon_3'|$  is large and  $\varepsilon_3''$  is small from Eqs. 2.9,10. So, we are searching for a material with small  $\varepsilon_3''$  to have low ohmic loss, and large  $|\varepsilon_3'|$  to have high field confinement. Unfortunately, these two criteria don not occur simultaneously in natural materials. Ultimately, the choice of the plasmonic material also depends on application. As a rule of thumb, for near-field light-matter interaction applications, we can define  $Q_p(\omega) = -\varepsilon''(\omega)/\varepsilon'(\omega)$ , as the frequency-dependent figure-of-merit of the material platform [21,22]. In the case of plasmonic nanocavities, another important aspect is the tunability of LSPR resonance. For instance, in *Au* nanorods, the LSPR resonance can be easily tuned at wavelengths above 700 nm, by slightly changing the length. But, due to the large dispersion of  $\varepsilon'(\omega)$  below 700 nm, all geometrical dimensions need be to scaled down significantly to achieve a high- $Q$  LSPR

resonance. In practice, the realization of nanoantennas with such small dimensions could be difficult with current fabrication technology. In Table 1, we have listed the generalized Drude parameters of the four most frequently used plasmonic materials: *Au*, *Ag*, *Cu* and *Al*.

***Noble metals (visible and NIR):*** *Au* and *Ag* are by far the most commonly used materials in plasmonics in visible and near NIR range. *Cu* is also sometimes used as a low-cost CMOS compatible alternative [23]. In almost the entire visible and NIR range (0.5 to 2  $\mu\text{m}$ ), *Ag* has the lowest loss and the highest  $Q_p$ , but unfortunately, it is prone to oxidation, especially in thin layers. As a result, for long-term use, plasmonic devices made out of *Ag* need to be covered by a protective layer. This is not desirable in near-field light-matter interaction applications, since in SPP waves,  $\Gamma$  and LDOS both peak at the interface of plasmonic material and decay rapidly with the distance. Hence, we most often resort to *Au* in these applications, despite its inferior performance compared to *Ag*.

***Aluminum (NUV and visible):*** In near ultraviolet (NUV) and low visible range (300 to 600  $\text{nm}$ ), *Al* is a good choice for near-field plasmonics, even though it is even more prone to oxidation than *Ag* [24-26]. The he most common plasmonic application of *Al* is in high chromaticity color filters due its low cost and high tunablity in the visible range [27,28].

***Graphene (MIR):*** Among the 2D materials, graphene is a good candidate in mid-infrared (MIR) region (5 to 10  $\mu\text{m}$ ) [29,30]. This range of spectrum is particularly suited for biosensing based on infrared spectroscopy, as the vibrational resonance of most biochemicals lie in this range. Therefore, graphene can be used to develop plasmonic biosensors based on *surface-enhanced infrared absorption (SEIRA)* spectroscopy [31,32]. Moreover, the 2D electron gas in graphene allows for some interesting properties for the surface plasmons that

cannot be found in bulk materials, such as  $p$ -polarized SPPs [33], and novel properties with potential applications in quantum plasmonics [34-36].

**Table 1 - Generalized Drude parameters for the four most common plasmonic material platforms. This model is only valid up to the interband transition limit,  $\omega_{inter}$ <sup>1</sup>.**

	$\epsilon_{\infty}$	$\omega_p$ (eV)	$\gamma$ (eV)	$\omega_{inter}$ (eV)
<b>Au</b>	3.7	9.2	0.02	3.9
<b>Ag</b>	6.9	8.9	0.07	2.3
<b>Cu</b>	6.7	8.7	0.07	2.1
<b>Al</b>	0.7	12.7	0.13	1.41

**Specialized material platforms:** Apart from metals highly doped semiconductors with an appreciable free carrier concentration, e.g. doped  $Ge$ , can also support SPPs [37]. Even though, the  $Q_p$  of doped semiconductors is typically low compared to the metals, these materials have some niche applications in the MIR range [38-40]. Another alternative platform for plasmonics is the class of materials known as “*topological isolators*”, including  $Bi_2Se_3$ ,  $Bi_{1.5}Sb_{0.5}Te_{1.8}Se_{1.2}$  etc. Topological insulators have been intensively studied in the recent years, due to ability to support gapless Dirac surface states at the surface that are protected from backscattering into bulk via time-reversal symmetry [41]. These metallic surface states can also be used for plasmonics in UV, visible and THz range, with some evidence that they can even outperform noble metals in certain ranges, which opens the door for some novel applications such as plasmonic spintronics [42-44].

**Alternate material platforms:** The ohmic loss of common material platforms is one of the main obstacles in the field of plasmonics, especially in applications such as optical

---

<sup>1</sup> This model is the generalized form of the Drude model (Eq. 2.2) losses due to interband effects [22]:  $\epsilon(\omega) = \epsilon_{\infty} - \omega_p^2/(\omega^2 + i\gamma\omega)$ , where  $\epsilon_{\infty}$  is the contribution of interband transition to permittivity, and  $\gamma = \tau^{-1}$  is the damping constant of the electron gas.

interconnects and metamaterials. Theoretically, even though, it is not possible to have a material with purely real permittivity at all frequencies (a lossless plasmonic material) due to causality, it is possible to have this condition satisfied in some frequency ranges. The theoretical electronic bandstructure for such a material with no loss due to interband or intraband transitions in  $\mathcal{E}'_{c,1} - \mathcal{E}_{c,1}$  to  $\mathcal{E}'_{c,2} - \mathcal{E}_F$  energy range is depicted in Fig. 4 ( $\mathcal{E}_F$  in this figure the Fermi level) [45]. As a result, there has been a significant effort in developing low-loss and CMOS compatible material platforms [22,45,46] with some modest level of success. The most prominent examples are *TiN* [47] with  $Q_p$  approaching *Au* in NIR, but still inferior to *Ag*. Transparent conductive oxides, including Indium Tin Oxide (ITO) and Aluminum Zinc Oxide (AZO), are other examples of these newly developed materials [48,49]. ITO, in particular, has found niche applications as a plasmonic platform for NIR and MIR range, especially appealing due to the possibility of electrical tuning and ultrafast all-optical switching [50-53].

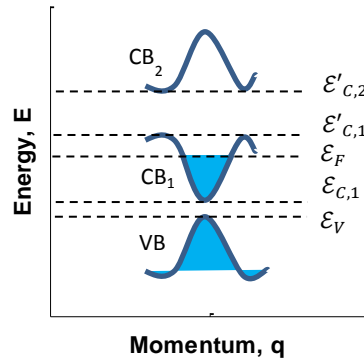


**Figure 5 - Electronic bandstructure of potential plasmonic material with no interband and intraband transition losses. A material with such electronic band-structure can sustain lossless SPPs in the energy band between  $\mathcal{E}'_{c,1} - \mathcal{E}_{c,1}$  to  $\mathcal{E}'_{c,2} - \mathcal{E}_F$ .**

The quality of material deposition or chemical synthesis also significantly affects the optical loss in plasmonic materials. For instance, chemically synthesized single crystalline *Au* and *Ag* nanoparticles tend to show higher quality factors compared to lithographically

fabricated nanoantennas, which are typically polycrystalline. Also, the quality of electron-beam deposited *Au*, *Ag*, *Cu* and *Al* films, which are typically used in lithographic fabrication of nanoantennas can be easily improved by some optimization during the deposition process [54].

As a final note, the ohmic loss in plasmonic materials can be a desirable effect in certain application including, photothermal therapy [55-62], local-heating, electric-plasmonic tweezing, heat-assisted optical or magnetic data recording, photothermal chemical catalysis, thermoelectric energy generation, and local self-limited welding [63-65].

### 2.3 Basics of Plasmonic Metamaterials

At the macroscopic level, the optical properties of a linear reciprocal medium is governed by three complex and frequency-dependant parameters: permittivity  $\epsilon$ , permeability  $\mu$ , and “*bianisotropy*”,  $\zeta$ . In an anisotropic material, these parameters are polarization dependant tensors. An example of an anisotropic material is 2D black phosphorus, which we will discuss in section 2.4. The electric displacement field  $\vec{D}$ , the magnetic flux density  $\vec{B}$ , electric field  $\vec{E}$ , and magnetic field  $\vec{H}$ , induced as the result of the light-matter interaction in a material can be described by the two following equations [66,67]:

$$\vec{D} = \bar{\epsilon} \vec{E} - \frac{i}{c} \bar{\zeta} \vec{H} \quad (2.23)$$

$$\vec{B} = \frac{i}{c} \bar{\zeta}^t \vec{E} + \bar{\mu} \vec{H} \quad (2.24)$$

where  $c$  is the speed of light and  $(\cdot)^t$  denotes the transpose operator. Since the magnetoelectric effect in most materials in nature is quite weak,  $\zeta$ , which is responsible for the

cross-coupling between electric and magnetic fields, is often very small. Many biomolecules and macromolecules, however, exhibit measurable “chirality”, a special case of bianisotropy, which we will discuss in Ch. 4, where  $\zeta$  is non-negligible. Valley polarization splitting discussed in the next section is also another example of chirality in 2D crystals.

Setting  $\zeta$  aside, if we write the complex permittivity and permeability as  $\varepsilon = \varepsilon' + i \varepsilon''$  and  $\mu = \mu' + i \mu''$ , we can classify materials based on the sign of  $\varepsilon'$  and  $\mu'$ . In transparent dielectrics, we have  $\varepsilon', \mu' > 0$ . In “electric plasmas”, which occur in non-magnetic metals at optical frequencies, we have  $\varepsilon' < 0, \mu' > 0$ . The negative value of  $\varepsilon'$  indicates that the direction of induced electric field (inside the material) is opposite to the direction of incident field. Materials with  $\varepsilon', \mu' < 0$ , and hence  $n' < 0$  are called negative-index materials (NIM) and are not frequent in nature, but  $\varepsilon', \mu' < 0$  can be obtained in carefully designed metamaterials, leading to exotic properties, such as *negative refraction* [68-71], and *backward propagation* [72,73]. Finally, in “magnetic plasmas”, also not found in nature at optical frequencies, we have  $\varepsilon' > 0, \mu' < 0$ , meaning that the direction of the induced magnetic field (inside the material) is opposite to the direction of incident magnetic field. Materials in the first and third category ( $\varepsilon'.\mu' > 0$ ) can sustain propagative waves, whereas the electromagnetic fields inside the materials in the second and third category ( $\varepsilon'.\mu' < 0$ ) are evanescent. However, propagative surface waves can exist at the boundary of two materials from the first and second category (surface plasmons), or two materials from third and fourth category. At optical frequencies, the vast majority of materials belong to first and second category with  $\mu' \approx \mu_0$ . One primary goal in the design of metamaterials is to reach areas of  $\varepsilon'$ - $\mu'$  parameter space that are not accessible in natural materials.

Additionally, we can categorize materials based on the imaginary parts of permittivity and permeability,  $\epsilon''$  and  $\mu''$ , or more commonly, based on the imaginary part of refractive index  $n''$ , with  $n'' > 0$  inferring an optical loss and  $n'' < 0$ , an optical gain in an active medium<sup>1</sup>. In Ch.7, we will discuss the application of gain materials for lasing. In the domain of metamaterial research, gain materials are sometimes used to overcome the optical loss that is one of the primary limitations of plasmonic metamaterials in certain far-field applications [74-76]. Another interesting application of gain media is in designing a new class of nanostructures where parity-time (PT) symmetry is broken using a tailored network of gain and loss [77,78]. PT-synthetic metamaterials could be used in a range of applications, including unidirectional devices or isolators, shown in Fig. 7.d [79] [80] and single-mode lasers [81,82].

The macroscopic description of light-matter interaction that we have discussed so far, only provides an insight into the “average” behavior of a medium upon excitation with light. At the microscopic level, the light-matter interaction process is more complex and involves several consecutive steps. First, the incident light excites atoms (or molecules) inside the medium. As a result, electric and magnetic dipoles,  $\vec{p}$  and  $\vec{m}$  are created at the location of atoms described by:

$$\vec{p} = \bar{\alpha} \vec{E} - i \bar{G} \vec{B} \quad (2.25)$$

$$\vec{m} = i \bar{G}^t \vec{E} + \bar{\chi} \vec{B} \quad (2.26)$$

where  $\bar{\alpha}$  is electric polarizability,  $\bar{\chi}$  is magnetic susceptibility and  $\bar{G}$  is the mixed electric-magnetic dipole polarizability. Subsequently, these electric and magnetic dipoles radiate

---

<sup>1</sup> This simple classical model of a gain medium is not sufficient, for describing many light-matter interaction effects in a active media. A quantum model for optical gain is provided in Ch. 7 to describe effects such as spontaneous and stimulated emission.

electromagnetic energy with a delay or phase retardation. The overall field inside the medium are the net result of radiation from these dipoles, plus the unabsorbed incident light and is not uniform at the atomic scale. However, since at optical frequencies, the wavelength is often much larger than the average distance between the atoms and molecules inside the medium ( $< 1 \text{ nm}$ ), the incident light does not experience the non-uniformity of the fields and “perceives” the material as a homogenous medium [83].

The basic idea behind the design of metamaterials for far-field applications is quite similar to the process that occurs in natural materials at the microscopic scale. If we can design sub-wavelength elements, called “*meta-atoms*”, with desirable optical properties, and repeat these fundamental building blocks with a periodicity that is quite small compared to the wavelength of the incident light, at the far-field, the meta-atoms can be modeled by effective electric and magnetic dipoles, whose net radiation can result in designer optical functionalities that are not accessible with natural materials. It is for this reason that metamaterials are traditionally regarded as “artificial materials”, rather than photonic or plasmonic devices. However, increasingly the boundary between the metamaterial and photonic research is becoming blurred and many metamaterial concepts are being employed in the design of novel photonic devices [84].

Another category of metamaterials are designed for near-field applications and change the properties of local electromagnetic fields in the vicinity of the nanostructures. Prominent examples of this class of metamaterials, which are more pertinent in near-field light-matter interaction applications, include hyperbolic metamaterials with hyperbolic or indefinite dispersion [47,85], and chiral metamaterials which generate enhanced chiral fields in their near-field [86,87]. Hyperbolic metamaterials can be used to modify the LDOS locally for applications, including the enhancement of spontaneous emission and decay rate of quantum

emitters [88-90] to sub-diffraction-limit imaging [91-93]. Figures 6. *a, b* shows two examples of hyperbolic metamaterials used for sensing applications [94,95]. Chiral metamaterials are discussed in detail in Ch. 5.

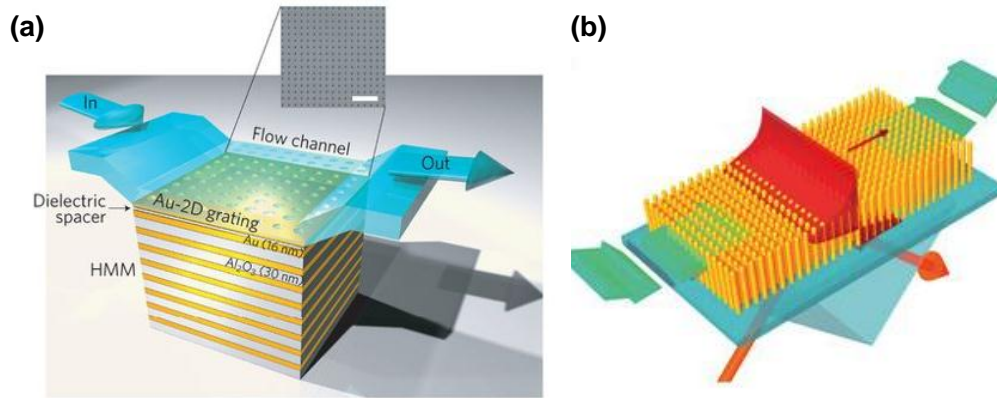


**Figure 6 - Two examples of metamaterials designed for sensing applications. (a) multilayer grating coupled hyperbolic metamaterial with integrated microfluidic channel [94], (b) Gold nanorod array hyperbolic metamaterial [95]**

Traditionally, most metamaterials are designed using plasmonic subunits, owing to the sub-wavelength nature of plasmonic elements in a 3D configuration. However, despite the great promises of 3D plasmonic metamaterials, many of their expected applications, particularly their far-field applications, did not materialize for two reasons: *a)* the optical loss inherent to plasmonic structures, *b)* the difficulties in scaling down the 3D structures to operate at optical frequencies [96]. Therefore, two main directions have emerged in metamaterial research: *metasurfaces* (or 2D metamaterials) [97] and *dielectric metamaterials* [98]. Metasurfaces, which can be regarded as the optical analog of 2D materials, can be fabricated more easily and typically induce less absorption loss, since they are composed of only one interaction layer. *Phase gradient metasurfaces* are an important sub-category of metasurfaces, in which the phase and amplitude of the scattered wavefronts are tailored by spatially varying the shape of meta-atoms in a larger unit-cell. An example of these metamaterials is shown in Fig. 7. *a* [99]. Different functionalities including negative

refraction [68,100], manipulation of the polarization [101], focalization of the light using a flat lens [102,103], and the generation of optical vortex [104], have been realized using phase-gradient metasurfaces. The second trend is designing meta-atoms using high refractive index dielectrics. Even though, the dielectric meta-atoms typically have larger dimensions, which reduces the degree of freedom in manipulating the wavefront, they induce less optical loss, which is particularly desirable for the design of transmissive devices [105-107]. Figure 7. *b* shows an example of a dielectric metasurface (silicon-based) designed for simultaneous control of phase and polarization [108].

Finally, the researchers have mostly utilized the linear response of active and passive meta-atoms to design metamaterials with various functionalities, so far. An emerging approach is to utilize the inherent material nonlinearity as a new degree of freedom to manipulate the flow of light. For instance, non-reciprocal propagation of light (optical diode) has been demonstrated using a flat nonlinear metamaterial, shown in Fig. 7. *c* [107]. The nonlinear effects in plasmonic and photonic devices are discussed in more detail in Ch. 6.

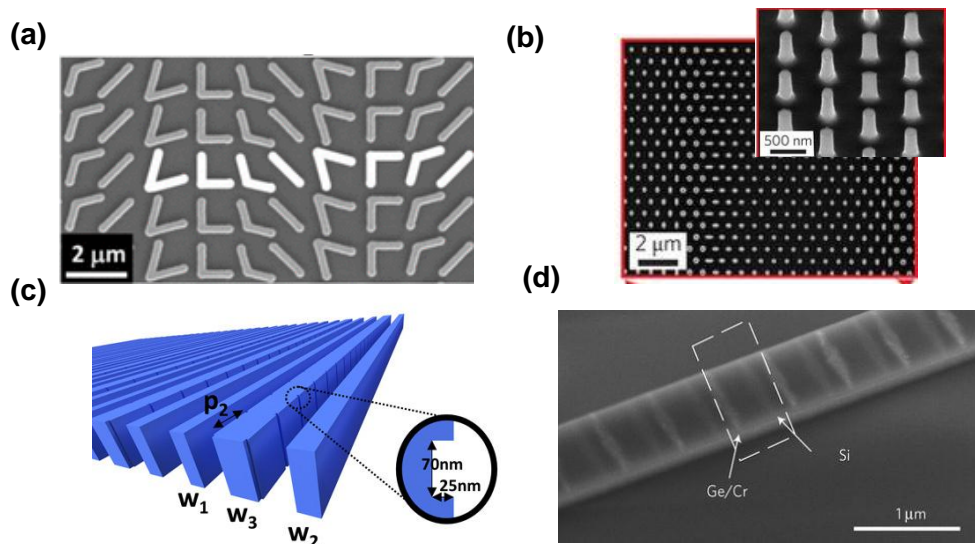


**Figure 7 - New developments in metamaterials research. (a) A plasmonic phase-array metasurface [99]; the unit-cell is composed of all the antennas colored in white. (b) A dielectric metasurface for**

simultaneous control of phase and polarization [108], (c) A dielectric metasurface with non-reciprocal optical response (optical diode) utilizing the Kerr nonlinearity of silicon [109]. (d) A non-reciprocal meta-device based on parity-time-symmetry

## 2.4 Light-Matter Interaction in Two-Dimensional Materials

Two-Dimensional (2D) crystals or “*van der Waals*” materials are a new class of low-dimensional materials composed of a single or a few layers of atoms. These materials exist in nature in bulk in the form of individual layers bonded together by weak van der Waals forces, and can be separated into single or several layer islands by mechanical exfoliation [110]. They can also be grown on a substrate using *chemical vapor deposition* (CVD) and other growth techniques [24]. Due to the *quantum confinement* effect, electronic and optical properties of 2D materials differ significantly from their bulk counterparts, similar to other low-dimensional materials. Generally, there are two approaches to enhance light-matter interaction in 2D materials: through their integration with plasmonic and photonic structures, or by using their intrinsic *polaritonic* surface waves. In the rest of this section, the electronic and optical properties of a few 2D materials with great potential in photonic and plasmonic applications are reviewed. Our primary focus will be on transition-metal dichalcogenides, which we will see again in Ch. 7.

### 2.4.1 Graphene, Hexagonal Boron Nitride and Black Phosphorous

The first discovered 2D material was graphene [111], which is a 2D arrangement of carbon atoms in honeycomb lattice with many intriguing electronic and photonic properties. It is a semi-metal with zero bandgap and an unusual electronic bandstructure, qualitatively shown in Fig. 8. *a*. Its electronic bandstructure has two so-called *Dirac points* at  $\kappa$  and  $\kappa'$  points of symmetry, where valence band (VB) and conduction band (CB) meet [112,113].

Near the Dirac points, the energy dispersion is linear<sup>1</sup>, i.e.  $\mathcal{E} = \hbar c^* q$ , and hence the electrons in graphene mimic relativistic particles with zero mass, *Dirac Fermions*, and have ballistic transport with an effective speed of  $c^* \simeq 10^6 m/s$  [114,115]. As a result of this ballistic transport, electrons in graphene have light-like behavior with straight-line trajectory as well as refraction and reflection across boundaries [116]. Also, as a result of the ballistic transport, graphene has a very high electron mobility [117,118]. The Fermi level  $\mathcal{E}_F$  of graphene, which is naturally at the intersection of VB and CB in pure samples, can be easily adjusted via chemical doping or electrostatic gating. Given these two electronic properties and the availability of epitaxial graphene at the wafer-scale, graphene is a great platform for high-speed electronics and a potential successor to silicon [119,120]. As discussed earlier, graphene is also an excellent plasmonic material for the MIR range. The electrostatic tuning of the  $\mathcal{E}_F$  can also be used for developing efficient and compact electro-optic modulators, switches and adaptive filters [121-123], through the integration of graphene with photonic and plasmonic devices.

Since the discovery of graphene, other 2D materials with varying electronic and optical properties have been isolated from the bulk, and in many cases have been successfully grown using CVD and other technics. Among the insulators, 2D hexagonal Boron Nitride (*hBN*) shown in Fig. 8. *b*, also known as “*white graphene*”, is a remarkable example [124,125], which has found applications as the isolation or encapsulation layer for other 2D materials [126], and as the interlayer spacer in vertical heterostructures of 2D materials [127,128]. Additionally, room-temperature single photon emission has been observed from atomic defects in 2D *hBN* at around 2 eV [129,130] opening new a avenue in quantum optic

---

<sup>1</sup> In most materials, the energy dispersion near the bandgap can be approximated by:  $\mathcal{E} = \hbar^2 q^2 / 2m^*$ , where  $m^*$  is the effective mass of electrons (or holes) in CB (or VB), and  $q$  is the electron momentum.

applications, such as quantum computing [131,132] and quantum key distribution [133-135]. One of the limitations of traditional solid-state single photon source has been the weak outcoupling efficiency of the single photon emission from the source, which can be vastly improved with 2D materials sources such as *hBN* [136]. Lastly, *hBN* also supports hyperbolic phonon polaritons in MIR range, which we will discuss in section 2.4.3.

Another intriguing 2D material is black Phosphorous (Black P), which is a semiconductor with small direct bandgap (0.3 to 2 eV depending on number of layers) [137]. Its energy bandgap can be further tuned by mean of chemical doping [138], mechanical strain [139], and most interestingly by applying a relatively modest transverse electric field due to the *Stark effect* [140]. Owing to this small tunable bandgap, Black P is suitable for developing broadband and tunable photodetectors in NIR and MIR range [141,142] and possibly other electro-optic devices. As another consequence of its low direct energy bandgap, it has some metal-like behaviors. It has high electron mobility  $\mu$ , making it suitable for electronic and optoelectronic application [137] and it supports SPPs [143]. As another fascinating property of Black P is its in-plane anisotropy [144], which is a direct result of its atomic structure with “puckered” hexagonal lattice shown Fig. 8. c. This unique property of Black P can be used to develop plasmonic devices with intrinsic anisotropy [145,146].

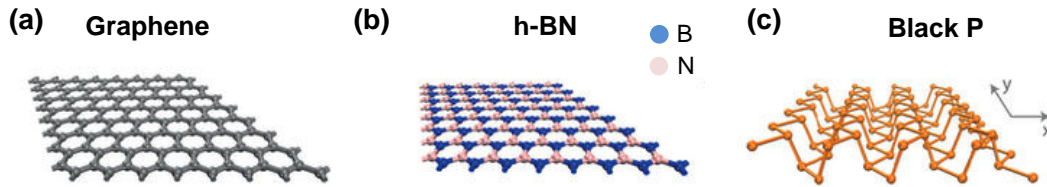


**Figure 8 - Atomic structure of graphene, *hBN* and Black P [147] (Image reproduced with permission). (a) Graphene: in-plane hexagonal lattice of C atoms (b) *h-BN*: atomic structure is similar to graphene, but with two dissimilar atoms (c) Black P: puckered hexagonal lattice of P atoms.**

## 2.4.2 Two-Dimensional Transition-Metal Dichalcogenides

*Transition-metal dichalcogenides* (TMDCs) are another class of 2D materials with a hexagonal atomic structure (1H)<sup>1</sup>. The electronic properties of TMDCs range from metallic in  $NbX_2$  and  $TaX_2$  to semiconducting in  $MoX_2$  and  $WX_2$  ( $X$  being a chalcogenide such as  $S$ ,  $Se$  and  $Te$ ) [150]. Semiconducting TMDCs are particularly appealing for electronic and photonic applications, due to their complementary material properties to graphene. Despite all its merits, graphene has one main shortcoming, which is the lack of energy bandgap (Fig. 9. a). For many optoelectronic applications, such as lasing, photodetection, photovoltaics, field-effect devices with large on-off voltage ratio, a semiconductor with a bandgap in visible and NIR range, such as semiconducting 2D TMDC is favourable. In single layer, these TMDCs have a direct bandgap in the visible and NIR region (1 to 2 eV) with two valleys at  $\kappa$  and  $\kappa'$  points of symmetry (Fig. 9. c), even though their bulk counterparts are indirect semiconductors (Fig. 9. d) [151]. Similar to Black P, the direct bandgap in these materials can be tuned using mechanical strain [152], alloying several TMDC [153] and by applying a transverse electric field [154].

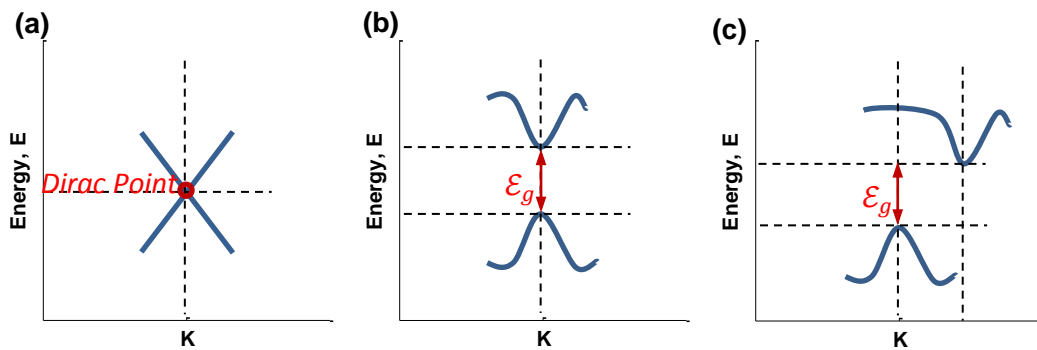


**Figure 9 - Qualitative electronic bandstructure of graphene and TMDCs. (a) Electronic bandstructure of graphene (b) electronic bandstructure of bulk TMDCs and (c) Electronic bandstructure of monolayer TMDCs.**

<sup>1</sup> Less common octahedral atomic structures (1T and 1T') with semi-metallic properties are also observed in some TMDCs [148,149].

As a result of this direct bandgap, semiconducting 2D TMDCs exhibit relatively large values of *quantum yield* in *photoluminescence* (PL) process [155,156], which can be further improved by chemical passivation of structural defects [157,158]. At room temperature, PL in semiconducting TMDCs is dominated by the contribution of (Mott-Wannier) *exciton*, a quasiparticle composed of an electron in CB and a hole in VB loosely bound together by the Coulomb force (Fig. 7.b). Due to the quantum confinement, the exciton *binding energy*  $\mathcal{E}_b$ , in semiconducting 2D TMDCs is significant (0.3 to 1 eV) and much larger than their bulk counterparts (Table 2). At low temperature, the contribution of *trions*<sup>1</sup> (or charged excitons) becomes significant, as well. Also, as a result of the direct bandgap, the *quantum efficiency*<sup>2</sup> of the *photocurrent* generation process in these materials is quite high [159,160]. There is a substantial interest in developing on-chip light sources such as photodiodes, and photocurrent-based devices such as photovoltaic cells and photodetectors using 2D TMDCs [161-164]. The absorption and PL in 2D TMDCs can be further enhanced by their integration with photonic and plasmonic nanostructures [165-168] and with sufficient enhancement optically pumped lasing can be achieved [169-171]. This application of 2D TMDCs is further discussed in Ch. 7. In another vein, tunable single photon emission in natural and artificial atomic defects in 2D TMDCs is also observed similar to 2D *hBN* [172-175].

Another property of hexagonal 2D TMDCs is the valley-polarization, which can be accomplished using the helicity of the light. As a consequence of the honeycomb lattice with broken inversion symmetry (Fig. 10. a), electron-states at the valleys of the hexagonal 2D TMDCs have an additional spin-like quantum number, known as *pseudospin* [176]. In other

---

<sup>1</sup> Trion is a charged quasiparticle composed of two electrons in CB and one hole in VB (negative trion) or one electron in the CB and two holes in the VB (positive trion).

<sup>2</sup> “Quantum yield” in PL is defined as the ratio of the number of photons emitted to the number of photons absorbed by the material and the “quantum efficiency” in photocurrent generation is the number of electrons collected divided by the number of photons absorbed.

words, there are two degenerate minima for the CB (or maxima for the VB) in momentum space, that are inequivalent. Selective population of one valley, called “valley polarization, can be accomplished optically using circularly polarized light [177-179]. Through the selective control of valley pseudospin, it is possible to develop electronic and optoelectronic “valleytronic” devices to transfer and process data, in much the same way that the spintronic devices rely on the selective control of electron spin [180-183].

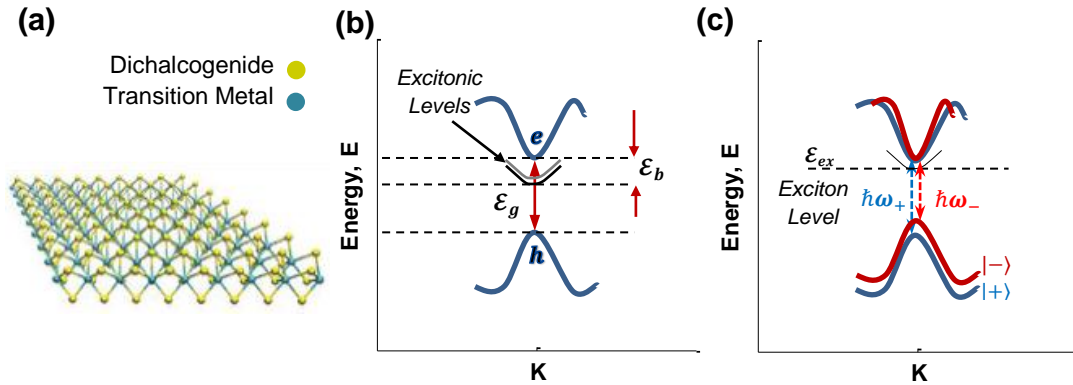


**Figure 10 - Properties of valley excitons in 2D TMDCs. (a) Atomic structure of hexagonal 2D TMDCs [147] (Image reproduced with permission). (b) Excitonic transitions and the valley-polarization splitting in semiconducting 2D TMDCs.  $\hbar\omega_+$  and  $\hbar\omega_-$  are the energy bandgap for electrons with positive and negative pseudospin.**

Phase transition is another useful property of 2D TMDCS [184]. Transition from a semiconducting (1H or 2H) to a semi-metallic (1T or 1T’) crystalline phase has been observed in some 2D TMDC, which can be triggered by temperature [185], strain [186], electrostatic gating [187,188] and by the hot-electron generated by plasmonic nanostructures under intense optical pumping [189]. The dynamic control of structural phase transitions in 2D TMDCs has applications in data recording, as well as low power and reconfigurable electronic and photonic circuits. *Mott transition* is another type of phase transition that has been observed in the semiconducting 2D TMDCs, in which the material undergoes a transition from an insulating phase to conductive electron-hole plasma, under intense photo-excitation [190]. Potentially, the Mott transition in 2D TMDCs can be used in applications such as all

optical switching and modulation. Some TMDCs also exhibit phase transition into material states with exotic properties such as superconductivity and charge density waves [191].

### 2.4.3 Polaritons in Two-Dimensional Materials

In section 2.1, we showed that the interface between a conductor  $A$  and a dielectric  $B$  can sustain a SPP wave, if  $\epsilon'_A < 0$  and  $|\epsilon'_A| > \epsilon_B$ . The nature of this surface wave was described as the coherent oscillation of electrons in conductor bound to its interface with the dielectric material. These conditions can be satisfied in a variety of materials, where the coherent oscillation of polarization charges, including electrons in the metals, but also phonons in polar insulators [192-194], excitons in semiconductors [195-197], magnons in ferromagnets (or antiferromagnets) [198,199], and cooper pairs in superconductors [200-202] can result in the formation of *polaritons*. All these surface waves can be used to confine light in sub-wavelength scales and hence are excellent vehicles for enhanced light-matter interaction.

Two-dimensional materials can also support surface polaritons [203,204]. As we mentioned earlier, graphene is an excellent platform for plasmonics in NIR and MIR. Black P also supports anisotropic plasmon polaritons from NIR to MIR range [143]. MIR phonon polaritons with hyperbolic dispersion have been observed in 2D *hBN*, which can be used as an alternative to the hyperbolic SPPs in plasmonic hyperbolic metamaterials [205]. The excitons in 2D TMDCs can also strongly couple to the photonic modes either intrinsic to the TMDCs or an external photonic or plasmonic structure and form exciton polaritons [166,206-209], which can be potentially condensated to form *Bose-Einstein condensates* (BEC) among other applications [210]. Finally, hybrid polaritons have been also observed in 2D material heterostructures or heterostructures composed of a 2D material and plasmonic

nanostructures. In Ch. 7, we discuss exciton-plasmon coupling in more detail. Another prominent example is plasmon-phonon polariton in graphene-*hBN* heterostructures, with increased polariton propagation length and the possibility of electrical tuning [211,212].

**Table 2 - Material classification, energy bandgap, main polariton type and field-effect mobility,  $\mu_{FE}$  (at room temperature) , exciton binding energy,  $\mathcal{E}_b$ , radiative lifetime,  $\tau_r$ , and workfunction  $|e\phi|$  for a few 2D materials of interest: *MoS<sub>2</sub>*, *MoSe<sub>2</sub>*, *WS<sub>2</sub>*, *WSe<sub>2</sub>*, Graphene, hexagonal Boron Nitride (*h-BN*) and Black Phosphorus (*Black P*). Data extracted from the following reference, a: [151], b: , c: , d: [213,214], e: [111], f: [137], g: [215], h: [216], i: [217], j:[218], k: [219] at 4 °K, l: [220] at  $T = 7$  °K, m: [221] (computational), n: [222] (computational), o: [223], p: [224]**

	Semiconducting TMDCs				Other 2D Materials		
	<i>MoS<sub>2</sub></i>	<i>MoSe<sub>2</sub></i>	<i>WS<sub>2</sub></i>	<i>WSe<sub>2</sub></i>	<i>Graphene</i>	<i>h-BN</i>	<i>Black P</i>
<i>Classification</i>	<i>semiconductor</i>				<i>semi-metal</i>	<i>insulator</i>	<i>semiconductor</i>
$\mathcal{E}_g$ (eV)	2 <sup>a</sup>	1.7 <sup>a</sup>	2.1 <sup>a</sup>	1.75 <sup>a</sup>	0	5.2 <sup>b</sup>	0.3 ~ 2 <sup>c</sup>
<i>Polariton Type</i>	<i>exciton</i>				<i>plasmon</i>	<i>phonon</i>	<i>plasmon</i>
$\mu_{FE}$ ( $\frac{cm^2}{V.S}$ )	10 ~ 200 <sup>d</sup>				~ 10 <sup>4e</sup>	—	~ 10 <sup>3f</sup>
$\mathcal{E}_b$ (meV)	~ 300 <sup>g</sup>	~ 650 <sup>h</sup>	~ 700 <sup>i</sup>	~ 370 <sup>j</sup>	—	—	—
$\tau_r$ (ps)	4 <sup>k</sup>	1.8 <sup>l</sup>	2.3 <sup>m</sup>	2 <sup>l</sup>	—	—	—
$ e\phi $ (eV)	5.07 <sup>n</sup>	4.57 <sup>n</sup>	4.73 <sup>n</sup>	4.21 <sup>n</sup>	4.6 <sup>o</sup>	—	5.16 <sup>p</sup>

## CHAPTER 3.

### MOLECULAR SENSING USING PLASMONIC NANOCUBES

Plasmonic nanocavities can be fabricated using lithographic techniques, discussed in Ch. 3 – 7, or grown chemically under controlled conditions in different shapes and sizes [225-229]. Chemically synthesized plasmonic nanoparticles are typically single crystalline and hence have higher Q-factor, which together with sharp edges and nanometer-sized gaps can lead to intense hotspots. For sensing applications, these nanoparticles can be used in the colloidal form or dispersed on a substrate using a variety of techniques such as *Langmuir-Blodgett method* [230,231]. However, controlling the location and orientation of nanoparticles after immobilization on a substrate is quite challenging unlike lithographically fabricated nanoantennas. Thus, more complex geometries and functionalities can be achieved using nanolithography. Another advantage of chemically grown nanoparticles is that they can be injected into living organisms for in situ or in vivo labeling [232] or photothermal therapy applications [62].

The resonance wavelength  $\lambda_{res}$  of a nanoparticle is highly dependent on its material composition and geometry. Figure 11. *a* shows the tunability range for the nanoparticles composed of *Au*, *Ag* and *Al*, as the three most common material platforms in plasmonics [25]. In the NIR range, the plasmon resonance in all three metals is quite tunable, but as we approach the interband transition, not only the ohmic loss is increased, but also the tuning of plasmon resonance becomes challenging. Generally, the LSPR resonance can be tuned down to 550 *nm* in *Au* nanoparticles, 400 *nm* in *Ag* nanoparticles and 200 *nm* in *Al* nanoparticles. More complex geometries can improve the tunability of the LSPR resonance in plasmonic nanoparticles (Fig. 11. *b*), and increase the figure-of-merit defined as  $Q/V_m$ . For

instance, nanorods with high aspect ratios are more easily tunable and provide larger field enhancement  $\Gamma$ , and larger LSPR wavelength shift in response to a perturbation, compared to nanodisks and nanospheres [233,234]. Another way to increase  $\Gamma$  significantly and to introduce new degrees of freedom for tuning the LSPR resonance, is incorporating dielectric gaps in the design of nanocavities [235] through ligand or DNA mediated self-assembly of colloidal nanoparticles into chains, e.g. *dimer*, *trimer*, *tetramer*, etc. [236,237], 2D lattices [238,239] or inhomogeneous superstructures [240,241].

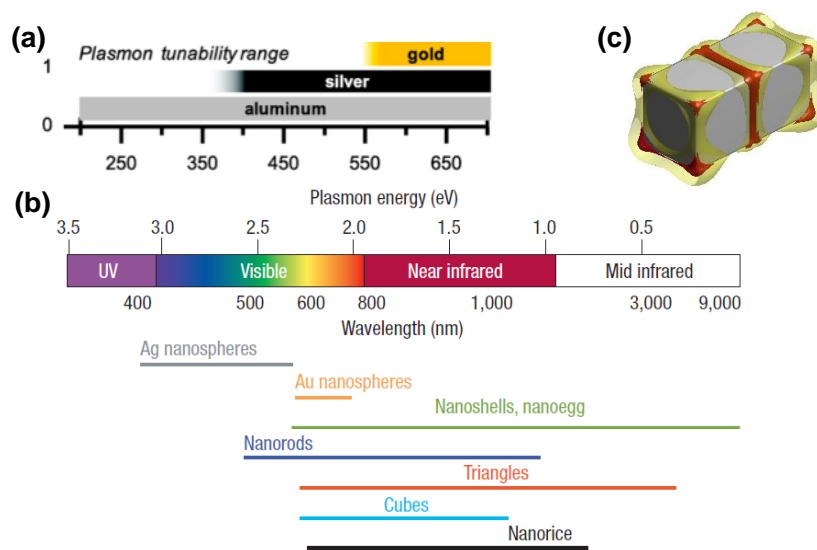


**Figure 11 - Tuning surface plasmon resonance in plasmonic nanoantennas. (a) Tunability range of the three most common material platforms, i.e. Au, Ag and Al (Image reproduced with permission from Ref. [25]) (b) Tunability range of nanoparticles with different shapes (Image reproduced with permission from Ref. [226]) (c) 3D representations of the hotspots in a face-to-face AgNC dimer with 42 nm edge length and 6 nm dielectric gap ( $H_2O$ ), the red and yellow isosurfaces shows the regions of space 30% and 12% maximum  $\Gamma$  at  $\lambda_{res}$**

Historically, plasmonic nanoparticles were first used in biosciences as ultra-bright labels for imaging applications [232,242], but later, label-free biosensing has emerged as one of the primary applications of plasmonic nanoparticles, besides photothermal therapy. In this chapter, we focus on the molecular sensing using LSPR wavelength shift in plasmonic nanoparticles and in the next two chapters; we expand to two other sensing modalities,

surface-enhanced Raman spectroscopy and metamaterial-enhanced chiroptical sensing, mainly lithographically fabricated plasmonic nanostructures.

### 3.1 Label-Free Biosensing Using Plasmonic Nanocavities

Most biosensing techniques employ some type of fluorescence or radio labeling scheme to record molecular binding events. There is however a significant amount of interest in label-free detection of biomolecules [243], due to their lower assaying costs and superior scalability and multiplexing potential. Most label-free detection methods, such as acoustic devices and field-effect transistors (FETs), have not been able to achieve the detection limit of label-based methods such as ELISA [244] employing fluorescence tags, but integrated photonic and plasmonic cavities can even surpass ELISA both in terms of detection limit and sensitivity. Label-free optical biosensing has been shown using high-Q photonic microcavities [245-247]. Low  $V_m$  plasmonic nanocavities can achieve similar or lower detection limits, approaching single molecule detection [225,248-250], in much more compact geometries, and with lower fabrication and instrumentation costs. Measurement of LSPR resonance wavelength shift is the first plasmonic sensing modality that we discuss in this dissertation. This is an evolution of the *surface-plasmon resonance* (SPR) [251,252] measurement method with significantly improved sensitivity and detection limit. In the rest of this section, we introduce the necessary terminology and definition used in molecular sensing using photonic and plasmonic cavities.

#### 3.1.1 Sensitivity Factor of a Nanocavity

For the case of single-molecule detection, the sensitivity of an optical resonator  $s_0$  can

be found from the first-order perturbation theory [253]:

$$s_0 = \left( \frac{\delta\omega}{\omega} \right)_{\bar{r}_0} = - \frac{\alpha_{ex} |\bar{E}(\bar{r}_0)|^2}{2 U_t} \quad (3.1)$$

$$U_t = \int \varepsilon(\bar{r}) |\bar{E}(\bar{r})|^2 d^3\bar{r} \quad (3.2)$$

where  $U_t$  is the total electromagnetic energy stored inside the cavity, and  $\alpha_{ex}$  is the excess polarizability of the molecule; i.e.  $\alpha_{ex} = \alpha_m - \alpha_a$  ( $\alpha_m$  and  $\alpha_a$  are the polarizability of the target molecule and the analyte). For a single layer of molecule uniformly coated on the surface of the resonator, the sensitivity  $s_l$  can be found by integrating the right hand side of Eq. 3.1 over the sensing area  $A_s$  [254]:

$$s_l = \left( \frac{\delta\omega}{\omega} \right)_{A_s} = - \frac{\alpha_{ex} \sigma_l}{4 U_e} \int_{A_s} |E(\bar{r})|^2 d^2\bar{r} \quad (3.3)$$

Similarly, for a small perturbation in a volume, the bulk sensitivity is found by integrating the right hand side of Eq. 3.1 over the sensing volume  $V_s$  [19,255]:

$$s_b = \left( \frac{\Delta\omega}{\omega} \right)_{V_s} = \frac{\Delta n_s}{n_s} \Gamma_s \quad (3.4)$$

where  $\Gamma_s = U_s/U_t$  is the confinement factor, i.e. the fraction of energy stored in the sensing region, with  $U_s = \int_{V_s} \varepsilon(\bar{r}) |\bar{E}(\bar{r})|^2 d^3\bar{r}$  being the energy stored in the sensing region.  $n_s$  is the refractive index of the analyte in the sensing region, and  $\Delta n_s$  is the small perturbation in  $n_s$ . For a bulk refractive index change, the bulk sensitivity factor  $m_b$  is defined as the wavelength shift per unit refractive index change ( $nm/r. i. u$ ):

$$m_b = \frac{\Delta\lambda}{\Delta n_s} = s_b \frac{\lambda_{res}}{\Delta n_s} = \frac{\Gamma_s \lambda_{res}}{n_s} \quad (3.5)$$

In the case of single-molecule and single-layer molecular detection,  $s_0$  and  $s_l$  are described as a function of electric polarizability  $\alpha_m$ , which is a microscopic quantity, whereas bulk  $s_b$  and  $m_b$  are functions of  $n_s = \sqrt{\mu\epsilon_0\epsilon_{r,s}}$ , a macroscopic property of material. These two quantities are related by *Clausius–Mossotti relation*:  $(\epsilon_r - 1)/(\epsilon_r + 2) = \sigma_b\alpha/\epsilon_0$  [256]. A very common scenario in sensing applications is a thin multi-layer film of molecules that does not cover the whole sensing region  $V_s$  [257,258]. In this case, the wavelength shift can be approximately described by:

$$\Delta\lambda = m_b \cdot (1 - e^{-2t/l_d}) \cdot \Delta n_s \quad (3.6)$$

where  $m_b$  is the sensitivity factor, and  $l_d$  is the characteristic decay length of LSPR resonance [259]. For a thin film,  $l_d$  is the skin depth defined in Ch. 2, but in the case of the LSPR resonance, it is simply a measure of average penetration of the field within the sensing volume, and it is closely related to  $V_m$ .

Going to back to the case of single molecule detection,  $s_0$  can be rewritten as  $s_0 = -\frac{1}{2}\alpha_{ex}|E_0|^2/V_m|E_{max}|^2$ . Thus, to maximize  $s_0$ , it is necessary to: *a)* reduce  $V_m$ , which is why plasmonic nanocavities are so effective, *b)* increase the ratio  $|E_0|/|E_{max}|$ , which occurs when the molecule is at the hotspot. Now, considering a single layer of molecules, to increase  $s_l$ , we should find a strategy to increase the ratio  $U_s/U_t$ , meaning that we need to pull the electromagnetic energy out of the resonator into the analyte. This is also valid for single molecule and bulk sensitivity and can be accomplished by incorporating dielectric gaps in the nanocavity design, for instance in closely spaced nanoparticle chains.

Ultimately, the *detection limit* of a molecular sensor is also dependent on the signal-to-noise ration (SNR) of the measurement apparatus and the minimum  $\Delta\lambda$ , it can detect [260]. Generally, the minimum detectable  $\Delta\lambda$  is inversely proportional to the resonance linewidth

and hence proportional to Q-factor. As a result,  $Q/V_m$  is the overall figure-of-merit for a molecular sensor based on resonance wavelength shift. As we will see in the next chapter, the linewidth of plasmonic nanoparticles can be further decreased using Fano-type coupling, which further increases the detection limit in label-free biosensing. For chemically synthesized plasmonic nanoparticles, it is more convenient to measure the absorption, scattering and extinction cross-sections ( $C_{abs}$ ,  $C_{sca}$  and  $C_{ext}$ ) in colloidal form, and sometimes the ratio  $\eta = Q_{sca}/Q_{ext}$  is used as the figure-of-merit, where  $Q_{sca}$  and  $Q_{ext}$  are the scattering and extinction efficiencies of the nanoparticle [233]. In the simple case of a nanosphere,  $Q_{sca} = C_{sca}/\pi r^2$ . The same relation holds between  $C_{abs}$  and  $Q_{abs}$ , and between  $C_{ext}$  and  $Q_{ext}$ , in a nanosphere [261].

### 3.2 Ultrasensitive Molecular Sensing Using Plasmonic Nanocube Chains

Gold and silver nanocubes (NCs) [262,263] and their derivatives: *nanocages* [264] and *nanoframes* [265] are among the most sensitive chemically-synthesized plasmonic nanoparticles due to several factors: their high Q-factor, low  $V_m$  and sharp edges resulting in intense hotspots. These plasmonic nanocavities exhibit high sensitivity in molecular sensing based on the shift of  $\lambda_{res}$ , which can be conveniently tuned in a wide range based on the application, and high field enhancement at the hotspots, which can, for instance, be used in surface-enhanced vibration spectroscopy, discussed in the next chapter. By arranging the nanocubes in a 1D arrays with nanometer sized gaps, the sensitivity and field enhancement can be further improved. In this section, we present a quantitative study of plasmonic nanocube chains in two different orientations: *face-to-face* (F-F) and *edge-to-edge* (E-E). The optical properties, and performance factors of NC chains with different lengths and

orientations are compared in two important regimes: *i*) large gap size,  $d_g > 1 \text{ nm}$ , where electromagnetic coupling is the dominant effect, *ii*) sub-nanometer gaps,  $d_g < 1 \text{ nm}$ , where the effect of plasmon tunneling is significant, in addition to the classical electromagnetic coupling.

### 3.2.1 Classical Electromagnetic Coupling

In the first part of our study, chains of *Au* and *Ag* plasmonic NCs with edge length of  $l = 21 \text{ nm}$  and gap size of  $d_g = 8.5 \text{ nm}$  are considered. With this separation gap, classical electromagnetic coupling is dominant, in both F-F and E-E configurations. The spectral response of this system, i.e. absorption, scattering or extinction cross section, depends on the number of NCs, the type of metal, and the NC orientation. For instance, Figs. 12. *a, b* show the extinction spectrum of F-F and E-E *Ag* NC chains with three different lengths: *dimer* ( $n = 2$ ), *trimer* ( $n = 3$ ) and *tetramer* ( $n = 4$ ). Our first observation is that  $\lambda_{res}$  increases as we increase the length of NC chain.

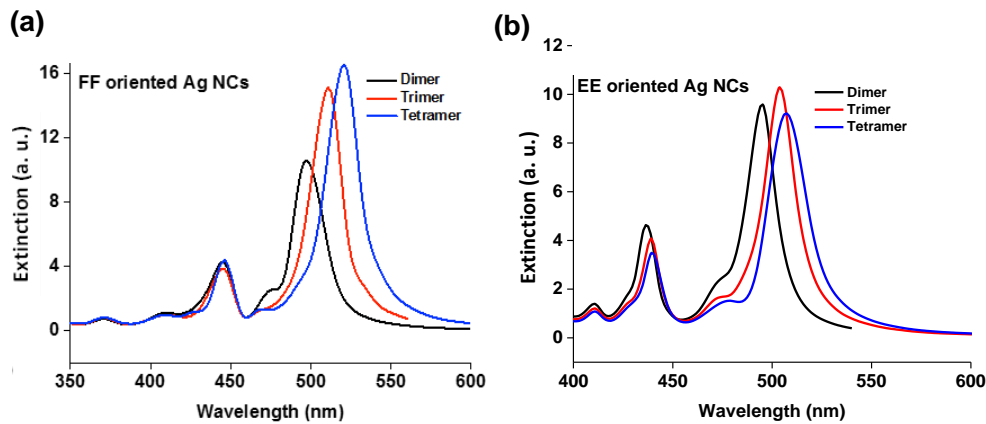


**Figure 12 - Extinction spectra of plasmonic NC chains of different lengths in F-F and E-E configurations. (a) Extinction spectrum of F-F *Ag* NC dimer, trimer and tetramer, (b) Extinction spectrum of E-E *Ag*NC dimer, trimer and tetramer**

The overall trend of  $\lambda_{res}$  vs. the refractive index of the surrounding medium is shown in Figs. 13. *a – d* for different lengths and configurations. Since the perturbation  $\Delta n$  is considered to be small relative to the refractive index of the surrounding medium, these curves are approximately linear, according to the first-order perturbation theory. The slope of these lines is the sensitivity  $m_b$  defined in Eq. 3.5.

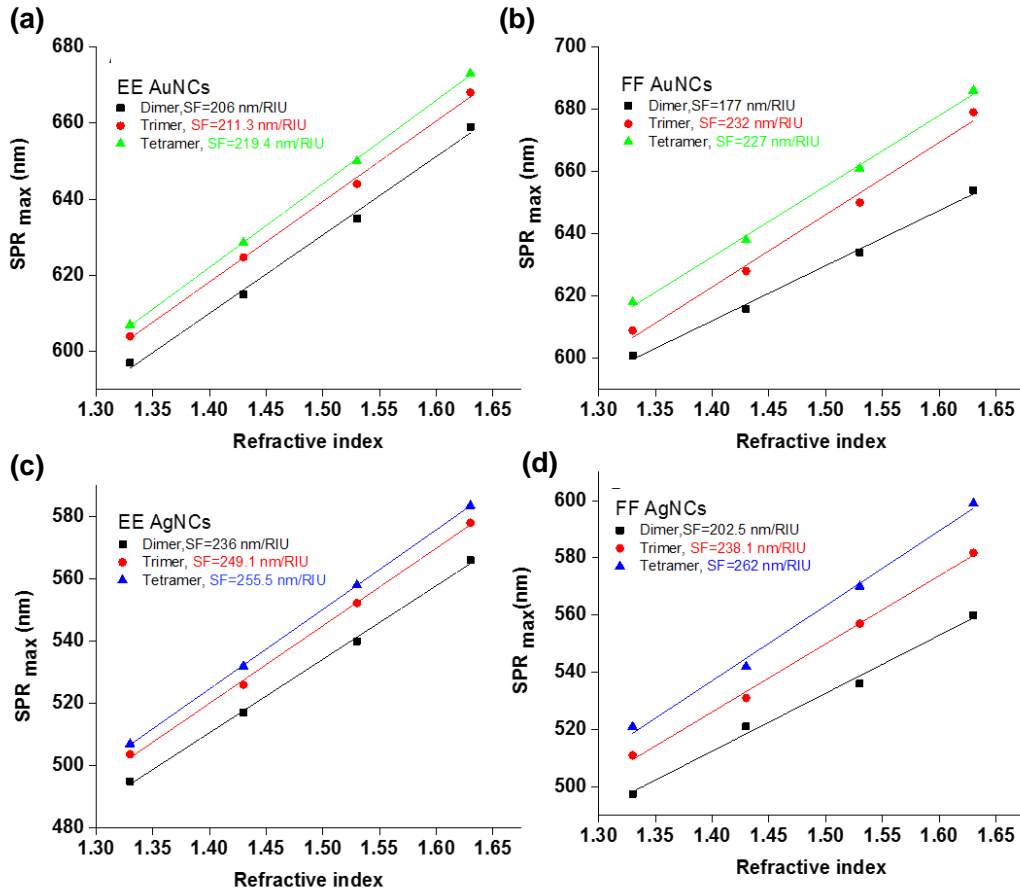


**Figure 13 - Sensitivity factor  $m_b$  of plasmonic NC chains of different lengths in F-F and E-E configurations. (a,b) Au NC chains in E-E and F-F configurations, (c,d) Ag NC chains in E-E and F-F configurations.**

Interestingly, an increase in the number of NCs in the 1D array results in an increase in  $m_b$ , and overall orienting the NCs in E-E configuration results in higher  $m_b$ , relative to F-F configuration, with a few exceptions (Fig. 14). For instance, F-F Au NC tetramer shows

lower  $m_b$  than F-F *Au* NC trimer. Besides the spectral response, the electric-field distribution, and the peak enhancement factor at the hot spots are also affected by changing the type of metal, the length of chain and configuration of the NCs.

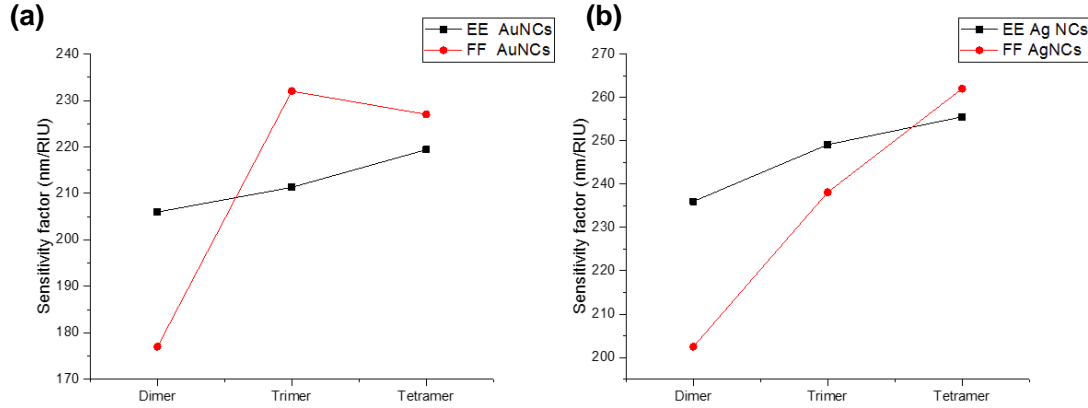


**Figure 14 - Evolution of the sensitivity factor  $m_b$  vs. the length of NC chains. (a)  $m_b$  of E-E and F-F *Au* NC dimer, trimer and tetramers, (b)  $m_b$  of E-E and F-F *Ag* NC dimer, trimer and tetramers**

The peak enhancement factor  $\Gamma_{max}$  which occurs at  $\lambda_{res}$  can be used as a measure of performance in molecular sensing based surface-enhanced vibrational spectroscopic technics. Figures 15. *a – c* show the electric-field distribution of *Au* NC dimer, timer and tetramer at  $\lambda_{res}$ , as an example. Overall, an increase in the number of NCs results in an increase in  $\Gamma_{max}$ , and E-E configuration tends to result in higher confinement of electric-field and higher enhancement compared to F-F configuration.

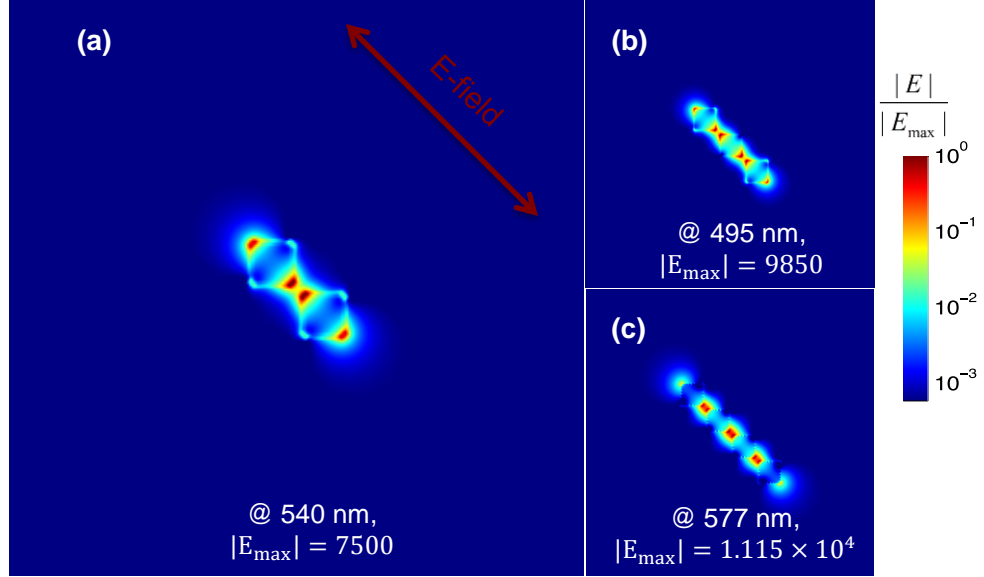


**Figure 15 - Normalized electric-field distribution of Ag NC chains in E-E configuration. (a) Dimer, (b) Trimer and (c) Tetramer**

### 3.2.2 Plasmon Tunnelling Effect in Nanocube Chains

So far, we have only discussed the optical response of NC chains with  $d_g > 1 \text{ nm}$ . With sub-nanometer separation distances, the electrons (and plasmons) can tunnel through the dielectric gap, producing a tunneling current that significantly alter the optical response of the plasmonic system [266-269], and hence the the classical model is no longer sufficient to predict the resonance spectrum and field distribution. Aside from the gap size, local topology of the junction, i.e. material type, shape and scale, also affects the plasmon tunneling [270,271]. This effect can be used in reverse direction for the tunneling-induced generation of SPPs [272]. It is possible to generate wide-band surface plasmons, by applying an electrical voltage across a sub-nanometer gap in a plasmonic junction [273], AFM tip [274] or dimer nanoantenna [275], which act as high- $\Gamma$  hotspots enhancing electrical generation of SPPs. In this section, we discuss the effect of plasmon tunneling on the optical resposne of NC chains with  $d_g < 1 \text{ nm}$ , where the effect of quantum tunneling becomes prominent

particularly in smaller nanoparticles. This is a very important consideration in practical plasmonic sensors as the common method of dispersing chemically synthesized nanoparticles on substrates naturally creates chains with very small gaps, as it can be seen in Fig. 16. Experimentally, it is also possible to control the separation gap between nanoparticles by coating them with chemical ligands of various lengths [276-278].

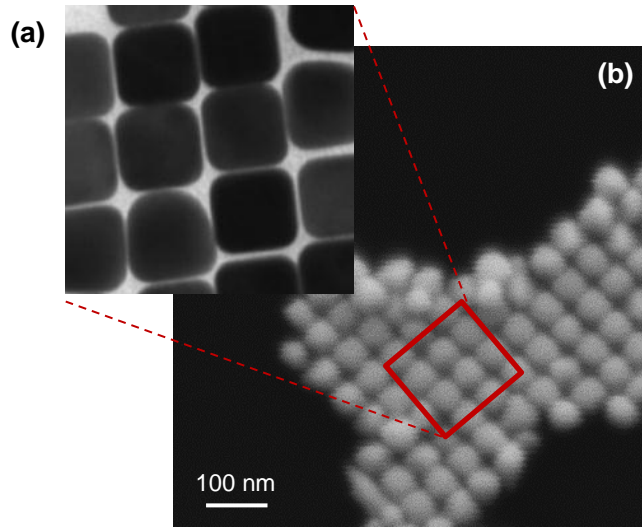


**Figure 16 - Naturally dispersed AuNCs on a surface tend to create face-to-face sub-nanometer gaps. (a) Transmission electron microscope (TEM) image of face-to-face NC assemblies with sub-nanometer gaps, (b) Oblique SEM image of the assembly with 15° tilt.**

For this study, a quantum corrected model (QCM) [279,280] was implemented within the FDTD framework to approximate the effect surface plasmon tunneling at the junctions between NCs. We performed a set of simulations for *Au* NC dimers, trimers and tetramers with the edge length of  $l = 21 \text{ nm}$ , the separation gap  $d_g = 0.2 \text{ nm}$  and the radius of curvature at the edge  $r_c = 5 \text{ nm}$ . The first set of simulations are pure electromagnetic simulation using FDTD method, which does not account for the effect of plasmon tunneling. Next, QCM was used to approximate the effect of tunneling on LSPR resonance by assuming a virtual conducting medium, *Au Jellium*, of  $0.2 \text{ nm}$  width between the NCs. The electric

permittivity of the tunneling channel is calculated using the modified version of Drude model, we saw in Ch.2.

$$\varepsilon(d_g, \omega) = \varepsilon_\infty - \frac{\omega_g^2}{\omega(\omega + i\gamma_g(d_g))} \quad (3.7)$$

where  $\gamma_g$ ,  $\omega_g$  and  $\varepsilon_\infty$  are the parameters for an equivalent Drude metal placed within the junction, which would produce the same current density, as it can be obtained by solving the 1D electron tunneling in a metal-dielectric-metal quantum barrier for a given barrier width  $d_g$  [281]. The real and imaginary parts of this complex permittivity for  $d_g = 0.2 \text{ nm}$  is plotted in Fig. 17. This approximation is only true if the radius of the curvature is large compared to the gap size and the Fermi electron wavelength. For NCs with extremely sharpe edges or sharp AFM tips, this model can potentially break down.

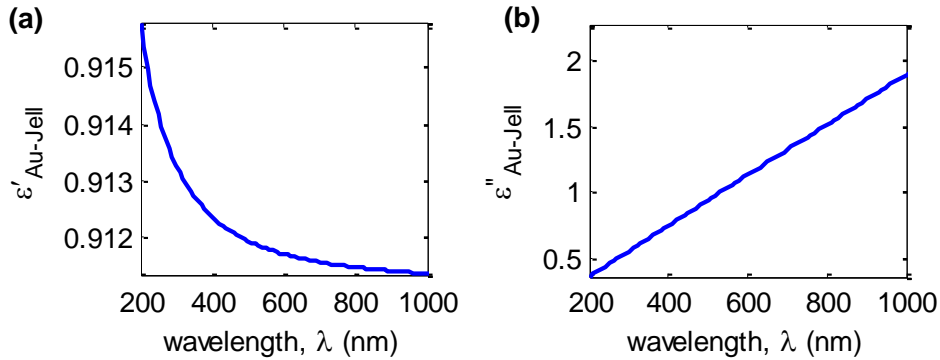


**Figure 17 – Permittivity of the Au Jellium used to estimate the effect of plasmon tunneling in QCM simulation. (a) Real and (b) imaginary part of the permittivity of the Au Jellium for the case of 0.2 nm separation gap.**

The effect of plasmon tunneling between two relatively large NCs in F-F orientation has been reported previously [282]. The quantum tunneling manifests itself as the damping of the dimer plasmon resonance in *electron energy loss spectroscopy* (EELS) measurements, as the gap size is reduced below 1 nm,. This is in direct contradiction with classical model, which predicts monotonic increase in the intensity of the dimer resonance. The second effect

of quantum tunneling is the appearance of a distinct mode at sub-nanometer gaps, called *tunneling charge transfer plasmon* (tCTP) mode. From our calculation, the effect of quantum tunneling on the the optical response of the NC chains is stronger in E-E configuration, which is due to the higher localization of the electric-field at the corners, where most of the tunneling occurs. Figures 18. *a – f* show the transmission spectra of dimer, trimer and tetramers *Au* NCs in E-E and F-F configurations in a square lattice array with the periodicity of  $1.5 \mu\text{m}$  at each direction (effectively uncoupled). As it can be seen in these figures, at large wavelengths a significant damping of the main LSPR modes can be observed due to the quantum tunneling, and the amount of damping is more significant in E-E configuration.

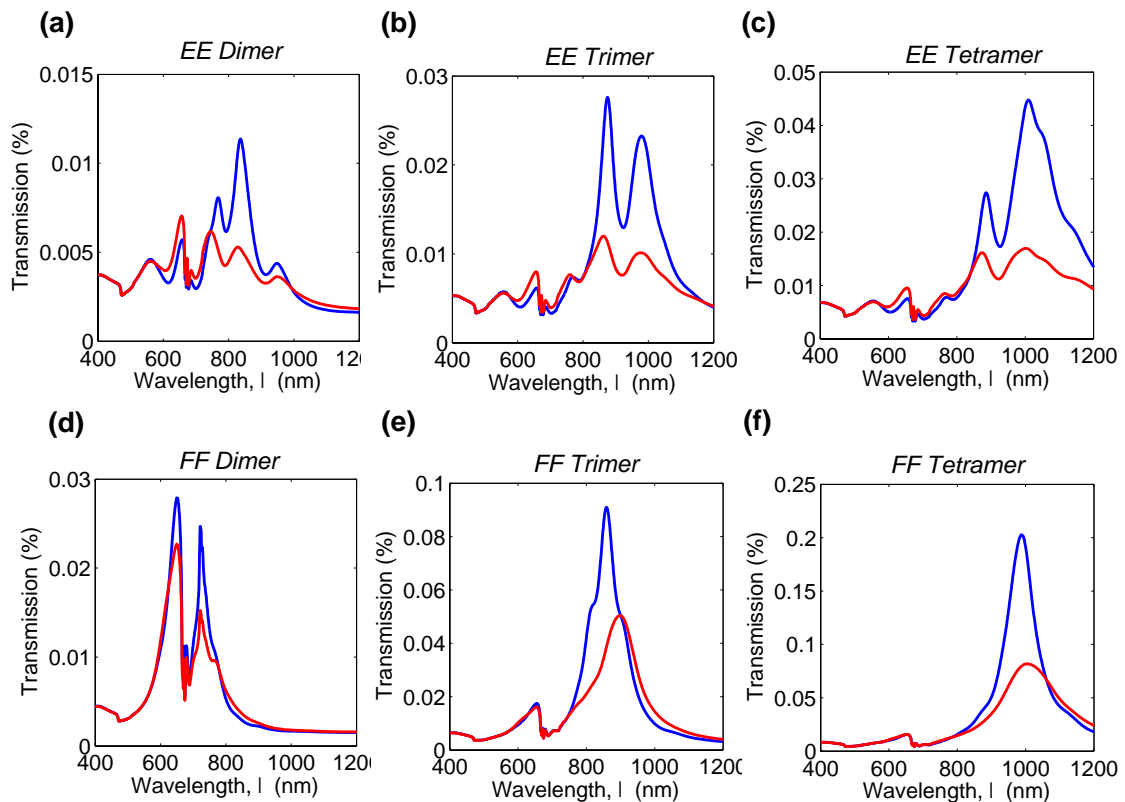


**Figure 18 - Effect of plasmon tunneling on the optical response of NC chains. (a-c) Transmission spectra for NC dimer, trimer and tetramer, respectively, with the  $0.2 \text{ nm}$  air gap and corner radius of  $5 \text{ nm}$  in E-E configuration, (d-f) Transmission spectra of NC chains with the same length and separation gap with F-F configuration (blue curves: classical model, red curves: quantum-corrected model).**

Plasmon tunneling also alters the electric field distribution profiles. For instance, Fig. 19 shows the electric field modeprofile of the the main LSPR band for E-E *Au* NC trimer at its resonance wavelength  $\lambda_{res} = 862 \text{ nm}$  from the QCM model.

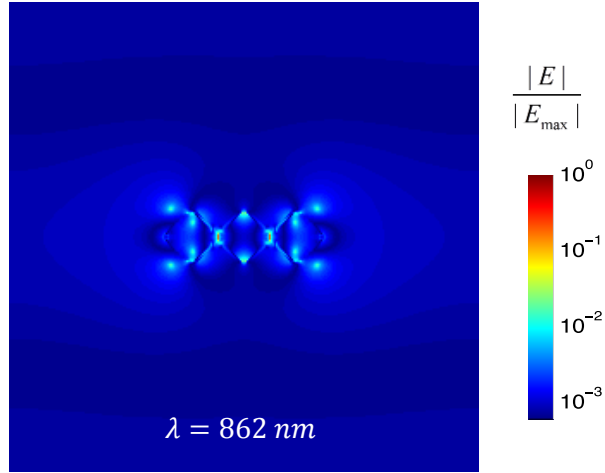


**Figure 19 - Electromagnetic field distribution calculated for the E-E oriented *Au* NC trimer at 0.2 nm separation distance from the QCM model.**

In general, quantum tunnelling induces a shift on  $\lambda_{res}$  and reduces the overall absorption cross-section of the plasmonic chain at resonance wavelengths as it can be seen in Figs. 18. *a – f*. As for electric-field distribution, the plasmon tunneling reduces the electric-field confinement at hot-spots. One final comment on the effect of plasmon tunneling is that even though, this effect generally reduces the absorption (or scattering) cross-section and the intensity of electric field at  $\lambda_{res}$ , it does not necessarily result in less sensitive sensors. The introduction of a biomolecule in the small air gap between the nanocube can change the height of the energy barrier between the two metal junctions and may even potentially lead to an increase in the sensitivity in the quantum-tunneling based biosensor compared to the classical sensors.

## CHAPTER 4.

### APPLICATION OF LATTICE PLASMONS IN SURFACE ENHANCED RAMAN SPECTROSCOPY

Spectral analysis of large biomolecules is invaluable in a number of applications, including medical diagnostics and label-free biosensing. Spectroscopic techniques, such as *Raman*, *coherent anti-Stokes Raman scattering (CARS)* and *infrared absorption (IRA)* spectroscopy, based on optical processes shown Figs. 10a-c, are of particular interest for non-destructive spectral analysis based on vibrational levels of molecules which can be associated to first-order molecular structures, i.e. the atomic composition and molecular bonds. It has been shown that the vibrational spectroscopy of proteins can be useful in diagnosing a number of diseases, including many types of cancer [283-286]. Raman spectroscopy and CARS<sup>1</sup> in particular are very useful for in-vivo and in-situ analysis of biological specimen using visible and NIR excitation [287,288]. However, most diagnostic experiments using vibrational spectroscopy techniques have been performed using traditional vibrational spectroscopy, which requires a large number of molecules. Development of assays suitable for vibrational spectroscopy using single or few molecules could lead to a substantial decrease in the amount of specimen necessary for these experiments, which is crucial in many applications, such as real-time spectral analysis [289] and early diagnostics of hard-to-cure diseases using trace biomarkers [290]. Surface-enhanced counterparts of vibrational spectroscopy techniques, SERS [291-294], SECARS [295-297] and SEIRA [298,299], rely on the amplification of Raman emission or enhanced IR absorption of molecules at the

---

<sup>1</sup> CARS is a nonlinear spectroscopic technique, in which the four-wave mixing (FWM) between a Stokes photon and two pump photons are utilized to generate one anti-Stokes photon; i.e.  $\chi^{(3)}(\omega_{AS}; \omega_p, \omega_p, -\omega_S)$  with  $\omega_{AS} = 2\omega_p - \omega_S$ . The details of FWM, as a third-order nonlinear process, are discussed in Ch.6.

hotspots of plasmonic nanostructures. In this section, we focus on SERS as the most versatile surface-enhanced vibrational technique.

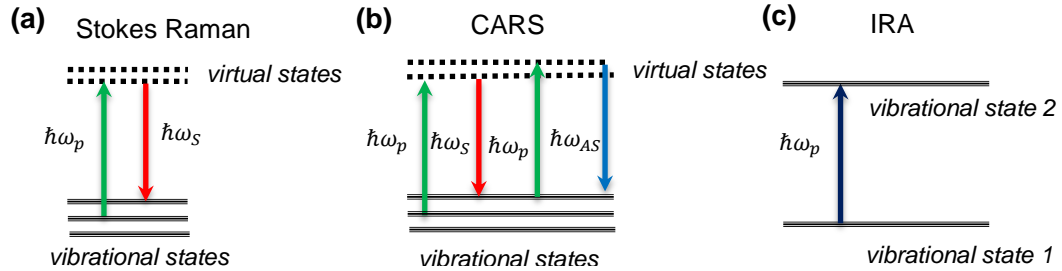


**Figure 20 - Optical processes used in vibrational spectroscopy. (a) Stokes Raman emission, (b) Coherent anti-Stokes Raman emission, (c) Infrared absorption between the vibrational levels of the molecule**

#### 4.1 Collective Resonance of Nanoantennas and Lattice Plasmons

In previous chapter, we saw the effect of near-field coupling between plasmonic nanocavities at very small separation distances relative to the resonance wavelength,  $\lambda_{res}$ , which results in localized gap modes. At distances comparable to  $\lambda_{res}$ , nanocavities are still coupled resulting in a slight extension of localized modes within the dielectric region. “*Collective resonance*” or “*lattice resonance*”, occurs once the nanocavities are placed in a periodic array, with a period  $p$  comparable to  $\lambda_{res}$ . The main signature of collective resonance is linewidth narrowing and the appearance of sharp non-Lorentzian resonance features in properly designed arrays [300,301]. This type of asymmetric resonance lineshape, which is now called *Fano resonance*, was first observed by Ugo Fano in quantum mechanical study of auto-ionization states of atoms [302], and was later also observed in various classical systems with different types of wavefunctions. The origin of Fano-resonance is the constructive and destructive interference between a narrow resonance and broad spectral line

(a wide resonance or a continuum), resulting in a distinct asymmetric lineshape as shown in Fig. 22, described by the following equation:

$$I(\omega) = \frac{(F\gamma + \omega - \omega_0)^2}{(\omega - \omega_0)^2 + \gamma^2} \quad (4.1)$$

where  $I(\omega)$  is the intensity at frequency  $\omega$ ,  $\omega_0$  and  $\gamma$  are the parameters determining the position and width of the Fano resonance, and  $F$  is the so-called the Fano parameter, describing the degree of asymmetry in lineshape. In classical optics, the first observation of this asymmetric lineshape was the *Wood's anomaly* in metallic gratings, which was later explained by Fano resonance [303]. In the domain of integrated photonics and plasmonics, Fano resonance is observed in various coupled dielectric structures [304,305], semiconductor nanostructures [306], plasmonic metamaterials [307,308] and coupled nanoantenna arrays [309-312], which is the main focus of this chapter. In nanoantenna arrays, the collective resonance, which is a Fano-type resonance, is the result of interference between the nanoantenna scattering (broad resonance) and the Bragg scattering (sharp resonance), and can be used to increase the detection limit in refractive index sensing as discussed in the previous chapter [313,314].

At near-field, these collective resonant features are accompanied by *lattice plasmon* (LP) waves [315,316], propagative Bloch waves that are direct result of coupling between nanoantennas, with properties such as high  $\Gamma$ , narrow linewidth, and efficient coupling to radiative modes (high excitation and collection efficiency), which make them attractive in a number of light-matter interaction applications. In this chapter, we will discuss the application of lattice plasmons in SERS.

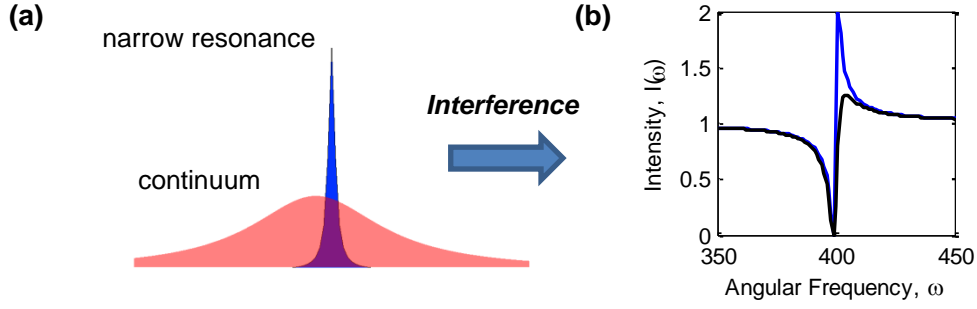


**Figure 21 - Fano resonance in optics. (a) the two interfering spectral lineshapes, (b) general form of Fano lineshape, Eq. 4.1 with  $\omega_0 = 400 \text{ rad.THz}$ , black curve:  $F = 1, \gamma = 1$ , black curve:  $F = 0.5, \gamma = 2$**

## 4.2 Emission Enhancement by Purcell Effect

Raman emission is a two-step process: *i*) absorption of the photon at  $\lambda_{exc}$ , *ii*) emission of another photon at a wavelength shifted according to the vibrational band of the molecules,  $\lambda_{em}$ . The enhancement in absorption process,  $\Gamma_{exc}$ , can be well described by the electric-field enhancement factor, i.e.  $\Gamma_{exc}$  at  $\lambda_{res}$ . In principle, the enhancement in radiative rate of the molecule or emission enhancement factor,  $\Gamma_{em}$ , in the vicinity of a nanostructure also known as *Purcell effect*, can be found using Fermi's golden rule, which involves the calculation of the partial LDOS describing the field and frequency overlap between a quantum emitter and eigenmodes of the nanostructure [12]. For an isolated optical cavity, this calculation reduces to the Purcell Factor,  $F(r, \phi)$  [317]:

$$F(r, \phi) = F_{max} \left| \frac{E(r)}{E_{max}} \right|^2 \cos(\theta) \quad (4.2)$$

$$F_{max} = \frac{3}{4\pi^2} \frac{\lambda^3}{n^2} \left( \frac{Q}{V_m} \right) \quad (4.3)$$

where  $r$  is the position of the quantum emitter (molecule),  $E(r)$  is the field that the emitter experiences at location  $r$  and  $\phi$  is the angle between the quantum emitter and cavity polarization. As we see from Eq. 4.3, once again  $Q/V_m$  is the main figure-of-merit for the optical cavity in Purcell effect, similar to the case of molecular detection discussed in the previous chapter. Numerically, it is often more convenient and more precise to place an electric dipole at the location of the molecule, with polarization of interest and then calculate the total emitted power of the dipole in closed surface in presence of the nanostructure,  $P_{i,struct}$  and its absence,  $P_{i,vac}$ , with  $i = x, y$  and  $z$ . Then, the emission enhancement factor in direction  $i$  can be found from [318]:

$$\Gamma_{i,em} = \frac{P_{i,struct}}{P_{i,vac}}, \quad i = x, y \text{ and } z \quad (4.4)$$

### 4.3 Surface-Enhanced Raman Spectroscopy Using Lattice Plasmons

A number of plasmonic structures can in essence provide the sufficient field enhancement in their hotspots for low concentration SERS-based spectral analysis [319-321]. In practice, however, the reported values for the average field enhancement in these structures are fairly modest partially due to the large variation of the field profile over the sensing area. Moreover, in the case of large biomolecules, the non-uniformity of the enhancement profile could result in the non-repeatability of the experiments due to substantial size of the biomolecules relative to the hot-spots. The conventional route to SERS is to use the LSPR resonances in an array of isolated nanoantennas. The high absorption (and scattering) cross section of nanoantennas near the resonance frequency results in a large enhancement of the Raman signal collected from the molecules located in the intense

hotspots. However, there is a practical limit to the intrinsic nanoantenna cross-sections, determined by nanoantenna geometry and composition.

A promising approach to improve the SERS enhancement is to use the LPs in a periodic nanoantenna array. Previously, LPs inside a nanoantenna array were used to enhance the stimulated emission, leading to lasing action [322] by increasing LDOS at the band-edge. However, this effect is very narrow-band and is not suitable for the enhancement of the wide-band Raman emission spectra. Our approach is to utilize the band-edge LPs at the excitation wavelength to increase the net absorption cross section of the array. Additionally, the two interacting layers of the nanostructure shown in Fig. 23, create intense hotspots in the vertically oriented gaps, which are coated selectively with molecular probes to form the sensing area. These two provisions collaboratively result in a large SERS enhancement over a large bandwidth, rivaling and potentially surpassing most nanofabricated SERS arrays. The rather uniform distribution of the SERS enhancement over the sensing area renders the structure particularly suitable for large biomolecules, such as proteins.

An array of gold nanodisks, stacked on an array of nanoapertures via supporting dielectric nanopillars, constitutes our nanostructure, illustrated in Figs. 23, 24.a. The dielectric nanopillars, composed of hydrogen-silsesquioxane (HSQ), act as the sensing area in SERS experiments. In order to maximize the light-matter interaction, the periodicity of the structure is selected such that a band-edge LP with near-zero group velocity is induced at the close vicinity of the excitation wavelength,  $\lambda_{exc}$ , as a direct consequence of the lateral coupling between the nanoantennas. Additionally, the structure is designed to confine the LSPR modes at the Fano resonance wavelength in the vertical gap between the two layers, providing a large and fairly uniform enhancement profile over the dielectric nanopillars due to the vertically oriented gap modes. We found that the highest enhancement factor occurs,

when the LP band-edge coincides with the resonance peak of LSPR resonance peak of the individual nanoantennas.

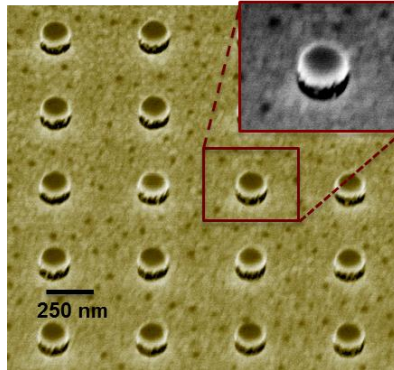


**Figure 22 - Scanning electron microscope image of bilayer nanoantenna array with 45 degree tilt, the inset shows a close-up view of one unit-cell**

The nanostructure shown in Fig. 23 has three distinct LSPR modes: a primarily disk mode at  $668\text{ nm}$  and two vertical gap modes at  $781\text{ nm}$  and  $937\text{ nm}$ , in which most of the energy is confined in the vertical gap between the nanoantenna and the nanoaperture (Figs. 24.d-f). Both of these two gap modes provide a large field enhancement with relatively uniform distribution over the dielectric surface as it can be seen in Fig. 24. *b*. In addition, the mode at  $781\text{ nm}$ , coincides with the band-edge of the second LP mode  $LP_2$  near the pump wavelength. This Fano-type plasmonic resonance is very narrow band, but it has a large absorption cross section and field enhancement at the resonance peak. Hence,  $LSPR_2$  is an excellent candidate for enhancing the narrow-band pump signal at  $785\text{ nm}$ . The second gap mode has a considerably larger bandwidth and contributes to the enhancement of the emitted Raman signal.

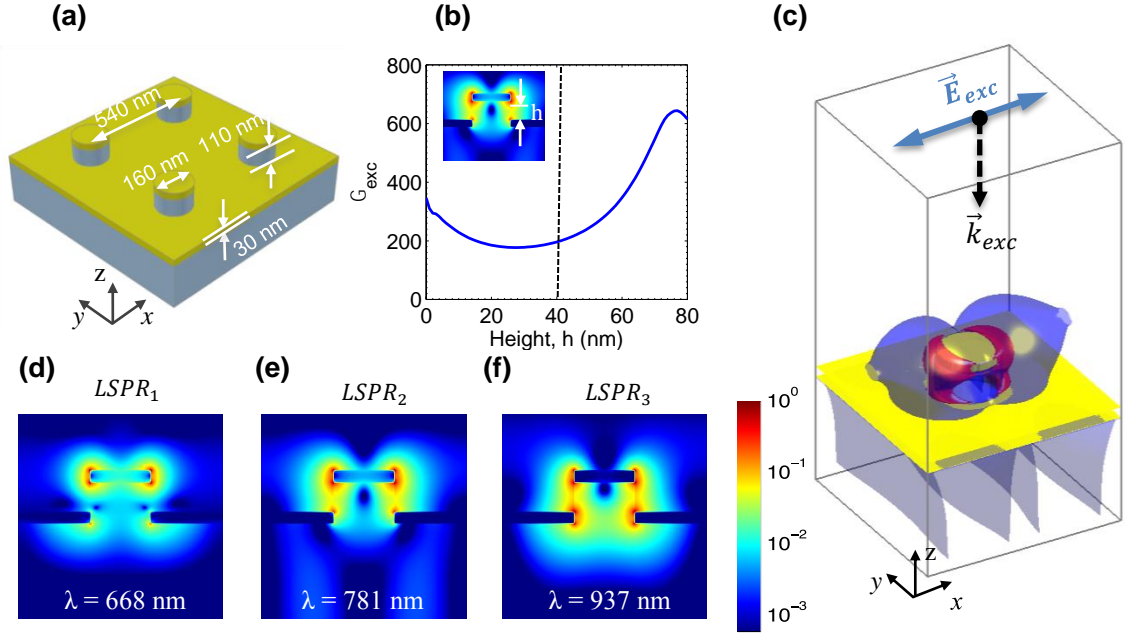


**Figure 23 -** Distribution of the enhancement factor at different wavelengths, (a) Schematic view of the bilayer nanoantenna including all geometrical parameters (b)  $\Gamma$  at  $\lambda_{exc}$  over the nanopillar height, as the sensing area, (c) 3D distribution of vertical gap mode (red) and horizontal LP mode (d-f) the three LSPR modes of the bilayer unit-cell

Table 3 shows the critical optical properties of the three LSPR modes: resonance wavelength,  $\lambda_{res}$ , resonance lifetime,  $\tau_{res}$  and mode volume,  $V_m$ .

**Table 3 -** Optical properties of the three LSPR modes of the structure shown in Fig. 13 from FDTD simulations.

	$\lambda_{res}$	$\tau_{res}$	$V_m$
<b><i>LSPR<sub>1</sub></i></b>	668 nm	13.04 fs	$2.04 \times 10^{-4} \lambda^3$
<b><i>LSPR<sub>2</sub></i></b>	781 nm	16.50 fs	$3.64 \times 10^{-4} \lambda^3$
<b><i>LSPR<sub>3</sub></i></b>	937 nm	15.63 fs	$8.04 \times 10^{-5} \lambda^3$

This nanostructure has two LP modes, each one with a band-edge at normal incidence that can be adjusted in a wide frequency range by changing the lattice constant. Nanopillar radius also has a minor effect on the LP band-edge. On the other hand, the resonance peaks of the LSPR modes can be adjusted in a wide frequency range by changing the nanopillar

radius and to some extent the lattice constant. Thus, the proposed structure can be tuned to operate within a wide frequency gamut for the simultaneous enhancement of the excitation and emission signals. In our structure, the second LP band-edge, shown in Fig. 25. *b* is used to enhanced the pump, as it can be excited more efficiently with the normally incident light and can be adjusted more easily.

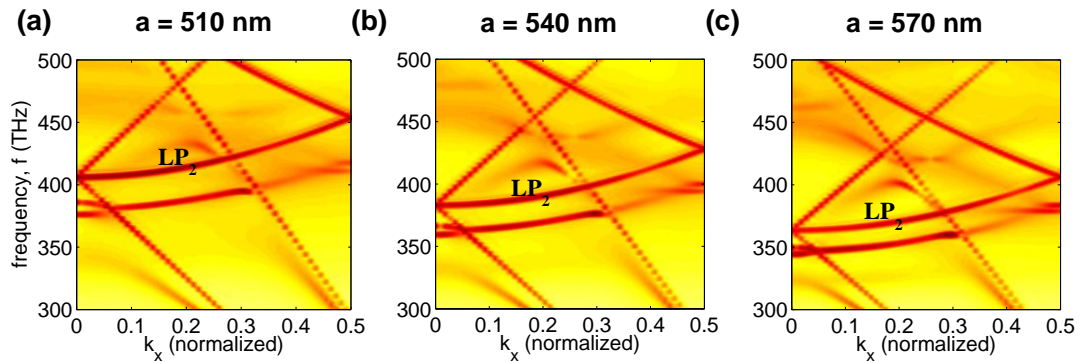


**Figure 24 - Tuning of the LP band-edge by change the periodicity. (a) Band-digram for the array with  $p = 510 \text{ nm}$ , (b) Band-diagram for the array with  $p = 540 \text{ nm}$  (optimal design), (c) Band-diagram for the array with  $p = 570 \text{ nm}$ .**

To assess the performance of our structure in SERS-based molecular sensing, we have calculated the local excitation and emission field enhancement spectra,  $\Gamma_{exc}$  and  $\Gamma_{em}$  respectively, using separate FDTD simulations. Figure 26. *b* shows the spectrum of  $\Gamma_{exc}$  under the normal incidence at two fixed points shown in Fig. 26. *a* (*Point A*: mid-pillar height, *Point B*: mid-disk height). The emission field enhancement,  $\Gamma_{em}$  for the three field components at *Point A* is shown in Fig. 26. *c*. In contrast to most reported works in plasmonic sensing, we use the dielectric surface of the nanopillars for the immobilization of the target molecules to lower the amount of analyte necessary for the coating of the nanostructure, which is an important consideration in many biosensing applications. The results shown in Figs. 26. *b, c* depict close to the worst case, i.e. the smallest  $\Gamma_{exc}$  and  $\Gamma_{em}$  over the sensing areas. Nevertheless, the total enhancement factor in this worst-case scenario

is comparable to the maximum enhancement factor in bowtie nanoantennas, which are one of the best performing nanofabricated nanoantennas, with air gaps as small as 50 nm [323-325]. The enhancement factor in our structure is higher at points that are closer to the surface of the nanopillar and / or are closer to the top nanodisk or the bottom nanoaperture as it can be seen from Fig. 24. b. Most notably, the high Raman enhancement is present all over the sensing area, whereas in bowtie nanoantennas, the SERS hotspot is concentrated at a very small region between the two triangles of the nanostructure.

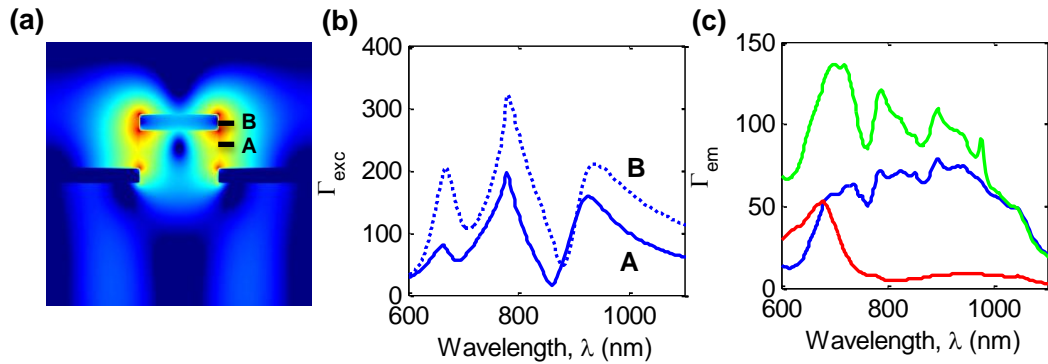


**Figure 25 - Excitation and emission enhancement factor spectra. (a) Two points 5 nm away from the surface of disk and nanopillar, (b)  $\Gamma_{exc}$  at point A (solid curve) and point B (dashed curve), (c)  $\Gamma_{em}$  calculated at point A for an x-polarized dipole (blue curve), y-polarized dipole (red curve) and z-polarized dipole (green curve)**

To demonstrate the high sensitivity of our device experimentally, nanoantenna arrays with different radii and periodicities were fabricated on a silicon wafer with a thick thermally grown  $SiO_2$  layer on top. A protein, namely streptavidin, was coated on the dielectric nanopillars by immersing the sample in an aquatic solution with the controlled concentration of 100 nM. Prior to the immobilization of streptavidin, the dielectric surface was functionalized using a process involving two self-assembled monolayers (SAMs), a layer of 3-aminopropyl-triethoxysilane (APTES) to provide free amine groups and a second SAM of NHS-biotin, as the linker to trap the protein molecules. The SERS spectrum of each array was collected using a Raman spectrometer and a near-infrared excitation laser at 785 nm.

Figure 27. *a* shows the Raman spectra acquired from the arrays with the lattice constants varying from 500 to 580 *nm* and with the fixed pillar radius of 80 *nm*. As expected from the simulations, the best Raman signal, shown with red curves in Figs. 27 – *a, b*, was acquired from the array with the periodicity of 540 *nm*. The variation of the SERS signal with the nanopillar radius, at a fixed lattice constant is less prominent with the strongest signal acquired from the array with 80 *nm* radius as it can be seen in Fig. 27. *b*. Our simulations had predicted that the band-edge of LP<sub>2</sub> should coincide with the second localized SPP resonance in the array with 80 *nm* nanopillars and the periodicity of 540 *nm*, which was confirmed with the experiments.

It should be noted that fabricated nanoantennas have slightly different geometry, from the ideal structure. Close inspection by scanning electron microscopy (SEM), has revealed that the fabricated nanoantennas are mushroom-shaped, see Fig. 23, with rims slightly extended outside the supporting nanopillars due to the nature of the electron beam deposition. This should also affect the geometry of the nanoapertures at the bottom of the nanopillars. Despite this non-ideal shape, a good agreement between the theoretical prediction and the experiment was observed, suggesting that performance of our nanostructure is not sensitive to the impact of the fabrication imperfections on the topology of the nanoantennas.

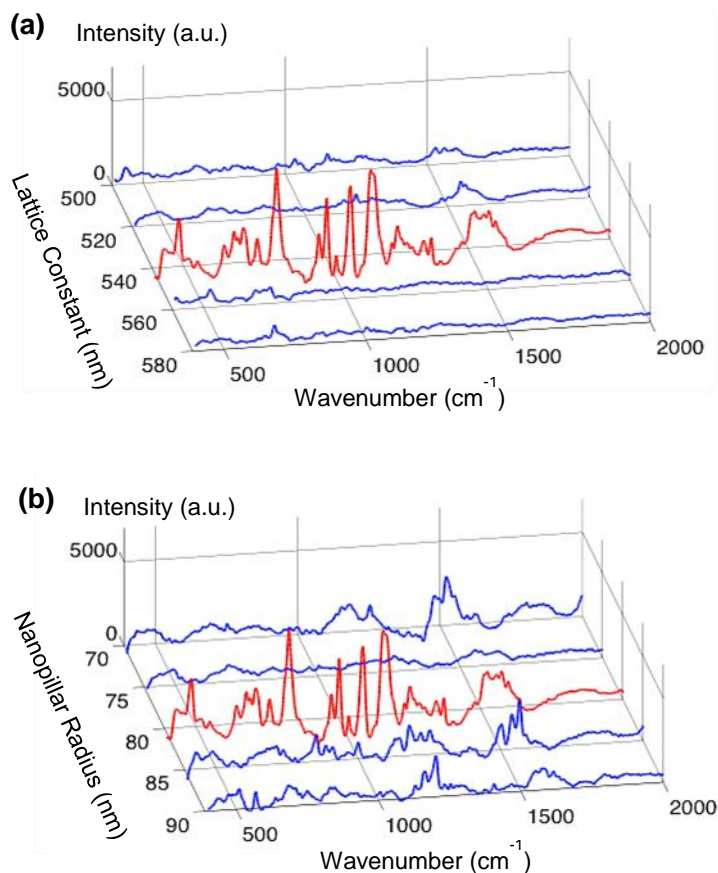


**Figure 26 - SERS spectra acquired from nanostructure with the overall desing of Fig. 12. *a* and varying periodicity and pillar radius. (a) Measurmetns from arrays with pillar radius fixed at 80 nm, and lattic constant varying from 500 to 580 nm. (b) Measurments from arrays with fixed lattice constant of 540 nm, and nanopillar radius varying from 70 to 90 nm**

In summary, we have desinged a novel bilayer plasmonic substrate for chip-scale SERS-based spectroscopic analysis of large biomolecules. Through the optimization of the horizontal coupling of the nanoantennas in the array, we were able to drastically improve the Raman scattering cross-section of the nanoantenna array. The vertical coupling between the two layers further increases the energy confinement in the vertical gaps and provides a more uniform enhancement profile over the dielectric nanopillars. By opting for the dielectric nanopillar as the immobilization surface, the target molecules are more efficiently excited and all contribute significantly to the overall collected Raman signal. In other words, all the

target molecules are bound to the surface coating at the hot-spots. These two effects collectively result in a large improvement in the overall efficiency of the SERS-based assay.

In experiments, we have successfully acquired the SERS spectrum of streptavidin, as an example of a large biomolecule, at the concentration of 100 *nM* using the optimized nanoantenna array, which to the best of our knowledge, shows a five-fold improvement compared to the previously reported plasmonic works [326]. Although we have used radially symmetric nanoantennas in this work to keep the sensitivity of the array to polarization as low as possible, the idea of using LP modes to increase the scattering cross section can be applied to other nanoantenna geometries to achieve even higher SERS enhancements. Our fabrication process is a great advantage in this regard, since higher aspect ratios and smaller gap sizes can be achieved using this method as compared to fabrication processes based on the lift-off or ion-beam milling.

## CHAPTER 5.

# CHIRAL METAMATERIALS AND CHIROPTICAL SPECTROSCOPY

Optical activity is an intrinsic property of chiral molecules and chiral assemblies, that is usually quantified by polarimetric techniques, such as *circular dichroism* (CD) spectroscopy. CD spectroscopy provides a quick and facile insight into the large-scale structure of the molecular systems, i.e. secondary and tertiary structures, in contrast to the vibrational spectroscopy techniques, discussed in previous chapter, which are typically more useful to analyze the first-order atomic structure of molecules, i.e. material composition and atomic bonds. Most biologically relevant molecules, including proteins, sugars, and nucleic acids, possess optical activity in the UV and low visible range of spectrum [327-329]. Some organometallic molecules, such as chlorophylls and certain synthetic anti-cancer compounds, have large chiral response in the high visible and NIR range [330-333].

The underlying optical process in CD spectroscopy is chiral light-matter interaction, which is the interaction between the light with helicity and the chiral molecules [334-337]. This optical process is typically very weak in natural materials, hence, the standard CD spectroscopy usually involves precise polarimetric measurements of a large number of target molecules in bulk or in high concentration solutions. However, chiral light-matter interaction can be quite strong in metamaterials. Furthermore, the interaction between the light and chiral molecules can be significantly enhanced in the near-field of chiral metamaterials. This property of chiral metamaterials can be utilized for chiroptical spectroscopy at the molecular level, which is particularly useful in biomedical applications. Aside from sensing, photonic and plasmonic chiral nanostructures can be used for

polarization beam splitting [338-340], generation of optical orbital angular momentum [341-344], generation and detection of chiral light [345-349] and spin current generation [44,350].

Before delving into the details of this metamaterial-based spectroscopic technique, we first discuss the basics of chirality, and chiral light-matter interaction in section 5.1. Then, in section 5.2, we see how the enhanced chirality in the vicinity of metamaterials can be used for biosensing applications.

## 5.1 Chirality in Materials and Metamaterials

### 5.1.1 What is chirality?

*Chirality*, also known as *optical activity* or *circular birefringence*, is a type of bianisotropy, described by Eqs. 2.23,24, where the  $\epsilon$ ,  $\mu$  and  $\zeta$  are scalars, i.e.  $\vec{D} = \epsilon_0 \epsilon_r \vec{E} - ic_0^{-1} \zeta \vec{H}$  and  $\vec{B} = ic_0^{-1} \zeta \vec{E} + \mu_0 \mu_r \vec{H}$ <sup>1</sup>. When an electromagnetic wave propagates through a medium, its electric component induces electric dipoles parallel to the electric field and the magnetic component induces magnetic dipoles parallel to the magnetic field. Additionally, in a chiral medium ( $\zeta \neq 0$ ), electric dipoles are induced by the magnetic fields and the magnetic dipoles by the electric fields. As a result, the net electric and magnetic fields inside the medium are slightly rotated. The polarization eigenstates are no longer linear, but rather circular polarization (CP) of the light [66]. Hence, two values of refractive index  $n_{\pm}$  can be assigned to the material, denoting the refractive index of the material for a plane-wave with right-hand circular (RHC) and left-hand circular (LHC) polarizations and  $\Delta n = n_+ - n_-$  can

---

<sup>1</sup> Equivalently, from Eqs. 2.25,26, the electric and magnetic dipole moments in a chiral medium can be described  $\vec{p} = \alpha \vec{E} - iG \vec{B}$  and  $\vec{m} = \chi \vec{B} + iG \vec{E}$ , where  $\alpha$ ,  $G$  and  $\chi$  are scalars.

be used as a measure of material chirality.

Metamaterials can also have optical activity, just like natural material. Physically, a molecule or structure is chiral, if it stays distinguishable from its mirror image upon any rotation or translation in space. Perhaps, the most intuitive example of chiral metamaterials is a 3D spiral shown in Fig. 28. *a*, which is resonant at a certain frequency for one CP [340]. However, resonant spiral at visible frequencies have very small dimensions and are extremely difficult to fabricate, hence, different designs have been proposed for meta-atoms that are easy to fabricate and at the same time have strong chirality. One systematic approach to design metamaterials with strong chirality at optical wavelengths that are also feasible to fabricate, is using the Burn-Kuhn (BK) model [351]. Figure 28. *b* shows an example of BK type chiral metamaterial, which are generally composed of two vertical layers. In section 5.3, we see the design of a BK type chiral metamaterial, which requires only one-step lithography.

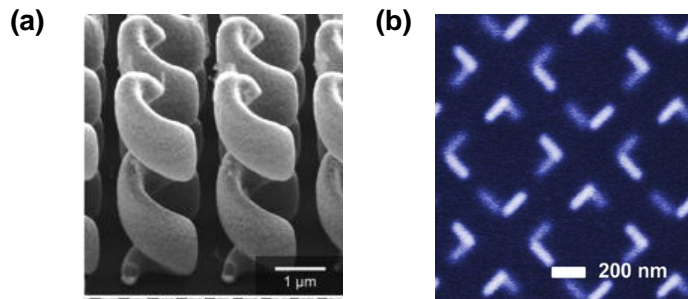


**Figure 27 – Two examples of chiral metamaterials, (a) Au helix antennas as an example of a chiral metamaterial (image reproduced with permission from Ref. [340]) (b) A Born-Kuhn type chiral metamaterial (image reproduced with permission from Ref. [351]); the dark and bright features in the microscope image are on two separate levels**

### 5.1.2 Circular Dichroism, Ellipticity and Optical Rotary Dispersion

The strength of chirality in a medium (material or metamaterial) can be quantified by the difference in its absorption, reflection or transmission, in response to RHC and LHC

light, which is called *circular dichroism* (CD). For instance, using the transmission as the linear response, which is used in the standard definition of CD in spectropolarimeter, we can define *absorptivity* as  $A = \log_{10}(I_0/I)$ , where  $I_0$  is the intensity of impinging light and  $I$  is the intensity of the light leaving the material. The ratio  $t = I_0/I$  is the *transmittance* of the medium. According to Beer-Lambert law, for a medium with length  $l$ , which contains optically active molecules with concentration  $c$ , we have  $A = \epsilon cl$ , where  $\epsilon$  is the *decadic absorption coefficient* [327]. In a chiral medium  $A_{\pm}$  are different and  $\Delta\epsilon = c^{-1}l^{-1}(A_- - A_+)$  is defined as the CD.

Another method to quantify the strength of chirality is to measure *ellipticity* using linearly polarized light. An impinging linearly polarized light can be divided into two RHC and LHC beams with the same intensity. Since the absorptivity of the chiral medium is different for the RHC and LHC beams, the outgoing intensities would differ and hence the sum of the two components would no longer have a linear polarization, but an elliptical polarization. Ellipticity  $\psi$  describes the shape of this ellipse, i.e.  $\psi = \arctan(b/a)$  with  $a$  and  $b$  being the length of the small and large axes of the ellipse, respectively. It can be shown that  $\psi = (45 \ln(10)/\pi) \Delta A \approx 33 \Delta A$  [328]. Many spectropolarimeters produce CD spectrum in the units of ellipticity (*mdeg*), even though they actually measure differential absorptivity.

Finally, the measurement of *optical rotary dispersion* (ORD) is the third method to quantify chiroptical properties, which involves measuring the rotation of a linearly polarized light traveling through a medium. This rotation angle is usually reported in terms of *specific rotation*  $[\alpha]$ , which is the total rotation  $\alpha$ , divided by the length of the medium  $l$ , and concentration of the chiral substance  $\rho$ ; i.e.  $[\alpha] = \alpha/\rho l$ .

### 5.1.3 Chiral Light-Matter Interaction

The quantities defined in the previous section all pertain to the far-field response of the chiral media. For an electromagnetic wave, the *chirality* pseudoscalar,  $C(\vec{r})$  can be defined for every point in space as a local measure of chirality [336]:

$$C(\vec{r}) = \frac{\epsilon_0}{2} \vec{E}(\vec{r}) \cdot \nabla \times \vec{E}(\vec{r}) + \frac{1}{2\mu_0} \vec{B}(\vec{r}) \cdot \nabla \times \vec{B}(\vec{r}) \quad (5.1)$$

For a CP plan-wave, the value of  $C$  is constant at every point  $\vec{r}$  in space; i.e.  $C_+(\vec{r}) = C_0$  for RHC plane-wave and  $C_-(\vec{r}) = -C_0$  for LHC plane-wave. Chiral metamaterials can locally enhance the chirality of electromagnetic waves, which is sometimes called *superchirality* [86]. Similar to the enhancement in electric field,  $\Gamma(\vec{r})$ , we can also define an enhancement in chirality,  $Y(\vec{r}) = C(\vec{r})/C_0$ . The absorption rate of a molecule at point  $\vec{r}_0$ , under the excitation with electromagnetic fields, depends on the local electric energy density  $U_e(\vec{r})$ , local magnetic energy density,  $U_m(\vec{r})$  and the local chirality,  $C(\vec{r})$ , according to the following equation [335,352]:

$$A(\vec{r}) = \frac{1}{\epsilon_0} \omega \alpha'' U_e(\vec{r}) + \mu_0 \omega \chi'' U_m(\vec{r}) - \frac{2}{\epsilon_0} G'' C(\vec{r}) \quad (5.2)$$

where  $\alpha''$ ,  $\chi''$  and  $G''$  are the imaginary parts of electric polarizability, magnetic susceptibility and mixed electric-magnetic dipole polarizability, respectively. As a result, the absorption rate of a chiral material with  $G \neq 0$  is different for RHC and LHC light and the CD spectrum measured from the material is described by:

$$CD(\vec{r}) = \frac{1}{\epsilon_0} \omega \alpha'' \Delta U_e(\vec{r}) - \frac{2}{\epsilon_0} G'' \Delta C(\vec{r}) \quad (5.3)$$

in which  $\Delta U_e(\vec{r}) = U_{e,+}(\vec{r}) - U_{e,-}(\vec{r})$ ,  $\Delta C(\vec{r}) = C_+(\vec{r}) - C_-(\vec{r})$ , and we have ignored the second term in Eq. 5.2, since  $\chi''$  is negligible in most materials. Hence, the effect of local chirality enhancement,  $\Upsilon$ , will be directly reflected in the CD measurements. This property of locally enhanced chiral light can be used in chiroptical spectroscopy [87,353]. In principle, since  $C$  is a pseudoscalar (as opposed to  $U_e$  which is a non-negative scalar), it is possible to perform chiroptical sensing even with a non-chiral nanocavity. However, chiral nanostructures are more efficient for chiroptical spectroscopy, since  $\Delta C$  is usually larger in chiral metamaterials.

#### 5.1.4 Planar Chirality

As we state earlier, a chiral metamaterial by definition needs to be asymmetric in all three dimensions, so that it would be distinguishable from its mirror image across any plane. However, there are a family of metasurfaces that are asymmetric only in the horizontal plane and there is no substantial vertical asymmetry in their design, aside from the difference in the refractive index between the substrate and the cladding. Even though, these structures are not chiral in strict terms, they can generate locally enhanced chiral fields, albeit not as strongly as 3D chiral nanostructures, and hence can generate a CD upon the attachment of a chiral material [87]. This phenomenon is sometimes known as *planar chirality* [354,355].

As we stated earlier, a chiral material or metamaterial should be distinguishable from its mirror image across any arbitrary plane. In fact, any chiral structure has a dual structure, which has exactly opposite CD and mirrored  $C$  distribution in space. The two structures are called *enantiomers*. Opposite enantiomers of chiral materials are often found in nature with sometimes slightly different chemical properties, and they are usually denoted by  $D/L$  (dextro-: right-handed / laevo: left-handed) or  $R/S$  (Rectus: right, or Sinister: left)

nomenclatures. To avoid confusion, in this manuscript, the *R/S* notation is used for the chiral molecules and the *D/L* notation is reserved for chiral or planar chiral metamaterials. Figure 28 shows two enantiomers of a chiral metasurface designed for generating valley current in TMDCs.

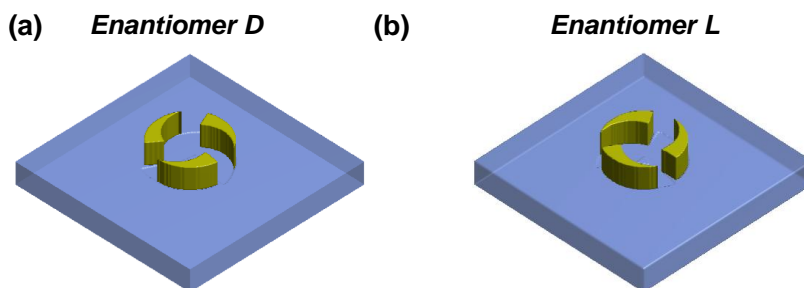


**Figure 28 – Two enantiomers of a chiral metasurface designed for valley current generation.**

## 5.2 Chiroptical Sensing Using an On-Resonance Chiral Metamaterial

As we stated earlier, in the close vicinity of a chiral nanostructure, the perceived optical activity of a biomolecule could be greatly amplified, due to the interaction with the locally enhanced chiral fields. Nonchiral plasmonic nanoparticles can modestly enhance the measured CD of chiral molecules [352,356-358], simply on the premise of their local electric and magnetic resonances. However, a greater enhancement of molecular CD can be achieved in the presence of locally enhanced chiral fields, existing in the vicinity of a chiral metamaterial [87,353,359,360]. Chiral nanostructures preferentially interact with LHC or RHC light, depending on the wavelength and the nanostructure design, and can also enhance the measured optical activity of molecules within the local fields [355,361-365]. The amplification of the apparent chiral response of molecules using these plasmonic nanocavities can be employed in chiroptical sensing, which has several advantages over other

plasmonic sensing modalities [225,366], such as, the possibility of differentiating enantiomers or chiral isomers, identification of secondary and higher order molecular structures, lower sensitivity to nonchiral perturbation in the environment, etc.

While planar chiral metamaterials can locally enhance chiral fields, chiral metamaterials with 3D arrangement have typically stronger enhancement of local chirality. Previously, off-resonance chiroptical sensing has been demonstrated using a planar chiral metamaterial [87]. It was shown that optically active biomolecules can be detected using planar chiral metamaterial by studying the disparity in the resonance shifts induces on the two enantiomers. The measured change in CD, in this experiment, was fairly modest due to the small chirality of the proposed planar metasurface, as well as the mismatch between the chiral resonance of the metamaterial and that of the target molecules. It has been suggested that in order to achieve a significant CD, at least a bilayer nanostructure, with three-dimensional arrangement of plasmonic nanoantennas is needed [86,362]. However, these nanostructures usually are hard to fabricate at small scales, due to the alignment error in consecutive lithographic steps, and often need a dielectric cap layer to preserve their strong chiral response. Upon the removal of the cap layer, which is an essential part of their design but undesirable for sensing, their chiral response is greatly attenuated.

In this section, we present a new three-dimensional chiral metamaterial that can be used for sensing applications without the limitations of the previous nanostructures. We show that the interaction between the metamaterial presented here and biomolecules with significant chirality in the same range can result in a large change in the chiroptical response of the overall system, beyond what could be achieved with a planar nanostructure. In addition this chiral metamaterial can be realized using a simple fabrication process with one-step

lithography, that preserves the scalability of the embossed nanostructures, which is crucial in practical applications at shorter wavelengths.

In order to explain the origin of the chirality in our embossed nanostructure, we can use the BK model [351,367,368], in which a bilayer nanostructure comprised of two closely spaced nanoantennas at an angle and in two vertical levels is presumed. The key feature of this design is the vertical separation between the two nanoantennas, which induces a phase difference between the two scattered waves with two different polarizations and creates chirality. The strong coupling between the two nanoantennas generates two hybrid plasmonic modes, called bonding and anti-bonding modes, which interact differently with RHC and LHC light. However, the realization of this bilayer nanostructure would require stringent lateral alignment, similar to other multi-layer stacked metamaterials [74,369,370], albeit to a lesser degree since the structure has only two layers. As a result, it becomes more difficult to scale down the nanostructure to shorter wavelengths, where most molecules of interest show significant CD response. To solve this problem, we take advantage of the optical properties of a self-aligned vertical nanoantenna- nanoaperture stack, to design a BK-type embossed chiral metamaterial with a one-step lithography process, developed previously for the fabrication of plasmonic nanostructured used for surface-enhanced Raman spectroscopy [371].

Figure 28. *a* illustrates one of the two enantiomers of the proposed chiral metamaterial *Enant D* with all geometrical dimension. Figure 28. *b* shows the fabricated metamaterial using our self-aligned fabrication technique. This nanostructure can be decomposed into two subunits,  $Arc_1$  and  $Arc_2$ , each having an arc-shaped plasmonic nanoantenna stacked on a nanoaperture via a dielectric nanowall, similar to the structure we saw in the previous chapter. The nanoantenna-nanoaperture system has two LSPR modes. The first resonant

mode has a lower  $\lambda_{res}$  and its electric field modeprofile is mostly concentrated around the nanoantenna and second mode has higher  $\lambda_{res}$  and its electric-field is mostly concentrated around the nanoaperture in the other. By matching the resonance of the nanoantenna mode in one nanoantenna- nanoaperture stack  $Arc_1$  with the nanoaperture mode of the other stack  $Arc_2$ , we can get the same effect as having two nanoantennas at two vertically separated layers, as presumed in the BK model. The dual nanostructure, *Enant L*, is the mirror image of the structure shown in Fig. 28.a versus any plane perpendicular to the  $x - y$  surface. Evidently, the local field distribution of *Enant L* with LHC incident light is also the mirror image of the local field distribution of *Enant D* in response to the RHC light.

Figures 28.c – e show the electric-field distribution in the vicinity of  $Arc_1$ ,  $Arc_2$  after resonance tuning separately and the complete met-atom, *Enant D*, at their resonance wavelengths, in response to RHC light, over the cylindrical surface S shown in the inset of Fig. 28.a. As it can be seen in these figures, in  $Arc_1$ , the field is mostly concentrated near the nanoantenna, whereas in  $Arc_2$ , the field is predominantly concentrated around the nanoaperture. This difference in the local distributions of the fields of  $Arc_1$  and  $Arc_2$  and the coupling between the two subunits results in the large CD response of the overall nanostructure.

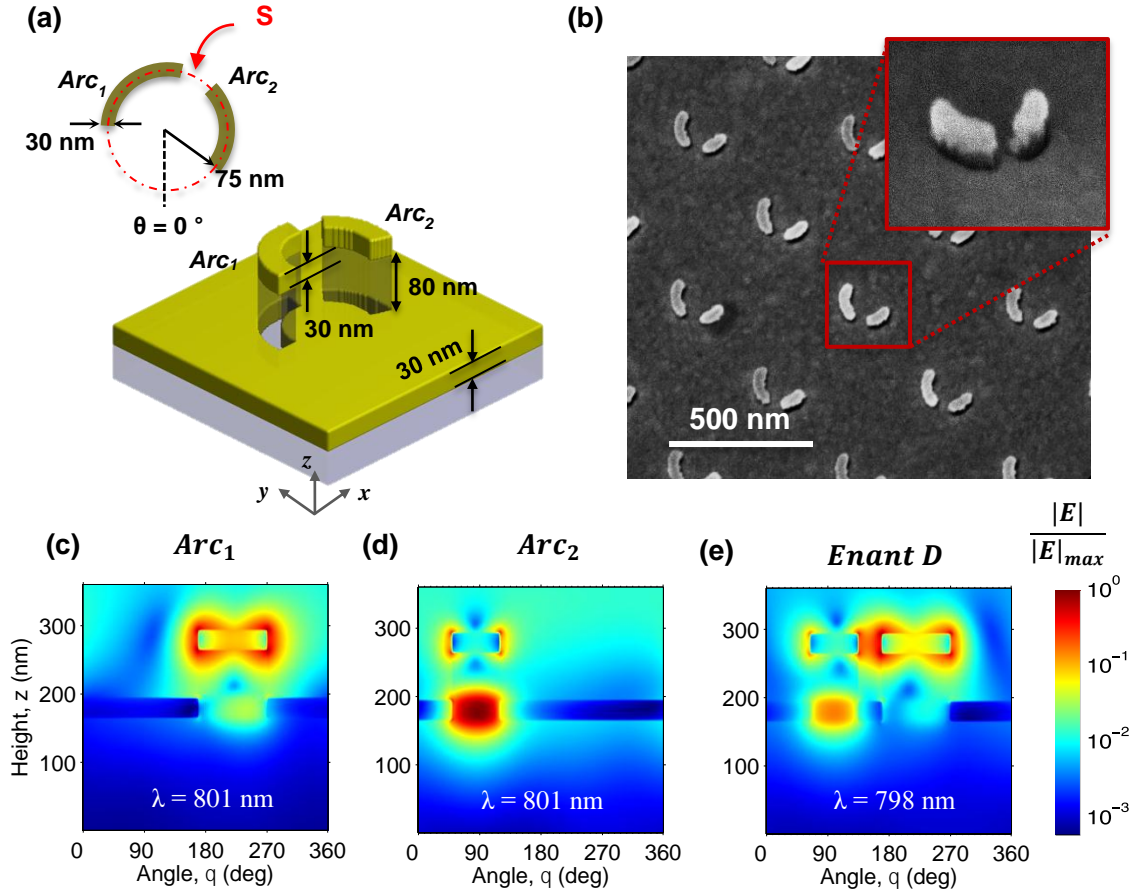


**Figure 29** - Design and fabrication of the bilayer chiral metamaterial. (a) Geometrical dimensions of a unit-cell of the embossed metamaterial (*Enant D*). The inner and outer radii of the two concentric arcs are 60 nm and 90 nm, respectively. The two arc-shaped nanoantenna-nanowall-nanoaperture stacks, *Arc*<sub>1</sub> and *Arc*<sub>2</sub>, have the opening angles of 100° and 70°, respectively, and the separation angle between the two arcs is 35°. (b) Top-view scanning electron micrograph (SEM) of the embossed chiral nanostructure (*Enant L*). The inset is an oblique close-up view of *Enant L* at 45° tilt. (c) Electric-field distribution of the nanoantenna mode in *Arc*<sub>1</sub>, in isolation, over the cylindrical surface *S* shown in the inset of Fig. 1.a at the wavelength of  $\lambda = 801 \text{ nm}$  (log-scale). (d) Similar E-field distribution for the nanoaperture mode of *Arc*<sub>2</sub>. (e) Electric-field distribution for complete *Enant D* at  $\lambda = 798 \text{ nm}$  (resonance wavelength of *Enant D* in response to RHC light).

In Figs 29.a,b, we have illustrated the distribution of the chirality enhancement factors,  $\Upsilon$  at  $\lambda_0 = 781.5 \text{ nm}$  ( $\Delta r$  peak for enantiomer D) under RHC and LHC excitation. As it can be seen from these figures, there is a large difference in the spatial distribution of the meta-atom in response to RHC and LHC light. The local chirality for RHC light is largely enhanced around the larger nanoantenna and the smaller nanoaperture, as it is expected from our design. Closer to the surface of the metamaterial, the enhancement in chirality is stronger,

with the overall maximum of 80.6 and minimum of  $-71.2$ , showing a substantial improvement over the values reported by planar chiral metamaterials [87]. Figure 29.c shows the difference in the enhancement of local chirality,  $\Delta Y$ , on a cylindrical surface  $1 \text{ nm}$  away from the outer radius of the *Enant D* in air ( $r = 91 \text{ nm}$ ) under RHC and LHC excitation at  $\lambda_0$ . Figure 27.d illustrates the difference in local energy density, i.e.  $\Delta \Gamma_u$ , over the same cylindrical surface. From Eq. 5.23, we can rewrite CD in terms of  $\Gamma_u = |\Gamma|^2$  and  $Y = C/C_0$ :

$$CD = \frac{1}{\varepsilon_0} \omega \alpha U_{e,0} \Delta \Gamma_u - \frac{2}{\varepsilon_0} G C_0 \Delta Y \quad (5.4)$$

where  $U_{e,0}$  and  $C_0$  are the electric energy density and chirality pseudoscalar of the RHC or LHC plane-wave with unit electric field,  $\Delta \Gamma_u = \Gamma_{u,+} - \Gamma_{u,-}$  and  $\Delta Y = Y_+ - Y_-$ . Hence, both  $\Delta \Gamma_u$  and  $\Delta Y$  affect the change in the  $CD$  of metamaterial induced by chiral molecules.

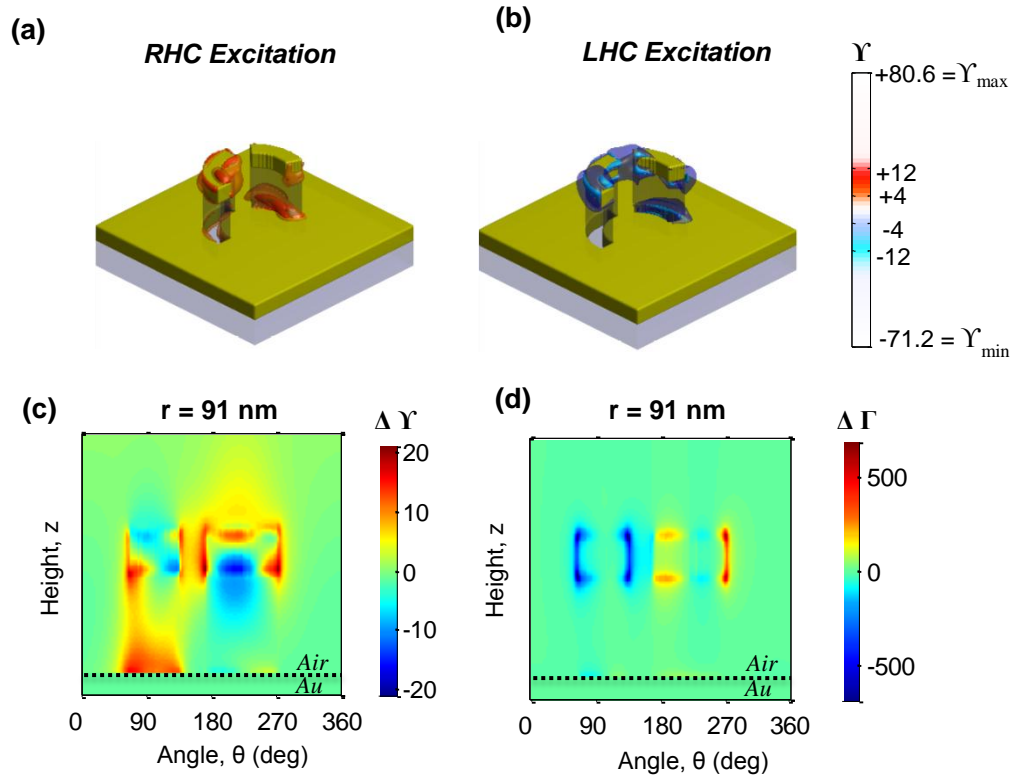


**Figure 30 - Distribution of the chirality enhancement,  $Y$ , and field enhancement,  $\Gamma$ , factors. (a,b) 3D distribution of  $Y$ , in the vicinity of *Enant D*, excited with RHC and LHC polarized light incident on the surface from the top. Blue and red surface shows the areas with  $\chi = \pm 3.8$  at  $\lambda = 781.5$  nm, respectively (RHC resonance wavelength). (c,d)  $\Delta \chi$  and  $\Delta \Gamma$  over a cylindrical surface of radius  $91$  nm ( $1$  nm away from outer surface of the nanopillars and nanoantennas)**

To further investigate the potential of the proposed chiral nanostructures for sensing, two separate arrays of *Enant D* and *Enant L* are fabricated on a silicon substrate with a  $6 \mu\text{m}$ -thick  $\text{SiO}_2$  layer on top, and used for the spectral analysis of chiral molecules. The details of our fabrication process are similar to the structure shown in the previous chapter. Traditionally, the transmission-mode CD spectrum is used to quantify the chiral response. Most often the chiral biomolecules of interest are dissolved at low concentration levels resulting in partially transparent solutions. In a chiral metamaterial, since the asymmetry in the transmission is accompanied by the asymmetry in the absorption and reflection, all three components of the linear response can be used to characterize the chiral response [372]. In the context of chiroptical sensing for instance, reflection-mode ORD has been used before to

detect chiral biomolecules [353]. For this structure, we choose to use the asymmetry in reflection response, as a measure of the chiral response of the coupled metamaterial-biomolecule system, due to stronger linear response of the designed material in reflection-mode. We used a polarization-resolved reflection measurement setup shown Fig. 30 to measure the reflection-mode CD spectrum of the fabricated metamaterial before and after coating with the chiral biomolecules. Two sets of linear polarizers and quarter-wave-plates were used to generate RHC and LHC light beams in the illumination path and separate the two polarization components of the reflected light in the collection path.

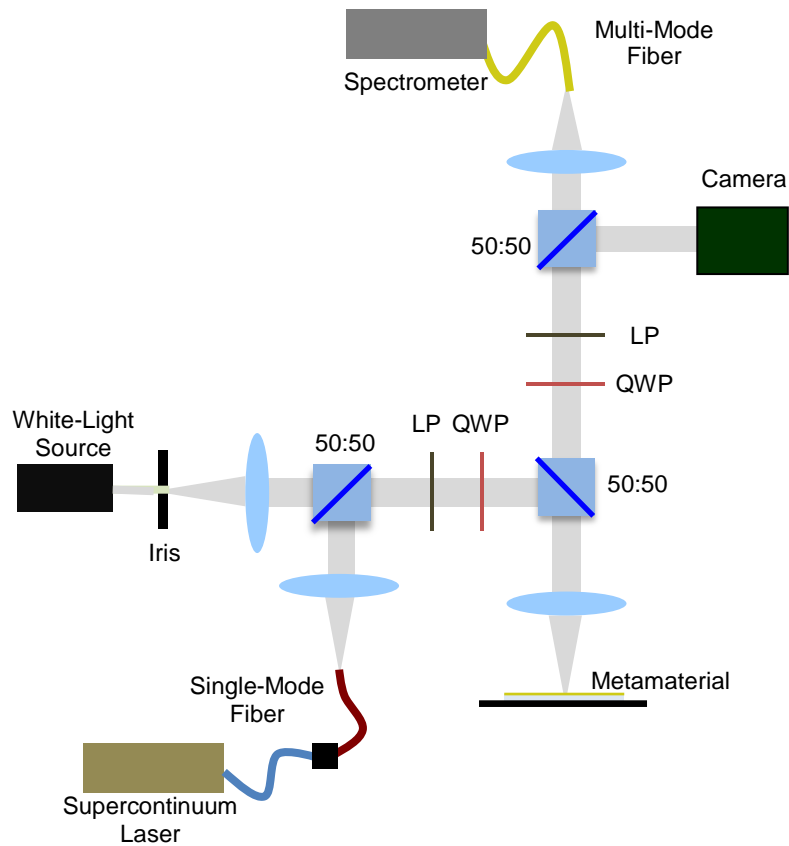


**Figure 31 - Schematic diagram of the polarization-resolved reflection setup. In this setup, the outputs of the white-light source and a supercontinuum laser are collimated and combined using a non-polarizing 50:50 beam-splitter. In the output, another 50:50 beam-splitter is used to direct two portions of the reflected light to the camera and the spectrometer. Two sets of linear polarizers and quarter-wave-plates are used to generate RHC and LHC light beams in the illumination path and separate the two polarization components of the reflected light in the collection path.**

The chiral response of the two enantiomers of the embossed nanostructure obtained from numerical simulation (FDTD) and experimental measurements are shown in Fig. 31. The blue and red curves in Figs. 31. *a, b* are the differential reflectance, i.e.  $\Delta r = r_+ - r_-$ , for *Enant D* and *Enant L*, respectively, with  $r_{\pm}$  being the reflection coefficients for RHC and LHC excitation. Both simulation and experimental results in show strong chirality that can be utilized in *CD*-based spectral analysis of chiral biomolecules with high sensitivity. The small asymmetry in the numerically calculated  $\Delta r$  spectra of *Enant D* and *Enant L*, in Fig. 29. *a* is caused of the linear birefringence in a square lattice arrangement of chiral meta-atoms, making the eigen-polarizations of the metamaterial slightly elliptical [340,364]. In applications that symmetric responses from the two enantiomers are needed, this asymmetry can be greatly reduced by arranging the meta-atoms in a  $C_3$  or  $C_4$  configuration [373], but in chiroptical sensing, we are interested in the perturbation of the linear chiral response of the nanostructure, in response to near-field chiral interaction with an optically active molecule. Hence, we can ignore the small linear birefringence of the metamaterial.

The measured differential reflectance,  $\Delta r$ , of the the two enantimers in Fig. 31. *b* show two anomalous dispersions with opposing polarities. This type of anomalous dispersion, also known as Cotton-Mouton (CM) effect [374], is the characteristic of chiral media, in which the CD or equivalently  $\Delta r$  undergoes an abrupt change in the vicinity of an absorption band [375-377]. In the measured spectra shown in Fig. 31. *b*, the distance between these two CM transitions is enlarged due to fabrication-induced variations, and consequently the  $\Delta r$  lineshape is slightly different from simulation. Nevertheless, both enantiomers show a strong chirality and can be used for CD-based spectral analysis, independently.

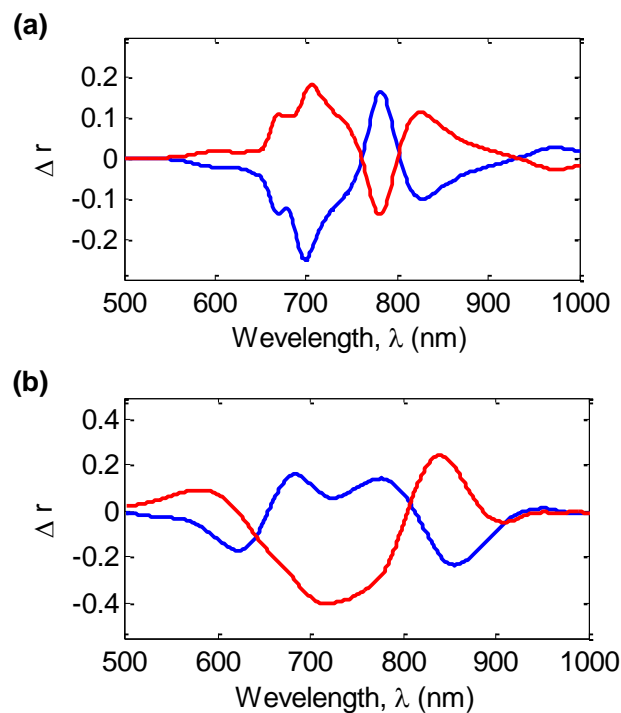


**Figure 32 - Differential reflectance,  $\Delta r$ , of *Enant D* and *Enant L* prior to coating with the chiral biomolecules. (a) Numerical simulations, (b) Measurements.**

To perform chiroptical sensing, we first coated the surface of the two nanostructures by a monolayer of two naturally occurring organometallic molecules, *Chlor A* and *Chlor B*, and a thin non-chiral layer of ALD oxide, as the control experiment. The concentration of the solvent is chosen such that a monolayer of chlorophyll would be formed via surface adsorption [378]. These molecules are the main components of the light harvesting complexes, found in plants and micro-organisms and are responsible for absorbing the sunlight and directing it to reaction centers to carry out photosynthesis [379]. Besides their strong absorption, *Chlor A* and *Chlor B* exhibit large CD responses in visible and NIR range, with two CD resonance dips at  $\lambda = 667 \text{ nm}$  and  $\lambda = 652 \text{ nm}$ , respectively (Fig. 32. a). These spectral features fall in the wavelength range that our bilayer nanostructures also show strong chirality and the locally enhanced chiral fields can greatly amplify the apparent CD of

the biomolecules bound to the surface. We define the reflection-mode circular dichroism,  $CD_r$  as:

$$CD_r = 33 (\log r_+ - \log r_-) \quad (5.5)$$

in conformity with the definition of CD in standard transmission-mode CD spectroscopy. The chiral interaction between the meta-atoms and the biomolecules results in an amplified asymmetry in the absorption in response to RHC and LHC light. We define the differential  $CD_r$ ,  $\Delta CD_r$ , as the difference between the  $CD_r$  spectra acquired from the coated metamaterial,  $CD_r^{MM+Mol}$ , and the uncoated metamaterials,  $CD_r^{MM}$ , i.e.  $\Delta CD_r = CD_r^{MM+Mol} - CD_r^{MM}$ . As we saw in section 5.2, the differential CD can be expressed as a function of local energy density and local chirality, which is basis of chiroptical sensing.

The adsorption of a chiral molecule on chiral meta-atoms is also typically ensued by opposing shifts on the CD response collected from the two enantiomers of a chiral metamaterial. This asymmetry in the CD response shifts has been previously used for superchirality-based sensing [87,353]. In on-resonance chiroptical sensing method, however, only one enantiomer with strong local chirality is adequate to perform spectral analysis based on the measured  $\Delta CD_r$ . Figures 32. *c, d* show the measured change in  $CD_r$  of *Enant D* and *Enant L*, coated by *Chlor A* and *Chlor B*. These results are in agreement with this analytical prediction, as *Chlor A* and *Chlor B* have similar non-chiral electrical permittivity and surface adsorption properties, and the difference in the large  $CD_r$  acquired from the two samples can only be attributed to the optical activity of these molecules. Both enantiomers of the nanostructure show a large change of several degrees in the  $CD_r$  in response to the adsorption of the chiral molecules, which a substantial improvement over the previously reported sensing devices that only show a  $CD$  change in the range of a few millidegrees [87],

and paves the way for precise CD-based spectral analysis for chiral molecules at very low concentration levels. The measured  $\Delta CD_r$  of the *Chlor B*-coated sample is stronger than the spectrum acquired from the *Chlor A*-coated sample, which we attribute to the more than four times stronger CD of *Chlor B* in the NIR wavelength range, as it can be seen in Fig. 32. *a*. Furthermore, for the samples coated with either molecule, we observe opposite behaviors from enantiomers *D* and *L*, which is expected from dual chiral metamaterials, and the  $\Delta CD_r$  spectra corresponding to *Enant D* (blue curves) have a blue shift with respect to the spectra acquired from *Enant L* (red curves).

*Chlor A* and *Chlor B* were coated on the nanostructure by immersing the sample in high concentration solutions. Two identical samples were soaked in 200  $\mu M$  solutions of *Chlor A* and *Chlor B* in pure methanol at room temperature and in dark, for 10 *min*. At this concentration level, chlorophylls are believed to form a monolayer on the surface of the nanostructure [378]. Consequently, the sample is cleaned in pure menthol to remove unattached residual molecules. The presence of self-assembled monolayer of chlorophylls was confirmed by performing surface-enhanced Raman spectroscopy (SERS) [61] from the metamaterial using a 785 *nm* near-IR laser with approximately 2.64 *mW* incident power.

Figure 32. *e* shows the result of a control experiment that we performed by depositing 1 *nm* of  $SiO_2$  using atomic layer deposition (ALD). As it can be seen from this figure the differential CD spectra is quite weak in the case of non-chiral molecules. Finally, we have done the same experiment with two opposite enantiomers of a synthetic organometallic compound, *chiral subphthalocyanine*, with strong chirality in the high visible and NIR range [380], see Fig. 32. *b*. Figure 32. *f* shows the  $\Delta CD_r$  spectra acquired from the metamaterial coated with *R* – *subphthalocyanine* (solid curves) and *S* – *subphthalocyanine* (dashed

curves). The difference between the  $\Delta CD_r$  acquired from *R* and *S* compounds can again be only attributed to the optical activity, since the non-chiral polarizability and surface properties of the two enantiomers are exactly the same. Interestingly, in the range of 600 to 700 nm, the absolute value of  $\Delta CD_r$  is higher for both enantiomers coated with *R*-*subphthalocyanine* compared to the case they are coated with *S*-*subphthalocyanine*. In the range of 500 to 600 nm, however, we observe the exact opposite behavior. Overall the shift for both metamaterials is in the same direction in the range of 500 to 700 nm, as expected. The *R/S* – *subphthalocyanines* were coated on the metamaterials using Langmuir-Blodgett Method [381]. The presence of these two compounds on the metamaterials was also confirmed by SERS measurements.

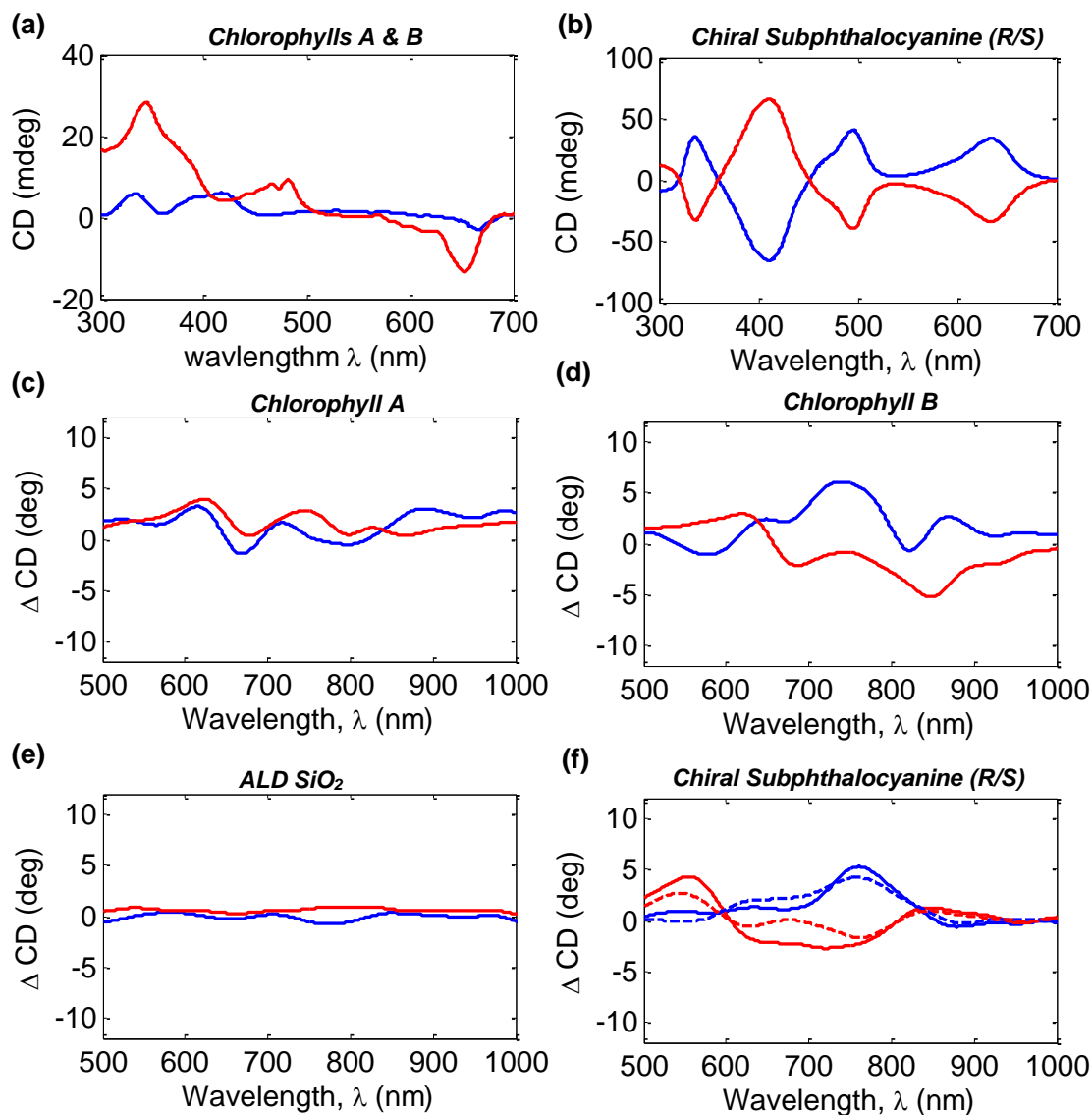


**Figure 33 - Metamaterial-Enhanced chiroptical sensing results.** (a) CD spectrum of *Chlor A* (blue curve) and *Chlor B* (red curve) at the concentration of  $200 \mu\text{M}$  in methanol, (b) CD spectrum of *R-subphthalocyanine* (blue curve) and *S-subphthalocyanine* (red curve) at the concentration of approximately  $1 \text{ mg/ml}$  in chloroform, (c)  $\Delta\text{CD}$  spectra acquired from *Enant D* (blue curve) and *Enant L* (red curve) coated with *Chlor A*, (d)  $\Delta\text{CD}$  spectra acquired from *Enant D* (blue curve) and *Enant L* (red curve) coated with *Chlor B*, (e)  $\Delta\text{CD}$  spectra acquired from *Enant D* (blue curve) and *Enant L* (red curve) coated with  $1 \text{ nm}$  ALD  $\text{SiO}_2$ , (f)  $\Delta\text{CD}$  spectra acquired from *Enant D* (blue curves) and *Enant L* (red curves) coated with *R-subphthalocyanine* (solid curves) and *S-subphthalocyanine* (dashed curves).

In contrast to the previous works, which use the difference in resonance shift induced by the chiral molecules on two opposite enantiomers, we have opted to use the entire  $\Delta\text{CD}_r$  spectra in both enantiomers independently, since this approach provides a more quantitative

measure for spectral analysis. In addition, the refractive index of the target molecules in this range has frequency dispersion, in addition to circular dichroism. Hence, modeling the change in  $CD$ , by a simple wavelength shift,  $\Delta\lambda$ , as it had been done previously, would not be accurate, in our case.

In conclusion, we have demonstrated chiroptical spectral analysis of chiral biomolecules at the molecular level using an on-resonance chiral metamaterials. Using these metamaterials, we measured the differential  $CD$  spectra from a monolayer of optically active biomolecules with very similar atomic compositions and enantiomers of a synthetic compound, and showed that we can distinguish them from the acquired  $\Delta CD_r$ . The values of  $\Delta CD_r$  reported in this work, show a very large improvement over the non-resonant experiments, performed using planar chiral metamaterial, nanoparticle assemblies or non-chiral nanoparticles, owing to the large chirality of the nanostructures and the spectral matching between the  $CD_r$  spectra of the metamaterials and target molecules. Similar experiments can be performed with other biomolecules that exhibit large CD response in the visible and NIR wavelength range, including organometallic compounds with significant pharmaceutical applications, including *Ru – arene* and *Ferrocene* –based anti-tumor drugs [331-333], and *rhodopsins* with important applications in optogenetics [382-386]. Two stereoisomers of a chiral compound can also be differentiated at the molecular level using this sensing method. Finally, given the scalability of this nanostructure, alternative metals such as *Ag* and *Al* can be used to design metamaterials that have strong CD in low visible and even UV ranges of the spectrum, opening the door to the spectral analysis of natural supramolecules and molecular assemblies using chiroptical spectroscopy at the molecular level.

## CHAPTER 6.

### NONLINEAR PLASMONIC NANOSTRUCTURES

Nonlinear optical effects are the key underlying processes in a host of advanced photonic functionalities, such as ultrafast pulse generation [387,388], photon entanglement [389], all optical signal processing [390,391], optical comb generation [392], supercontinuum generation [393,394], generation of optical solitons [395,396], as well as spectroscopic techniques such as Raman and CARS, discussed in Ch. 3, and nonlinear imaging technique, including second-harmonic microscopy [397,398] and stimulated Raman scattering microscopy [399]. These effects stem from the direct photon-photon interaction, which is only mediated by the material, unlike resonant scattering processes such as fluorescence, which result from consequent material absorption and emission. Since nonlinear effects do not rely on material absorption and emission with relatively long lifetimes ( $> 1 \text{ psec}$ ), they are typically much faster than fluorescence and PL and are quite suitable for ultrafast switching and modulation applications.

Compared to fluorescence, at low intensities, nonlinear effects are quite weak in most materials, but since they scale superlinearly with electric field amplitude, the conversion efficiency in nonlinear processes can become comparable with fluorescence, with sufficient field enhancement. As we saw in previous chapters, plasmonic nanostructures can provide extremely high values of field enhancement, and hence are ideal platforms for nonlinear optics, particularly in applications that are not susceptible to material loss.

This chapter is dedicated to the nonlinear optical effects in plasmonic nanostructures, with a specific focus on the effect of phase or excitation angle in coupled nanostructures,

which is often overlooked in nonlinear plasmonics literature. We first start with a brief classical description of nonlinear light-matter interaction in section 6.1. In section 6.2, we review nonlinear effects in plasmonic nanostructures. In section 6.3, we discuss the effect of phase-matching in second-harmonic generation using a bilayer coupled nanostructure. Finally, in section 6.4, we present our preliminary experimental results showing the effect of lattice-plasmon band-edge and phase-matching on second-harmonic generation.

## 6.1 Classical Description of Nonlinear Light-Matter Interaction

For a nonlinear medium the time-domain wave equation, i.e. generalized time-domain version of Eq. 2.1, can be written as:

$$\nabla \times \nabla \times \vec{E} + \frac{n^2}{c^2} \frac{\partial^2}{\partial t^2} \vec{E}(t) = - \frac{1}{\epsilon_0 c^2} \frac{\partial^2}{\partial t^2} \vec{P}(t) \quad (6.1)$$

where  $\vec{P}(t)$  is the induced dipole moment (or induced polarization) per unit volume. In a lossless isotropic material with no frequency dispersion, the dipole moment,  $\vec{P}(t)$ , can be found from:

$$\vec{P}(t) = \epsilon_0 \chi^{(1)} \vec{E}(t) + \epsilon_0 \chi^{(2)} \vec{E}^2(t) + \epsilon_0 \chi^{(3)} \vec{E}^3(t) + \dots \quad (6.2)$$

The first term in Eq. 6.2,  $\vec{P}^{(1)}(t) = \epsilon_0 \chi^{(1)} \vec{E}(t)$ , is the linear induced dipole moment, and  $\chi^{(1)}$  is the linear susceptibility, which is in the order of unity (dimensionless) in natural materials ( $\epsilon_r = 1 + \chi^{(1)}$  in a linear material). The second term  $\vec{P}^{(2)}(t) = \epsilon_0 \chi^{(2)} \vec{E}^2(t)$  is the second-order induced dipole moment, and  $\chi^{(2)}$  is called second-order susceptibility, which is in the order of  $10^{-12}$  (V/m). Similarly, the third term,  $\vec{P}^{(3)}(t) = \epsilon_0 \chi^{(3)} \vec{E}^3(t)$  is the third-

order induced dipole moment, and  $\chi^{(3)}$  is called third-order susceptibility, in the order of  $10^{-24}$  ( $V^2/m^2$ ), and so on [400,401]. In optical frequencies, however, many materials of interest are dispersive, lossy or anisotropic. In the case of second-order nonlinearity, the  $x, y$  and  $z$  components of nonlinear polarization at the frequency  $\omega_3$ ,  $P_i(\omega_3)$   $i = x, y$  and  $z$ , induced by two overlapping electric fields with frequencies  $\omega_1$  and  $\omega_2$ , with  $\omega_3 = \omega_1 + \omega_2$ , is:

$$P_i^{(2)}(\omega_3) = \varepsilon_0 D \sum_{jk} \chi_{ijk}^{(2)}(\omega_3; \omega_1, \omega_2) E_j(\omega_1) E_k(\omega_2) \quad (6.3)$$

where  $i, j$  and  $k$  refer to the Cartesian components of electric field and nonlinear polarization. The degeneracy factor  $D$  is the number of distinct permutations of the frequencies  $\omega_1$  and  $\omega_2$ . In *second-harmonic generation* (SHG), where we have  $\omega_1 = \omega_2$ ,  $D = 1$ , whereas in *sum-frequency generation* (SFG) and *difference-frequency generation* (DFG),  $\omega_1 \neq \omega_2$ , and hence  $D = 2$ . In this generalized case  $\chi_{ijk}^{(2)}$  is a complex tensor relating the complex amplitude (phasor) components of electric field and polarization, hence the relative phase of the two electric-field components  $E_j(\omega_1)$  and  $E_k(\omega_2)$  has an impact on the nonlinear response. Similarly, for the case of third-order nonlinearity, also known as *Kerr nonlinearity*, we have:

$$P_i^{(3)}(\omega_4) = \varepsilon_0 D \sum_{jkl} \chi_{ijkl}^{(3)}(\omega_4; \omega_1, \omega_2, \omega_3) E_j(\omega_1) E_k(\omega_2) E_l(\omega_3) \quad (6.4)$$

In *third-harmonic generation* (THG), we have  $\omega_1 = \omega_2 = \omega_3$ ,  $\omega_4 = 3\omega_1$  and hence  $D = 1$  again, but in *four-wave mixing* (FWM), in the most general case, we have  $\omega_1 \neq \omega_2 \neq \omega_3$  and  $\omega_4 = \pm\omega_1 \pm \omega_2 \pm \omega_3$ , and  $D = 6$ . It is also possible to use third-order nonlinearity, and a DC voltage to produce second harmonic with a nonlinear process known as *electric-*

*field induced second-harmonic* (EFISH), using  $\chi_{ijkl}^{(3)}(2\omega_0; \omega_0, \omega_0, 0)$ , which is especially interesting for the high-speed electrical control of the second-harmonic signal [402,403].

Nonlinear optical processes have various applications in integrated photonics and plasmonics. All optical modulation and switching, using *carrier-induced nonlinear effects*, such as two-photon absorption, free-carrier dispersion, etc., as well as Kerr nonlinearity, have been demonstrated in photonic waveguides and microcavities [391,404,405], and plasmonic nanostructures [406] [407,408]. Ultrafast electro-optic modulation of second harmonic signal using the EFISH process has been shown using plasmonic nanocavities [409,410]. Generation of ultrashort pulses in deep ultraviolet (DUV) and extreme ultraviolet (EUV) [411-414], nonlinear near-field imaging using FWM at a metallic nanotip [415-417] and surface-enhanced coherent anti-Stokes Raman (SECARS) spectroscopy, which we discussed in Ch. 3, are among other applications of nonlinear effects in plasmonic nanostructures. Other notable optical processes demonstrated using photonic and plasmonic nanostructures include generation of frequency combs [392], optical solitons [418,419] and optical supercontinuum [420,421] with many potential applications.

## 6.2 Nonlinear Plasmonics

### 6.2.1 Second-order Nonlinearity in Plasmonic Nanostructures

From the Lorentz model of the atom, which describes an atom by an anharmonic oscillator, it can be deduced that second-order nonlinearity vanishes<sup>1</sup>, i.e.  $\chi^{(2)} = 0$ , in centrosymmetric media (a medium with inversion symmetry) [400]. The break of inversion

---

<sup>1</sup> In general, all even-order nonlinearities vanish in a centrosymmetric medium.

symmetry can occur due to the asymmetry in atomic structure, which results in “bulk” second-order nonlinearity. For instance, the atomic structure of hexagonal TMDCs shown Fig. 33. *a* lacks inversion symmetry, hence 2D TMDCs with an odd number of layers show strong second-order nonlinearity [422-426]. Inversion symmetry can also be broken at the boundary of two media, leading to surface second-order nonlinearity, which is especially strong at the boundary of metals and dielectrics. This type of second-order nonlinearity is particularly useful in molecular sensing. The adsorption of any molecule at the surface, Fig. 33. *b*, can significantly change the surface second-order susceptibility,  $\chi_s^{(2)}$ , and hence the SHG collected from the surface can be used to record molecular binding and even the orientation of molecules at the surface [427-429].

Most plasmonic nanostructures are composed of *Au*, *Ag* and *Al* which have centrosymmetric atomic structures. Hence,  $\chi_s^{(2)}$  is the primary source of second-order nonlinearity intrinsic to plasmonic nanostructures, in the absence of other nonlinear materials [430-433]. Plasmonic nanostructures can also be used to enhance the external second-order nonlinearity of other materials in their local field [434-437]. Additionally, the asymmetric distribution of local fields in plasmonic nanocavities [438-440], e.g. in asymmetric nanocup shown in Fig. 33. *c*, and magnetic resonance in a magnetic metamaterials [441,442] is also known to be other sources of second-order nonlinearity unique to plasmonic nanostructures.

### 6.2.2 Other Nonlinear Effects in Plasmonic Nanostructures

*Au*, *Ag*, *Al* and graphene, as the most common plasmonic materials, have relatively large  $\chi^{(3)}$  and third-order nonlinear processes have been shown using intrinsic  $\chi^{(3)}$  of plasmonic nanostructures made of these materials [443-448]. Similar to the case of second-

order nonlinearity, plasmonic nanostructures can also be used to enhance the third-order nonlinear response of other materials [449-451].

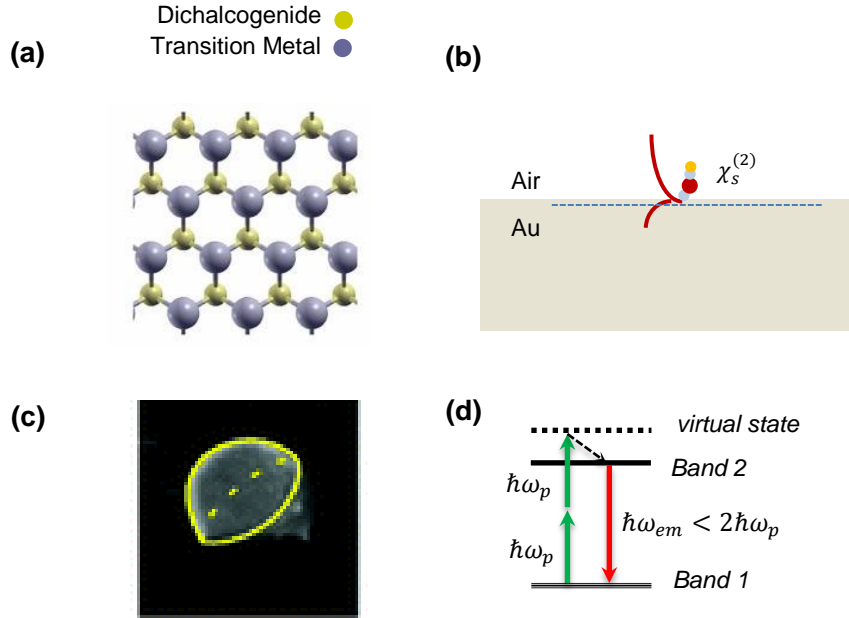


**Figure 34 - Bulk second-order nonlinearity vs. surface second-order nonlinearity. (a) Atomic structure of monolayer hexagonal TMDC from the top: the crystal lattice has no inversion center (image reproduced with permission from Ref. [452]) (b) Breaking inversion-symmetry at the interface of two materials, e.g. Au and air. (c) Breaking inversion symmetry at the nanoantenna-level in asymmetric nanocup (image reproduced with permission from Ref. [438]), (d) Two-photon photoluminescence process**

Two-photon photoluminescence (TPPL), shown in Figs. 33. *d*, is another commonly observed nonlinear process in plasmonics, which is due to the interband transition in metals [453,454]. As a result of the bright and broadband TPPL in the visible region, plasmonic nanoparticles are sometimes used as imaging tags [455],[242] or as two-photon gain materials [456]. Besides TPPL, hot-electron intraband transition, i.e. the radiative decay of hot-electrons induced within the metal [457], is another optical process that results in the emission of the light continuum in visible and NIR range [458,459]. The hot-electrons generated in plasmonic nanostructures can also be transferred to other material for

applications such as photodetection [189,460,461], photon upconversion [462] and structural change in phase-change materials [189].

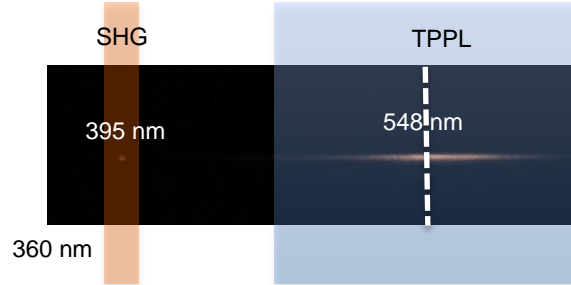


**Figure 35 - Typical acquired spectrum in SHG measurements from plasmonic nanostructures. This particular spectrum has been acquired from an Au nanoantenna array with a femtosecond laser tuned at 790 nm. The wide-band spectrum centered at 548 nm corresponds to the TPPL of Au and the sharp peak at 395 nm (precisely 1/2 of the pump wavelength) is the second harmonic signal.**

### 6.2.3 Phase-Matching and Quasi-Phase-Matching

From the coupled wave equation for SFG, it can be shown that the intensity of second harmonic (SHG is a special case of SFG) in a medium depends on the wavevector mismatch,  $\Delta k = 2k_1 - k_2$ , where  $k_1$  and  $k_2$  are the momenta of the pump and SHG signals with frequencies  $\omega_1$  and  $\omega_2 = 2\omega_1$ , according to  $I_2 = I_{2,max} \text{sinc}^2(\Delta k \cdot L/2)$ , with  $L$  being the interaction length [400]. Hence, the efficient generation of the output field requires that  $\Delta k = 0$ , or equivalently  $n(\omega_1) = n(\omega_2)$  known as *phase-matching* condition. But, this condition is difficult to achieve in normal materials due to frequency dispersion of the refractive index. In nonlinear crystals often used in free-space nonlinear optics, the most common procedure is to use the material birefringence, i.e. dependence of refractive index on the direction of polarization, to achieve phase-matching.

*Quasi-phase-matching* is an alternative technique that can be used whenever phase-matching is not feasible, which relies on the periodic structuring of the material to

compensate for the momentum mismatch. The basic idea is that in a nanostructure with periodicity,  $p$ , the grating wavevectors,  $k_m = m 2\pi/p$ , with  $m = \pm 1, \pm 2, \dots$  is added to the momentum of the pump photons and hence the modified wavevector mismatch is:

$$\Delta k = 2k_1 - k_2 + m \frac{2\pi}{p} \quad (6.5)$$

By setting  $\Delta k = 0$  and assuming first-order interaction ( $m = -1$ ), which is desirable in most applications, the optimal period of the nanostructure would be  $p = 2\pi/(2k_1 - k_3)$  for SHG. The quantity  $L_{coh} = p/2$  is often called the coherence length of nonlinear process and depends on the material and pump frequency. Quasi-phase-matching can be achieved for other second and third order nonlinear processes in a similar fashion. Alternatively, quasi-phase-matching can be explained using photonic bandstructure, which is discussed in the next section. For simplicity, we refer to quasi-phase-matching as phase-matching, in the rest of this chapter.

### 6.3 Phase-Matched Nonlinear Plasmonic Nanostructure

The effect of phase-matching (or  $k$ -matching) between the fundamental and nonlinear output signal is often ignored in plasmonic nanostructures, since the interaction region in plasmonic nanostructures is usually quite small ( $\sim 20 \text{ nm}$  in visible), and the two waves experience a small change while propagating through this region. However, in certain plasmonic nanostructures, including structures that support LP waves, the fundamental and output signal can propagate through the medium over several periods and the effect of  $k$ -matching on the amplitude of the nonlinear signal can become significant. Previously, LPs have been used to control and enhance high harmonic generation [432,440,442,463,464]

[465] and four-wave mixing [466] in plasmonic nanostructures. However, a comprehensive study of the effect of phase-matching in nanostructures that support propagating LP modes is lacking in literature, and is the subject of our study in this section. Figure 35 shows the schematic view of the nanostructure, we have chosen for this study, which is quite similar to the structure used in Ch. 3, but coated with a dielectric cladding, PMMA or flowable oxide (FOx), to increase the sharpness and hence the  $\Gamma$  of the Fano resonance peak associated with LP modes.

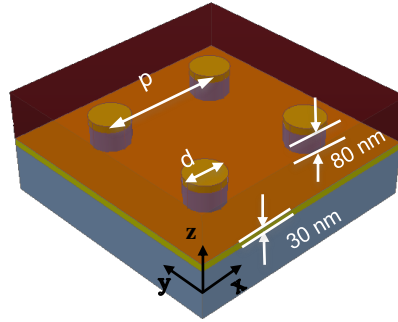


**Figure 36 - Schematic view of bilayer nanostructure used to study the effect of phase-matching between the excitation light and LP waves and between the fundamental and second-harmonic LP waves**

Dispersion of this nanostructure with  $p = 580 \text{ nm}$ ,  $d = 160 \text{ nm}$  and FOx cladding, i.e.  $D_1(k_1, f_1) = 0$  and  $D_2(k_2, f_2) = 0$  for fundamental mode and second-harmonic, respectively, are shown in Figs. 38. *a, b*.

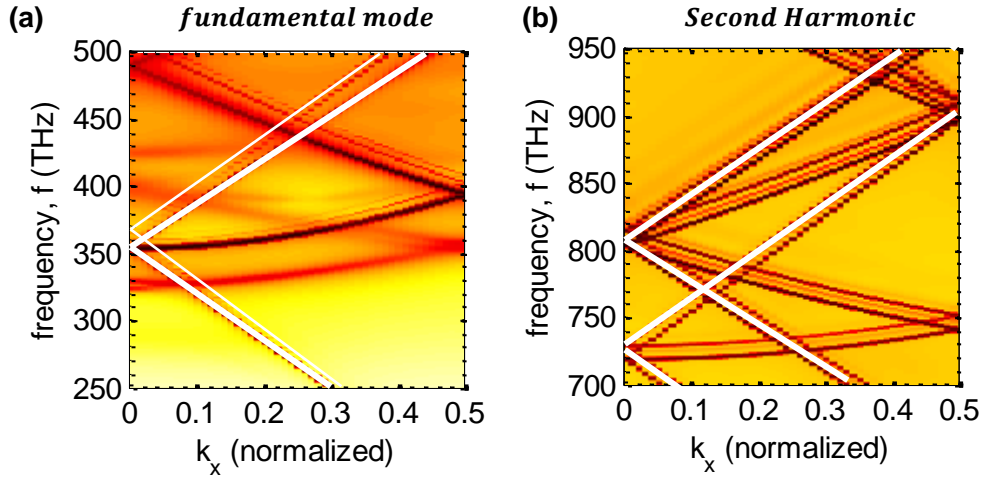


**Figure 37 - Band-diagram of the nanostructure at the sweeping range of the excitation pump and the SHG signal. (a) band-diagram at the fundametnal mode frequency range for  $p = 520 \text{ nm}$  (c) band-diagram at the SHG range for  $p = 520 \text{ nm}$ . The straight white lines are light-line of  $\text{SiO}_2$  and  $\text{FOX}$ .**

To satisfy the quasi-matching-condition, we should find points in the dispersion where  $k_1 = k_2/2$  and  $f_1 = f_2/2$ . To find these points, we have superimposed  $D_1(2k_1, f_1)$  and  $D_2(k_2, f/2)$  in Fig. 39. The bands marked by blue lines show the dispersion relation of the fundamental mode stretched by a factor of 2 in the direction of  $k_x$ , i.e.  $D_1(2k_1, f_1)$ ; all the other bands show the dispersion relation for the second harmonic signal compressed by a factor of 2 in the direction of frequency; i.e.  $D_2(k_2, f_2/2)$ . The phase-matching occurs at the two intersections, which are approximately at: a)  $2 \times k_1 = 0.58/2$  and  $\omega_1 = 365 \text{ THz}$  ( $\lambda_1 = 822 \text{ nm}$ ) and b)  $2 \times k_1 = 0.65/2$  and  $\omega_1 = 370 \text{ THz}$  ( $\lambda_1 = 810 \text{ nm}$ ). We expect to see two peaks in angle-resolved SHG generation, which we discuss in the next section, corresponding to these two phase-matched  $k$  and frequency combinations.

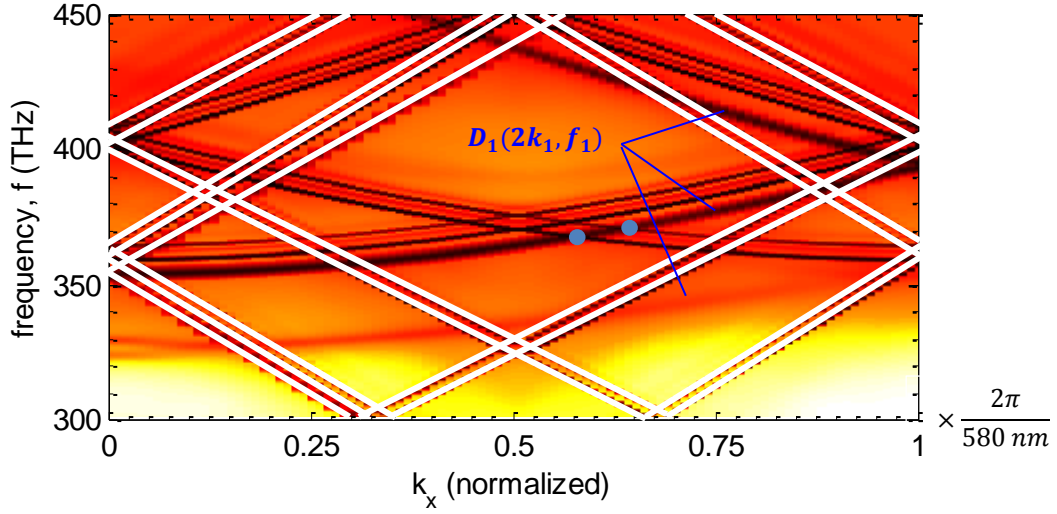


Figure 38 - Quasi-phase-matching between FM and SH LP modes for  $p = 580 \text{ nm}$ . The bands shown by blue line show the dispersion relation of the fundamental mode stretched by a factor of 2 in the direction of  $k_x$ , i.e.  $D_1(2k_1, f_1)$ ; all the other bands show the dispersion relation for the SH signal compressed by a factor of 2 in frequency; i.e.  $D_2(k_2, f_2/2)$ . The phase-matching occurs at the intersection of the two dispersions, where  $k_1 = k_2/2$  and  $f_1 = f/2$ , shown by blue dots.

## 6.4 Preliminary Experimental Results

### 6.4.1 Effect of Stationary Band-Edge LPs at the Fundamental Mode

The first prominent effect in SHG using a periodic nanostructure is the effect of LP band-edge. As we explained in Ch. 3, the band-edge is the part of the band, where  $k_x \approx 0$  and hence the normally impinging excitation efficiently couples to LP mode. At the LP band-edge, the dispersion relation is also quite flat indicating small  $v_g$ . Hence, the LP waves in this region are essentially stationary and can induce a large enhancement in SHG. Figures 38. a, b show the SHG measurement and simulation results for three different arrays with the periodicity of 520, 540 and 560 nm and nanopillar radius fixed at 80 nm. These figures show a large peak at around 780 nm for the array with  $p = 560 \text{ nm}$ , which can be attributed to its LP band-edge, as it can be seen from the numerical reflection spectra of

Fig. 40. *d*. There is a notable difference between the measured reflection spectra of Fig. 40. *c* and the simulated results of Fig. 40. *d*, which is the significant widening of Fano resonance at the LP band-edge. This effect is well-documented in literature and is attributed to the sensitivity of this type of resonance to refractive index asymmetry between the substrate and cladding and can be improved by better refractive index matching [300]. The results presented in this part show the effect of band-edge LPs at the pump frequency in SHG enhancement, but SHG can also be enhanced by the band-edge LPs at the second harmonic frequency, which we will see in the next section.

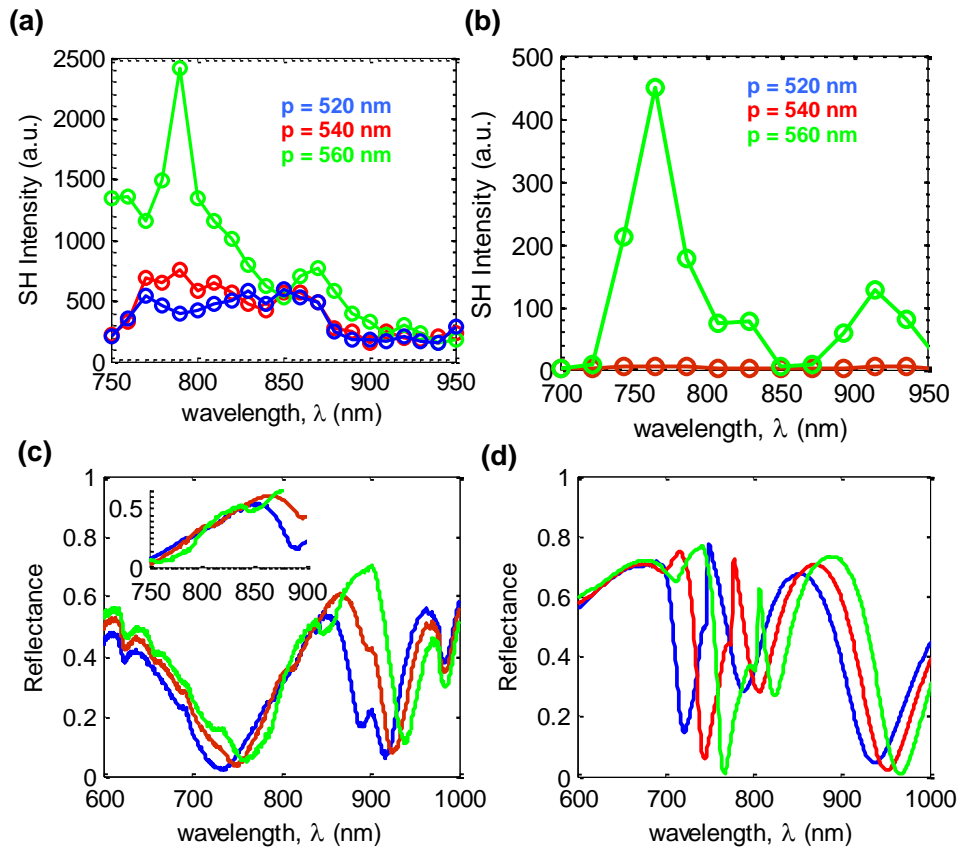


**Figure 39 - Linear and nonlinear response of the bilayer array at normal incidence. (a) SHG signal collected from the array with  $p = 520, 540$  and  $560$  nm and  $d = 160$  nm, (b) Simulation results for the SHG signals collected from these arrays. (c) experimental reflection spectra of these array under normal incidence, (d) Simulated reflection spectra**

#### 6.4.2 *Effect of Phase-Matching between Fundamental and Second-Harmonic LPs*

In order to investigate the effect of phase-matching on the intensity of the second harmonic signal, we need to be able to change the excitation angle. Figure 41 shows the schematic view of the angle-resolved SHG measurement setup. First a tunable femtosecond *Ti:Sapphire* laser is used to generate the excitation pulse with peak intensity sweeping from 740 to 980 nm. An attenuator with the optical density of  $OD = 2$  is used to reduced the pump power. The size of the beam coming out of the pulsed laser is reduced using a narrow slit placed placed immediately after the attenuator.

The key component of this setup is a moving mirror mounted on a micrometer controlled stage, which makes a lateral translation  $\Delta x$  of the laser beam with respect to the center of the objective lens. The refraction of the laser beam by the objective lens ( $NA = 1.25$  and magnification of  $\times 50$ ) turns this lateral translation into an excitation angle  $\theta$  and hence the  $k_x$  of the excitation light can be controlled. In the collection path two dichroic mirrors are placed, which can be activated independently to divert all or part of the second harmonic signal plus the reflected pump towards the spectrometer or the imaging camera. In the part of the collection path ending to the spectrometer, a short-pass filter is placed to filter out the reflected pump before the spectrometer to reduce the stray light.

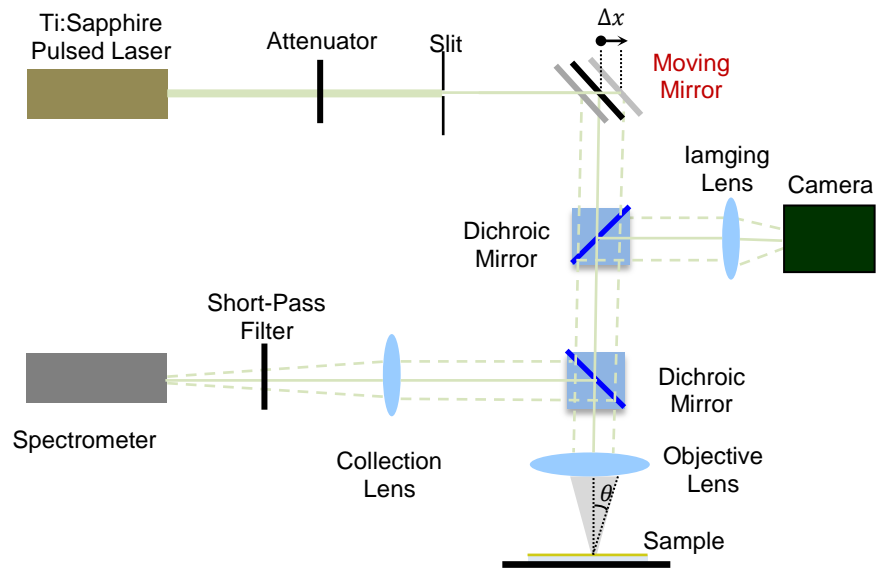


**Figure 40 - Schematic view of angle-resolved SHG measurement setup. The moving mirror is used in this setup to translate the narrow-beam coming out of the slit off the center of the objective lens. This lateral translation is turned into the excitation angle or  $k_x$  after**

The results of angle-resolved SHG measurements are presented in Fig. 42, which shows the amplitude of the SHG signal measured with the pump wavelength varying from 740 to 980 nm and the excitation angle from 0 to 65 deg. Four important features can be seen in this heatmap: *I*) Peak in SHG due to LP band-edge over the second harmonic, *II*) Two peaks in SHG due to phase-matching, *III*) Peak in SHG due to second LP band-edge over the fundamental mode, *IV*) Peak in SHG due to first LP band-edge over the fundamental mode.

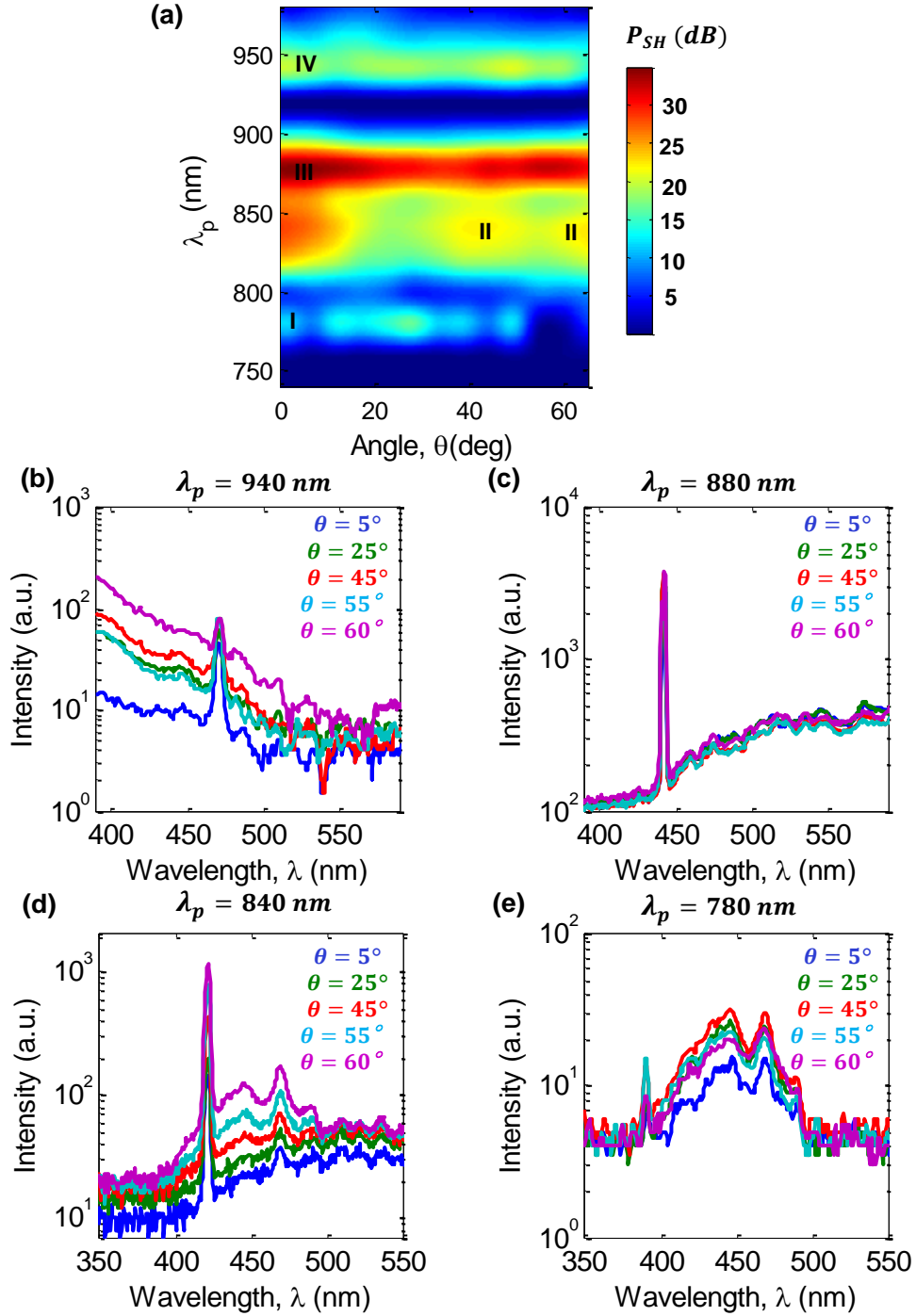


**Figure 41 - Evolution of SESHG signal vs. excitation angle and pump wavelength, (a) Intensity of the SH signal acquired from angle-resolved SHG measurements, showing four important features: I) Peak in SHG due to LP band-edge over the SH, II) Two peaks in SHG due to phase-matching, III) Peak in SHG due to second LP band-edge over the FM, IV) Peak in SHG due to first LP band-edge over the FM, (b) Evolution of the SESHG peak at 470 nm near the first fundamental mode lattice plasmon band-edge, (c) Evolution of the SESHG peak at 440 nm near the second fundamental mode lattice plasmon band-edge, (d) Evolution of the SESHG peak at 420 nm near the QPM wavelengths, (e) Evolution of the SESHG peak at 390 nm near the second harmonic lattice plasmon band-edge.**

## CHAPTER 7.

# PLASMONIC LASING IN TWO-DIMENTIONAL SEMICONDUCTORS

One of the most prominent optical properties of semiconducting 2D TMDCs, as we discussed in Ch. 2, is the high photoluminescence quantum yield dominated by Mott-Wannier excitons in their direct bandgap [155,156]. This spontaneous emission process can be enhanced through the Purcell effect, discussed in Ch. 3, by embedding 2D TMDCs within photonic or plasmonic nanostructures [165-167]. A more attractive case would be the observation of stimulated emission or lasing in 2D TMDC by their intergration in integrated optical cavities, which could be used as an on-chip coherent light source. Even though, lasing action has been shown with some level of success in TMDCs embedded within photonic crystal cavities and microdisk resonators [169-171], development of compact and low threshold plasmonic nanolasers has been elusive thus far.

In this chapter, we discuss a novel plasmonic laser composed of a 2D TMDC integrated within a plasmonic nanocavity. We start by an introduction into theory of lasing in section 7.1. In section 7.2, the results of our measurements for temperate-dependent PL of two different monolayer TMDCs, which constitute the gain medium of our proposed nanolasers are presented. In section 7.3, we discuss two topics that are crucial for the design of our 2D TMDC-based nanolaser: *surface plasmon lasers*, also know as *spasers*, and plasmon-exciton interaction in plasmonic nanostructures coupled to semiconductors. In section 7.4, we present the design and fabrication of an optically-pumped nanolaser incorporating a monolayer  $MoS_2$

as its gain medium, and finally in section 7.5, we discuss the design and fabrication of our proposed electrically pumped TMDC-based plasmonic diode laser.

## 7.1 Population Inversion, Stimulated Emission and Lasing Action

For most gain media, the lasing action in a photonic or plasmonic cavity can be described by the four-level quantum system depicted in Fig. 41. The molecule or atom in the gain medium is assumed to be initially at ground state,  $|0\rangle$ . The excitation field or pump induces the absorption of a photon with energy  $\hbar\omega_{ex}$  and the medium transitions from  $|0\rangle$  to the excited state,  $|3\rangle$ . After a fast non-radiative transition from the  $|3\rangle$  to the upper laser level  $|2\rangle$ , a photon with energy  $\hbar\omega_{em}$  is emitted and the gain medium transitions to the lower laser level  $|1\rangle$ . Another fast non-radiative transition occurs at the end, from state  $|1\rangle$  to the state  $|0\rangle$ . The time evolution of the population density of molecules or atoms at different energy levels can be described by the “rate equation” model [467]. The rate equations for this four-level system can be written as:

$$\dot{N}_3 = w(N_0 - N_3) - \gamma_{32}N_3 \quad (7.1)$$

$$\dot{N}_2 = \gamma_{32}N_3 - \gamma_{21}N_2 + \sigma(N_2 - N_1)I/\hbar\omega_{em} \quad (7.2)$$

$$\dot{N}_1 = \gamma_{21}N_2 - \gamma_{10}N_1 - \sigma(N_2 - N_1)I/\hbar\omega_{em} \quad (7.3)$$

$$\dot{N}_0 = \gamma_{10}N_1 - w(N_0 - N_3) \quad (7.4)$$

where  $N_i$  is the population level for state  $|i\rangle$ <sup>1</sup>,  $w$  is the pumping rate,  $\gamma_{ij} = \tau_{ij}^{-1}$  is the rate of transition from state  $|i\rangle$  to  $|j\rangle$  ( $\tau_{ij}$  is the transition lifetime),  $\sigma$  is the laser cross-section and  $I$  is the laser intensity ( $W/m^2$ ). The absorption and spontaneous emission processes are taken into account by adding the terms  $\pm\sigma(N_2 - N_1)I/\hbar\omega_{em}$  in Eqs.7.2,3. “Population inversion” occurs when  $N_2 > N_1$ . At the steady state ( $\dot{N}_i = 0$ ) and weak-pumping regime ( $w \ll \gamma_{32}, \gamma_{10}$ ), it can be shown that in the four-level system described by Eqs. 7.1 – 4, the relative population inversion ratio defined as  $r_{pi} = \frac{N_2 - N_1}{N} \simeq \frac{w}{\gamma_{21} + w}$ , assuming  $\gamma_{32}, \gamma_{10} \gg \gamma_{21}$  and small  $I$ .

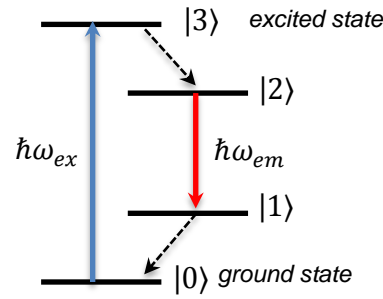


**Figure 42 - Four-level quantum model of the lasing action.**  $|0\rangle$  and  $|3\rangle$  in this model are ground and excited states associated to the absorption process with energy  $\hbar\omega_{ex}$ .  $|1\rangle$  and  $|2\rangle$  are the laser states associated to the emission process with energy  $\hbar\omega_{em}$ .

In a photonic or plasmonic cavity, it can be shown that the simplified rate equations for the carrier (exciton) population,  $s$ , and photon population,  $p$ , can be written as<sup>2</sup> [468,469]:

$$\dot{s} = w - \gamma_{sp}s - \beta\gamma_{sp}a s \cdot p \quad (7.5)$$

<sup>1</sup> An additional condition is the conservation of total population density, i.e.  $dN/dt = 0$  with  $N = N_0 + N_1 + N_2 + N_3$ .

<sup>2</sup> To simplify the equations, we have ignored the effect of exciton population density where the gain medium becomes transparent  $s_{tr}$ , as well as the non-radiative decay rate of excitons  $\gamma_{nr}$ , in Eqs. 7.5,6. To take  $s_{tr}$  into account, the term  $a s \cdot p$  should be replaced by  $a (s - s_{tr}) \cdot p$  in both equations, and  $\gamma_{nr}$  can be taken into account, by changing the second term in Eq. 7.5 into  $(\gamma_{sp} - \gamma_{nr})s$ .

$$\dot{p} = -\gamma_0 p + \Gamma \beta \gamma_{sp} s + \Gamma \beta \gamma_{sp} a s.p \quad (7.6)$$

where  $w$  is the pumping rate, (total)  $\gamma_{sp}$  is the spontaneous emission rate (equal to  $\gamma_{21}$  in the four-level model),  $\beta = \gamma'_{sp}/\gamma_{sp}$  is the spontaneous emission coupling factor with  $\gamma'_{sp}$  being the rate of spontaneous emission into the cavity ( $\beta$  is a figure-of-merit of the cavity),  $\gamma_0 = \tau_0^{-1}$  is the decay rate of photons in the cavity ( $\tau_0$  is the lifetime of the cavity resonance), the term  $a s.p$  in Eqs. 7.5,6 represents the “*stimulated emission*”, it is proportional to  $s.p$  with the coefficient  $a$ , and  $\Gamma$  is the cavity confinement factor.

Stimulate emission is a key effect leading to the lasing action (also used in optical amplifiers), in which photons in the cavity induce the decay of electrons from excited state to ground state. Whereas, in spontaneous emission, the transition occurs without the influence of external radiation [467]. The “*lasing threshold*” is the onset of lasing action, defined as the condition for which the stimulated emission equals the spontaneous emission; i.e.  $a.p = 1$ . The lasing action is often preceded by the amplified spontaneous emission or Purcell effect. Once the lasing threshold is surpassed, the stimulate emission will be dominant, and the spontaneous emission will be greatly suppressed (it is responsible for the weak and broadband background emission of the lasers). This leads to “*linewidth narrowing*”; one of the signatures of lasing action in optical cavities, meaning that in continuous-wave (CW) lasers the FWHM of the laser-line is much smaller than FWHM of the cavity resonance. As a result of the cavity resonance, the laser emission also has high *spatial and temporal (or phase) coherence*, i.e. the fields have strong correlations at different locations and at different instances of time. The linewidth of a CW laser is related to its temporal coherence. A narrow linewidth is an indication of high temporal coherence.

## 7.2 Temperature-Dependent Photoluminescence of 2D TMDCs

An integral part of any laser is a gain medium which converts the electrical or optical pump to emission photons with sufficient *quantum yield* (QY) to initiate lasing action. In a TMDC-based nanolaser, the intrinsic PL of the TMDC would be the source of spontaneous emission, so it is crucial to characterize the PL spectra of the monolayer TMDCs to design our TMDC-based nanolasers. In TMDCs, as any other semiconductor, the energy bandgap and hence the PL is highly temperature dependent [470]. In general, by decreasing the temperature, three main effects can be observed in the PL of TMDCs: *a*) The peak intensities increase significantly, which shows an increase in QY, *b*) the PL peaks generally become sharper, which means narrower gain profile for the laser, *c*) For the direct-gap luminescence peaks associated with excitons and trions, a monotonic blue-shift is usually observed.

We have measured the PL spectra of two monolayer TMDCs,  $MoS_2$  and  $MoSe_2$  grown using CVD technic [471-473]. Figures 42. *a, b* show the PL of these two TMDCs at room temperature (blue curves) and at 5 °K (red curves). As we can see in Fig. 44. *a*, three main peaks can be observed in the PL curve of  $MoS_2$  at low temperatures:  $B$ ,  $X^0$ , and  $L$ . Based on the available reports in literature, we assign  $X^0$  to the A-exciton which is the main excitonic level in TMDCs and  $B$  to the B-exciton, which is a signature of multi-layer TMDCs [155,474]. We also speculate that the peak  $L$  could be assigned to either bound excitons, whose energy has been reduced by the additional binding defects either due to impurity or due to the substrate [475]. For  $MoSe_2$ , an additional peak,  $X^-$  is observed, which can be assigned to negative trions [476]. Figures 42. *c, d* show the progression of PL in  $MoS_2$  and  $MoSe_2$  by decreasing the temperature, showing an increase in QY, sharpness and a monotonic blueshift for exciton and trion energies, i.e.  $X^0$ ,  $X^-$ , and  $B$  peaks.

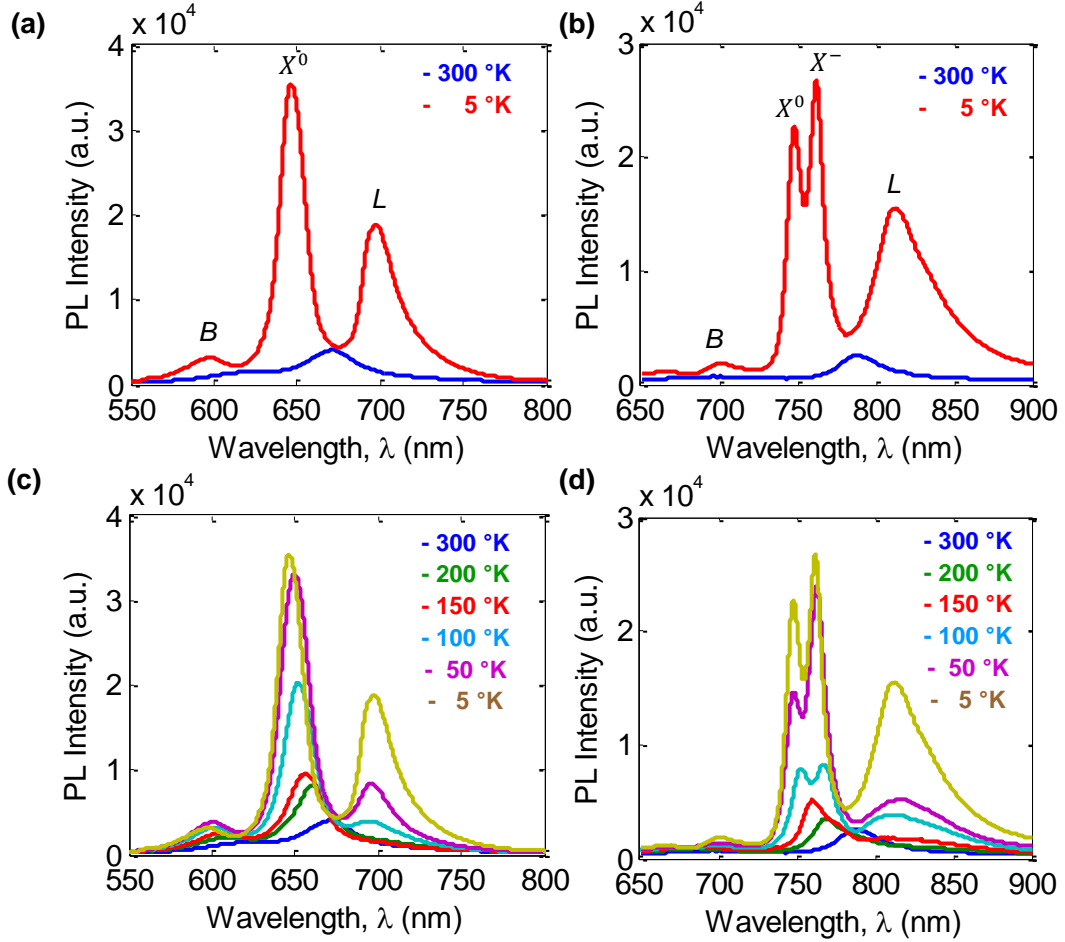


**Figure 43 - Temperature-dependant gain profile of 2D  $MoS_2$  and  $MoSe_2$ . (a) PL of monolayer  $MoS_2$  at 300 °K and 5 °K (b) PL of monolayer  $MoSe_2$  at 300 °K and 5 °K, (c) Temperature dependance of PL spectrum of monolayer  $MoS_2$  (d) Temperature dependance of PL spectrum of monolayer  $MoSe_2$**

### 7.3 Plasmon-Exciton Coupling and Plasmonic Nanolasers

Low threshold and compact lasers with high direct modulation speeds are of particular interest in applications such as high speed communication, information processing and optical interconnects. Lasing action has been previously demonstrated in large integrated photonic microcavities, such as microdisk and microrings [477-479] with high Q-factor, but low field confinement, resulting in relatively high lasing thresholds. The lasing threshold can

be to some extent improved using PhC cavities with smaller optical mode volume  $V_m$  and simultaneously high Q-factors [480,481]. However, the overall footprint of PhC microcavities is still quite large and the  $V_m$  in these resonators is still bound by the diffraction limit. In 2D materials which is the focus of this chapter, lasing has been observed using both microdisk resonators [169,171] and PhC microcavities [170].

Surface plasmon lasers, also known as *spasers*, can potentially reach lower lasing thresholds in much smaller footprints [4,482]. Besides the potential applications in integrated photonic and plasmonic circuits, spasers can be used as ultrasensitive active plasmonic sensors, utilizing the high sensitivity of the stimulated emission of plasmons to the environment [483,484] or as high-contrast labels in biological imaging. [485]. Lasing action has been demonstrated in a number of different plasmonic nanostructures [5,322,486-490] using bulk semiconductors or organic dyes as the gain medium.

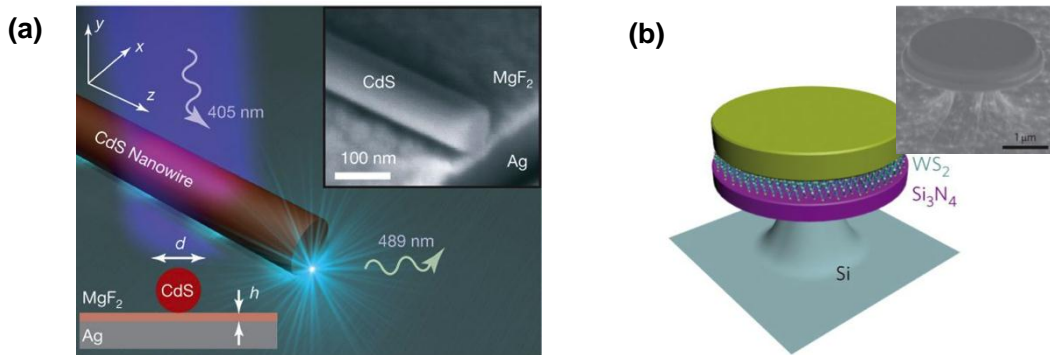


**Figure 44 - Lasing action in low-dimensional materials. (a) An example of a plasmonic laser composed of a *CdS* nanowire coupled to a *Ag* film (Image reproduce with permission from Ref. [5]). (b) An example of TMDC-based laser composed of a monolayer *WS<sub>2</sub>* coupled to *SiN* microdisk (Image reproduced with permission from Ref. [169])**

Demonstration of surface plasmon lasing in 2D materials has however been elusive thus far and the value of Purcell enhancements reported in literature from plasmonic structures such as plasmonic nanoantennas has been less than expected. [491-493]. This could be attributed to the strong coupling between excitons in TMDCs and plasmons in

nanoantennas and the formation of *plasmon-excitons*, also known as *plexcitons* [494,495]. One of the signatures of strong exciton-plasmon coupling is *vacuum Rabi splitting* (VRS)<sup>1</sup>, which has been observed in high  $Q/V_m$  microcavities coupled to low-dimensional materials, such as quantum dots and quantum wells [496,497].

Strong exciton-plasmon coupling and VRS has also been observed in plasmonic nanoantennas coupled 2D semiconductors [498-501]. While the strong-coupling between excitons and plasmons or photons can be attractive for quantum applications, including the generation of single photons [502], entangled photons [503], exciton-polariton condensates [197,208] or the development of quantum logic devices [504], for the purpose of lasing, the system needs to operate in the Purcell enhancement or weak coupling regime. In fact, it has been shown that the strong coupling between excitons and photons can lead to the inhibition or quenching of spontaneous emission [502,505].

#### 7.4 Monolayer TMDC Plasmonic Nanolaser

This section is dedicated to the design and demonstration of a plasmonic nanolaser composed of a monolayer TMDC embedded within a plasmonic nanocavity. Although, modest enhancement of spontaneous emission in 2D TMDs has been demonstrated previously using a variety of plasmonic nanostructures, the reported numbers of enhancement factor has been consistently below what is predicted by theory and achieving stimulated emission has proven to be elusive. This could be due to a number of reasons: *a)* the hybrid excitonic-plasmonic systems would operate in strong coupling regime, which is not ideal for

---

<sup>1</sup> Vacuum Rabi splitting occurs when the coupling strength between two same energy oscillators, e.g. plasmons and exciton, exceeds their mean decay rates and as a result the coupled system has two eigenstates with a splitting in energy.

lasing, *b*) the thermal effects at the hotspots of plasmonic nanostructures, limiting the pump power, *c*) the saturation of the optical gain in small regions of TMDCs, resulting in an insufficient optical gain to compensate for the intrinsic loss in plasmonic nanostructure. As we saw in Ch. 3, the Purcell factor  $F$ , of a quantum emitter weakly coupled to a photonic or plasmonic cavity, depends on both quality factor and the confinement of electromagnetic fields ( $V_m$ ). In a plasmonic nanostructure, the Q-factor is typically quite modest, and the field confinement at hotspots plays a more significant role. However, extremely high field confinement can result in strong coupling with excitons and plasmons as we discussed in the previous section, which deviates the system from the Purcell enhancement regime, or undesired thermal or gain saturation effects.

Here, we present the lasing action in a monolayer TMDC embedded within a plasmonic nanocavity that avoids all these shortcomings using a careful design that balances the two key elements in Purcell enhancement: Q-factor and  $V_m$ , as we will describe in the rest of this chapter.

#### 7.4.1 *Design and fabrication of the Plasmonic Nanocavity*

Figure 44 illustrates the basic design of plasmonic nanoslit-nanogroove (NS-NG) nanocavity comprised of a deep V-shaped nanoslit (NS) sandwiched between two sets of shallowly-etched nanogroove (NGs) all carved inside a thin layer of *Au*. The highest value of PL enhancement reported from TMDCs has been reported from a NG structure, which is the basis of our design [165]. Each individual NG in the left and right halves of the nanostructure supports a relatively wideband local resonance that is confined to its edges, but is loosely coupled to the resonant modes in the adjacent NGs resulting in a laterally propagative LP mode in the absence of the nanoslit. The NS in the middle of the nanocavity has a larger

depth and is etched to the bottom of *Au* layer in order to electrically isolate the two parts of the nanocavity, which is needed for electrical pumping, as we will discuss in the next section. Due to the larger size, resonance wavelength is larger in the NS compared to NGs, and hence the laterally propagating LP mode at the NS resonance wavelength is partially reflected by the two periodic NWs, serving as two Bragg reflectors confining the light to the NS in the middle of the cavity. As a result, using smaller loosely coupled plasmonic nanocavities, a larger plasmonic cavity can be designed with narrower linewidth, at the cost of a slight increase to the overall mode-volume.

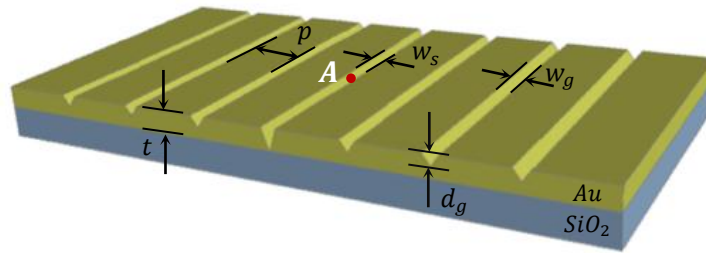


**Figure 45 - Schematic view of NS-NG plasmonic nanocavity, showing the fixed design parameters: *Au* thickness  $t = 100 \text{ nm}$ , groove depth  $w_g = 100 \text{ nm}$  and slit depth  $w_s = 100 \text{ nm}$ , and the design parameters used in optimization: Bragg reflectors period  $p$  and groove depth  $d_g$ .**

The plasmonic nanolaser is formed by transferring a layer of TMDC on top of the nanostructure shown in Fig. 44. The critical geometrical parameters in this structure are *Au* film thickness  $t$  fixed at  $100 \text{ nm}$ , NG and NS period  $p$ , NS depth also fixed at  $100 \text{ nm}$  (for electrical isolation), NG depth  $d_g$ , NG width  $w_g$  fixed at  $100 \text{ nm}$ , and NS width  $w_s$  also fixed at  $100 \text{ nm}$ . The value of  $w_g$  and  $w_s$  are chosen based on the minimal lateral feature size that could be practically achieved in *focused-ion beam* (FIB) milling of *Au*.

The first step in the design of the nanolaser is to optimize the nanocavity such that its strongest resonance peak would have an excellent spectral overlap with the gain profile of

TMDC (low temperature PL lineshape) and high values  $\Gamma$  at its high gain region. For instance, for  $MoS_2$ , the low temperature PL peaks at  $648\text{ nm}$ , so defining a gain bandwidth of  $20\text{ nm}$ , we optimize the cavity such that it would have strongest resonance with the range of  $638\text{ to }650\text{ nm}$ . Similarly, the high temperature gain region for  $MoS_2$  is chosen to be in the range of  $660\text{ to }680\text{ nm}$ .

Setting fixed geometrical parameters aside,  $d_g$  and  $p$  are the two design parameters for optimizing the cavity resonance, and choosing the enhancement factor at point A (middle of NS and  $0.35\text{ nm}$  above the top  $Au$  surface) shown in Fig. 44,  $\Gamma_A$  as the optimization parameter, we optimize the nanocavity with the presence of TMDC, which is assumed to be  $0.7\text{ nm}$  thick with the complex refractive index extracted from Ref. [506], by sweeping the values of  $p$  and  $d_g$ , and recording the maximum of  $\Gamma_A$  in the gain region from numerical simulations. In the case of  $MoS_2$ , this optimization problem results in the heatmaps shown in Fig. 45. *a, b*, corresponding to the high temperature (HT) and low temperature (LT) PL gain regions. From these two heatmaps, we conclude that for monolayer  $MoS_2$  the NS-NG nanocavity with  $p = 630\text{ nm}$  and  $d_g = 45\text{ nm}$  is optimal and at HT, and the cavity with  $p = 586\text{ nm}$  and  $d_g = 38\text{ nm}$  is optimal at LT.

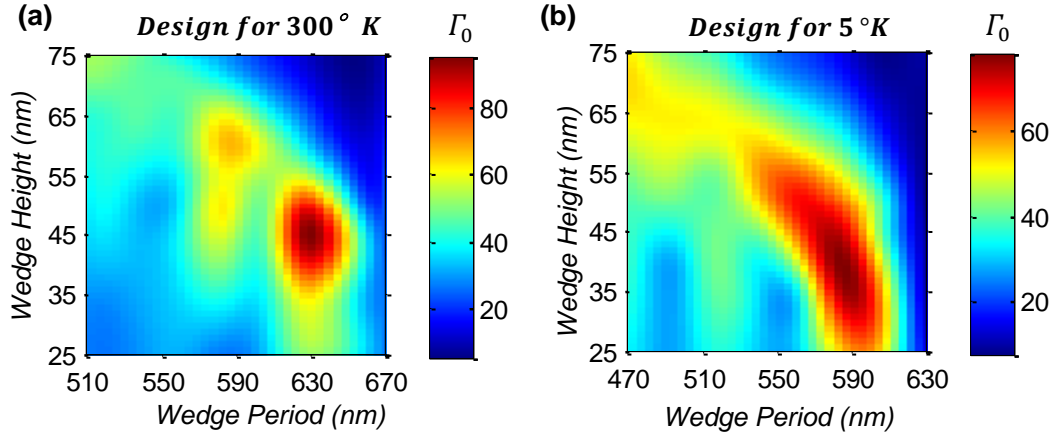


**Figure 46 - Optimization of NS-NG nanolaser with monolayer  $MoS_2$  as the gain medium. (a) Heatmap of total enhancement factor  $\Gamma_0$  at point A in Fig. 44 for the cavity with optimized design parameters to operate at 300 °K:  $p = 630 \text{ nm}$ ,  $d_g = 45 \text{ nm}$ . The gain region of monolayer  $MoS_2$  at 300 °K is assumed to be 660 to 680 nm. (b) Heatmap of the total enhancement factor  $\Gamma_0$  at point A in Fig. 44 for the cavity with optimized design parameters to operate at 5 °K:  $p = 586 \text{ nm}$ ,  $d_g = 38 \text{ nm}$ . The gain region of monolayer  $MoS_2$  at 5 °K is assumed to be 638 to 648 nm.**

The spectral response of these optimized resonators is shown in Figs. 46. *a, b*. The blue curves in these figures show the spectral response for the unloaded cavities (without  $MoS_2$ ) and the red curves correspond to the loaded cavities (with a monolayer  $MoS_2$ ). The dashed curves in the two figures show the (qualitative) gain profile of single-layer  $MoS_2$  at their respective temperatures. In the case of cavity designed for the nanolaser operating at 300 °K, the Q-factor and  $\Gamma$  are higher in the loaded cavity, compared to the unloaded cavity ( $Q'_0 = 76, \Gamma'_0 = 62$  compared to  $Q_0 = 62, \Gamma_0 = 48$ ), which at first look seems counter-intuitive, given the lossy nature of TMDCs. But, it should be noted that the optimization has been performed for the loaded cavities, hence the nanocavity that is optimal with TMDC could be sub-optimal without it, so it is in fact possible to have a lower Q and  $\Gamma$  in the unloaded with the unloaded cavities. In the case of the cavity designed for the nanolaser operating a 5 °K, however, Q and  $\Gamma$  are lower in the case of loaded cavities ( $Q'_0 = 45, \Gamma'_0 = 62$  compared to  $Q_0 = 50, \Gamma_0 = 95$ ). The  $MoS_2$  layer also induces a red-shift in the  $\lambda_{res}$  from 671 to 680 nm

for the cavity designed for 300 °K operation, and from 642 to 646 nm for the cavity designed for operation at 5 °K.

PL in 2D TMDC originate from the bright in-plane excitons to the most part [507], which only respond to the in-plane components of the electric field<sup>1</sup>. Hence, only the in-plane component of electric-field will affect the PL enhancement and lasing. The distribution profile of the lateral enhancement factor,  $\Gamma_x = |E_x|/|E_0|$  at the  $\lambda_{res} = 641.8 \text{ nm}$  and at the excitation pump,  $\lambda_{exc} = 488 \text{ nm}$  are shown in *Figures 44.c, d* (the spectra of *Figs. 46.a, b* are for the total enhancement factor, i.e.  $\Gamma$ ).

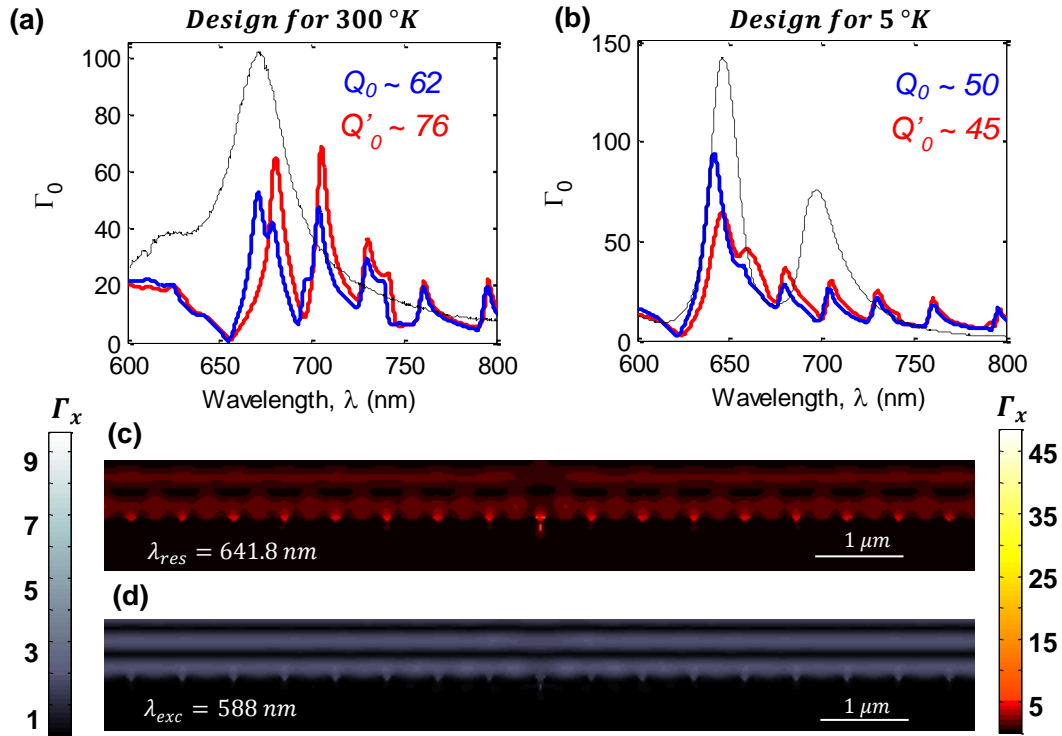


**Figure 47 - Spectral response and  $\Gamma_x$  distribution of the  $\text{MoS}_2$ -loaded nanocavity. (a) Total enhancement factor  $\Gamma$  at *point A* in *Fig. 44* for the cavity with optimized design parameters to operate at 300 °K:  $p = 630 \text{ nm}$ ,  $h = 45 \text{ nm}$  ( $\lambda_{res} = 670.9 \text{ nm}$ ,  $\lambda'_{res} = 680.5 \text{ nm}$ ) (b) Total enhancement factor  $\Gamma$  at *point A* in *Fig. 44* for the cavity with optimized design parameters to operate at 5 °K:  $p = 586 \text{ nm}$ ,  $h = 38 \text{ nm}$  ( $\lambda_{res} = 641.8 \text{ nm}$ ,  $\lambda'_{res} = 645.9$ ), (c)  $\Gamma_x$  distribution**

<sup>1</sup> Dark excitons with out-of-plane effective dipole have also been observed in some TMDCs such as  $\text{WS}_2$  and  $\text{WSe}_2$ , which can couple to out-of-plane component of the electric field [508-510].

profile at  $\lambda_{res} = 561.8 \text{ nm}$  for the cavity design of *Fig. 45. b* (Optimal design for  $MoS_2$  at  $5^\circ K$ ) (d)  $\Gamma_x$  distribution profile at  $\lambda_{exc} = 588 \text{ nm}$ , for the cavity design of *Fig. 45. b* (Optimal design for  $MoS_2$  at  $5^\circ K$ )

The fabrication of the NS-NG plasmonic nanocavity, shown in *Fig. 47. a*, has been performed using FIB milling (FEI Nova Nanolab 200 FIB/SEM). First, a  $100 \text{ nm}$ -thick layer of  $Au$  is deposited on a silicon wafer with  $6 \mu\text{m}$  of thermal  $SiO_2$  grown on top. Then, two aligned patterns are etched consequently on the thin gold film: first pattern forming the deep NS, shown in *Fig. 47. c*, and the second pattern the NGs of the left and right Bragg reflectors. The triangular shape of the NS and NGs is due to the natural etching profile of FIB, the lateral dimension of NS and all NGs is  $100 \text{ nm}$ , which was chosen based on the practical resolution limit of FIB.

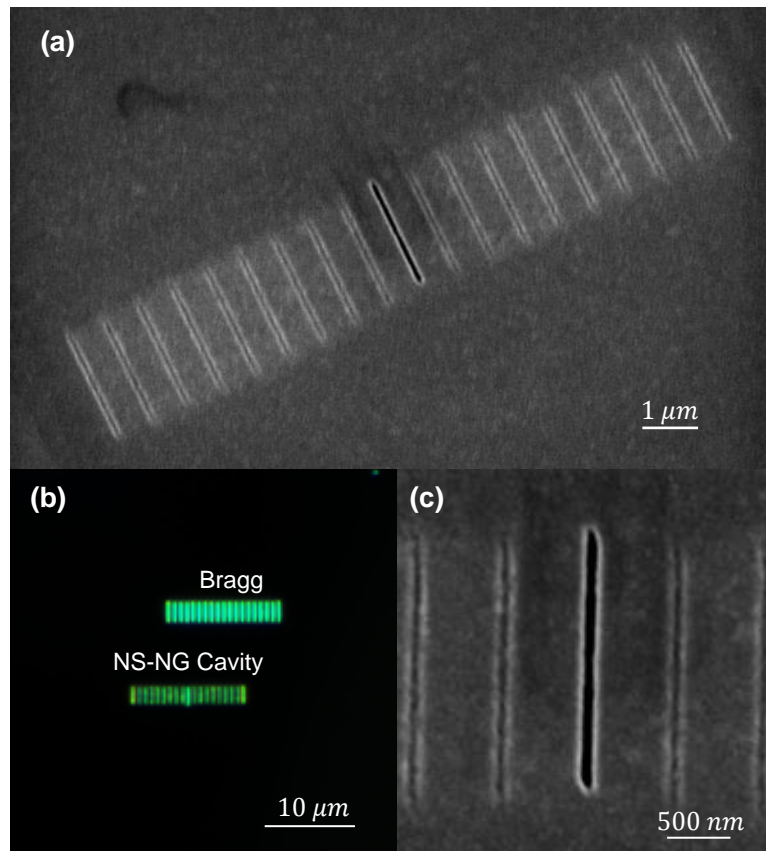


**Figure 48** Fabrication of the NS-NG plasmonic nanocavity using FIB milling. (a) SEM image of the NS-NG cavity fabricated for nanolaser operating at  $650 \text{ nm}$ , using monolayer CVD  $MoS_2$ . (b) Dark-

**field optical micrograph of the same structure and a Bragg, (c) Up-close SEM view of the NS etched deeply next to NG Braggs**

The last step in the fabrication of the plasmonic nanolaser is the transfer of TMDCs, which has been accomplished using two different methods, based on the type of TMDC layer. In the first method, discussed in this section, the wet-transfer of CVD-grown monolayer TMDC was done physically under an optical microscope.

First, by immersing the  $MoS_2$  substrate in buffer oxide etchant (BOE) solution, the  $MoS_2$  flakes are released, which float on the surface of the solution. Then, a flexible polycarbonate sheet with a small opening window was prepared and used to fish an appropriately sized flake from the solution. After taking out the polycarbonate sheet from BOE, the flake was fixed in its place using tapes and was gently immersed in water to remove BOE. The small window carved within the polycarbonate sheets makes the  $MoS_2$  flakes float on air with no VdW attachment to the polycarbonate sheet which is useful for material transfer. Next, the polycarbonate sheet was put on top of the substrate containing nanocavity under an optical microscope to align the  $MoS_2$  flake with the nanostructure. Finally, the  $MoS_2$  flake is detached from the polycarbonate sheet using a tweezer and the sample was baked at 200 °C for 30 *min* to evaporate water and activate the VdW force between the TMDC and the top surface of the nanostructure. An SEM image of the sample after NS-NG cavity designed after the transfer of CVD-grown monolayer  $MoS_2$  using this method, is shown in Fig. 48. This method is only useful with large TMDC flakes that are seen in CVD-grown 2D TMDCs. In the case of exfoliated TMDCs, the monolayer regions tend to be very small and a different method is used for material transfer, which we will describe in the next section.

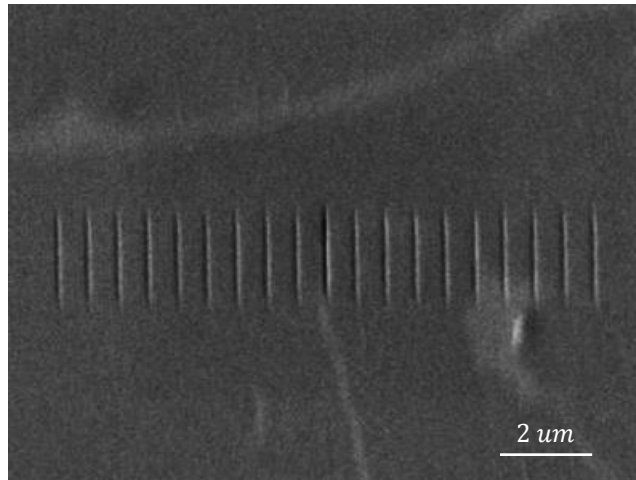


Figure 49 - SEM image of  $MoS_2$  plasmonic nanolaser after material transfer.

While the nearfield enhancement factor spectra shown in Fig.46, are useful to predict the Purcell factor of the cavity, in practice the cavity resonance needs to be characterized using its far-field spectral response, i.e. reflection or transmission. Figures 49. *a, b* show the simulated reflection spectra of  $MoS_2$  nanolasers designed to operate at 300 °K and 5 °K.

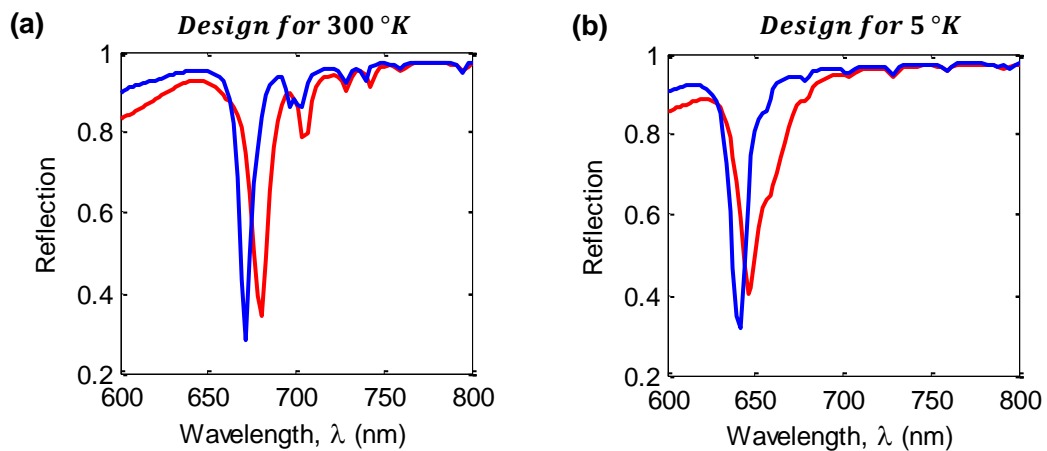


Figure 50 - Reflection spectra of the designed  $MoS_2$ -based plasmonic nanolasers. (a) Reflection spectrum of the laser desinged to operate at 300 °K, (b) Reflection spectrum of the laser desinged to ooperate at 5 °K.

## 7.5 Electrification of Monolayer TMDC Plasmonic Nanolaser

While optically-pumped plasmonic lasers have been demonstrated using a number of nanostructures and material platforms, electrically-pumped plasmon lasing has been so far out of reach. In this section, we proposed an electrically-pumped monolayer semiconductor plasmonic diode laser using Schottkey-barrier junction between *Au* and TMDC, building on the design optically-pumped nanolaser presented in the previous section. An integral part of any semiconductor diode laser is a *light-emitting diode* (LED): a heterostructure or junction, in which the radiative recombination of electrons and holes, or *electroluminescence* occurs.

### 7.5.1 Two-dimensional TMDC light-emitting diodes

LEDs were among the first optoelectronic devices that have been demonstrated using 2D TMDCs. Two main heterostructures types have been proposed to create LEDs in 2D TMDCs [511]: *a*) vertical heterostructures, *b*) lateral heterostructures. Since chemical doping of 2D TMDCs is difficult, the heterostructures are typically formed using two different materials or by applying electrostatic gating in a sheet of a TMDC to modify the Fermi levels locally to form lateral heterojunctions.

In the vertical heterostructure design typically either two different types of TMDCs, or one TMDC and a different 2D or bulk material, e.g. graphene, *black – P* or doped *Si*, are stacked vertically to form a vertical *P – N* junction shown in Fig. 50. *a* and the photons are generated by the vertical transfer and recombination of the electron and holes [164,452,512-514]. However, in lateral heterostructures design, shown in Fig. 50. *b*, typically only one type of TMDC is used, and electrostatically-configured lateral *P – N* junction is formed using two independent voltage gates to tune the Fermi level locally and form a horizontal *P – N* junction [162,515,516]. In principle, lateral heterostructures of two different 2D TMDCs

can also be used to make LEDs [517,518], but to this date there is no report of such LED device.

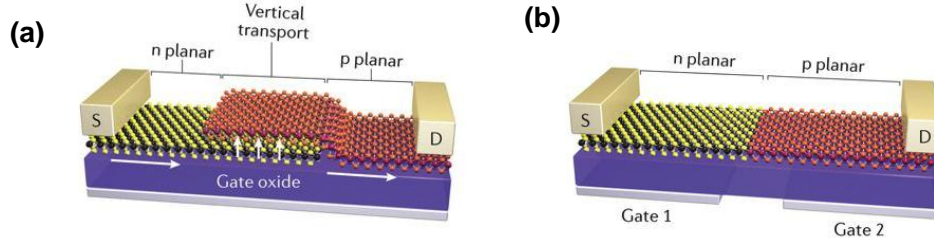


**Figure 51 - Two different type of LED designs using 2D TMDCs. (a) LED design using a vertical heterostructure (image reproduced with permission from Ref. [511]), (b) LED design using horizontal heterostructure (image reproduced with permission from Ref. [511])**

Aside from lateral and vertical heterostructures, 2D LEDs have been designed using single defects in monolayer TMDC sheets [519], and by using the metal-semiconductor Schottky-barrier junction between the contact metals and the TMDCs [163,520-522]. In this method, which is particularly suitable for plasmonic devices, the electroluminescence occurs due to the hot carrier process. At high bias voltages, the electrons injected into the conduction band experience a strong band bending at the TMDC-metal contact shown in Fig. 51, and excitons are generated via impact excitation. This type of junction has been previously used for photodetection using plasmonic nanostructures [460,523] and has been shown theoretically to be also suitable for electrically-pumped amplification of surface plasmons at the levels that can fully compensate for the propagation loss and achieve stimulated emission of SPPs with relatively small values of threshold current [524-526].

For instance, for the case of *Au* nanocavity and monolayer *MoSe<sub>2</sub>*, which is studied in the next section, given the workfunction of *Au* ( $|e\phi| = 5.2 \text{ eV}$  [521]) and *MoSe<sub>2</sub>* ( $|e\phi| = 4.57 \text{ eV}$  from Table 2), the Schottky-barrier height  $e\phi_B$  is approximately  $-0.63 \text{ eV}$ , meaning that light emission occurs due to the scenario depicted in Fig. 51. *a* ( $V_A < V_B$ ).

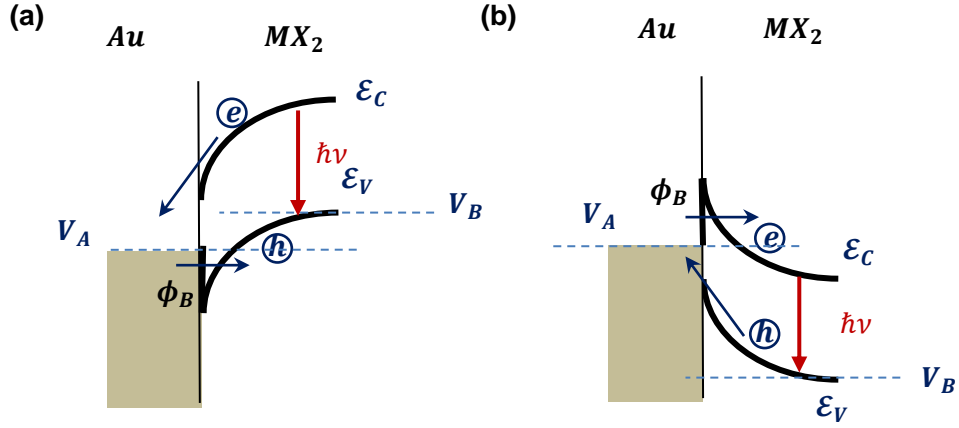
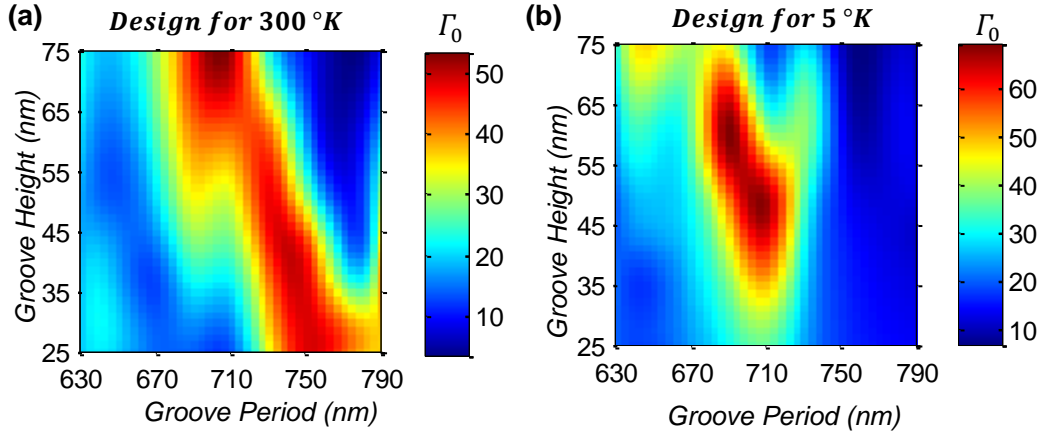


Figure 52 - Metal-semiconductor Schottky-Barrier diode in Au and 2D TMDC ( $MX_2$ ) junction. (a) Schottky-Barrier diode with  $\phi_B < 0$  and  $V_A - V_B < 0$ ,  $V_A$  and  $V_B$  being the Au and TMDC ( $MX_2$ ) voltage, (b) Schottky-Barrier diode with  $\phi_B > 0$  and  $V_A - V_B > 0$

### 7.5.2 Design and fabrication of $MoSe_2$ plasmonic diode laser

First, we modify the nanocavity design presented earlier for optically-pumped plasmonic lasing to for  $MoSe_2$  as our 2D TMDC of choice. Similar to the case of  $MoS_2$ , we optimize the NS-NG plasmonic nanocavity by searching over the space of periodicity  $p$  and NG depth  $d_g$ , and keeping all other parameters fixed. Figure 52 shows the heatmaps for  $\Gamma_0$  at *point A* shown in *Fig. 42* for the two nanocavities designed to operate at  $5^\circ K$  and  $300^\circ K$ . At  $5^\circ K$ , the high gain region of  $MoSe_2$  is chosen to be in the range of  $780$  to  $800\text{ nm}$ , and at  $300^\circ K$  in  $744$  to  $764\text{ nm}$  range. This optimization results in two solutions in both cases, one of which is chosen by comparing the quality factors.



**Figure 53 - Optimization of NS-NG nanolaser with monolayer  $MoSe_2$  as the gain medium. (a) Heatmap of the total enhancement factor  $\Gamma_0$  at *point A* in Fig. 44 for the cavity with optimized design parameters to operate at 300 °K: 1)  $p = 742 \text{ nm}$ ,  $h = 38 \text{ nm}$ , 2)  $p = 702 \text{ nm}$ ,  $h = 75 \text{ nm}$ . The gain region of monolayer  $MoSe_2$  at 300 °K is assumed to be 780 to 800 nm. (b) Heatmap of the total enhancement factor  $\Gamma_0$  at *point A* in Fig. 44 for the cavity with optimized design parameters to operate at 5 °K: 1)  $p = 706 \text{ nm}$ ,  $h = 49 \text{ nm}$ , 2)  $p = 690 \text{ nm}$ ,  $h = 69 \text{ nm}$ . The gain region of monolayer  $MoS_2$  at 5 °K is assumed to be 744 to 764 nm.**

The spectral response of the optimal NS-NG nanocavities designed for the operation at the HT and LT are shown in Figs. 53. *a, b*, respectively, showing a high Q-factor resonance with high  $\Gamma_0$  and an excellent spectral overlap with the gain at respective temperatures. The distribution profile of the lateral enhancement factor,  $\Gamma_x = |E_x|/|E_0|$  at  $\lambda_{res} = 760 \text{ nm}$  and at the excitation pump,  $\lambda_{exc} = 633 \text{ nm}$  are shown in Figures 53. *c, d*.

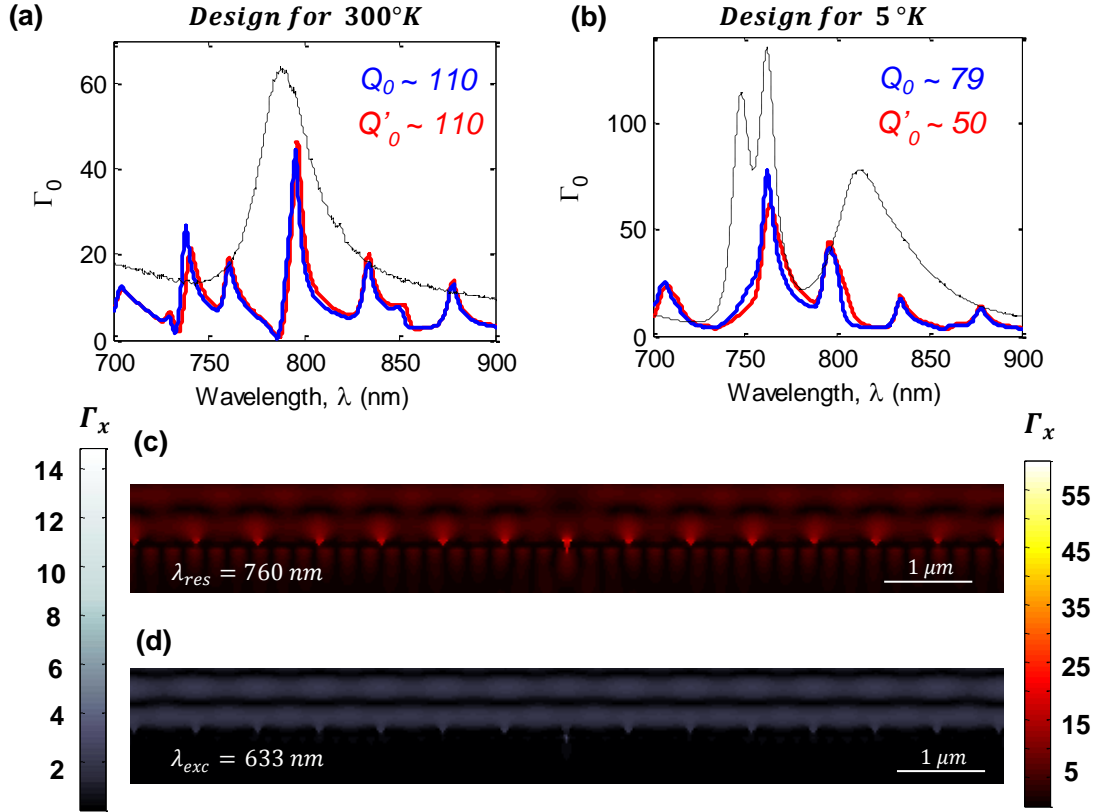


**Figure 54 - Spectral response and  $\Gamma_x$  distribution of the  $MoSe_2$ -loaded nanocavity. (a) Total enhancement factor  $\Gamma$  at *point A* in Fig. 44 for the cavity with optimized design parameters to operate at 300 °K:  $p = 750 \text{ nm}$ ,  $h = 35 \text{ nm}$  ( $\lambda_0 = 795.7 \text{ nm}$ ,  $\lambda'_0 = 768.8 \text{ nm}$ ) (b) Total enhancement factor  $\Gamma$  at *point A* in Fig. 44 for the cavity with optimized design parameters to operate at 5 °K:  $p = 706 \text{ nm}$ ,  $h = 50 \text{ nm}$  ( $\lambda_0 = 762 \text{ nm}$ ,  $\lambda'_0 = 763.4$ ) (c)  $\Gamma_x$  distribution profile at  $\lambda_{res} = 760 \text{ nm}$  for the cavity design of Fig. 45. b (Optimal design for  $MoSe_2$  at 5 °K) (d)  $\Gamma_x$  distribution profile at  $\lambda_{exc} = 633 \text{ nm}$ , for the cavity design of Fig. 45. b (Optimal design for  $MoSe_2$  at 5 °K)**

Fabrication of the plasmonic nanocavity has been slightly modified to electrically isolate the two halves of the nanocavity for electrical pumping. First, *Au* pads are formed using EBL lithography (EBL resist: PMMA A4, thickness 200 nm), deposition of 3 nm *Ti* as the adhesion layer and 100 nm *Au* using electron-beam evaporation and lift-off process. Then, the same two-step FIB milling has been performed using the alignment marks created in the previous steps to etch the NS and NGs. Figures 54. a – c show the SEM images and optical micrographs of the final NS-NG nanocavity prior to  $MoSe_2$  transfer.

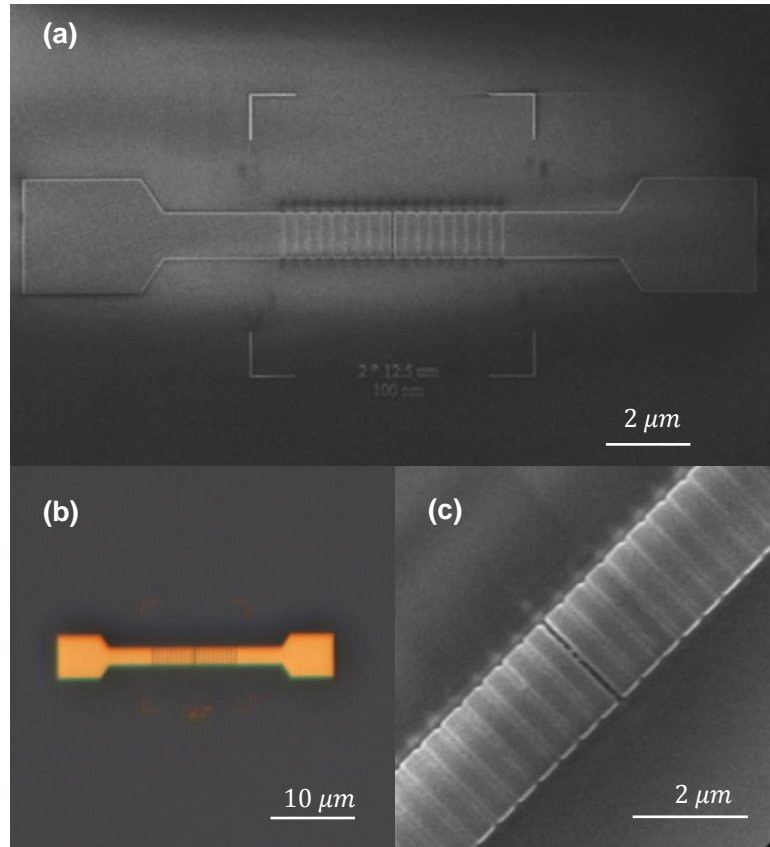


**Figure 55 - Fabrication of the 2D TMDC plasmonic diode laser. (a) SEM image of the NS-NG plasmonic nanocavity fabricated for operation with  $MoSe_2$  at  $5^\circ K$ , (b) Optical micrograph of the same structure, (c) Close-up SEM on the NS and adjacent NGs**

For electrically-pumped nanolasers, we have used exfoliated  $MoSe_2$  flakes, which tend to have higher QY compared to CVD-grown flakes, but are smaller in size. The alignment precision of the wet transfer process, described in previous section, is not sufficient for small monolayer regions of exfoliated TMDCs, and hence we have chosen to use a different method; dry transfer using a micromanipulator under optical microscope [527]. First, a thin layer of polycarbonate (PC) is prepared by dripping a drop of PC solution (Sigma Aldrich, 6% dissolved in chloroform) on a glass slide, putting another glass slide on top and separating the two glass slides by sliding them on top of each other. Then, an adhesive tape with an opening window is attached on the PC film to pick up the film. A piece of polydimethylsiloxane (PDMS) is prepared and attached on a second glass slide by plasma

activation. Then, the adhesive tape is put on top of the second glass slide, in a way that it is attached to bottom glass from the two sides, the PC film is between the tape and PDMS, and the open window is aligned on top of the PDMS exposing the surface of PC for material transfer. The prepared PDMS-PC-tape stack is then put on a third substrate containing exfoliated TMDCs (*Si* substrate with 300 nm thermally grown  $SiO_2$ ) and the sandwich layer is heated to 150 °C to partially melt PC film and make it sticky. Next, the two substrates are detached and flakes of TMDC are picked up in the opening window, where there is a direct contact between PC and TMDC substrate. At the next step, the stack (now containing the TMDC flakes) are put on top of the target substrate containing plasmonic nanocavities under a precise microamnipulator to align the monolayer regions of a flake with the nanocavity, and the sandwich is heated to 250 °C to completely melt the PC and transfer the TMDC flakes and melted PC to the target substrate. Finally, after waiting for the target substrate to cool down, the PC is removed by immersing the sample in chloroform. Figure 55 shows a microscope image of plasmonic nanolaser after the dry transfer process.

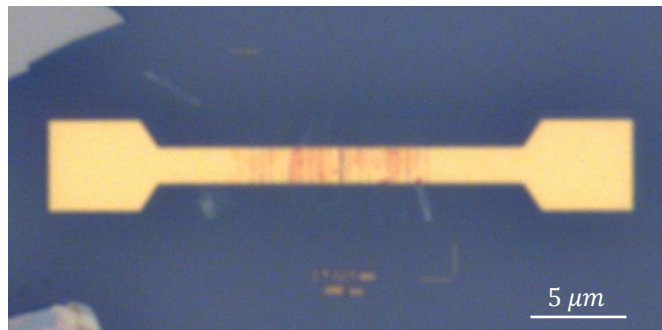


**Figure 56 - Optical micrograph of the  $MoSe_2$  nanolaser after dry transfer of the single-layer material.**

Figures 56. *a, b* shows the numerically calculated reflection spectra of  $MoSe_2$ -based plasmonic nanolasers designed to operate at 300 °K and 5 °K.

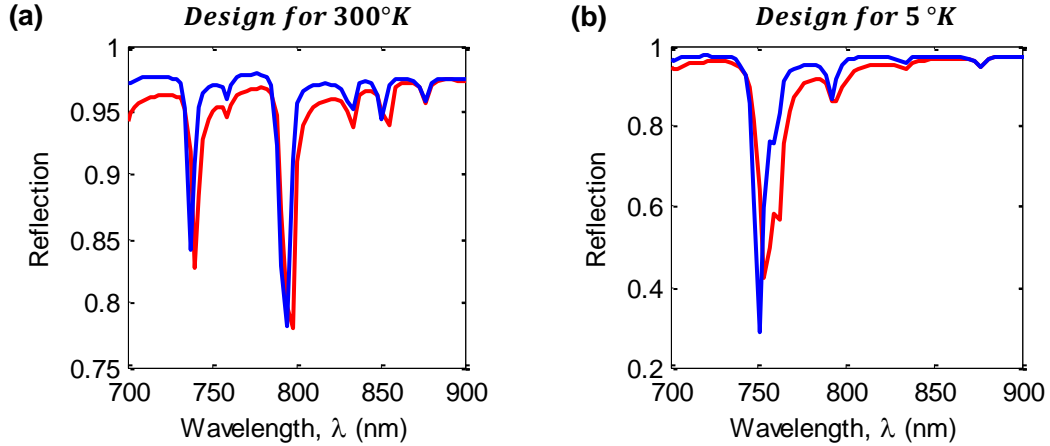


**Figure 57 - Reflection spectra of the desinged  $MoSe_2$ -based plasmonic nanolasers. (a) Reflection spectrum of the laser desinged to ooperate at  $300\text{ }^\circ K$ , (b) Reflection spectrum of the laser desinged to ooperate at  $5\text{ }^\circ K$ .**

## 7.6 Lasing Action in monolayer TMDC-Loaded Plasmonic Nanocavities

So far, we have seen the passive response of the designed nanolasers at low excitation power only considering the complex refractive index of the TMDCs. In order to model lasing action in the nanostructure, we have implemented the four-level quantum system shown in Fig. 41 for the the optical gain (or PL) of TMDCs, within the FDTD framework (Lumerical Inc.). Figure 57 shows the population density, i.e.  $\rho_i = N_i/N$ , of the  $MoS_2$  plasmonic nanolaser at levels  $|0\rangle$  to  $|3\rangle$  in *Eqs.* 7.1 – 4, when the structure is excited with a CW pump at  $\lambda_{exc} = 500\text{ nm}$  and with  $0.99\text{ mW}$  power assuming a spot size of approximately  $1\text{ }\mu m$  ( $I_{exc} = 1.26 \times 10^9\text{ W/m}^2$ ). The inset shows the Rabi oscillation [467] between photons and excitons (between levels  $|1\rangle$  and  $|2\rangle$ ), which is the signature of stimulated emission.

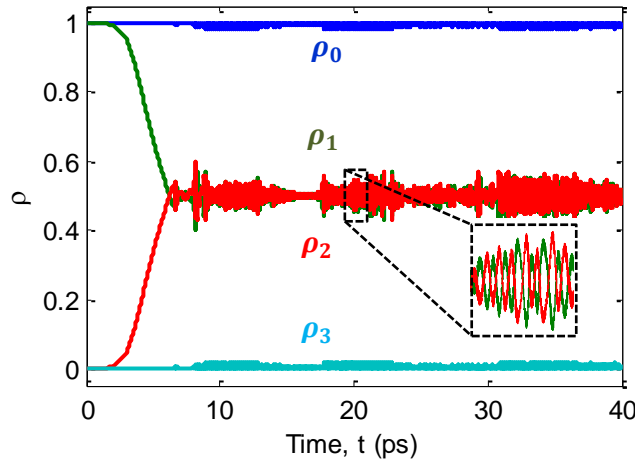


**Figure 58 - Population levels of the  $MoS_2$  plasmonic nanolaser at levels  $|0\rangle$  to  $|3\rangle$  for  $p_{exc} = 0.99 \text{ mW}$ . The inset shows the Rabi oscillation between between levels  $|1\rangle$  and  $|2\rangle$ .**

*Figure 58.a* shows the evolution of the emission spectrum from the  $MoS_2$  plasmonic nanolaser for by changing the excitation power  $p_{exc}$  of the CW pump with  $\lambda_{exc} = 500 \text{ nm}$  linearly from  $0.41$  to  $0.99 \text{ mW}$  assuming again a spot size of approximately  $1 \text{ }\mu\text{m}$  (excitation laser intensity  $I_{exc}$  from  $0.52$  to  $1.26 \text{ GW}/\text{m}^2$ ). The radiative transition lifetime from level  $|2\rangle$  to level  $|1\rangle$ ,  $\tau_{21}$  is assumed to be  $4.8 \text{ ps}$  extracted from *Table 2*. The fast nonradiative transitions from level  $|3\rangle$  to level  $|2\rangle$ ,  $\tau_{32}$ , and from level  $|1\rangle$  to level  $|0\rangle$ ,  $\tau_{10}$  are set at  $1 \text{ fs}$ . The QY of the  $MoS_2$  is assumed to be  $5\%$ . The saturation carrier density  $N_s$  for both  $MoS_2$  and  $MoSe_2$  is approximated to be at  $10^{13} \text{ cm}^{-2}$  [528]. *Figures 51.b – d* show the electric modeprofile at  $p_{exc} = 0.67 \text{ mW}$  ( $I_{exc} = 0.85 \times 10^9 \text{ W}/\text{m}^2$ ) at the three stimulated emission peaks with  $\lambda_{em} = 540, 550, 559 \text{ nm}$ .

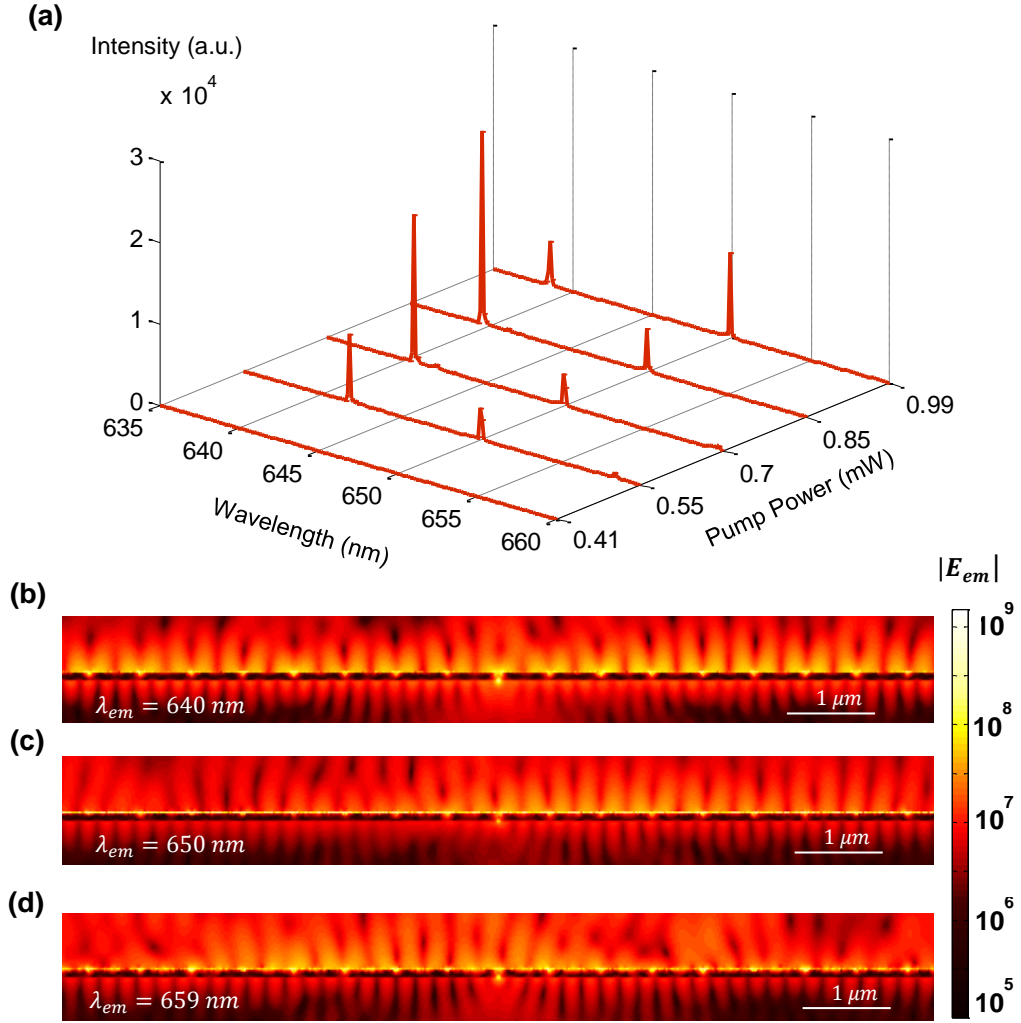


**Figure 59** - Active numerical simulation of the monolayer  $MoS_2$  plasmonic nanolaser with optical pumping using a CW laser polarized in x-direction with  $\lambda_{exc} = 500 \text{ nm}$ . (a) Evolution of emission spectrum by changing the pump power from 0.41 to 0.99 mW (b-d) Emission modeprofile with  $p_{exc} = 0.67 \text{ mW}$  ( $I_{exc} = 0.85 \times 10^9 \text{ W/m}^2$ ).

Similar numerical simulations have been performed for the monolayer  $MoSe_2$  nanolaser, assuming  $\tau_{21} = 1.8 \text{ ps}$ ,  $\tau_{32} = \tau_{10} = 1 \text{ fs}$ ,  $QY = 5\%$ ,  $N_s \approx 10^{13} \text{ cm}^{-2}$  and a CW pump at  $\lambda_{exc} = 650 \text{ nm}$ . Figure 59.a shows the evolution of the emission spectrum from  $MoSe_2$  plasmonic nanolaser for by changing the excitation power  $p_{exc}$  of the CW pump linearly from 0.85 to 01.76 mW.

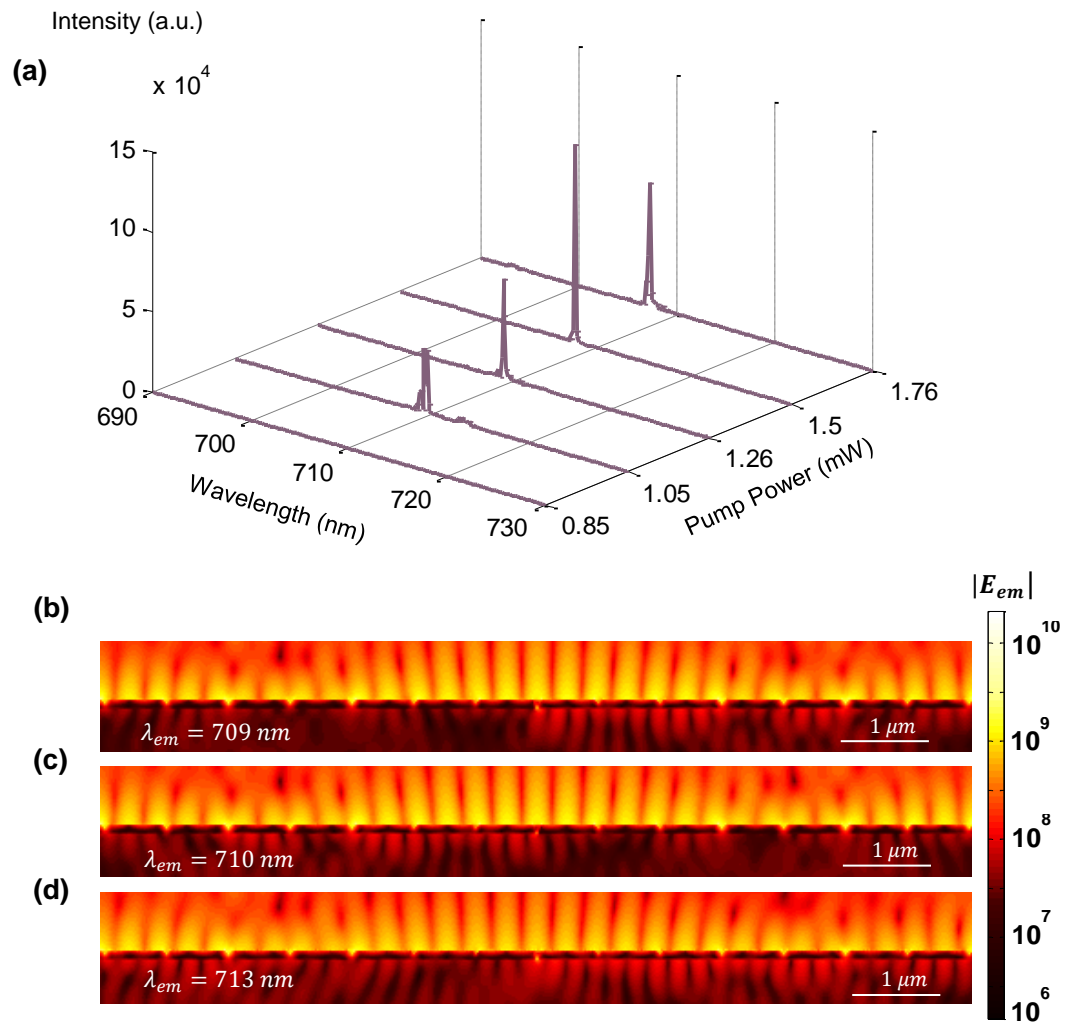


Figure 60 - Active numerical modeling of the monolayer  $MoSe_2$  plasmonic nanolaser with optical pumping using a CW laser polarized in x-direction with  $\lambda_{exc} = 650 \text{ nm}$ . (a) Evolution of emission spectrum by changing the pump power from 0.85 to 1.76 mW (b-d) Emission modeprofile with  $p_{exc} = 1.05 \text{ mW}$  .

## CHAPTER 8.

### EPILOGUE

#### 8.1 Brief Summary of Contributions

The objective of this thesis was to develop a new class of plasmonic nanostructures and metamaterials for nanoscale light-matter interaction applications including: *sensing, spectroscopy, nonlinear optics and lasing in monolayer TMDCs*. To this end, we set out by studying various types of plasmonic nanostructures and metamaterials to have a global view of the advantages and shortcomings of each nanostructure and its potential applications. We then used this understanding to design and experimentally demonstrate several plasmonic nanodevices for different applications. During these investigations, we focused on practical applications in which plasmonic nanostructures can either outperform the existing solutions or can uniquely solve unaddressed practical needs. We believe this thesis provides a strong foundation for future research endeavors in nano-optics for a range of applications that could benefit from enhanced light-matter interaction in nanoscale.

The first part of this thesis was dedicated to the application of plasmonic nanostructure in molecular sensing, which included the design, and experimental demonstration of plasmonic biosensors with three different modalities: *LSPR resonance wavelength shift, surface-enhanced vibration spectroscopy* and *chiroptical spectroscopy*. Our first study was on the theoretical investigation of one-dimensional arrays of chemically synthesized plasmonic nanocubes with sub-10 nm dielectric gaps as a practical platform for molecular sensing based on resonance wavelength shift and surface-enhanced vibrational spectroscopy. We performed a comprehensive performance analysis of nanocube chains with different

lengths, orientations and material compositions, concluding that the edge-to-edge configuration is favorable in most cases. Moreover, we expanded upon this study by considering *plasmon tunneling* in sub-1 nm dielectric gaps, as an important consideration in practical applications.

Next, we focused on lattice plasmons and Fano resonance in strongly coupled plasmonic nanoantenna arrays. We designed and experimentally demonstrated a plasmonic biosensor for surface-enhanced Raman spectroscopy, which utilizes lattice plasmons in a lithographically fabricated bilayer nanoantenna array. We first developed a unique nanoantenna geometry and fabrication method with the two main advantages of *a) scalability of the fabrication method, b) efficiency in the amount of analyte needed for sensing by limiting the sensing area to the vertical gap between the two layers*. Then, we showed that by tuning the lattice plasmons in the nanoantenna array, such that their band-edge coincide with pump wavelength, we can get the maximum enhancement factor in SERS.

Our third developed nanodevice was a chiral plasmonic metamaterial that was used to detect and differentiate chiral biomolecules at the molecular level. We showed that the locally enhanced chiral fields of this plasmonic metamaterial can be utilized to amplify the chiroptical response of the chiral molecules, which was manifested in the large change in circular dichroism spectrum acquired from the device. One the of key aspects of our design is the fabrication of 3D chiral metamaterial with one-step lithography, which renders the structure scalable to low visible and UV wavelength, where most biomolecules of interest show significant chirality. Chiroptical sensing using this nanodevice was experimentally demonstrated on several chiral molecules.

The second part of this thesis was dedicated to the plasmonically-enhanced generation of light, including two sub-areas: *nonlinear plasmonics* and *plasmonic lasing*. In the nonlinear work, we investigated the effect of *quasi-phase-matching* and *lattice plasmons band-edge* on surface-enhanced second harmonic generation. Theoretically, we predicted that with proper geometrical parameters, it should be possible to achieve the quasi-phase-matching condition for discrete sets of pump wavelength and excitation angles. Then, in experimental studies, SESHG signal was collected from a bilayer nanoantenna array similar to the nanostructure used for SERS with different excitation wavelengths and excitation angles. The collected signal showed clearly the effect of lattice plasmon band-edge on both fundamental mode and second harmonic, as well as some evidence of the quasi-phase-matching predicted by the theory.

Next, we designed monolayer semiconductor plasmonic nanolasers using a new plasmonic nanocavity based on slits and grooves. The designed nanocavities were optimized to operate near the bandgaps of  $MoS_2$  and  $MoSe_2$  as the gain media and a theoretical study of the optically-pumped lasing using an active model of the hybrid nanostructures was performed. The two nanolasers were fabricated using a combination of EBL, FIB milling, wet and dry transfer of  $MoS_2$  and  $MoSe_2$ . In the end, we discuss how the Schottky-barrier diode in the metal-semiconductor junction in the fabricated nanostructures can be used to demonstrate electrically-pumped lasing.

Considering the extraordinary potential of the field of plasmonics in miniaturization of on-chip optical devices, lowering their power consumption and improving their other performance metrics, the concepts presented in this thesis can open new avenues in developing a new generation of plasmonic biosensors, light sources, photodetectors, etc. However, despite the scientific breakthroughs over the last decade, the field of plasmonics is

not mature enough for large-scale commercialization. Major practical and technological challenges remain to be resolved, specifically in terms of material development and nanofabrication, to facilitate the wide-scale adoption of plasmonic nanodevices in industry.

## 8.2 Future Directions

Based on the concepts and nanodevices presented in this thesis, we envision the next steps and new directions, which we have detailed underneath for each work.

*Molecular sensing using nanocubes:* the next step in molecular sensing using nanocubes would be developing a fabrication method to realize 1D arrays of nanocubes with controlled geometry and orientation in a robust and repeatable fashion. This could be accomplished using a combination of nanolithography and chemical synthesis of nanocubes to overcome the challenges faced in fabricating small nanocubes using nanolithography and in placing the chemically synthesized nanocubes in precise locations [529]. A polymer template can be prepared using EBL to trap chemically synthesized nanocubes and form the nanocube chains with a high degree of control on location and orientation. The realization of these nanocube chains would enable experimental measurement of performance parameters in sensing applications. As for the nanocube chains with sub-1 nm dielectric gaps, EELS measurements together with high resolution AFM measurements need to be performed on individual arrays to confirm the theory due to the unrepeatability of sub-1nm gaps even with EBL, and the high sensitivity of plasmon tunneling to the gap size.

*Molecular sensing using lattice plasmons:* the next step in molecular sensing using lattice plasmons could be expanding into new sensing modalities. The sharp Fano signature

of lattice resonance in a nanoantenna array can be used for ultrasensitive detection of molecules using resonance wavelength shift, potentially with the naked eye. Additionally, other surface-enhanced vibrational spectroscopy techniques, including SEIRA and SECARS can also be implemented using this concept, each one having unique application scenarios and advantages over SERS.

*Chiroptical spectroscopy:* several next steps and new directions can be envisioned for chiroptical spectroscopy using chiral metamaterials. First, some theoretical aspects of chiral light-matter interaction in the presence of chiral metamaterial are not yet completely understood and merits further investigation. Secondly, given the scalability of the nanostructure developed and large appeal of chiroptical sensing in low visible and UV range, the next step could be scaling down this design by switching to other plasmonic materials such as *Ag* or *Al* to be able to detect a range of chiral biomolecules, including proteins, DNA, sugars, etc. The third direction can be combining chiroptical spectroscopy with SERS to develop the plasmonic analog of chiral Raman spectroscopy [327], which can provide new insights into the molecular structures, not attainable by SERS and chiroptical spectroscopy separately.

*Nonlinear plasmonics:* the next step in nonlinear plasmonic could be targeting a new application. One interesting application for SESHG could be the nonlinear sensing of molecules given the sensitivity of surface nonlinearity to adsorption of molecules. More studies can also be done on the hot-carrier induced light generation, which we observed in our experiments and its potential applications. We can also envision the extension of this work to other nonlinear processes, possibly by integrating a material with large Kerr nonlinearity, such as ITO or a semiconductor to demonstrate THG and FWM.

*Plasmonic lasing*: experimental demonstration of optically-pumped plasmon lasing in 2D TMDCs is the next logical step in this works. Then, we can explore electrically-pumped lasing using the Schottky-barrier diode between the 2D TMDCs and *Au*. The same concepts can be used to develop plasmonic *optical semiconductor amplifier* using optical and electrical pumping of a plasmonic waveguide coupled to 2D TMDCs.

Finally, new applications can be envisioned based on the concepts and nanodevices developed in this thesis. For instance, many new novel structures can be implemented using the combination of high-Q chemically synthesized nanocubes and lithographic fabrication of templates. The high sensitivity of lattice resonance in plasmonic nanoantenna array can be used for ultrafast switching by photocarrier generation in semiconductors such as ITO. The locally enhanced chiral fields of the chiral metamaterials can be used to generate valley currents in TMDCs and lastly, the Schottky-barrier diode proposed for electrical-pumping of the TMDC-based nanolaser can also be used high sensitivity photodetection in TMDCs.

## APPENDIX A.

### A.1. Theory of Resonant Metamaterial Enhanced Chiral Light-Matter Interaction

In this section, we provide an analytical treatment of the differential CD response of a chiral metamaterial induced by an optically active molecule in its near field. The perturbation in the electromagnetic field energy  $dU$  induced by a chiral molecule is described by:

$$dU = \frac{1}{2} (\vec{E}^* \cdot \vec{p}_m + \vec{B}^* \cdot \vec{m}_m) \simeq \frac{\alpha_m}{\epsilon_0} U_e + \frac{G_m}{\omega} C \quad (\text{A.1})$$

Where  $\vec{p}_m = \alpha_m \vec{E} - iG_m \vec{B}$  and  $\vec{m}_m = \chi_m \vec{E} + iG_m \vec{B}$  are the electric and magnetic dipole moments of the the molecule,  $U_e = \frac{1}{2} \epsilon_0 |\vec{E}|^2$  and  $C = \omega \text{Im}\{\vec{E}^* \times \vec{B}\}$  are the electric energy density and chirality pseudoscalar at the position of the molecule,  $\alpha_m$  is the electric polarizability,  $G_m$  is the mixed electric-magnetic polarizability (i.e., chirality) and  $\chi_m$  is the magnetic susceptibility which is negligible in most materials.

The circular dichroism of the metamaterial with a resonant plasmonic mode is a result of the difference between RHC and LHC resonance wavelengths. The perturbation by the dielectric and chiral polarizability of molecules at a specific frequency bound to the metamaterial surface can be estimated by the shift in the resonant modes corresponding to RHC and LHC modes.

Assuming a weak perturbation of electromagnetic fields, small  $dU$ , we can use the linear approximation to find the change in complex frequency, i.e.  $d\omega = \left(\frac{dU}{U_T}\right) \omega$ , where  $U_T$  is the total energy confined by the chiral resonator (in our notations, we use  $d(\cdot)$  for an infinitesimal perturbation and  $\Delta(\cdot)$  for the subtraction of two quantities or spectra). This

change in frequency for the chiral resonant modes shift can be decomposed into two real and imaginary components; i.e.  $d\omega = d\omega' + id\omega''$ . The real part  $d\omega'$  shows the shift in scattering and the imaginary part  $d\omega''$  denotes the change in the net absorption of the chiral molecules. Using the linear approximation, we have  $d\omega' = \omega \left( \frac{U_e}{U_T} \right) \alpha'_m + \left( \frac{C}{U_T} \right) G'_m$  and  $d\omega'' = \omega \left( \frac{U_e}{U_T} \right) \alpha''_m + \left( \frac{C}{U_T} \right) G''_m$  in terms of the real and imaginary parts of  $\alpha_m$  and  $G_m$ .

The change in the CD of the chiral resonator is proportional to the change in the resonance frequency of the RHC and LHC modes of the resonators,  $\Delta CD = (\beta'_+ d\omega'_+ + i\beta''_+ d\omega''_+) - (\beta'_- d\omega'_- + i\beta''_- d\omega''_-)$ , where  $\beta'_\pm = \left( \frac{\partial R^\pm}{\partial \omega'_\pm} \right) \frac{1}{R^\pm}$  and  $\beta''_\pm = \left( \frac{\partial R^\pm}{\partial \omega''_\pm} \right) \frac{1}{R^\pm}$ , with  $R^\pm$  being the reflection of the RHC and LHC excitation beams, respectively. Assuming that the sensitivities of the RHC and LHC resonances in response to the attachment of molecule are approximately the same, we have  $\beta'_+ = \beta'_- = \beta'$  and  $\beta''_+ = \beta''_- = \beta''$ , and  $\Delta CD$  can be rewritten as  $\Delta CD = \beta'(d\omega'_+ - d\omega'_-) + i\beta''(d\omega''_+ - d\omega''_-)$  or:

$$\Delta CD = \beta' \left( \omega \left( \frac{\Delta U_e}{U_T} \right) \alpha'_m + \left( \frac{\Delta C}{U_T} \right) G'_m \right) + i\beta'' \left( \omega \left( \frac{\Delta U_e}{U_T} \right) \alpha''_m + \left( \frac{\Delta C}{U_T} \right) G''_m \right) \quad (\text{A.2})$$

where  $\Delta U_e = U_e^+ - U_e^-$  and  $\Delta C = C^+ - C^-$ . Assuming that RHC and LHC resonances are reasonably close,  $\Delta U_e$  is quite small, while the difference in chirality pseudoscalar  $\Delta C$  of the two resonance modes can be quite large. So, their absolute values add up ( $|\Delta C| = |C^+| + |C^-|$ ). Therefore, while  $G_m \ll \alpha_m$ , the effect of the  $G_m$  on  $\Delta CD$  is the dominant factor.

An equivalent argument for dominance of chiral permittivity on differential CD can be done using the far-field linear response. The change in differential reflectance due to the attachment of molecule can be written as  $\Delta r_{MM+Mol} - \Delta r_{MM} = dr^+ - dr^-$ , where  $dr^\pm = r_{MM+Mol}^\pm - r_{MM}^\pm$  is the change in reflectance after coating in response to RHC and LHC light.

The RHC and LHC reflections can in turn be rewritten in terms of the total change in the electric permittivity of the environment  $\varepsilon^\pm$ , as  $dr^\pm = (dr/d\varepsilon)^\pm d\varepsilon^\pm$ . Assuming that  $\lambda_{res}^\pm$  are reasonably close, for a small perturbation in  $d\varepsilon^\pm$ , we can assume similar sensitivity to RHC and LHC light, i.e.  $(dr/d\varepsilon)^+ = (dr/d\varepsilon)^- = (dr/d\varepsilon)$ , and hence  $\Delta r_{MM+Mol} - \Delta r_{MM} = (dr/d\varepsilon) (d\varepsilon^+ - d\varepsilon^-)$ . A non-chiral perturbation, i.e.  $d\varepsilon^+ = d\varepsilon^-$ , would result in, and  $\Delta r_{MM+Mol} = \Delta r_{MM}$  hence  $\Delta CD \simeq 0$ .

## REFERENCES

- [1] Abbe, E. VII.—On the Estimation of Aperture in the Microscope. *Journal of Microscopy* **1**, 388-423 (1881).
- [2] Harootunian, A., Betzig, E., Isaacson, M. & Lewis, A. Super-resolution fluorescence near-field scanning optical microscopy. *Applied Physics Letters* **49**, 674-676 (1986).
- [3] Airy, G. B. On the diffraction of an object-glass with circular aperture. *Transactions of the Cambridge Philosophical Society* **5**, 283 (1835).
- [4] Bergman, D. J. & Stockman, M. I. Surface plasmon amplification by stimulated emission of radiation: quantum generation of coherent surface plasmons in nanosystems. *Physical review letters* **90**, 027402 (2003).
- [5] Oulton, R. F., Sorger, V. J., Zentgraf, T., Ma, R.-M., Gladden, C., Dai, L. *et al.* Plasmon lasers at deep subwavelength scale. *Nature* **461**, 629-632 (2009).
- [6] Berini, P. & De Leon, I. Surface plasmon–polariton amplifiers and lasers. *Nature Photonics* **6**, 16 (2012).
- [7] Wood, R. W. XLII. On a remarkable case of uneven distribution of light in a diffraction grating spectrum. *The London, Edinburgh, and Dublin Philosophical Magazine and Journal of Science* **4**, 396-402 (1902).
- [8] Pines, D. & Bohm, D. A collective description of electron interactions: II. Collective vs individual particle aspects of the interactions. *Physical Review* **85**, 338 (1952).
- [9] Ritchie, R. Plasma losses by fast electrons in thin films. *Physical Review* **106**, 874 (1957).
- [10] Ashcroft, N. & Mermin, N. *Solid State Physics*. (Saunders, 1976).
- [11] Raether, H. *Surface plasmons on smooth surfaces*. (Springer, 1988).
- [12] Novotny, L. & Hecht, B. *Principles of nano-optics*. (Cambridge university press, 2012).
- [13] Fabre, C., Sandoghdar, V., Treppe, N. & Cugliandolo, L. F. *Quantum Optics and Nanophotonics*. Vol. 101 (Oxford University Press, 2017).
- [14] Joulain, K., Carminati, R., Mulet, J.-P. & Greffet, J.-J. Definition and measurement of the local density of electromagnetic states close to an interface. *Physical Review B* **68**, 245405 (2003).

- [15] Boriskina, S. V., Ghasemi, H. & Chen, G. Plasmonic materials for energy: From physics to applications. *Materials Today* **16**, 375-386 (2013).
- [16] Christensen, T., Yan, W., Raza, S., Jauho, A.-P., Mortensen, N. A. & Wubs, M. Nonlocal response of metallic nanospheres probed by light, electrons, and atoms. *Acs Nano* **8**, 1745-1758 (2014).
- [17] Dionne, J., Sweatlock, L., Atwater, H. & Polman, A. Planar metal plasmon waveguides: frequency-dependent dispersion, propagation, localization, and loss beyond the free electron model. *Physical Review B* **72**, 075405 (2005).
- [18] Sauvan, C., Hugonin, J.-P., Maksymov, I. & Lalanne, P. Theory of the spontaneous optical emission of nanosize photonic and plasmon resonators. *Physical Review Letters* **110**, 237401 (2013).
- [19] Joannopoulos, J. D., Johnson, S. G., Winn, J. N. & Meade, R. D. *Photonic crystals: molding the flow of light*. (Princeton university press, 2011).
- [20] Barnes, W. L., Dereux, A. & Ebbesen, T. W. Surface plasmon subwavelength optics. *Nature* **424**, 824-830 (2003).
- [21] Fan, X., Zheng, W. & Singh, D. J. Light scattering and surface plasmons on small spherical particles. *Light: Science & Applications* **3**, e179 (2014).
- [22] West, P. R., Ishii, S., Naik, G. V., Emani, N. K., Shalaev, V. M. & Boltasseva, A. Searching for better plasmonic materials. *Laser & Photonics Reviews* **4**, 795-808 (2010).
- [23] Fedyanin, D. Y., Yakubovsky, D. I., Kirtaev, R. V. & Volkov, V. S. Ultralow-loss CMOS copper plasmonic waveguides. *Nano letters* **16**, 362-366 (2015).
- [24] Knight, M. W., Liu, L., Wang, Y., Brown, L., Mukherjee, S., King, N. S. *et al.* Aluminum plasmonic nanoantennas. *Nano letters* **12**, 6000-6004 (2012).
- [25] Knight, M. W., King, N. S., Liu, L., Everitt, H. O., Nordlander, P. & Halas, N. J. Aluminum for plasmonics. *ACS nano* **8**, 834-840 (2013).
- [26] King, N. S., Liu, L., Yang, X., Cerjan, B., Everitt, H. O., Nordlander, P. *et al.* Fano resonant aluminum nanoclusters for plasmonic colorimetric sensing. *ACS nano* **9**, 10628-10636 (2015).
- [27] Olson, J., Manjavacas, A., Liu, L., Chang, W.-S., Foerster, B., King, N. S. *et al.* Vivid, full-color aluminum plasmonic pixels. *Proceedings of the National Academy of Sciences* **111**, 14348-14353 (2014).
- [28] Tseng, M. L., Yang, J., Semmlinger, M., Zhang, C., Nordlander, P. & Halas, N. J. Two-Dimensional Active Tuning of an Aluminum Plasmonic Array for Full-Spectrum Response. *Nano letters* **17**, 6034-6039 (2017).

- [29] Grigorenko, A., Polini, M. & Novoselov, K. Graphene plasmonics. *Nature photonics* **6**, 749 (2012).
- [30] Ju, L., Geng, B., Horng, J., Girit, C., Martin, M., Hao, Z. *et al.* Graphene plasmonics for tunable terahertz metamaterials. *Nature nanotechnology* **6**, 630 (2011).
- [31] Rodrigo, D., Limaj, O., Janner, D., Etezadi, D., de Abajo, F. J. G., Pruneri, V. *et al.* Mid-infrared plasmonic biosensing with graphene. *Science* **349**, 165-168 (2015).
- [32] Li, Y., Yan, H., Farmer, D. B., Meng, X., Zhu, W., Osgood, R. M. *et al.* Graphene plasmon enhanced vibrational sensing of surface-adsorbed layers. *Nano letters* **14**, 1573-1577 (2014).
- [33] Christensen, J., Manjavacas, A., Thongrattanasiri, S., Koppens, F. H. & García de Abajo, F. J. Graphene plasmon waveguiding and hybridization in individual and paired nanoribbons. *ACS nano* **6**, 431-440 (2011).
- [34] Garcia de Abajo, F. J. Graphene plasmonics: challenges and opportunities. *Acs Photonics* **1**, 135-152 (2014).
- [35] Koppens, F. H., Chang, D. E. & Garcia de Abajo, F. J. Graphene plasmonics: a platform for strong light-matter interactions. *Nano letters* **11**, 3370-3377 (2011).
- [36] Gullans, M., Chang, D., Koppens, F., de Abajo, F. G. & Lukin, M. D. Single-photon nonlinear optics with graphene plasmons. *Physical review letters* **111**, 247401 (2013).
- [37] Luther, J. M., Jain, P. K., Ewers, T. & Alivisatos, A. P. Localized surface plasmon resonances arising from free carriers in doped quantum dots. *Nature materials* **10**, 361 (2011).
- [38] Seren, H. R., Zhang, J., Keiser, G. R., Maddox, S. J., Zhao, X., Fan, K. *et al.* Nonlinear terahertz devices utilizing semiconducting plasmonic metamaterials. *Light: Science & Applications* **5**, e16078 (2016).
- [39] Fischer, M. P., Schmidt, C., Sakat, E., Stock, J., Samarelli, A., Frigerio, J. *et al.* Optical activation of germanium plasmonic antennas in the mid-infrared. *Physical review letters* **117**, 047401 (2016).
- [40] Baldassarre, L., Sakat, E., Frigerio, J., Samarelli, A., Gallacher, K., Calandrini, E. *et al.* Midinfrared plasmon-enhanced spectroscopy with germanium antennas on silicon substrates. *Nano letters* **15**, 7225-7231 (2015).
- [41] Chen, Y., Analytis, J. G., Chu, J.-H., Liu, Z., Mo, S.-K., Qi, X.-L. *et al.* Experimental realization of a three-dimensional topological insulator, Bi<sub>2</sub>Te<sub>3</sub>. *science* **325**, 178-181 (2009).

- [42] Di Pietro, P., Ortolani, M., Limaj, O., Di Gaspare, A., Giliberti, V., Giorgianni, F. *et al.* Observation of Dirac plasmons in a topological insulator. *Nature nanotechnology* **8**, 556 (2013).
- [43] Ou, J.-Y., So, J.-K., Adamo, G., Sulaev, A., Wang, L. & Zheludev, N. I. Ultraviolet and visible range plasmonics in the topological insulator Bi<sub>1.5</sub>Sb<sub>0.5</sub>Te<sub>1.8</sub>Se<sub>1.2</sub>. *Nature communications* **5**, 5139 (2014).
- [44] Uchida, K., Adachi, H., Kikuchi, D., Ito, S., Qiu, Z., Maekawa, S. *et al.* Generation of spin currents by surface plasmon resonance. *Nature communications* **6**, 5910 (2015).
- [45] Naik, G. V., Shalaev, V. M. & Boltasseva, A. Alternative plasmonic materials: beyond gold and silver. *Advanced Materials* **25**, 3264-3294 (2013).
- [46] Boltasseva, A. & Atwater, H. A. Low-loss plasmonic metamaterials. *Science* **331**, 290-291 (2011).
- [47] Naik, G. V., Saha, B., Liu, J., Saber, S. M., Stach, E. A., Irudayaraj, J. M. *et al.* Epitaxial superlattices with titanium nitride as a plasmonic component for optical hyperbolic metamaterials. *Proceedings of the National Academy of Sciences* **111**, 7546-7551 (2014).
- [48] Naik, G. V., Liu, J., Kildishev, A. V., Shalaev, V. M. & Boltasseva, A. Demonstration of Al: ZnO as a plasmonic component for near-infrared metamaterials. *Proceedings of the National Academy of Sciences* **109**, 8834-8838 (2012).
- [49] Gordon, T. R., Paik, T., Klein, D. R., Naik, G. V., Caglayan, H., Boltasseva, A. *et al.* Shape-dependent plasmonic response and directed self-assembly in a new semiconductor building block, indium-doped cadmium oxide (ICO). *Nano letters* **13**, 2857-2863 (2013).
- [50] Liu, X., Kang, J.-H., Yuan, H., Park, J., Kim, S. J., Cui, Y. *et al.* Electrical tuning of a quantum plasmonic resonance. *Nature nanotechnology* **12**, 866 (2017).
- [51] Guo, P., Schaller, R. D., Ketterson, J. B. & Chang, R. P. Ultrafast switching of tunable infrared plasmons in indium tin oxide nanorod arrays with large absolute amplitude. *Nature Photonics* **10**, 267 (2016).
- [52] Abb, M., Wang, Y., Papasimakis, N., De Groot, C. & Muskens, O. L. Surface-enhanced infrared spectroscopy using metal oxide plasmonic antenna arrays. *Nano letters* **14**, 346-352 (2013).
- [53] Kanehara, M., Koike, H., Yoshinaga, T. & Teranishi, T. Indium tin oxide nanoparticles with compositionally tunable surface plasmon resonance frequencies in the near-IR region. *Journal of the American Chemical Society* **131**, 17736-17737 (2009).

- [54] McPeak, K. M., Jayanti, S. V., Kress, S. J., Meyer, S., Iotti, S., Rossinelli, A. *et al.* Plasmonic films can easily be better: rules and recipes. *ACS photonics* **2**, 326-333 (2015).
- [55] Huang, X., El-Sayed, I. H., Qian, W. & El-Sayed, M. A. Cancer cell imaging and photothermal therapy in the near-infrared region by using gold nanorods. *J Am Chem Soc* **128**, 2115-2120 (2006).
- [56] Huang, X., Jain, P. K., El-Sayed, I. H. & El-Sayed, M. A. Gold nanoparticles: interesting optical properties and recent applications in cancer diagnostics and therapy. (2007).
- [57] Agarwal, A., Mackey, M. A., El-Sayed, M. A. & Bellamkonda, R. V. Remote triggered release of doxorubicin in tumors by synergistic application of thermosensitive liposomes and gold nanorods. *ACS nano* **5**, 4919-4926 (2011).
- [58] Huang, X., Peng, X., Wang, Y., Wang, Y., Shin, D. M., El-Sayed, M. A. *et al.* A reexamination of active and passive tumor targeting by using rod-shaped gold nanocrystals and covalently conjugated peptide ligands. *ACS nano* **4**, 5887-5896 (2010).
- [59] Aioub, M., Panikkanvalappil, S. R. & El-Sayed, M. A. Platinum-coated gold nanorods: Efficient reactive oxygen scavengers that prevent oxidative damage toward healthy, untreated cells during plasmonic photothermal therapy. *ACS nano* **11**, 579-586 (2017).
- [60] Lukianova-Hleb, E. Y., Ren, X., Sawant, R. R., Wu, X., Torchilin, V. P. & Lapotko, D. O. On-demand intracellular amplification of chemoradiation with cancer-specific plasmonic nanobubbles. *Nature medicine* **20**, 778-784 (2014).
- [61] Hirsch, L. R., Stafford, R. J., Bankson, J., Sershen, S. R., Rivera, B., Price, R. *et al.* Nanoshell-mediated near-infrared thermal therapy of tumors under magnetic resonance guidance. *Proceedings of the National Academy of Sciences* **100**, 13549-13554 (2003).
- [62] Huang, X., Jain, P. K., El-Sayed, I. H. & El-Sayed, M. A. Plasmonic photothermal therapy (PPTT) using gold nanoparticles. *Lasers in medical science* **23**, 217 (2008).
- [63] Ndukaife, J. C., Shalaev, V. M. & Boltasseva, A. Plasmonics—turning loss into gain. *Science* **351**, 334-335 (2016).
- [64] Garnett, E. C., Cai, W., Cha, J. J., Mahmood, F., Connor, S. T., Christoforo, M. G. *et al.* Self-limited plasmonic welding of silver nanowire junctions. *Nature materials* **11**, 241 (2012).

- [65] Zhang, X., Li, X., Reish, M. E., Zhang, D., Su, N. Q., Gutiérrez, Y. *et al.* Plasmon-Enhanced Catalysis: Distinguishing Thermal and Nonthermal Effects. (2018).
- [66] Kriegler, C. E., Rill, M. S., Linden, S. & Wegener, M. Bianisotropic photonic metamaterials. *IEEE journal of selected topics in quantum electronics* **16**, 367-375 (2010).
- [67] Kong, J. A. Theorems of bianisotropic media. *Proceedings of the IEEE* **60**, 1036-1046 (1972).
- [68] Yu, N., Genevet, P., Kats, M. A., Aieta, F., Tetienne, J.-P., Capasso, F. *et al.* Light propagation with phase discontinuities: generalized laws of reflection and refraction. *science* **334**, 333-337 (2011).
- [69] Soukoulis, C. M., Linden, S. & Wegener, M. Negative refractive index at optical wavelengths. *Science* **315**, 47-49 (2007).
- [70] Shelby, R. A., Smith, D. R. & Schultz, S. Experimental verification of a negative index of refraction. *science* **292**, 77-79 (2001).
- [71] Smith, D. R., Padilla, W. J., Vier, D., Nemat-Nasser, S. C. & Schultz, S. Composite medium with simultaneously negative permeability and permittivity. *Physical review letters* **84**, 4184 (2000).
- [72] Gehring, G. M., Schweinsberg, A., Barsi, C., Kostinski, N. & Boyd, R. W. Observation of backward pulse propagation through a medium with a negative group velocity. *Science* **312**, 895-897 (2006).
- [73] Dolling, G., Enkrich, C., Wegener, M., Soukoulis, C. M. & Linden, S. Simultaneous negative phase and group velocity of light in a metamaterial. *Science* **312**, 892-894 (2006).
- [74] Xiao, S., Drachev, V. P., Kildishev, A. V., Ni, X., Chettiar, U. K., Yuan, H.-K. *et al.* Loss-free and active optical negative-index metamaterials. *Nature* **466**, 735 (2010).
- [75] Hess, O., Pendry, J. B., Maier, S. A., Oulton, R. F., Hamm, J. & Tsakmakidis, K. Active nanoplasmonic metamaterials. *Nature materials* **11**, 573 (2012).
- [76] Wuestner, S., Pusch, A., Tsakmakidis, K. L., Hamm, J. M. & Hess, O. Overcoming losses with gain in a negative refractive index metamaterial. *Physical review letters* **105**, 127401 (2010).
- [77] Rüter, C. E., Makris, K. G., El-Ganainy, R., Christodoulides, D. N., Segev, M. & Kip, D. Observation of parity–time symmetry in optics. *Nature physics* **6**, 192 (2010).

- [78] Regensburger, A., Bersch, C., Miri, M.-A., Onishchukov, G., Christodoulides, D. N. & Peschel, U. Parity–time synthetic photonic lattices. *Nature* **488**, 167 (2012).
- [79] Feng, L., Xu, Y.-L., Fegadolli, W. S., Lu, M.-H., Oliveira, J. E., Almeida, V. R. *et al.* Experimental demonstration of a unidirectional reflectionless parity-time metamaterial at optical frequencies. *Nature materials* **12**, 108 (2013).
- [80] Chang, L., Jiang, X., Hua, S., Yang, C., Wen, J., Jiang, L. *et al.* Parity–time symmetry and variable optical isolation in active–passive-coupled microresonators. *Nature photonics* **8**, 524 (2014).
- [81] Feng, L., Wong, Z. J., Ma, R.-M., Wang, Y. & Zhang, X. Single-mode laser by parity-time symmetry breaking. *Science* **346**, 972-975 (2014).
- [82] Hodaei, H., Miri, M.-A., Heinrich, M., Christodoulides, D. N. & Khajavikhan, M. Parity-time–symmetric microring lasers. *Science* **346**, 975-978 (2014).
- [83] Cai, W. & Shalaev, V. M. *Optical metamaterials*. Vol. 10 (Springer, 2010).
- [84] Zheludev, N. I. & Kivshar, Y. S. From metamaterials to metadevices. *Nature materials* **11**, 917 (2012).
- [85] Poddubny, A., Iorsh, I., Belov, P. & Kivshar, Y. Hyperbolic metamaterials. *Nature Photonics* **7**, 948 (2013).
- [86] Schäferling, M., Dregely, D., Hentschel, M. & Giessen, H. Tailoring enhanced optical chirality: design principles for chiral plasmonic nanostructures. *Physical Review X* **2**, 031010 (2012).
- [87] Hendry, E., Carpy, T., Johnston, J., Popland, M., Mikhaylovskiy, R., Laphorn, A. *et al.* Ultrasensitive detection and characterization of biomolecules using superchiral fields. *Nature nanotechnology* **5**, 783-787 (2010).
- [88] Lu, D., Kan, J. J., Fullerton, E. E. & Liu, Z. Enhancing spontaneous emission rates of molecules using nanopatterned multilayer hyperbolic metamaterials. *Nature nanotechnology* **9**, 48 (2014).
- [89] Krishnamoorthy, H. N., Jacob, Z., Narimanov, E., Kretzschmar, I. & Menon, V. M. Topological transitions in metamaterials. *Science* **336**, 205-209 (2012).
- [90] Kim, J., Drachev, V. P., Jacob, Z., Naik, G. V., Boltasseva, A., Narimanov, E. E. *et al.* Improving the radiative decay rate for dye molecules with hyperbolic metamaterials. *Optics express* **20**, 8100-8116 (2012).
- [91] Liu, Z., Lee, H., Xiong, Y., Sun, C. & Zhang, X. Far-field optical hyperlens magnifying sub-diffraction-limited objects. *science* **315**, 1686-1686 (2007).

- [92] Rho, J., Ye, Z., Xiong, Y., Yin, X., Liu, Z., Choi, H. *et al.* Spherical hyperlens for two-dimensional sub-diffractive imaging at visible frequencies. *Nature communications* **1**, 143 (2010).
- [93] Yang, X., Yao, J., Rho, J., Yin, X. & Zhang, X. Experimental realization of three-dimensional indefinite cavities at the nanoscale with anomalous scaling laws. *Nature Photonics* **6**, 450 (2012).
- [94] Sreekanth, K. V., Alapan, Y., ElKabbash, M., Ilker, E., Hinczewski, M., Gurkan, U. A. *et al.* Extreme sensitivity biosensing platform based on hyperbolic metamaterials. *Nature materials* **15**, 621 (2016).
- [95] Kabashin, A., Evans, P., Pastkovsky, S., Hendren, W., Wurtz, G., Atkinson, R. *et al.* Plasmonic nanorod metamaterials for biosensing. *Nature materials* **8**, 867 (2009).
- [96] Meinzer, N., Barnes, W. L. & Hooper, I. R. Plasmonic meta-atoms and metasurfaces. *Nature Photonics* **8**, 889 (2014).
- [97] Yu, N. & Capasso, F. Flat optics with designer metasurfaces. *Nature materials* **13**, 139 (2014).
- [98] Jahani, S. & Jacob, Z. All-dielectric metamaterials. *Nature nanotechnology* **11**, 23 (2016).
- [99] Yu, N., Genevet, P., Aieta, F., Kats, M. A., Blanchard, R., Aoust, G. *et al.* Flat optics: controlling wavefronts with optical antenna metasurfaces. *IEEE Journal of Selected Topics in Quantum Electronics* **19**, 4700423-4700423 (2013).
- [100] Aieta, F., Genevet, P., Yu, N., Kats, M. A., Gaburro, Z. & Capasso, F. Out-of-plane reflection and refraction of light by anisotropic optical antenna metasurfaces with phase discontinuities. *Nano letters* **12**, 1702-1706 (2012).
- [101] Yu, N., Aieta, F., Genevet, P., Kats, M. A., Gaburro, Z. & Capasso, F. A broadband, background-free quarter-wave plate based on plasmonic metasurfaces. *Nano letters* **12**, 6328-6333 (2012).
- [102] Aieta, F., Genevet, P., Kats, M. A., Yu, N., Blanchard, R., Gaburro, Z. *et al.* Aberration-free ultrathin flat lenses and axicons at telecom wavelengths based on plasmonic metasurfaces. *Nano letters* **12**, 4932-4936 (2012).
- [103] Khorasaninejad, M., Aieta, F., Kanhaiya, P., Kats, M. A., Genevet, P., Rousso, D. *et al.* Achromatic metasurface lens at telecommunication wavelengths. *Nano letters* **15**, 5358-5362 (2015).
- [104] Genevet, P., Yu, N., Aieta, F., Lin, J., Kats, M. A., Blanchard, R. *et al.* Ultra-thin plasmonic optical vortex plate based on phase discontinuities. *Applied Physics Letters* **100**, 013101 (2012).

- [105] Lin, D., Fan, P., Hasman, E. & Brongersma, M. L. Dielectric gradient metasurface optical elements. *science* **345**, 298-302 (2014).
- [106] Moitra, P., Yang, Y., Anderson, Z., Kravchenko, I. I., Briggs, D. P. & Valentine, J. Realization of an all-dielectric zero-index optical metamaterial. *Nature Photonics* **7**, 791 (2013).
- [107] Yang, Y., Kravchenko, I. I., Briggs, D. P. & Valentine, J. All-dielectric metasurface analogue of electromagnetically induced transparency. *Nature communications* **5**, 5753 (2014).
- [108] Arbabi, A., Horie, Y., Bagheri, M. & Faraon, A. Dielectric metasurfaces for complete control of phase and polarization with subwavelength spatial resolution and high transmission. *Nature nanotechnology* **10**, 937 (2015).
- [109] Lawrence, M., Barton III, D. R. & Dionne, J. A. Nonreciprocal flat optics with silicon metasurfaces. *Nano letters* **18**, 1104-1109 (2018).
- [110] Novoselov, K., Jiang, D., Schedin, F., Booth, T., Khotkevich, V., Morozov, S. *et al.* Two-dimensional atomic crystals. *Proceedings of the National Academy of Sciences of the United States of America* **102**, 10451-10453 (2005).
- [111] Novoselov, K. S., Geim, A. K., Morozov, S. V., Jiang, D., Zhang, Y., Dubonos, S. V. *et al.* Electric field effect in atomically thin carbon films. *science* **306**, 666-669 (2004).
- [112] Orlita, M., Faugeras, C., Plochocka, P., Neugebauer, P., Martinez, G., Maude, D. K. *et al.* Approaching the Dirac point in high-mobility multilayer epitaxial graphene. *Physical review letters* **101**, 267601 (2008).
- [113] Zhang, Y., Tan, Y.-W., Stormer, H. L. & Kim, P. Experimental observation of the quantum Hall effect and Berry's phase in graphene. *nature* **438**, 201 (2005).
- [114] Novoselov, K. S., Geim, A. K., Morozov, S., Jiang, D., Katsnelson, M., Grigorieva, I. *et al.* Two-dimensional gas of massless Dirac fermions in graphene. *nature* **438**, 197 (2005).
- [115] Tombros, N., Jozsa, C., Popinciuc, M., Jonkman, H. T. & Van Wees, B. J. Electronic spin transport and spin precession in single graphene layers at room temperature. *Nature* **448**, 571 (2007).
- [116] Chen, S., Han, Z., Elahi, M. M., Habib, K. M., Wang, L., Wen, B. *et al.* Electron optics with pn junctions in ballistic graphene. *Science* **353**, 1522-1525 (2016).
- [117] Berger, C., Song, Z., Li, X., Wu, X., Brown, N., Naud, C. *et al.* Electronic confinement and coherence in patterned epitaxial graphene. *Science* **312**, 1191-1196 (2006).

- [118] Banszerus, L., Schmitz, M., Engels, S., Goldsche, M., Watanabe, K., Taniguchi, T. *et al.* Ballistic transport exceeding 28  $\mu\text{m}$  in CVD grown graphene. *Nano letters* **16**, 1387-1391 (2016).
- [119] Lemme, M. C., Echtermeyer, T. J., Baus, M. & Kurz, H. A graphene field-effect device. *IEEE Electron Device Letters* **28**, 282-284 (2007).
- [120] Lin, Y.-M., Dimitrakopoulos, C., Jenkins, K. A., Farmer, D. B., Chiu, H.-Y., Grill, A. *et al.* 100-GHz transistors from wafer-scale epitaxial graphene. *Science* **327**, 662-662 (2010).
- [121] Liu, M., Yin, X., Ulin-Avila, E., Geng, B., Zentgraf, T., Ju, L. *et al.* A graphene-based broadband optical modulator. *Nature* **474**, 64 (2011).
- [122] Ansell, D., Radko, I., Han, Z., Rodriguez, F., Bozhevolnyi, S. & Grigorenko, A. Hybrid graphene plasmonic waveguide modulators. *Nature communications* **6**, 8846 (2015).
- [123] Bao, Q. & Loh, K. P. Graphene photonics, plasmonics, and broadband optoelectronic devices. *ACS nano* **6**, 3677-3694 (2012).
- [124] Song, L., Ci, L., Lu, H., Sorokin, P. B., Jin, C., Ni, J. *et al.* Large scale growth and characterization of atomic hexagonal boron nitride layers. *Nano letters* **10**, 3209-3215 (2010).
- [125] Kim, K. K., Hsu, A., Jia, X., Kim, S. M., Shi, Y., Hofmann, M. *et al.* Synthesis of monolayer hexagonal boron nitride on Cu foil using chemical vapor deposition. *Nano letters* **12**, 161-166 (2011).
- [126] Wang, L., Chen, Z., Dean, C. R., Taniguchi, T., Watanabe, K., Brus, L. E. *et al.* Negligible environmental sensitivity of graphene in a hexagonal boron nitride/graphene/h-BN sandwich structure. *Acs Nano* **6**, 9314-9319 (2012).
- [127] Wang, X. & Xia, F. Van der Waals heterostructures: Stacked 2D materials shed light. *Nature materials* **14**, 264 (2015).
- [128] Britnell, L., Gorbachev, R., Jalil, R., Belle, B., Schedin, F., Mishchenko, A. *et al.* Field-effect tunneling transistor based on vertical graphene heterostructures. *Science* **335**, 947-950 (2012).
- [129] Tran, T. T., Bray, K., Ford, M. J., Toth, M. & Aharonovich, I. Quantum emission from hexagonal boron nitride monolayers. *Nature nanotechnology* **11**, 37 (2016).
- [130] Grosso, G., Moon, H., Lienhard, B., Ali, S., Efetov, D. K., Furchi, M. M. *et al.* Tunable and high-purity room temperature single-photon emission from atomic defects in hexagonal boron nitride. *Nature communications* **8**, 705 (2017).
- [131] O'brien, J. L. Optical quantum computing. *Science* **318**, 1567-1570 (2007).

- [132] Varnava, M., Browne, D. E. & Rudolph, T. How good must single photon sources and detectors be for efficient linear optical quantum computation? *Physical Review Letters* **100**, 060502 (2008).
- [133] Bennett, C. H., Brassard, G. & Mermin, N. D. Quantum cryptography without Bell's theorem. *Physical Review Letters* **68**, 557 (1992).
- [134] Gottesman, D., Lo, H.-K., Lutkenhaus, N. & Preskill, J. in *Information Theory, 2004. ISIT 2004. Proceedings. International Symposium on.* 136 (IEEE).
- [135] Mousavi, S. S. & Gallion, P. Decoy-state quantum key distribution using homodyne detection. *Phys Rev A* **80**, 012327 (2009).
- [136] Wrachtrup, J. 2D materials: Single photons at room temperature. *Nature nanotechnology* **11**, 7 (2016).
- [137] Ling, X., Wang, H., Huang, S., Xia, F. & Dresselhaus, M. S. The renaissance of black phosphorus. *Proceedings of the National Academy of Sciences* **112**, 4523-4530 (2015).
- [138] Kim, J., Baik, S. S., Ryu, S. H., Sohn, Y., Park, S., Park, B.-G. *et al.* Observation of tunable band gap and anisotropic Dirac semimetal state in black phosphorus. *Science* **349**, 723-726 (2015).
- [139] Rodin, A., Carvalho, A. & Neto, A. C. Strain-induced gap modification in black phosphorus. *Physical review letters* **112**, 176801 (2014).
- [140] Deng, B., Tran, V., Xie, Y., Jiang, H., Li, C., Guo, Q. *et al.* Efficient electrical control of thin-film black phosphorus bandgap. *Nature communications* **8**, 14474 (2017).
- [141] Yuan, H., Liu, X., Afshinmanesh, F., Li, W., Xu, G., Sun, J. *et al.* Polarization-sensitive broadband photodetector using a black phosphorus vertical p-n junction. *Nature nanotechnology* **10**, 707 (2015).
- [142] Guo, Q., Pospischil, A., Bhuiyan, M., Jiang, H., Tian, H., Farmer, D. *et al.* Black phosphorus mid-infrared photodetectors with high gain. *Nano letters* **16**, 4648-4655 (2016).
- [143] Low, T., Roldán, R., Wang, H., Xia, F., Avouris, P., Moreno, L. M. *et al.* Plasmons and screening in monolayer and multilayer black phosphorus. *Physical review letters* **113**, 106802 (2014).
- [144] Xia, F., Wang, H. & Jia, Y. Rediscovering black phosphorus as an anisotropic layered material for optoelectronics and electronics. *Nature communications* **5**, 4458 (2014).

- [145] Nemilentsau, A., Low, T. & Hanson, G. Anisotropic 2D materials for tunable hyperbolic plasmonics. *Physical review letters* **116**, 066804 (2016).
- [146] Liu, Z. & Aydin, K. Localized surface plasmons in nanostructured monolayer black phosphorus. *Nano letters* **16**, 3457-3462 (2016).
- [147] Xia, F., Wang, H., Xiao, D., Dubey, M. & Ramasubramaniam, A. Two-dimensional material nanophotonics. *Nature Photonics* **8**, 899 (2014).
- [148] Acerce, M., Voiry, D. & Chhowalla, M. Metallic 1T phase MoS<sub>2</sub> nanosheets as supercapacitor electrode materials. *Nature nanotechnology* **10**, 313 (2015).
- [149] Yin, X., Wang, Q., Cao, L., Tang, C. S., Luo, X., Zheng, Y. *et al.* Tunable inverted gap in monolayer quasi-metallic MoS<sub>2</sub> induced by strong charge-lattice coupling. *Nature communications* **8**, 486 (2017).
- [150] Wang, Q. H., Kalantar-Zadeh, K., Kis, A., Coleman, J. N. & Strano, M. S. Electronics and optoelectronics of two-dimensional transition metal dichalcogenides. *Nature nanotechnology* **7**, 699-712 (2012).
- [151] Mak, K. F. & Shan, J. Photonics and optoelectronics of 2D semiconductor transition metal dichalcogenides. *Nature Photonics* **10**, 216 (2016).
- [152] Manzeli, S., Allain, A., Ghadimi, A. & Kis, A. Piezoresistivity and strain-induced band gap tuning in atomically thin MoS<sub>2</sub>. *Nano letters* **15**, 5330-5335 (2015).
- [153] Chen, Y., Xi, J., Dumcenco, D. O., Liu, Z., Suenaga, K., Wang, D. *et al.* Tunable band gap photoluminescence from atomically thin transition-metal dichalcogenide alloys. *Acs Nano* **7**, 4610-4616 (2013).
- [154] Chu, T., Ilatikhameneh, H., Klimeck, G., Rahman, R. & Chen, Z. Electrically tunable bandgaps in bilayer MoS<sub>2</sub>. *Nano letters* **15**, 8000-8007 (2015).
- [155] Mak, K. F., Lee, C., Hone, J., Shan, J. & Heinz, T. F. Atomically thin MoS<sub>2</sub>: a new direct-gap semiconductor. *Physical review letters* **105**, 136805 (2010).
- [156] Wang, H., Zhang, C. & Rana, F. Ultrafast dynamics of defect-assisted electron-hole recombination in monolayer MoS<sub>2</sub>. *Nano letters* **15**, 339-345 (2014).
- [157] Amani, M., Lien, D.-H., Kiriya, D., Xiao, J., Azcatl, A., Noh, J. *et al.* Near-unity photoluminescence quantum yield in MoS<sub>2</sub>. *Science* **350**, 1065-1068 (2015).
- [158] Kim, H., Lien, D.-H., Amani, M., Ager, J. W. & Javey, A. Highly Stable Near-Unity Photoluminescence Yield in Monolayer MoS<sub>2</sub> by Fluoropolymer Encapsulation and Superacid Treatment. *ACS nano* **11**, 5179-5185 (2017).
- [159] Yin, Z., Li, H., Li, H., Jiang, L., Shi, Y., Sun, Y. *et al.* Single-layer MoS<sub>2</sub> phototransistors. *ACS nano* **6**, 74-80 (2011).

- [160] Lee, H. S., Min, S.-W., Chang, Y.-G., Park, M. K., Nam, T., Kim, H. *et al.* MoS<sub>2</sub> nanosheet phototransistors with thickness-modulated optical energy gap. *Nano letters* **12**, 3695-3700 (2012).
- [161] Baugher, B. W., Churchill, H. O., Yang, Y. & Jarillo-Herrero, P. Optoelectronic devices based on electrically tunable p–n diodes in a monolayer dichalcogenide. *Nature nanotechnology* **9**, 262 (2014).
- [162] Pospischil, A., Furchi, M. M. & Mueller, T. Solar-energy conversion and light emission in an atomic monolayer pn diode. *Nature nanotechnology* **9**, 257-261 (2014).
- [163] Sundaram, R., Engel, M., Lombardo, A., Krupke, R., Ferrari, A., Avouris, P. *et al.* Electroluminescence in single layer MoS<sub>2</sub>. *Nano letters* **13**, 1416-1421 (2013).
- [164] Cheng, R., Li, D., Zhou, H., Wang, C., Yin, A., Jiang, S. *et al.* Electroluminescence and photocurrent generation from atomically sharp WSe<sub>2</sub>/MoS<sub>2</sub> heterojunction p–n diodes. *Nano letters* **14**, 5590-5597 (2014).
- [165] Wang, Z., Dong, Z., Gu, Y., Chang, Y.-H., Zhang, L., Li, L.-J. *et al.* Giant photoluminescence enhancement in tungsten-diselenide–gold plasmonic hybrid structures. *Nature communications* **7**, 11283 (2016).
- [166] Galfsky, T., Sun, Z., Considine, C. R., Chou, C.-T., Ko, W.-C., Lee, Y.-H. *et al.* Broadband enhancement of spontaneous emission in two-dimensional semiconductors using photonic hypercrystals. *Nano letters* **16**, 4940-4945 (2016).
- [167] Reed, J. C., Zhu, A. Y., Zhu, H., Yi, F. & Cubukcu, E. Wavelength tunable microdisk cavity light source with a chemically enhanced MoS<sub>2</sub> emitter. *Nano letters* **15**, 1967-1971 (2015).
- [168] Jariwala, D., Davoyan, A. R., Tagliabue, G., Sherrott, M. C., Wong, J. & Atwater, H. A. Near-unity absorption in van der Waals semiconductors for ultrathin optoelectronics. *Nano letters* **16**, 5482-5487 (2016).
- [169] Ye, Y., Wong, Z. J., Lu, X., Ni, X., Zhu, H., Chen, X. *et al.* Monolayer excitonic laser. *Nature Photonics* **9**, 733 (2015).
- [170] Wu, S., Buckley, S., Schaibley, J. R., Feng, L., Yan, J., Mandrus, D. G. *et al.* Monolayer semiconductor nanocavity lasers with ultralow thresholds. *Nature* **520**, 69 (2015).
- [171] Salehzadeh, O., Djavid, M., Tran, N. H., Shih, I. & Mi, Z. Optically pumped two-dimensional MoS<sub>2</sub> lasers operating at room-temperature. *Nano letters* **15**, 5302-5306 (2015).

- [172] Chakraborty, C., Kinnischtzke, L., Goodfellow, K. M., Beams, R. & Vamivakas, A. N. Voltage-controlled quantum light from an atomically thin semiconductor. *Nature nanotechnology* **10**, 507 (2015).
- [173] He, Y.-M., Clark, G., Schaibley, J. R., He, Y., Chen, M.-C., Wei, Y.-J. *et al.* Single quantum emitters in monolayer semiconductors. *Nature nanotechnology* **10**, 497 (2015).
- [174] Koperski, M., Nogajewski, K., Arora, A., Cherkez, V., Mallet, P., Veuillen, J.-Y. *et al.* Single photon emitters in exfoliated WSe<sub>2</sub> structures. *Nature nanotechnology* **10**, 503-506 (2015).
- [175] Srivastava, A., Sidler, M., Allain, A. V., Lembke, D. S., Kis, A. & Imamoğlu, A. Optically active quantum dots in monolayer WSe<sub>2</sub>. *Nature nanotechnology* **10**, 491 (2015).
- [176] Xu, X., Yao, W., Xiao, D. & Heinz, T. F. Spin and pseudospins in layered transition metal dichalcogenides. *Nature Physics* **10**, 343 (2014).
- [177] Xiao, D., Liu, G.-B., Feng, W., Xu, X. & Yao, W. Coupled spin and valley physics in monolayers of MoS<sub>2</sub> and other group-VI dichalcogenides. *Physical Review Letters* **108**, 196802 (2012).
- [178] Mak, K. F., He, K., Shan, J. & Heinz, T. F. Control of valley polarization in monolayer MoS<sub>2</sub> by optical helicity. *Nature nanotechnology* **7**, 494 (2012).
- [179] Jones, A. M., Yu, H., Ghimire, N. J., Wu, S., Aivazian, G., Ross, J. S. *et al.* Optical generation of excitonic valley coherence in monolayer WSe<sub>2</sub>. *Nature nanotechnology* **8**, 634 (2013).
- [180] Yao, W., Xiao, D. & Niu, Q. Valley-dependent optoelectronics from inversion symmetry breaking. *Physical Review B* **77**, 235406 (2008).
- [181] Mak, K. F., McGill, K. L., Park, J. & McEuen, P. L. The valley Hall effect in MoS<sub>2</sub> transistors. *Science* **344**, 1489-1492 (2014).
- [182] Luo, Y. K., Xu, J., Zhu, T., Wu, G., McCormick, E. J., Zhan, W. *et al.* Opto-valleytronic spin injection in monolayer MoS<sub>2</sub>/Few-layer graphene hybrid spin valves. *Nano letters* **17**, 3877-3883 (2017).
- [183] Rycerz, A., Tworzydło, J. & Beenakker, C. Valley filter and valley valve in graphene. *Nature Physics* **3**, 172 (2007).
- [184] Yang, H., Kim, S. W., Chhowalla, M. & Lee, Y. H. Structural and quantum-state phase transitions in van der Waals layered materials. *Nature Physics* **13**, 931 (2017).

- [185] Duerloo, K.-A. N. & Reed, E. J. Structural phase transitions by design in monolayer alloys. *ACS nano* **10**, 289-297 (2015).
- [186] Conley, H. J., Wang, B., Ziegler, J. I., Haglund Jr, R. F., Pantelides, S. T. & Bolotin, K. I. Bandgap engineering of strained monolayer and bilayer MoS<sub>2</sub>. *Nano letters* **13**, 3626-3630 (2013).
- [187] Li, Y., Duerloo, K.-A. N., Wauson, K. & Reed, E. J. Structural semiconductor-to-semimetal phase transition in two-dimensional materials induced by electrostatic gating. *Nature communications* **7**, 10671 (2016).
- [188] Wang, Y., Xiao, J., Zhu, H., Li, Y., Alsaied, Y., Fong, K. Y. *et al.* Structural phase transition in monolayer MoTe<sub>2</sub> driven by electrostatic doping. *Nature* **550**, 487 (2017).
- [189] Kang, Y., Najmaei, S., Liu, Z., Bao, Y., Wang, Y., Zhu, X. *et al.* Plasmonic hot electron induced structural phase transition in a MoS<sub>2</sub> monolayer. *Advanced Materials* **26**, 6467-6471 (2014).
- [190] Chernikov, A., Ruppert, C., Hill, H. M., Rigosi, A. F. & Heinz, T. F. Population inversion and giant bandgap renormalization in atomically thin WS<sub>2</sub> layers. *Nature Photonics* **9**, 466 (2015).
- [191] Sipoš, B., Kusmartseva, A. F., Akrap, A., Berger, H., Forró, L. & Tutiš, E. From Mott state to superconductivity in 1T-TaS<sub>2</sub>. *Nature materials* **7**, 960 (2008).
- [192] Schuller, J. A., Zia, R., Taubner, T. & Brongersma, M. L. Dielectric metamaterials based on electric and magnetic resonances of silicon carbide particles. *Physical review letters* **99**, 107401 (2007).
- [193] Caldwell, J. D., Glembocki, O. J., Francescato, Y., Sharac, N., Giannini, V., Bezares, F. J. *et al.* Low-loss, extreme subdiffraction photon confinement via silicon carbide localized surface phonon polariton resonators. *Nano letters* **13**, 3690-3697 (2013).
- [194] Brown, L. V., Davanco, M., Sun, Z., Kretinin, A., Chen, Y., Matson, J. R. *et al.* Nanoscale mapping and spectroscopy of non-radiative hyperbolic modes in hexagonal boron nitride nanostructures. *arXiv preprint arXiv:1710.10285* (2017).
- [195] Weisbuch, C., Nishioka, M., Ishikawa, A. & Arakawa, Y. Observation of the coupled exciton-photon mode splitting in a semiconductor quantum microcavity. *Physical Review Letters* **69**, 3314 (1992).
- [196] Kasprzak, J., Richard, M., Kundermann, S., Baas, A., Jembrun, P., Keeling, J. *et al.* Bose–Einstein condensation of exciton polaritons. *Nature* **443**, 409 (2006).
- [197] Deng, H., Weihs, G., Santori, C., Bloch, J. & Yamamoto, Y. Condensation of semiconductor microcavity exciton polaritons. *Science* **298**, 199-202 (2002).

- [198] Yao, B., Gui, Y., Xiao, Y., Guo, H., Chen, X., Lu, W. *et al.* Theory and experiment on cavity magnon-polariton in the one-dimensional configuration. *Physical Review B* **92**, 184407 (2015).
- [199] Němec, P., Fiebig, M., Kampfrath, T. & Kimel, A. Antiferromagnetic optospintronics. *Nature Physics*, 1 (2018).
- [200] Laussy, F. P., Kavokin, A. V. & Shelykh, I. A. Exciton-polariton mediated superconductivity. *Physical review letters* **104**, 106402 (2010).
- [201] Houck, A. A., Türeci, H. E. & Koch, J. On-chip quantum simulation with superconducting circuits. *Nature Physics* **8**, 292 (2012).
- [202] Günter, G., Anappara, A. A., Hees, J., Sell, A., Biasiol, G., Sorba, L. *et al.* Sub-cycle switch-on of ultrastrong light–matter interaction. *Nature* **458**, 178 (2009).
- [203] Basov, D., Fogler, M. & de Abajo, F. G. Polaritons in van der Waals materials. *Science* **354**, aag1992 (2016).
- [204] Low, T., Chaves, A., Caldwell, J. D., Kumar, A., Fang, N. X., Avouris, P. *et al.* Polaritons in layered two-dimensional materials. *Nature materials* **16**, 182 (2017).
- [205] Dai, S., Fei, Z., Ma, Q., Rodin, A., Wagner, M., McLeod, A. *et al.* Tunable phonon polaritons in atomically thin van der Waals crystals of boron nitride. *Science* **343**, 1125-1129 (2014).
- [206] Hu, F., Luan, Y., Scott, M., Yan, J., Mandrus, D., Xu, X. *et al.* Imaging exciton–polariton transport in MoSe<sub>2</sub> waveguides. *Nature Photonics* **11**, 356 (2017).
- [207] Dufferwiel, S., Schwarz, S., Withers, F., Trichet, A., Li, F., Sich, M. *et al.* Exciton–polaritons in van der Waals heterostructures embedded in tunable microcavities. *Nature communications* **6**, 8579 (2015).
- [208] Lundt, N., Klemmt, S., Cherotchenko, E., Betzold, S., Iff, O., Nalitov, A. V. *et al.* Room-temperature Tamm-plasmon exciton-polaritons with a WSe<sub>2</sub> monolayer. *Nature communications* **7**, 13328 (2016).
- [209] Fei, Z., Scott, M., Gosztola, D., Foley IV, J., Yan, J., Mandrus, D. *et al.* Nano-optical imaging of WSe<sub>2</sub> waveguide modes revealing light-exciton interactions. *Physical Review B* **94**, 081402 (2016).
- [210] Liu, X., Bao, W., Li, Q., Ropp, C., Wang, Y. & Zhang, X. Control of coherently coupled exciton polaritons in monolayer Tungsten Disulphide. *Physical review letters* **119**, 027403 (2017).
- [211] Dai, S., Ma, Q., Liu, M., Andersen, T., Fei, Z., Goldflam, M. *et al.* Graphene on hexagonal boron nitride as a tunable hyperbolic metamaterial. *Nature nanotechnology* **10**, nNano.2015.2131 (2015).

- [212] Brar, V. W., Jang, M. S., Sherrott, M., Kim, S., Lopez, J. J., Kim, L. B. *et al.* Hybrid surface-phonon-plasmon polariton modes in graphene/monolayer h-BN heterostructures. *Nano letters* **14**, 3876-3880 (2014).
- [213] Fang, H., Chuang, S., Chang, T. C., Takei, K., Takahashi, T. & Javey, A. High-performance single layered WSe<sub>2</sub> p-FETs with chemically doped contacts. *Nano letters* **12**, 3788-3792 (2012).
- [214] Wang, H., Yu, L., Lee, Y.-H., Shi, Y., Hsu, A., Chin, M. L. *et al.* Integrated circuits based on bilayer MoS<sub>2</sub> transistors. *Nano letters* **12**, 4674-4680 (2012).
- [215] Rigosi, A. F., Hill, H. M., Rim, K. T., Flynn, G. W. & Heinz, T. F. Electronic band gaps and exciton binding energies in monolayer M<sub>o</sub> x W<sub>1-x</sub> S<sub>2</sub> transition metal dichalcogenide alloys probed by scanning tunneling and optical spectroscopy. *Physical Review B* **94**, 075440 (2016).
- [216] Ugeda, M. M., Bradley, A. J., Shi, S.-F., Felipe, H., Zhang, Y., Qiu, D. Y. *et al.* Giant bandgap renormalization and excitonic effects in a monolayer transition metal dichalcogenide semiconductor. *Nature materials* **13**, 1091 (2014).
- [217] Ye, Z., Cao, T., O'Brien, K., Zhu, H., Yin, X., Wang, Y. *et al.* Probing excitonic dark states in single-layer tungsten disulphide. *Nature* **513**, 214 (2014).
- [218] He, K., Kumar, N., Zhao, L., Wang, Z., Mak, K. F., Zhao, H. *et al.* Tightly bound excitons in monolayer WSe<sub>2</sub>. *Physical review letters* **113**, 026803 (2014).
- [219] Lagarde, D., Bouet, L., Marie, X., Zhu, C., Liu, B., Amand, T. *et al.* Carrier and polarization dynamics in monolayer MoS<sub>2</sub>. *Physical review letters* **112**, 047401 (2014).
- [220] Robert, C., Lagarde, D., Cadiz, F., Wang, G., Lassagne, B., Amand, T. *et al.* Exciton radiative lifetime in transition metal dichalcogenide monolayers. *Physical Review B* **93**, 205423 (2016).
- [221] Palummo, M., Bernardi, M. & Grossman, J. C. Exciton radiative lifetimes in two-dimensional transition metal dichalcogenides. *Nano letters* **15**, 2794-2800 (2015).
- [222] Gong, C., Zhang, H., Wang, W., Colombo, L., Wallace, R. M. & Cho, K. Band alignment of two-dimensional transition metal dichalcogenides: Application in tunnel field effect transistors. *Applied Physics Letters* **103**, 053513 (2013).
- [223] Yu, Y.-J., Zhao, Y., Ryu, S., Brus, L. E., Kim, K. S. & Kim, P. Tuning the graphene work function by electric field effect. *Nano letters* **9**, 3430-3434 (2009).
- [224] Gong, K., Zhang, L., Ji, W. & Guo, H. Electrical contacts to monolayer black phosphorus: A first-principles investigation. *Physical Review B* **90**, 125441 (2014).

- [225] Anker, J. N., Hall, W. P., Lyandres, O., Shah, N. C., Zhao, J. & Van Duyne, R. P. Biosensing with plasmonic nanosensors. *Nature materials* **7**, 442-453 (2008).
- [226] Lal, S., Link, S. & Halas, N. J. Nano-optics from sensing to waveguiding. *Nature photonics* **1**, 641-648 (2007).
- [227] Jain, P. K. & El-Sayed, M. A. Noble metal nanoparticle pairs: effect of medium for enhanced nanosensing. *Nano letters* **8**, 4347-4352 (2008).
- [228] Eustis, S. & El-Sayed, M. A. Why gold nanoparticles are more precious than pretty gold: noble metal surface plasmon resonance and its enhancement of the radiative and nonradiative properties of nanocrystals of different shapes. *Chemical society reviews* **35**, 209-217 (2006).
- [229] Nam, J.-M., Thaxton, C. S. & Mirkin, C. A. Nanoparticle-based bio-bar codes for the ultrasensitive detection of proteins. *science* **301**, 1884-1886 (2003).
- [230] Mahmoud, M. & El-Sayed, M. Aggregation of gold nanoframes reduces, rather than enhances, SERS efficiency due to the trade-off of the inter-and intraparticle plasmonic fields. *Nano letters* **9**, 3025-3031 (2009).
- [231] Mahmoud, M. & El-Sayed, M. Comparative study of the assemblies and the resulting plasmon fields of Langmuir– Blodgett assembled monolayers of silver nanocubes and gold nanocages. *The Journal of Physical Chemistry C* **112**, 14618-14625 (2008).
- [232] Schultz, S., Smith, D. R., Mock, J. J. & Schultz, D. A. Single-target molecule detection with nonbleaching multicolor optical immunolabels. *Proceedings of the National Academy of Sciences* **97**, 996-1001 (2000).
- [233] Huang, X., Neretina, S. & El-Sayed, M. A. Gold nanorods: from synthesis and properties to biological and biomedical applications. *Advanced Materials* **21**, 4880-4910 (2009).
- [234] Nikoobakht, B. & El-Sayed, M. A. Preparation and growth mechanism of gold nanorods (NRs) using seed-mediated growth method. *Chemistry of Materials* **15**, 1957-1962 (2003).
- [235] Jain, P. K., Huang, W. & El-Sayed, M. A. On the universal scaling behavior of the distance decay of plasmon coupling in metal nanoparticle pairs: a plasmon ruler equation. *Nano Letters* **7**, 2080-2088 (2007).
- [236] Hooshmand, N., Mousavi, H. S., Panikkanvalappil, S. R., Adibi, A. & El-Sayed, M. A. High-sensitivity molecular sensing using plasmonic nanocube chains in classical and quantum coupling regimes. *Nano Today* **17**, 14-22 (2017).

- [237] Theiss, J., Pavaskar, P., Echternach, P. M., Muller, R. E. & Cronin, S. B. Plasmonic nanoparticle arrays with nanometer separation for high-performance SERS substrates. *Nano letters* **10**, 2749-2754 (2010).
- [238] Nie, Z., Petukhova, A. & Kumacheva, E. Properties and emerging applications of self-assembled structures made from inorganic nanoparticles. *Nature nanotechnology* **5**, 15 (2010).
- [239] Macfarlane, R. J., Lee, B., Jones, M. R., Harris, N., Schatz, G. C. & Mirkin, C. A. Nanoparticle superlattice engineering with DNA. *science* **334**, 204-208 (2011).
- [240] Chou, L. Y., Zagorovsky, K. & Chan, W. C. DNA assembly of nanoparticle superstructures for controlled biological delivery and elimination. *Nature nanotechnology* **9**, 148-155 (2014).
- [241] Zhang, C., Macfarlane, R. J., Young, K. L., Choi, C. H. J., Hao, L., Auyeung, E. *et al.* A general approach to DNA-programmable atom equivalents. *Nature materials* **12**, 741 (2013).
- [242] Durr, N. J., Larson, T., Smith, D. K., Korgel, B. A., Sokolov, K. & Ben-Yakar, A. Two-photon luminescence imaging of cancer cells using molecularly targeted gold nanorods. *Nano letters* **7**, 941-945 (2007).
- [243] Cooper, M. A. Label-free screening of bio-molecular interactions. *Analytical and bioanalytical chemistry* **377**, 834-842 (2003).
- [244] Lequin, R. M. Enzyme immunoassay (EIA)/enzyme-linked immunosorbent assay (ELISA). *Clinical chemistry* **51**, 2415-2418 (2005).
- [245] Armani, A. M., Kulkarni, R. P., Fraser, S. E., Flagan, R. C. & Vahala, K. J. Label-free, single-molecule detection with optical microcavities. *science* **317**, 783-787 (2007).
- [246] Lu, T., Lee, H., Chen, T., Herchak, S., Kim, J.-H., Fraser, S. E. *et al.* High sensitivity nanoparticle detection using optical microcavities. *Proceedings of the National Academy of Sciences* **108**, 5976-5979 (2011).
- [247] Vollmer, F. & Arnold, S. Whispering-gallery-mode biosensing: label-free detection down to single molecules. *Nature methods* **5**, 591 (2008).
- [248] Georganopoulou, D. G., Chang, L., Nam, J.-M., Thaxton, C. S., Mufson, E. J., Klein, W. L. *et al.* Nanoparticle-based detection in cerebral spinal fluid of a soluble pathogenic biomarker for Alzheimer's disease. *Proceedings of the National Academy of Sciences of the United States of America* **102**, 2273-2276 (2005).
- [249] Haes, A. J., Chang, L., Klein, W. L. & Van Duyne, R. P. Detection of a biomarker for Alzheimer's disease from synthetic and clinical samples using a nanoscale

- optical biosensor. *Journal of the American Chemical Society* **127**, 2264-2271 (2005).
- [250] Brolo, A. G. Plasmonics for future biosensors. *Nature Photonics* **6**, 709 (2012).
- [251] Nakatani, K., Sando, S. & Saito, I. Scanning of guanine–guanine mismatches in DNA by synthetic ligands using surface plasmon resonance. *Nature biotechnology* **19**, 51 (2001).
- [252] Yonzon, C. R., Jeoung, E., Zou, S., Schatz, G. C., Mrksich, M. & Van Duyne, R. P. A comparative analysis of localized and propagating surface plasmon resonance sensors: the binding of concanavalin A to a monosaccharide functionalized self-assembled monolayer. *Journal of the American Chemical Society* **126**, 12669-12676 (2004).
- [253] Baaske, M. D., Foreman, M. R. & Vollmer, F. Single-molecule nucleic acid interactions monitored on a label-free microcavity biosensor platform. *Nature nanotechnology* **9**, 933 (2014).
- [254] Arnold, S., Khoshshima, M., Teraoka, I., Holler, S. & Vollmer, F. Shift of whispering-gallery modes in microspheres by protein adsorption. *Optics letters* **28**, 272-274 (2003).
- [255] Senlik, Ö., Tang, L., Tor-ngern, P. & Yoshie, T. Optical microcavities clad by low-absorption electrode media. *IEEE Photonics Journal* **2**, 794-801 (2010).
- [256] Rysselberghe, P. V. Remarks concerning the Clausius-Mossotti law. *The Journal of Physical Chemistry* **36**, 1152-1155 (1932).
- [257] Willets, K. A. & Van Duyne, R. P. Localized surface plasmon resonance spectroscopy and sensing. *Annu. Rev. Phys. Chem.* **58**, 267-297 (2007).
- [258] Kiel, M., Klötzer, M., Mitzscherling, S. & Bargheer, M. Measuring the range of plasmonic interaction. *Langmuir* **28**, 4800-4804 (2012).
- [259] Russell, K. J., Yeung, K. Y. & Hu, E. Measuring the mode volume of plasmonic nanocavities using coupled optical emitters. *Physical Review B* **85**, 245445 (2012).
- [260] Dahlin, A. B., Tegenfeldt, J. O. & Höök, F. Improving the instrumental resolution of sensors based on localized surface plasmon resonance. *Analytical chemistry* **78**, 4416-4423 (2006).
- [261] Bohren, C. F. & Huffman, D. R. *Absorption and scattering by a sphere*. (Wiley Online Library, 1983).

- [262] Sherry, L. J., Chang, S.-H., Schatz, G. C., Van Duyne, R. P., Wiley, B. J. & Xia, Y. Localized surface plasmon resonance spectroscopy of single silver nanocubes. *Nano Lett* **5**, 2034-2038 (2005).
- [263] Bordley, J. A., Hooshmand, N. & El-Sayed, M. A. The coupling between gold or silver nanocubes in their homo-dimers: a new coupling mechanism at short separation distances. *Nano letters* **15**, 3391-3397 (2015).
- [264] Mahmoud, M., Snyder, B. & El-Sayed, M. Surface plasmon fields and coupling in the hollow gold nanoparticles and surface-enhanced Raman spectroscopy. Theory and experiment. *The Journal of Physical Chemistry C* **114**, 7436-7443 (2010).
- [265] Mahmoud, M. A. & El-Sayed, M. A. Gold nanoframes: Very high surface plasmon fields and excellent near-infrared sensors. *Journal of the American Chemical Society* **132**, 12704-12710 (2010).
- [266] Tan, S. F., Wu, L., Yang, J. K., Bai, P., Bosman, M. & Nijhuis, C. A. Quantum plasmon resonances controlled by molecular tunnel junctions. *Science* **343**, 1496-1499 (2014).
- [267] Ward, D. R., Hüser, F., Pauly, F., Cuevas, J. C. & Natelson, D. Optical rectification and field enhancement in a plasmonic nanogap. *Nature nanotechnology* **5**, 732 (2010).
- [268] Savage, K. J., Hawkeye, M. M., Esteban, R., Borisov, A. G., Aizpurua, J. & Baumberg, J. J. Revealing the quantum regime in tunnelling plasmonics. *Nature* **491**, 574-577 (2012).
- [269] Scholl, J. A., García-Etxarri, A., Koh, A. L. & Dionne, J. A. Observation of quantum tunneling between two plasmonic nanoparticles. *Nano letters* **13**, 564-569 (2013).
- [270] Mortensen, N. A., Raza, S., Wubs, M., Søndergaard, T. & Bozhevolnyi, S. I. A generalized non-local optical response theory for plasmonic nanostructures. *Nature communications* **5**, 3809 (2014).
- [271] Christensen, T., Yan, W., Jauho, A.-P., Soljačić, M. & Mortensen, N. A. Quantum corrections in nanoplasmonics: shape, scale, and material. *Physical review letters* **118**, 157402 (2017).
- [272] Lambe, J. & McCarthy, S. Light emission from inelastic electron tunneling. *Physical Review Letters* **37**, 923 (1976).
- [273] Parzefall, M., Bharadwaj, P., Jain, A., Taniguchi, T., Watanabe, K. & Novotny, L. Antenna-coupled photon emission from hexagonal boron nitride tunnel junctions. *Nature nanotechnology* **10**, 1058-1063 (2015).

- [274] Berndt, R., Gimzewski, J. K. & Johansson, P. Inelastic tunneling excitation of tip-induced plasmon modes on noble-metal surfaces. *Physical review letters* **67**, 3796 (1991).
- [275] Gurunaryanan, S. P., Verellen, N., Zharinov, V. S., James Shirley, F., Moshchalkov, V. V., Heyns, M. *et al.* Electrically driven unidirectional optical nanoantennas. *Nano letters* (2017).
- [276] Lerch, S. & Reinhard, B. M. Quantum Plasmonics: Optical Monitoring of DNA-Mediated Charge Transfer in Plasmon Rulers. *Advanced Materials* **28**, 2030-2036 (2016).
- [277] Lim, D.-K., Jeon, K.-S., Hwang, J.-H., Kim, H., Kwon, S., Suh, Y. D. *et al.* Highly uniform and reproducible surface-enhanced Raman scattering from DNA-tailorable nanoparticles with 1-nm interior gap. *Nature nanotechnology* **6**, 452 (2011).
- [278] Thacker, V. V., Herrmann, L. O., Sigle, D. O., Zhang, T., Liedl, T., Baumberg, J. J. *et al.* DNA origami based assembly of gold nanoparticle dimers for surface-enhanced Raman scattering. *Nature communications* **5**, 3448 (2014).
- [279] Zhu, W., Esteban, R., Borisov, A. G., Baumberg, J. J., Nordlander, P., Lezec, H. J. *et al.* Quantum mechanical effects in plasmonic structures with subnanometre gaps. *Nature communications* **7**, 11495 (2016).
- [280] Esteban, R., Borisov, A. G., Nordlander, P. & Aizpurua, J. Bridging quantum and classical plasmonics with a quantum-corrected model. *Nature communications* **3**, 825 (2012).
- [281] Kelly, K. L., Coronado, E., Zhao, L. L. & Schatz, G. C. The Optical Properties of Metal Nanoparticles: The Influence of Size, Shape, and Dielectric Environment. *The Journal of Physical Chemistry B* **107**, 668-677, doi:10.1021/jp026731y (2002).
- [282] Tan, S. F., Wu, L., Yang, J. K. W., Bai, P., Bosman, M. & Nijhuis, C. A. Quantum Plasmon Resonances Controlled by Molecular Tunnel Junctions. *Science* **343**, 1496-1499, doi:10.1126/science.1248797 (2014).
- [283] Gniadecka, M., Philipsen, P. A., Sigurdsson, S., Wessel, S., Nielsen, O. F., Christensen, D. H. *et al.* Melanoma diagnosis by Raman spectroscopy and neural networks: structure alterations in proteins and lipids in intact cancer tissue. *Journal of Investigative Dermatology* **122**, 443-449 (2004).
- [284] Krafft, C., Steiner, G., Beleites, C. & Salzer, R. Disease recognition by infrared and Raman spectroscopy. *Journal of biophotonics* **2**, 13-28 (2009).

- [285] Kendall, C., Isabelle, M., Bazant-Hegemark, F., Hutchings, J., Orr, L., Babrah, J. *et al.* Vibrational spectroscopy: a clinical tool for cancer diagnostics. *Analyst* **134**, 1029-1045 (2009).
- [286] Brozek-Pluska, B., Musial, J., Kordek, R., Bailo, E., Dieing, T. & Abramczyk, H. Raman spectroscopy and imaging: applications in human breast cancer diagnosis. *Analyst* **137**, 3773-3780 (2012).
- [287] Evans, C. L. & Xie, X. S. Coherent anti-Stokes Raman scattering microscopy: chemical imaging for biology and medicine. *Annu. Rev. Anal. Chem.* **1**, 883-909 (2008).
- [288] Camp Jr, C. H., Lee, Y. J., Heddleston, J. M., Hartshorn, C. M., Walker, A. R. H., Rich, J. N. *et al.* High-speed coherent Raman fingerprint imaging of biological tissues. *Nature photonics* **8**, 627 (2014).
- [289] Lu, W., Singh, A. K., Khan, S. A., Senapati, D., Yu, H. & Ray, P. C. Gold nanopopcorn-based targeted diagnosis, nanotherapy treatment, and in situ monitoring of photothermal therapy response of prostate cancer cells using surface-enhanced Raman spectroscopy. *Journal of the American Chemical Society* **132**, 18103-18114 (2010).
- [290] Porter, M. D., Lipert, R. J., Siperko, L. M., Wang, G. & Narayanan, R. SERS as a bioassay platform: fundamentals, design, and applications. *Chemical Society Reviews* **37**, 1001-1011 (2008).
- [291] Haynes, C. L., McFarland, A. D. & Duyne, R. P. V. (ACS Publications, 2005).
- [292] Nie, S. & Emory, S. R. Probing single molecules and single nanoparticles by surface-enhanced Raman scattering. *science* **275**, 1102-1106 (1997).
- [293] Xu, H., Bjerneld, E. J., Käll, M. & Börjesson, L. Spectroscopy of single hemoglobin molecules by surface enhanced Raman scattering. *Physical review letters* **83**, 4357 (1999).
- [294] Kneipp, K., Kneipp, H., Itzkan, I., Dasari, R. R. & Feld, M. S. Ultrasensitive chemical analysis by Raman spectroscopy. *Chemical reviews* **99**, 2957-2976 (1999).
- [295] Zhang, Y., Zhen, Y.-R., Neumann, O., Day, J. K., Nordlander, P. & Halas, N. J. Coherent anti-Stokes Raman scattering with single-molecule sensitivity using a plasmonic Fano resonance. *Nature communications* **5**, 4424 (2014).
- [296] Yampolsky, S., Fishman, D. A., Dey, S., Hulkko, E., Banik, M., Potma, E. O. *et al.* Seeing a single molecule vibrate through time-resolved coherent anti-Stokes Raman scattering. *Nature Photonics* **8**, 650 (2014).

- [297] Steuwe, C., Kaminski, C. F., Baumberg, J. J. & Mahajan, S. Surface enhanced coherent anti-Stokes Raman scattering on nanostructured gold surfaces. *Nano letters* **11**, 5339-5343 (2011).
- [298] Osawa, M. Dynamic processes in electrochemical reactions studied by surface-enhanced infrared absorption spectroscopy (SEIRAS). *Bulletin of the Chemical Society of Japan* **70**, 2861-2880 (1997).
- [299] Le, F., Brandl, D. W., Urzhumov, Y. A., Wang, H., Kundu, J., Halas, N. J. *et al.* Metallic nanoparticle arrays: a common substrate for both surface-enhanced Raman scattering and surface-enhanced infrared absorption. *ACS nano* **2**, 707-718 (2008).
- [300] Auguie, B. & Barnes, W. L. Collective resonances in gold nanoparticle arrays. *Physical review letters* **101**, 143902 (2008).
- [301] Giannini, V., Vecchi, G. & Rivas, J. G. Lighting up multipolar surface plasmon polaritons by collective resonances in arrays of nanoantennas. *Physical review letters* **105**, 266801 (2010).
- [302] Fano, U. Effects of configuration interaction on intensities and phase shifts. *Physical Review* **124**, 1866 (1961).
- [303] Hessel, A. & Oliner, A. A new theory of Wood's anomalies on optical gratings. *Applied optics* **4**, 1275-1297 (1965).
- [304] Xu, Q., Sandhu, S., Povinelli, M. L., Shakya, J., Fan, S. & Lipson, M. Experimental realization of an on-chip all-optical analogue to electromagnetically induced transparency. *Physical review letters* **96**, 123901 (2006).
- [305] Fan, S. & Joannopoulos, J. Analysis of guided resonances in photonic crystal slabs. *Physical Review B* **65**, 235112 (2002).
- [306] Fan, P., Yu, Z., Fan, S. & Brongersma, M. L. Optical Fano resonance of an individual semiconductor nanostructure. *Nature materials* **13**, 471 (2014).
- [307] Fedotov, V., Rose, M., Prosvirnin, S., Papasimakis, N. & Zheludev, N. Sharp trapped-mode resonances in planar metamaterials with a broken structural symmetry. *Physical review letters* **99**, 147401 (2007).
- [308] Liu, N., Langguth, L., Weiss, T., Kästel, J., Fleischhauer, M., Pfau, T. *et al.* Plasmonic analogue of electromagnetically induced transparency at the Drude damping limit. *Nature materials* **8**, 758 (2009).
- [309] Stuart, H. R. & Hall, D. G. Enhanced dipole-dipole interaction between elementary radiators near a surface. *Physical Review Letters* **80**, 5663 (1998).

- [310] Lamprecht, B., Schider, G., Lechner, R., Ditlbacher, H., Krenn, J., Leitner, A. *et al.* Metal nanoparticle gratings: influence of dipolar particle interaction on the plasmon resonance. *Physical review letters* **84**, 4721 (2000).
- [311] Chu, Y., Schonbrun, E., Yang, T. & Crozier, K. B. Experimental observation of narrow surface plasmon resonances in gold nanoparticle arrays. *Applied Physics Letters* **93**, 181108 (2008).
- [312] Hicks, E. M., Zou, S., Schatz, G. C., Spears, K. G., Van Duyne, R. P., Gunnarsson, L. *et al.* Controlling plasmon line shapes through diffractive coupling in linear arrays of cylindrical nanoparticles fabricated by electron beam lithography. *Nano letters* **5**, 1065-1070 (2005).
- [313] Yanik, A. A., Cetin, A. E., Huang, M., Artar, A., Mousavi, S. H., Khanikaev, A. *et al.* Seeing protein monolayers with naked eye through plasmonic Fano resonances. *Proceedings of the National Academy of Sciences* **108**, 11784-11789 (2011).
- [314] Stewart, M. E., Mack, N. H., Malyarchuk, V., Soares, J. A., Lee, T.-W., Gray, S. K. *et al.* Quantitative multispectral biosensing and 1D imaging using quasi-3D plasmonic crystals. *Proceedings of the National Academy of Sciences* **103**, 17143-17148 (2006).
- [315] Zhou, W. & Odom, T. W. Tunable subradiant lattice plasmons by out-of-plane dipolar interactions. *Nature nanotechnology* **6**, 423-427 (2011).
- [316] Vakevainen, A., Moerland, R., Rekola, H., Eskelinen, A.-P., Martikainen, J.-P., Kim, D.-H. *et al.* Plasmonic surface lattice resonances at the strong coupling regime. *Nano letters* **14**, 1721-1727 (2013).
- [317] Purcell, E. Proceedings of the american physical society. *Phys. Rev* **69**, 674-674 (1946).
- [318] Xu, Y., Lee, R. K. & Yariv, A. Quantum analysis and the classical analysis of spontaneous emission in a microcavity. *Physical Review A* **61**, 033807 (2000).
- [319] Talley, C. E., Jackson, J. B., Oubre, C., Grady, N. K., Hollars, C. W., Lane, S. M. *et al.* Surface-enhanced Raman scattering from individual Au nanoparticles and nanoparticle dimer substrates. *Nano letters* **5**, 1569-1574 (2005).
- [320] Jackson, J., Westcott, S., Hirsch, L., West, J. & Halas, N. Controlling the surface enhanced Raman effect via the nanoshell geometry. *Applied Physics Letters* **82**, 257-259 (2003).
- [321] Li, J. F., Huang, Y. F., Ding, Y., Yang, Z. L., Li, S. B., Zhou, X. S. *et al.* Shell-isolated nanoparticle-enhanced Raman spectroscopy. *nature* **464**, 392-395 (2010).

- [322] Zhou, W., Dridi, M., Suh, J. Y., Kim, C. H., Co, D. T., Wasielewski, M. R. *et al.* Lasing action in strongly coupled plasmonic nanocavity arrays. *Nature nanotechnology* **8**, 506-511 (2013).
- [323] Schuck, P., Fromm, D., Sundaramurthy, A., Kino, G. & Moerner, W. Improving the mismatch between light and nanoscale objects with gold bowtie nanoantennas. *Physical review letters* **94**, 017402 (2005).
- [324] Kinkhabwala, A., Yu, Z., Fan, S., Avlasevich, Y., Müllen, K. & Moerner, W. Large single-molecule fluorescence enhancements produced by a bowtie nanoantenna. *Nature Photonics* **3**, 654 (2009).
- [325] Fromm, D. P., Sundaramurthy, A., Schuck, P. J., Kino, G. & Moerner, W. Gap-dependent optical coupling of single “bowtie” nanoantennas resonant in the visible. *Nano letters* **4**, 957-961 (2004).
- [326] Galarreta, B. C., Norton, P. R. & Lagugné-Labarthe, F. o. SERS detection of streptavidin/biotin monolayer assemblies. *Langmuir* **27**, 1494-1498 (2011).
- [327] Berova, N. & Nakanishi, K. *Circular dichroism: principles and applications*. (John Wiley & Sons, 2000).
- [328] Nordén, B. *Circular dichroism and linear dichroism*. Vol. 1 (Oxford University Press, USA, 1997).
- [329] Fasman, G. D. *Circular dichroism and the conformational analysis of biomolecules*. (Springer Science & Business Media, 2013).
- [330] Jaouen, G. & Salmain, M. *Bioorganometallic chemistry: Applications in drug discovery, biocatalysis, and imaging*. (John Wiley & Sons, 2015).
- [331] Dougan, S. J., Habtemariam, A., McHale, S. E., Parsons, S. & Sadler, P. J. Catalytic organometallic anticancer complexes. *Proceedings of the National Academy of Sciences* **105**, 11628-11633 (2008).
- [332] Chen, H., Parkinson, J. A., Nováková, O., Bella, J., Wang, F., Dawson, A. *et al.* Induced-fit recognition of DNA by organometallic complexes with dynamic stereogenic centers. *Proceedings of the National Academy of Sciences* **100**, 14623-14628 (2003).
- [333] Beeren, S. R. & Sanders, J. K. Ferrocene-amino acid macrocycles as hydrazone-based receptors for anions. *Chemical Science* **2**, 1560-1567 (2011).
- [334] Tischler, N., Fernandez-Corbaton, I., Zambrana-Puyalto, X., Minovich, A., Vidal, X., Juan, M. L. *et al.* Experimental control of optical helicity in nanophotonics. *Light: Science and Applications* **3**, e183 (2014).

- [335] Tang, Y. & Cohen, A. E. Enhanced enantioselectivity in excitation of chiral molecules by superchiral light. *Science* **332**, 333-336 (2011).
- [336] Tang, Y. & Cohen, A. E. Optical chirality and its interaction with matter. *Physical review letters* **104**, 163901 (2010).
- [337] Zheng, Z.-g., Li, Y., Bisoyi, H. K., Wang, L., Bunning, T. J. & Li, Q. Three-dimensional control of the helical axis of a chiral nematic liquid crystal by light. *Nature* **531**, 352-356 (2016).
- [338] Zhao, Y., Belkin, M. & Alù, A. Twisted optical metamaterials for planarized ultrathin broadband circular polarizers. *Nature communications* **3**, 870 (2012).
- [339] Turner, M. D., Saba, M., Zhang, Q., Cumming, B. P., Schröder-Turk, G. E. & Gu, M. Miniature chiral beamsplitter based on gyroid photonic crystals. *Nature Photonics* **7**, 801-805 (2013).
- [340] Gansel, J. K., Thiel, M., Rill, M. S., Decker, M., Bade, K., Saile, V. *et al.* Gold helix photonic metamaterial as broadband circular polarizer. *Science* **325**, 1513-1515 (2009).
- [341] Karimi, E., Schulz, S. A., De Leon, I., Qassim, H., Upham, J. & Boyd, R. W. Generating optical orbital angular momentum at visible wavelengths using a plasmonic metasurface. *Light: Science and Applications* **3**, e167 (2014).
- [342] Li, G., Kang, M., Chen, S., Zhang, S., Pun, E. Y.-B., Cheah, K. W. *et al.* Spin-enabled plasmonic metasurfaces for manipulating orbital angular momentum of light. *Nano letters* **13**, 4148-4151 (2013).
- [343] Kildishev, A. V., Boltasseva, A. & Shalaev, V. M. Planar photonics with metasurfaces. *Science* **339**, 1232009 (2013).
- [344] Shitrit, N., Yulevich, I., Maguid, E., Ozeri, D., Veksler, D., Kleiner, V. *et al.* Spin-optical metamaterial route to spin-controlled photonics. *Science* **340**, 724-726 (2013).
- [345] Poulidakos, L. V., Thureja, P., Stollmann, A., De Leo, E. & Norris, D. J. Chiral Light Design and Detection Inspired by Optical Antenna Theory. *Nano letters* (2018).
- [346] Li, W., Coppens, Z. J., Besteiro, L. V., Wang, W., Govorov, A. O. & Valentine, J. Circularly polarized light detection with hot electrons in chiral plasmonic metamaterials. *Nature communications* **6**, 8379 (2015).
- [347] Rodrigues, S. P., Cui, Y., Lan, S., Kang, L. & Cai, W. Metamaterials Enable Chiral-Selective Enhancement of Two-Photon Luminescence from Quantum Emitters. *Advanced Materials* **27**, 1124-1130 (2015).

- [348] Li, Z., Li, Y., Han, T., Wang, X., Yu, Y., Tay, B. *et al.* Tailoring MoS<sub>2</sub> Exciton–Plasmon Interaction by Optical Spin–Orbit Coupling. *ACS nano* **11**, 1165-1171 (2016).
- [349] Meinzer, N., Hendry, E. & Barnes, W. L. Probing the chiral nature of electromagnetic fields surrounding plasmonic nanostructures. *Physical Review B* **88**, 041407 (2013).
- [350] Yin, P., Tan, Y., Fang, H., Hegde, M. & Radovanovic, P. V. Plasmon-induced carrier polarization in semiconductor nanocrystals. *Nature nanotechnology*, 1 (2018).
- [351] Yin, X., Schäferling, M., Metzger, B. & Giessen, H. Interpreting chiral nanophotonic spectra: the plasmonic Born–Kuhn model. *Nano letters* **13**, 6238-6243 (2013).
- [352] García-Etxarri, A. & Dionne, J. A. Surface-enhanced circular dichroism spectroscopy mediated by nonchiral nanoantennas. *Physical Review B* **87**, 235409 (2013).
- [353] Tullius, R., Karimullah, A. S., Rodier, M., Fitzpatrick, B., Gadegaard, N., Barron, L. D. *et al.* “Superchiral” spectroscopy: detection of protein higher order hierarchical structure with chiral plasmonic nanostructures. *Journal of the American Chemical Society* **137**, 8380-8383 (2015).
- [354] Papakostas, A., Potts, A., Bagnall, D., Prosvirnin, S., Coles, H. & Zheludev, N. Optical manifestations of planar chirality. *Phys Rev Lett* **90**, 107404 (2003).
- [355] Kuwata-Gonokami, M., Saito, N., Ino, Y., Kauranen, M., Jefimovs, K., Vallius, T. *et al.* Giant optical activity in quasi-two-dimensional planar nanostructures. *Phys Rev Lett* **95**, 227401 (2005).
- [356] Lu, F., Tian, Y., Liu, M., Su, D., Zhang, H., Govorov, A. O. *et al.* Discrete nanocubes as plasmonic reporters of molecular chirality. *Nano letters* **13**, 3145-3151 (2013).
- [357] Zhu, Z., Liu, W., Li, Z., Han, B., Zhou, Y., Gao, Y. *et al.* Manipulation of collective optical activity in one-dimensional plasmonic assembly. *ACS nano* **6**, 2326-2332 (2012).
- [358] Maoz, B. M., Chaikin, Y., Tesler, A. B., Bar Elli, O., Fan, Z., Govorov, A. O. *et al.* Amplification of chiroptical activity of chiral biomolecules by surface plasmons. *Nano letters* **13**, 1203-1209 (2013).
- [359] Quidant, R. & Kreuzer, M. Biosensing: Plasmons offer a helping hand. *Nature nanotechnology* **5**, 762-763 (2010).

- [360] Valev, V. K., Baumberg, J., De Clercq, B., Braz, N., Zheng, X., Osley, E. *et al.* Nonlinear superchiral meta-surfaces: Tuning chirality and disentangling non-reciprocity at the nanoscale. *Advanced Materials* **26**, 4074-4081 (2014).
- [361] Kuzyk, A., Schreiber, R., Fan, Z., Pardatscher, G., Roller, E.-M., Högele, A. *et al.* DNA-based self-assembly of chiral plasmonic nanostructures with tailored optical response. *Nature* **483**, 311-314 (2012).
- [362] Fan, Z. & Govorov, A. O. Plasmonic circular dichroism of chiral metal nanoparticle assemblies. *Nano letters* **10**, 2580-2587 (2010).
- [363] Hentschel, M., Schäferling, M., Weiss, T., Liu, N. & Giessen, H. Three-dimensional chiral plasmonic oligomers. *Nano letters* **12**, 2542-2547 (2012).
- [364] Cui, Y., Kang, L., Lan, S., Rodrigues, S. & Cai, W. Giant chiral optical response from a twisted-arc metamaterial. *Nano letters* **14**, 1021-1025 (2014).
- [365] Liu, N., Guo, H., Fu, L., Kaiser, S., Schweizer, H. & Giessen, H. Three-dimensional photonic metamaterials at optical frequencies. *Nature materials* **7**, 31-37 (2008).
- [366] Adato, R., Yanik, A. A., Amsden, J. J., Kaplan, D. L., Omenetto, F. G., Hong, M. K. *et al.* Ultra-sensitive vibrational spectroscopy of protein monolayers with plasmonic nanoantenna arrays. *Proceedings of the National Academy of Sciences* **106**, 19227-19232 (2009).
- [367] Rogacheva, A., Fedotov, V., Schwanecke, A. & Zheludev, N. Giant gyrotropy due to electromagnetic-field coupling in a bilayered chiral structure. *Physical review letters* **97**, 177401 (2006).
- [368] Lan, X., Lu, X., Shen, C., Ke, Y., Ni, W. & Wang, Q. Au nanorod helical superstructures with designed chirality. *Journal of the American Chemical Society* **137**, 457-462 (2014).
- [369] García-Meca, C., Hurtado, J., Martí, J., Martínez, A., Dickson, W. & Zayats, A. V. Low-loss multilayered metamaterial exhibiting a negative index of refraction at visible wavelengths. *Physical review letters* **106**, 067402 (2011).
- [370] Zhao, Y., Shi, J., Sun, L., Li, X. & Alù, A. Alignment-Free Three-Dimensional Optical Metamaterials. *Advanced Materials* **26**, 1439-1445 (2014).
- [371] Shams Mousavi, S. H., Eftekhari, A. A., Atabaki, A. H. & Adibi, A. Band-edge bilayer plasmonic nanostructure for surface enhanced Raman spectroscopy. *Acs Photonics* **2**, 1546-1551 (2015).
- [372] Fedotov, V., Mladyonov, P., Prosvirnin, S., Rogacheva, A., Chen, Y. & Zheludev, N. Asymmetric propagation of electromagnetic waves through a planar chiral structure. *Physical review letters* **97**, 167401 (2006).

- [373] Chen, S., Li, G., Zeuner, F., Wong, W. H., Pun, E. Y. B., Zentgraf, T. *et al.* Symmetry-selective third-harmonic generation from plasmonic metacrystals. *Physical review letters* **113**, 033901 (2014).
- [374] Blout, E. & Stryer, L. Anomalous optical rotatory dispersion of dye: polypeptide complexes. *Proceedings of the National Academy of Sciences* **45**, 1591-1593 (1959).
- [375] Ma, W., Kuang, H., Xu, L., Ding, L., Xu, C., Wang, L. *et al.* Attomolar DNA detection with chiral nanorod assemblies. *Nature communications* **4**, 2689 (2013).
- [376] Mark, A. G., Gibbs, J. G., Lee, T.-C. & Fischer, P. Hybrid nanocolloids with programmed three-dimensional shape and material composition. *Nature materials* **12**, 802 (2013).
- [377] Fan, Z. & Govorov, A. O. Chiral nanocrystals: plasmonic spectra and circular dichroism. *Nano letters* **12**, 3283-3289 (2012).
- [378] Thomas, L. L., Kim, J. H. & Cotton, T. M. Comparative study of resonance Raman and surface-enhanced resonance Raman chlorophyll a spectra using Soret and red excitation. *Journal of the American Chemical Society* **112**, 9378-9386 (1990).
- [379] Scholes, G. D., Fleming, G. R., Olaya-Castro, A. & Van Grondelle, R. Lessons from nature about solar light harvesting. *Nature chemistry* **3**, 763 (2011).
- [380] Zhao, L., Qi, D., Wang, K., Wang, T., Han, B., Tang, Z. *et al.* Integration of inherent and induced chirality into subphthalocyanine analogue. *Scientific reports* **6**, 28026 (2016).
- [381] Petty, M. C. *Langmuir-Blodgett films: an introduction*. (Cambridge University Press, 1996).
- [382] Wu, S. & El-Sayed, M. A. CD spectrum of bacteriorhodopsin: best evidence against exciton model. *Biophysical journal* **60**, 190-197 (1991).
- [383] Boyden, E. S., Zhang, F., Bamberg, E., Nagel, G. & Deisseroth, K. Millisecond-timescale, genetically targeted optical control of neural activity. *Nature neuroscience* **8**, 1263 (2005).
- [384] Zhang, F., Wang, L.-P., Boyden, E. S. & Deisseroth, K. Channelrhodopsin-2 and optical control of excitable cells. *Nature methods* **3**, 785 (2006).
- [385] El-Sayed, M., Lin, C. & Mason, W. Is there an excitonic interaction or antenna system in bacteriorhodopsin? *Proceedings of the National Academy of Sciences* **86**, 5376-5379 (1989).

- [386] Pescitelli, G., Kato, H. E., Oishi, S., Ito, J., Maturana, A. s. D., Nureki, O. *et al.* Exciton circular dichroism in channelrhodopsin. *The Journal of Physical Chemistry B* **118**, 11873-11885 (2014).
- [387] Scalora, M., Dowling, J. P., Bowden, C. M. & Bloemer, M. J. Optical limiting and switching of ultrashort pulses in nonlinear photonic band gap materials. *Physical review letters* **73**, 1368 (1994).
- [388] Steinmeyer, G., Sutter, D., Gallmann, L., Matuschek, N. & Keller, U. Frontiers in ultrashort pulse generation: pushing the limits in linear and nonlinear optics. *Science* **286**, 1507-1512 (1999).
- [389] Silberhorn, C., Lam, P. K., Weiss, O., König, F., Korolkova, N. & Leuchs, G. Generation of continuous variable Einstein-Podolsky-Rosen entanglement via the Kerr nonlinearity in an optical fiber. *Physical Review Letters* **86**, 4267 (2001).
- [390] Foster, M. A., Turner, A. C., Sharping, J. E., Schmidt, B. S., Lipson, M. & Gaeta, A. L. Broad-band optical parametric gain on a silicon photonic chip. *Nature* **441**, 960 (2006).
- [391] Koos, C., Vorreau, P., Vallaitis, T., Dumon, P., Bogaerts, W., Baets, R. *et al.* All-optical high-speed signal processing with silicon-organic hybrid slot waveguides. *Nature photonics* **3**, 216 (2009).
- [392] Del'Haye, P., Schliesser, A., Arcizet, O., Wilken, T., Holzwarth, R. & Kippenberg, T. J. Optical frequency comb generation from a monolithic microresonator. *Nature* **450**, 1214 (2007).
- [393] Dudley, J. M., Genty, G. & Coen, S. Supercontinuum generation in photonic crystal fiber. *Reviews of modern physics* **78**, 1135 (2006).
- [394] Herrmann, J., Griebner, U., Zhavoronkov, N., Husakou, A., Nickel, D., Knight, J. *et al.* Experimental evidence for supercontinuum generation by fission of higher-order solitons in photonic fibers. *Physical Review Letters* **88**, 173901 (2002).
- [395] Zhang, J., Lin, Q., Piredda, G., Boyd, R. W., Agrawal, G. P. & Fauchet, P. M. Optical solitons in a silicon waveguide. *Optics Express* **15**, 7682-7688 (2007).
- [396] Herr, T., Brasch, V., Jost, J. D., Wang, C. Y., Kondratiev, N. M., Gorodetsky, M. L. *et al.* Temporal solitons in optical microresonators. *Nature Photonics* **8**, 145 (2014).
- [397] Zoumi, A., Yeh, A. & Tromberg, B. J. Imaging cells and extracellular matrix in vivo by using second-harmonic generation and two-photon excited fluorescence. *Proceedings of the National Academy of Sciences* **99**, 11014-11019 (2002).

- [398] Campagnola, P. J. & Loew, L. M. Second-harmonic imaging microscopy for visualizing biomolecular arrays in cells, tissues and organisms. *Nature biotechnology* **21**, 1356-1360 (2003).
- [399] Freudiger, C. W., Min, W., Saar, B. G., Lu, S., Holtom, G. R., He, C. *et al.* Label-free biomedical imaging with high sensitivity by stimulated Raman scattering microscopy. *Science* **322**, 1857-1861 (2008).
- [400] Boyd, R. W. *Nonlinear optics*. (Academic press, 2003).
- [401] Harutyunyan, H., Volpe, G. & Novotny, L. Nonlinear optical antennas. *Optical antennas, Cambridge University Press, New York*, 131-143 (2012).
- [402] Hakuta, K., Marmet, L. & Stoicheff, B. Electric-field-induced second-harmonic generation with reduced absorption in atomic hydrogen. *Physical review letters* **66**, 596 (1991).
- [403] Terhune, R., Maker, P. & Savage, C. Optical harmonic generation in calcite. *Physical Review Letters* **8**, 404 (1962).
- [404] Almeida, V. R., Barrios, C. A., Panepucci, R. R. & Lipson, M. All-optical control of light on a silicon chip. *Nature* **431**, 1081 (2004).
- [405] Nozaki, K., Tanabe, T., Shinya, A., Matsuo, S., Sato, T., Taniyama, H. *et al.* Sub-femtojoule all-optical switching using a photonic-crystal nanocavity. *Nature Photonics* **4**, 477 (2010).
- [406] Pacifici, D., Lezec, H. J. & Atwater, H. A. All-optical modulation by plasmonic excitation of CdSe quantum dots. *Nature photonics* **1**, 402 (2007).
- [407] MacDonald, K. F., Sámson, Z. L., Stockman, M. I. & Zheludev, N. I. Ultrafast active plasmonics. *Nature Photonics* **3**, 55 (2009).
- [408] Chang, D. E., Sørensen, A. S., Demler, E. A. & Lukin, M. D. A single-photon transistor using nanoscale surface plasmons. *Nature Physics* **3**, 807 (2007).
- [409] Cai, W., Vasudev, A. P. & Brongersma, M. L. Electrically controlled nonlinear generation of light with plasmonics. *Science* **333**, 1720-1723 (2011).
- [410] Kang, L., Cui, Y., Lan, S., Rodrigues, S. P., Brongersma, M. L. & Cai, W. Electrifying photonic metamaterials for tunable nonlinear optics. *Nature communications* **5** (2014).
- [411] Park, I.-Y., Kim, S., Choi, J., Lee, D.-H., Kim, Y.-J., Kling, M. F. *et al.* Plasmonic generation of ultrashort extreme-ultraviolet light pulses. *Nature Photonics* **5**, 677 (2011).

- [412] Sivis, M., Duwe, M., Abel, B. & Ropers, C. Extreme-ultraviolet light generation in plasmonic nanostructures. *Nature Physics* **9**, 304 (2013).
- [413] Han, S., Kim, H., Kim, Y. W., Kim, Y.-J., Kim, S., Park, I.-Y. *et al.* High-harmonic generation by field enhanced femtosecond pulses in metal-sapphire nanostructure. *Nature communications* **7**, 13105 (2016).
- [414] Kim, S., Jin, J., Kim, Y.-J., Park, I.-Y., Kim, Y. & Kim, S.-W. High-harmonic generation by resonant plasmon field enhancement. *Nature* **453**, 757-760 (2008).
- [415] Harutyunyan, H., Palomba, S., Renger, J., Quidant, R. & Novotny, L. Nonlinear dark-field microscopy. *Nano letters* **10**, 5076-5079 (2010).
- [416] Palomba, S. & Novotny, L. Near-field imaging with a localized nonlinear light source. *Nano letters* **9**, 3801-3804 (2009).
- [417] Kravtsov, V., Ulbricht, R., Atkin, J. M. & Raschke, M. B. Plasmonic nanofocused four-wave mixing for femtosecond near-field imaging. *Nature nanotechnology* **11**, 459 (2016).
- [418] Fleischer, J. W., Segev, M., Efremidis, N. K. & Christodoulides, D. N. Observation of two-dimensional discrete solitons in optically induced nonlinear photonic lattices. *Nature* **422**, 147 (2003).
- [419] Ye, F., Mihalache, D., Hu, B. & Panoiu, N. C. Subwavelength plasmonic lattice solitons in arrays of metallic nanowires. *Physical review letters* **104**, 106802 (2010).
- [420] Krasavin, A., Ginzburg, P., Wurtz, G. & Zayats, A. Nonlocality-driven supercontinuum white light generation in plasmonic nanostructures. *Nature communications* **7**, 11497 (2016).
- [421] Halir, R., Okawachi, Y., Levy, J., Foster, M., Lipson, M. & Gaeta, A. Ultrabroadband supercontinuum generation in a CMOS-compatible platform. *Optics letters* **37**, 1685-1687 (2012).
- [422] Wang, G., Marie, X., Gerber, I., Amand, T., Lagarde, D., Bouet, L. *et al.* Giant enhancement of the optical second-harmonic emission of WSe<sub>2</sub> monolayers by laser excitation at exciton resonances. *Physical review letters* **114**, 097403 (2015).
- [423] Yin, X., Ye, Z., Chenet, D. A., Ye, Y., O'Brien, K., Hone, J. C. *et al.* Edge nonlinear optics on a MoS<sub>2</sub> atomic monolayer. *Science* **344**, 488-490 (2014).
- [424] Chen, H., Corboliou, V., Solntsev, A. S., Choi, D.-Y., Vincenti, M. A., De Ceglia, D. *et al.* Enhanced second-harmonic generation from two-dimensional MoSe<sub>2</sub> on a silicon waveguide. *Light: Science & Applications* **6**, e17060 (2017).

- [425] Kumar, N., Najmaei, S., Cui, Q., Ceballos, F., Ajayan, P. M., Lou, J. *et al.* Second harmonic microscopy of monolayer MoS<sub>2</sub>. *Physical Review B* **87**, 161403 (2013).
- [426] Seyler, K. L., Schaibley, J. R., Gong, P., Rivera, P., Jones, A. M., Wu, S. *et al.* Electrical control of second-harmonic generation in a WSe<sub>2</sub> monolayer transistor. *Nature nanotechnology* **10**, 407 (2015).
- [427] Shen, Y. Surface properties probed by second-harmonic and sum-frequency generation. *Nature* **337**, 519-525 (1989).
- [428] Corn, R. M. & Higgins, D. A. Optical second harmonic generation as a probe of surface chemistry. *Chemical reviews* **94**, 107-125 (1994).
- [429] Geiger, F. M. Second harmonic generation, sum frequency generation, and  $\chi(3)$ : dissecting environmental interfaces with a nonlinear optical Swiss Army knife. *Annual review of physical chemistry* **60**, 61-83 (2009).
- [430] Celebrano, M., Wu, X., Baselli, M., Großmann, S., Biagioni, P., Locatelli, A. *et al.* Mode matching in multiresonant plasmonic nanoantennas for enhanced second harmonic generation. *Nature nanotechnology* **10**, 412 (2015).
- [431] Butet, J., Duboisset, J., Bachelier, G., Russier-Antoine, I., Benichou, E., Jonin, C. *et al.* Optical second harmonic generation of single metallic nanoparticles embedded in a homogeneous medium. *Nano letters* **10**, 1717-1721 (2010).
- [432] Thyagarajan, K., Butet, J. r. m. & Martin, O. J. Augmenting second harmonic generation using Fano resonances in plasmonic systems. *Nano letters* **13**, 1847-1851 (2013).
- [433] Bouhelier, A., Beversluis, M., Hartschuh, A. & Novotny, L. Near-field second-harmonic generation induced by local field enhancement. *Physical review letters* **90**, 013903 (2003).
- [434] Pu, Y., Grange, R., Hsieh, C.-L. & Psaltis, D. Nonlinear optical properties of core-shell nanocavities for enhanced second-harmonic generation. *Physical review letters* **104**, 207402 (2010).
- [435] Lehr, D., Reinhold, J. r., Thiele, I., Hartung, H., Dietrich, K., Menzel, C. *et al.* Enhancing second harmonic generation in gold nanoring resonators filled with lithium niobate. *Nano letters* **15**, 1025-1030 (2015).
- [436] Wang, Z., Dong, Z., Zhu, H., Jin, L., Chiu, M.-H., Li, L.-J. *et al.* Selectively Plasmon-Enhanced Second-Harmonic Generation from Monolayer Tungsten Diselenide on Flexible Substrates. *ACS nano* (2018).

- [437] Wen, X., Xu, W., Zhao, W., Khurgin, J. B. & Xiong, Q. Plasmonic Hot Carriers-Controlled Second Harmonic Generation in WSe<sub>2</sub> Bilayers. *Nano letters* **18**, 1686-1692 (2018).
- [438] Zhang, Y., Grady, N. K., Ayala-Orozco, C. & Halas, N. J. Three-dimensional nanostructures as highly efficient generators of second harmonic light. *Nano letters* **11**, 5519-5523 (2011).
- [439] Canfield, B. K., Husu, H., Laukkanen, J., Bai, B., Kuittinen, M., Turunen, J. *et al.* Local field asymmetry drives second-harmonic generation in noncentrosymmetric nanodimers. *Nano Letters* **7**, 1251-1255 (2007).
- [440] Husu, H., Siikanen, R., Makitalo, J., Lehtolahti, J., Laukkanen, J., Kuittinen, M. *et al.* Metamaterials with tailored nonlinear optical response. *Nano letters* **12**, 673-677 (2012).
- [441] Klein, M. W., Enkrich, C., Wegener, M. & Linden, S. Second-harmonic generation from magnetic metamaterials. *Science* **313**, 502-504 (2006).
- [442] Linden, S., Niesler, F., Förstner, J., Grynko, Y., Meier, T. & Wegener, M. Collective effects in second-harmonic generation from split-ring-resonator arrays. *Physical review letters* **109**, 015502 (2012).
- [443] Zhang, Y., Wen, F., Zhen, Y.-R., Nordlander, P. & Halas, N. J. Coherent Fano resonances in a plasmonic nanocluster enhance optical four-wave mixing. *Proceedings of the National Academy of Sciences* **110**, 9215-9219 (2013).
- [444] Danckwerts, M. & Novotny, L. Optical frequency mixing at coupled gold nanoparticles. *Physical Review Letters* **98**, 026104 (2007).
- [445] Castro-Lopez, M., Brinks, D., Sapienza, R. & van Hulst, N. F. Aluminum for nonlinear plasmonics: resonance-driven polarized luminescence of Al, Ag, and Au nanoantennas. *Nano letters* **11**, 4674-4678 (2011).
- [446] Gu, T., Petrone, N., McMillan, J. F., van der Zande, A., Yu, M., Lo, G.-Q. *et al.* Regenerative oscillation and four-wave mixing in graphene optoelectronics. *Nature Photonics* **6**, 554 (2012).
- [447] Soavi, G., Wang, G., Rostami, H., Purdie, D. G., De Fazio, D., Ma, T. *et al.* Broadband, electrically tunable third-harmonic generation in graphene. *Nature nanotechnology*, 1 (2018).
- [448] Hafez, H., Kovalev, S., Deinert, J., Mics, Z., Green, B., Awari, N. *et al.* Extremely efficient terahertz high-harmonic generation in graphene by hot Dirac fermions. *Nature* (2018).

- [449] Harutyunyan, H., Volpe, G., Quidant, R. & Novotny, L. Enhancing the nonlinear optical response using multifrequency gold-nanowire antennas. *Physical review letters* **108**, 217403 (2012).
- [450] Aouani, H., Rahmani, M., Navarro-Cía, M. & Maier, S. A. Third-harmonic-upconversion enhancement from a single semiconductor nanoparticle coupled to a plasmonic antenna. *Nature nanotechnology* **9**, 290 (2014).
- [451] Nielsen, M. P., Shi, X., Dichtl, P., Maier, S. A. & Oulton, R. F. Giant nonlinear response at a plasmonic nanofocus drives efficient four-wave mixing. *Science* **358**, 1179-1181 (2017).
- [452] Britnell, L., Ribeiro, R., Eckmann, A., Jalil, R., Belle, B., Mishchenko, A. *et al.* Strong light-matter interactions in heterostructures of atomically thin films. *Science* **340**, 1311-1314 (2013).
- [453] Bouhelier, A., Bachelot, R., Lerondel, G., Kostcheev, S., Royer, P. & Wiederrecht, G. Surface plasmon characteristics of tunable photoluminescence in single gold nanorods. *Physical review letters* **95**, 267405 (2005).
- [454] Boyd, G., Yu, Z. & Shen, Y. Photoinduced luminescence from the noble metals and its enhancement on roughened surfaces. *Physical Review B* **33**, 7923 (1986).
- [455] Wang, H., Huff, T. B., Zweifel, D. A., He, W., Low, P. S., Wei, A. *et al.* In vitro and in vivo two-photon luminescence imaging of single gold nanorods. *Proceedings of the National Academy of Sciences of the United States of America* **102**, 15752-15756 (2005).
- [456] Shi, C., Soltani, S. & Armani, A. M. Gold nanorod plasmonic upconversion microlaser. *Nano letters* **13**, 5827-5831 (2013).
- [457] Harutyunyan, H., Martinson, A. B., Rosenmann, D., Khorashad, L. K., Besteiro, L. V., Govorov, A. O. *et al.* Anomalous ultrafast dynamics of hot plasmonic electrons in nanostructures with hot spots. *Nature nanotechnology* **10**, 770 (2015).
- [458] Haug, T., Klemm, P., Bange, S. & Lupton, J. M. Hot-electron intraband luminescence from single hot spots in noble-metal nanoparticle films. *Physical review letters* **115**, 067403 (2015).
- [459] Beversluis, M. R., Bouhelier, A. & Novotny, L. Continuum generation from single gold nanostructures through near-field mediated intraband transitions. *Physical Review B* **68**, 115433 (2003).
- [460] Sobhani, A., Knight, M. W., Wang, Y., Zheng, B., King, N. S., Brown, L. V. *et al.* Narrowband photodetection in the near-infrared with a plasmon-induced hot electron device. *Nature communications* **4**, 1643 (2013).

- [461] Chalabi, H., Schoen, D. & Brongersma, M. L. Hot-electron photodetection with a plasmonic nanostripe antenna. *Nano letters* **14**, 1374-1380 (2014).
- [462] Naik, G. V. & Dionne, J. A. Photon upconversion with hot carriers in plasmonic systems. *Applied Physics Letters* **107**, 133902 (2015).
- [463] Walsh, G. F. & Dal Negro, L. Enhanced second harmonic generation by photonic-plasmonic Fano-type coupling in nanoplasmonic arrays. *Nano letters* **13**, 3111-3117 (2013).
- [464] Genevet, P., Tetienne, J.-P., Gatzogiannis, E., Blanchard, R., Kats, M. A., Scully, M. O. *et al.* Large enhancement of nonlinear optical phenomena by plasmonic nanocavity gratings. *Nano Letters* **10**, 4880-4883 (2010).
- [465] Li, G., Chen, S., Pholchai, N., Reineke, B., Wong, P. W. H., Pun, E. Y. B. *et al.* Continuous control of the nonlinearity phase for harmonic generations. *Nature materials* **14**, 607 (2015).
- [466] Renger, J., Quidant, R., Van Hulst, N. & Novotny, L. Surface-enhanced nonlinear four-wave mixing. *Physical review letters* **104**, 046803 (2010).
- [467] Grynberg, G., Aspect, A. & Fabre, C. *Introduction to quantum optics: from the semi-classical approach to quantized light.* (Cambridge university press, 2010).
- [468] Strauf, S., Hennessy, K., Rakher, M., Choi, Y.-S., Badolato, A., Andreani, L. *et al.* Self-tuned quantum dot gain in photonic crystal lasers. *Physical review letters* **96**, 127404 (2006).
- [469] Yariv, A. Quantum electronics, 3rd. Edn. (John Wiley & Sons, New York, 1988) p **389** (1989).
- [470] Fan, H. Temperature dependence of the energy gap in semiconductors. *Physical Review* **82**, 900 (1951).
- [471] Najmaei, S., Liu, Z., Zhou, W., Zou, X., Shi, G., Lei, S. *et al.* Vapour phase growth and grain boundary structure of molybdenum disulphide atomic layers. *Nature materials* **12**, 754 (2013).
- [472] Wang, X., Gong, Y., Shi, G., Chow, W. L., Keyshar, K., Ye, G. *et al.* Chemical vapor deposition growth of crystalline monolayer MoSe<sub>2</sub>. *ACS nano* **8**, 5125-5131 (2014).
- [473] Wu, S., Huang, C., Aivazian, G., Ross, J. S., Cobden, D. H. & Xu, X. Vapor-solid growth of high optical quality MoS<sub>2</sub> monolayers with near-unity valley polarization. *Acs Nano* **7**, 2768-2772 (2013).

- [474] Eda, G., Yamaguchi, H., Voiry, D., Fujita, T., Chen, M. & Chhowalla, M. Photoluminescence from chemically exfoliated MoS<sub>2</sub>. *Nano letters* **11**, 5111-5116 (2011).
- [475] Korn, T., Heydrich, S., Hirmer, M., Schmutzler, J. & Schüller, C. Low-temperature photocarrier dynamics in monolayer MoS<sub>2</sub>. *Applied Physics Letters* **99**, 102109 (2011).
- [476] Ross, J. S., Wu, S., Yu, H., Ghimire, N. J., Jones, A. M., Aivazian, G. *et al.* Electrical control of neutral and charged excitons in a monolayer semiconductor. *Nature communications* **4**, 1474 (2013).
- [477] McCall, S., Levi, A., Slusher, R., Pearson, S. & Logan, R. Whispering-gallery mode microdisk lasers. *Applied physics letters* **60**, 289-291 (1992).
- [478] Faist, J., Gmachl, C., Striccoli, M., Sirtori, C., Capasso, F., Sivco, D. L. *et al.* Quantum cascade disk lasers. *Applied physics letters* **69**, 2456-2458 (1996).
- [479] Mahler, L., Tredicucci, A., Beltram, F., Walther, C., Faist, J., Witzigmann, B. *et al.* Vertically emitting microdisk lasers. *Nature Photonics* **3**, 46 (2009).
- [480] Altug, H., Englund, D. & Vučković, J. Ultrafast photonic crystal nanocavity laser. *Nature physics* **2**, 484 (2006).
- [481] Ellis, B., Mayer, M. A., Shambat, G., Sarmiento, T., Harris, J., Haller, E. E. *et al.* Ultralow-threshold electrically pumped quantum-dot photonic-crystal nanocavity laser. *Nature photonics* **5**, 297 (2011).
- [482] Zheludev, N. I., Prosvirnin, S., Papisimakis, N. & Fedotov, V. Lasing spaser. *Nature Photonics* **2**, 351 (2008).
- [483] Ma, R.-M., Ota, S., Li, Y., Yang, S. & Zhang, X. Explosives detection in a lasing plasmon nanocavity. *Nature nanotechnology* **9**, 600 (2014).
- [484] Stockman, M. I. Nanoplasmonic sensing and detection. *Science* **348**, 287-288 (2015).
- [485] Galanzha, E. I., Weingold, R., Nedosekin, D. A., Sarimollaoglu, M., Nolan, J., Harrington, W. *et al.* Spaser as a biological probe. *Nature communications* **8**, 15528 (2017).
- [486] Seidel, J., Grafström, S. & Eng, L. Stimulated emission of surface plasmons at the interface between a silver film and an optically pumped dye solution. *Physical review letters* **94**, 177401 (2005).
- [487] Noginov, M., Zhu, G., Belgrave, A., Bakker, R., Shalae, V., Narimanov, E. *et al.* Demonstration of a spaser-based nanolaser. *Nature* **460**, 1110 (2009).

- [488] Bermúdez-Ureña, E., Tutuncuoglu, G., Cuerda, J., Smith, C. L., Bravo-Abad, J., Bozhevolnyi, S. I. *et al.* Plasmonic waveguide-integrated nanowire laser. *Nano letters* **17**, 747-754 (2017).
- [489] Ma, R.-M., Oulton, R. F., Sorger, V. J., Bartal, G. & Zhang, X. Room-temperature sub-diffraction-limited plasmon laser by total internal reflection. *Nature materials* **10**, 110 (2011).
- [490] van Beijnum, F., van Veldhoven, P. J., Geluk, E. J., de Dood, M. J., Gert, W. & van Exter, M. P. Surface plasmon lasing observed in metal hole arrays. *Physical review letters* **110**, 206802 (2013).
- [491] Kern, J., Trügler, A., Niehues, I., Ewering, J., Schmidt, R., Schneider, R. *et al.* Nanoantenna-enhanced light–matter interaction in atomically thin WS<sub>2</sub>. *ACS Photonics* **2**, 1260-1265 (2015).
- [492] Palacios, E., Park, S., Lauhon, L. & Aydin, K. Identifying excitation and emission rate contributions to plasmon-enhanced photoluminescence from monolayer MoS<sub>2</sub> using a tapered gold nanoantenna. *ACS Photonics* **4**, 1602-1606 (2017).
- [493] Taghinejad, H., Shams-Mousavi, S. H., Gong, Y., Taghinejad, M., Eftekhar, A. A., Ajayan, P. *et al.* Lattice Plasmon Induced Large Enhancement of Excitonic Emission in Monolayer Metal Dichalcogenides. *Plasmonics* **12**, 1975-1981 (2017).
- [494] Fofang, N. T., Grady, N. K., Fan, Z., Govorov, A. O. & Halas, N. J. Plexciton dynamics: exciton–plasmon coupling in a J-aggregate–Au nanoshell complex provides a mechanism for nonlinearity. *Nano letters* **11**, 1556-1560 (2011).
- [495] Manjavacas, A., Abajo, F. G. a. d. & Nordlander, P. Quantum plexcitonics: strongly interacting plasmons and excitons. *nano letters* **11**, 2318-2323 (2011).
- [496] Khitrova, G., Gibbs, H., Kira, M., Koch, S. W. & Scherer, A. Vacuum Rabi splitting in semiconductors. *Nature Physics* **2**, 81 (2006).
- [497] Vasa, P., Pomraenke, R., Schwieger, S., Mazur, Y. I., Kunets, V., Srinivasan, P. *et al.* Coherent exciton–surface-plasmon-polariton interaction in hybrid metal-semiconductor nanostructures. *Physical review letters* **101**, 116801 (2008).
- [498] Liu, W., Lee, B., Naylor, C. H., Ee, H.-S., Park, J., Johnson, A. C. *et al.* Strong exciton–plasmon coupling in MoS<sub>2</sub> coupled with plasmonic lattice. *Nano letters* **16**, 1262-1269 (2016).
- [499] Lee, B., Liu, W., Naylor, C. H., Park, J., Malek, S. C., Berger, J. S. *et al.* Electrical tuning of exciton–plasmon polariton coupling in monolayer MoS<sub>2</sub> integrated with plasmonic nanoantenna lattice. *Nano letters* **17**, 4541-4547 (2017).

- [500] Zheng, D., Zhang, S., Deng, Q., Kang, M., Nordlander, P. & Xu, H. Manipulating Coherent Plasmon–Exciton Interaction in a Single Silver Nanorod on Monolayer WSe<sub>2</sub>. *Nano letters* **17**, 3809-3814 (2017).
- [501] Kleemann, M.-E., Chikkaraddy, R., Alexeev, E. M., Kos, D., Carnegie, C., Deacon, W. *et al.* Strong-coupling of WSe<sub>2</sub> in ultra-compact plasmonic nanocavities at room temperature. *Nature communications* **8**, 1296 (2017).
- [502] Englund, D., Fattal, D., Waks, E., Solomon, G., Zhang, B., Nakaoka, T. *et al.* Controlling the spontaneous emission rate of single quantum dots in a two-dimensional photonic crystal. *Physical review letters* **95**, 013904 (2005).
- [503] Togan, E., Chu, Y., Trifonov, A., Jiang, L., Maze, J., Childress, L. *et al.* Quantum entanglement between an optical photon and a solid-state spin qubit. *Nature* **466**, 730 (2010).
- [504] Fushman, I., Englund, D., Faraon, A., Stoltz, N., Petroff, P. & Vučković, J. Controlled phase shifts with a single quantum dot. *science* **320**, 769-772 (2008).
- [505] Bayer, M., Reinecke, T., Weidner, F., Larionov, A., McDonald, A. & Forchel, A. Inhibition and enhancement of the spontaneous emission of quantum dots in structured microresonators. *Physical review letters* **86**, 3168 (2001).
- [506] Li, Y., Chernikov, A., Zhang, X., Rigosi, A., Hill, H. M., van der Zande, A. M. *et al.* Measurement of the optical dielectric function of monolayer transition-metal dichalcogenides: MoS<sub>2</sub>, MoSe<sub>2</sub>, WS<sub>2</sub>, and WSe<sub>2</sub>. *Physical Review B* **90**, 205422 (2014).
- [507] Arora, A., Noky, J., Drüppel, M., Jariwala, B., Deilmann, T., Schneider, R. *et al.* Highly Anisotropic in-Plane Excitons in Atomically Thin and Bulklike 1 T'-ReSe<sub>2</sub>. *Nano letters* **17**, 3202-3207 (2017).
- [508] Zhang, X.-X., You, Y., Zhao, S. Y. F. & Heinz, T. F. Experimental evidence for dark excitons in monolayer WSe<sub>2</sub>. *Physical review letters* **115**, 257403 (2015).
- [509] Zhang, X.-X., Cao, T., Lu, Z., Lin, Y.-C., Zhang, F., Wang, Y. *et al.* Magnetic brightening and control of dark excitons in monolayer WSe<sub>2</sub>. *Nature nanotechnology* **12**, 883 (2017).
- [510] Zhou, Y., Scuri, G., Wild, D. S., High, A. A., Dibos, A., Jauregui, L. A. *et al.* Probing dark excitons in atomically thin semiconductors via near-field coupling to surface plasmon polaritons. *Nature nanotechnology* **12**, 856 (2017).
- [511] Liu, Y., Weiss, N. O., Duan, X., Cheng, H.-C., Huang, Y. & Duan, X. Van der Waals heterostructures and devices. *Nature Reviews Materials* **1**, 16042 (2016).

- [512] Withers, F., Del Pozo-Zamudio, O., Mishchenko, A., Rooney, A., Gholinia, A., Watanabe, K. *et al.* Light-emitting diodes by band-structure engineering in van der Waals heterostructures. *Nature materials* **14**, 301 (2015).
- [513] Hone, J. & Kim, P. Atomically thin p–n junctions with van der Waals heterointerfaces. (2014).
- [514] Furchi, M. M., Pospischil, A., Libisch, F., Burgdörfer, J. & Mueller, T. Photovoltaic effect in an electrically tunable van der Waals heterojunction. *Nano letters* **14**, 4785-4791 (2014).
- [515] Ross, J. S., Klement, P., Jones, A. M., Ghimire, N. J., Yan, J., Mandrus, D. G. *et al.* Electrically tunable excitonic light-emitting diodes based on monolayer WSe<sub>2</sub> pn junctions. *Nature nanotechnology* **9**, 268-272 (2014).
- [516] Lopez-Sanchez, O., Alarcon Llado, E., Koman, V., Fontcuberta i Morral, A., Radenovic, A. & Kis, A. Light generation and harvesting in a van der Waals heterostructure. *Acs Nano* **8**, 3042-3048 (2014).
- [517] Li, M.-Y., Shi, Y., Cheng, C.-C., Lu, L.-S., Lin, Y.-C., Tang, H.-L. *et al.* Epitaxial growth of a monolayer WSe<sub>2</sub>-MoS<sub>2</sub> lateral pn junction with an atomically sharp interface. *Science* **349**, 524-528 (2015).
- [518] Zhang, X.-Q., Lin, C.-H., Tseng, Y.-W., Huang, K.-H. & Lee, Y.-H. Synthesis of lateral heterostructures of semiconducting atomic layers. *Nano letters* **15**, 410-415 (2014).
- [519] Clark, G., Schaibley, J. R., Ross, J., Taniguchi, T., Watanabe, K., Hendrickson, J. R. *et al.* Single defect light-emitting diode in a van der Waals heterostructure. *Nano letters* **16**, 3944-3948 (2016).
- [520] Lien, D.-H., Amani, M., Desai, S. B., Ahn, G. H., Han, K., He, J.-H. *et al.* Large-area and bright pulsed electroluminescence in monolayer semiconductors. *Nature communications* **9**, 1229 (2018).
- [521] Allain, A., Kang, J., Banerjee, K. & Kis, A. Electrical contacts to two-dimensional semiconductors. *Nature Materials* **14**, 1195 (2015).
- [522] Kim, C., Moon, I., Lee, D., Choi, M. S., Ahmed, F., Nam, S. *et al.* Fermi level pinning at electrical metal contacts of monolayer molybdenum dichalcogenides. *ACS nano* **11**, 1588-1596 (2017).
- [523] Knight, M. W., Sobhani, H., Nordlander, P. & Halas, N. J. Photodetection with active optical antennas. *Science* **332**, 702-704 (2011).
- [524] Fedyanin, D. Y., Krasavin, A. V., Arsenin, A. V. & Zayats, A. V. Surface plasmon polariton amplification upon electrical injection in highly integrated plasmonic circuits. *Nano letters* **12**, 2459-2463 (2012).

- [525] Svintsov, D. A., Arsenin, A. V. & Fedyanin, D. Y. Full loss compensation in hybrid plasmonic waveguides under electrical pumping. *Optics Express* **23**, 19358-19375 (2015).
- [526] Livani, A. M. & Kaatuzian, H. Design and simulation of an electrically pumped Schottky-junction-based plasmonic amplifier. *Applied optics* **54**, 2164-2173 (2015).
- [527] Zomer, P., Guimarães, M., Brant, J., Tombros, N. & Van Wees, B. Fast pick up technique for high quality heterostructures of bilayer graphene and hexagonal boron nitride. *Applied Physics Letters* **105**, 013101 (2014).
- [528] Kumar, N., Cui, Q., Ceballos, F., He, D., Wang, Y. & Zhao, H. Exciton-exciton annihilation in MoSe<sub>2</sub> monolayers. *Physical Review B* **89**, 125427 (2014).
- [529] Lin, Q.-Y., Li, Z., Brown, K. A., O'Brien, M. N., Ross, M. B., Zhou, Y. *et al.* Strong coupling between plasmonic gap modes and photonic lattice modes in DNA-assembled gold nanocube arrays. *Nano letters* **15**, 4699-4703 (2015).